

UNIVERSIDADE DE SÃO PAULO  
INSTITUTO DE QUÍMICA DE SÃO CARLOS

William Marcondes Facchinatto

**Physicochemical studies of chemically modified chitosans through Solid-  
State Nuclear Magnetic Resonance: from properties to applications**

São Carlos, Brazil

May 2021



WILLIAM MARCONDES FACCHINATTO

**Physicochemical studies of chemically modified chitosans through Solid-State Nuclear Magnetic Resonance: from properties to applications**

Thesis submitted to Instituto de Química de São Carlos of Universidade de São Paulo in partial of fulfillment of the requirements for the degree of Doctor of Sciences.

Physical Chemistry Graduate Program

Supervisor: Dr. Luiz Alberto Colnago

**Revised Copy**

The original copy can be found in the revised collection of the IQSC-USP Library

São Carlos, Brazil

May 2021

Autorizo a reprodução e divulgação total ou parcial deste trabalho, por qualquer meio convencional ou eletrônico para fins de estudo e pesquisa, desde que citada a fonte.

**Assinatura:** 

**Data:** 04 de maio de 2021

*Ficha Catalográfica elaborada pela Seção de Referência e Atendimento ao Usuário do SBI/IQSC*

Facchinatto, William Marcondes

Physicochemical studies of chemically modified chitosans through Solid-State Nuclear Magnetic Resonance: from properties to applications / William Marcondes Facchinatto. — São Carlos, 2021.

186 f.

Tese (Doutorado em Físico-Química) — Instituto de Química de São Carlos / Universidade de São Paulo, 2021.

Edição revisada

Orientador: Prof. Dr. Luiz Alberto Colnago

1. Quitosana. 2. RMN no estado sólido. 3. Nanowhiskers de quitina. 4. Nanopartículas anfífilas. 5. Candidíase vulvovaginal. I. Título.



To your contagious joy, simplicity and charisma...  
...that defined your character and guided your life,  
which I have always admired and will always be remembered...

I dedicate this professional stage and personal experience to you

**Mercedes Eleonor Lamas Marcondes**

(1933-2016)



## ACKNOWLEDGEMENTS

First of all, I would like to thank Carla Ferezin for her companionship, good times and for the support and encouragement on those of greatest difficulty. Nevertheless, to my dogs Diva and Hugo for every day's affection and happiness, and to my family members, especially to my aunt Rejane Lamas Marcondes, who helped me a lot to get here.

To my supervisor Dr. Luiz Alberto Colnago for having openly accepted me in his research group at Embrapa Instrumentation, for his confidence in my work and for all the opportunities that allowed my professional development.

To professors Dr. Eduardo Ribeiro de Azevedo (IFSC/USP) and Dr. Sergio Paulo Campana Filho (IQSC/USP) for the helpness and collaborative support provided throughout the evolution of this work.

To professor Dr. Bruno Sarmento and Dr. José das Neves for supervision and co-supervision, respectively, at the Institute for Research and Innovation in Health (i3S) / National Institute of Biomedical Engineering (INEB)/ University of Porto (UP) in the city of Porto, Portugal, during the period abroad held by doctoral fellowship.

To professors Dr<sup>a</sup>. Sonia Maria Cabral de Menezes (PETROBRAS) and Dr<sup>a</sup>. Rosane Aguiar da Silva San Gil (IQ/UFRJ) for accepting to participate as examination board and to all contributions made and properly included in the final version of this Thesis.

To professors, researchers and esteemed partners Tiago Bueno de Moraes, Rubens Bernardes Filho, Danilo Martins dos Santos, Andrea Bukzem, Daniella de Souza e Silva, Anderson Fiamingo, Filipe Habitzreuter, Douglas Flores, Rodrigo Garcia, Joana Galante and Letícia Mesquita for their valuable collaboration in different stages throughout this work.

To the technicians and administrative team of IQSC/ USP and Embrapa Instrumentation, in particular to Viviane Faria Soares for her unmatched efficiency and promptness.

To all my friends and to the excellent "relaxation" moments with the colleagues of the NMR Group from Embrapa Instrumentation and Macromolecular Materials and Lignocellulosic Fibers Group from IQSC/USP.

I also thank the Brazilian funding agencies São Paulo Research Foundation, FAPESP, for the granting of scholarships and financial assistance in Brazil (2016/20970-2) and Portugal (2019/11135-0), and National Council for Scientific and Technological Development, CNPq, (141353/2016-3) for funding the first months of the doctorate. This study was financed in part by National Council for the Improvement of Higher Education, CAPES – Finance Code 001.



*“Escrever com desenvoltura é uma arte que exige formação, treino, sensibilidade. A arte não é o automático, a arte é, sim, dedicação.”*

MARIO SERGIO CORTELLA

Pensar bem nos faz bem!

*“O conhecimento emerge apenas através da invenção e da reinvenção, através da inquietante, impaciente, contínua e esperançosa investigação que os seres humanos buscam no mundo, com o mundo e uns com os outros.”*

PAULO FREIRE

A Pedagogia do Oprimido



## RESUMO

O objetivo principal desta Tese está focado na condição preparativa para a investigação das propriedades de quitosanas modificadas quimicamente e o potencial de aplicação desses materiais em diferentes áreas do conhecimento. Para tanto, diferentes técnicas de RMN em alto e baixo campo magnético foram aplicadas a fim de elucidar características intrínsecas de quitinas, quitosanas e derivados certas vezes já verificados por outros métodos. Para atender ao requisito de cada objetivo específico, foram realizadas diversas caracterizações, incluindo não espectroscópicas e ensaios biológicas. Estudos independentes foram desenvolvidos e apresentados sequencialmente da maneira mais clara e concisa possível, sendo divididos em cinco Capítulos distintos, cada um diretamente relacionado a alguma proposta inovadora. Embora relacionados entre si, o estado da arte e as aplicabilidades específicas foram exploradas. Assim, foi proposta no CAPÍTULO I uma nova abordagem baseada em espectroscopia de  $^{13}\text{C}$  NMR de estado sólido de alta resolução para quantificar o índice de cristalinidade de quitosanas (Ch) preparadas com diferentes graus médios de acetilação ( $\overline{DA}$ ) e massa molar ( $\overline{M}_w$ ). Os resultados mostram que o ordenamento das cadeias a curto alcance pode ser atribuída através dos sinais C4/C6 no  $^{13}\text{C}$  CPMAS, sendo que o procedimento de desconvolução entre as fases revelou cristalinidade crescente com ( $\overline{DA}$ ), confirmado pela análise multivariada SVD. No CAPÍTULO II, o mesmo conjunto de quitosanas foi analisado por relaxometria no domínio do tempo (RMN-DT) usando a sequência de pulso RK-ROSE para adquirir o sinal de  $^1\text{H}$  NMR de materiais no estado sólido. Os dados de RK-ROSE foram modelados usando regressão multivariada PLS, que mostrou uma elevada correlação entre o perfil de decaimento do sinal e os graus médios de acetilação e índice de cristalinidade. No CAPÍTULO III, foram sistematicamente investigados os efeitos do tamanho de partícula / granulometria na acidólise da  $\beta$ -quitina (BCH) visando a preparação de *nanowhiskers* de  $\beta$ -quitina (CWH). Os resultados mostraram que as características dos *nanowhiskers* podem ser acessadas escolhendo-se adequadamente o tamanho médio de partícula da quitina de partida. No CAPÍTULO IV, duas amostras de N-(2-hidroxi)-propil-3-trimetilamônio, O-palmitoil quitosana (DPCat) com diferentes graus médios de quaternização denominados como DPCat35 ( $\overline{DQ} = 35\%$ ) e DPCat80 ( $\overline{DQ} = 80\%$ ), foram sintetizados com sucesso pela reação de GTMAC com o derivado de O-palmitoil quitosana (DPCh) ( $\overline{DS} = 12\%$ ). Esses derivados anfífilos de quitosana eram totalmente solúveis em água e mostraram aumento significativo da estabilidade eletrostática de uma nanoestrutura micelar automontada devido à sua camada externa carregada positivamente. Ensaios mucoadesivos e de citotoxicidade *in vitro* para células de fibroblastos saudáveis de camundongo (Balb/C 3T3) e linhagens celulares de câncer de próstata humano (DU145) e de câncer de fígado (HepG2/C3A) revelaram que as propriedades biológicas dos derivados de DPCat eram fortemente dependentes de  $\overline{DQ}$ . DPCat35 apresentou melhores interações com o tecido biológico e com as glicoproteínas mucinas em pH 7,4. Esses derivados DPCat foram usados posteriormente no CAPÍTULO V como nanocarreadores de clotrimazol (CLT-NPs) para o tratamento tópico da candidíase vulvovaginal (VVC). O nanossistema apresentou liberação sustentada de fármaco independente do pH por até 24 horas, o que afetou tanto a atividade anti-Candida *in vitro* quanto a citotoxicidade. CLT-NPs apresentou valores de índice de seletividade favoráveis para um conjunto de cepas padrão e isolados clínicos de *Candida* spp. e linhas celulares do trato genital feminino (HEC-1-A, Ca Ski e HeLa), em comparação com o fármaco livre. CLT-NPs também melhorou a permeabilidade da droga *in vitro* em monocamadas de células HEC-1-A e Ca Ski, sugerindo assim que o nanotransportador pode fornecer níveis mais elevados de tecido da mucosa do composto ativo. O formato autêntico deste documento torna-o especialmente útil como ponto de partida para o desenvolvimento de diferentes segmentos de pesquisa. Dessa forma, estudos alternativos podem ampliar o foco e a aplicabilidade dos materiais e caracterizações aqui utilizados, estendendo o conhecimento para inovações distintas.

**Palavras-chave:** RMN de estado sólido, RMN no domínio do tempo, morfologia, quitosana, *nanowhiskers* de quitina, derivado anfífilo de quitosana com carga positiva permante, nanopartículas, liberação sustentada de antifúngico, candidíase vulvovaginal



## ABSTRACT

The main objective of this Thesis is to control the preparative condition for investigating the properties of chemically modified chitosans and the potential application of these materials in different fields of knowledge. For such a goal, different high- and low-NMR techniques were applied in order to elucidate intrinsic characteristics of chitins, chitosans and derivatives sometimes already verified through other methods. To fulfill the requirement of each specific objective, it were performed a series of characterizations, including non-spectroscopic and biological assays. In this sense, different studies were developed and sequentially presented in a clear and concise manner as possible, being divided into five distinguished Chapters, each one straightly related to some innovative proposal for a given research field. Although related to each other, specific state-of-the-art and applicabilities were explored. It was proposed in CHAPTER I a novel approach relied on high-resolution solid-state  $^{13}\text{C}$  NMR spectroscopy to quantify the crystallinity index of chitosans (Ch) prepared with variable average degrees of acetylation ( $\overline{DA}$ ) and average weight molecular weight ( $\overline{M}_w$ ). The results show that the short-range ordering can be assigned to C4/C6 signals on  $^{13}\text{C}$  CPMAS and, for our case, the deconvolution procedure between disordered and ordered phases revealed increasing crystallinity with  $\overline{DA}$ , as confirmed by SVD multivariate analysis. In CHAPTER II, the same set of chitosans were analyzed by time-domain relaxometry (TD-NMR) using the RK-ROSE pulse sequence to acquire  $^1\text{H}$  NMR signal of solid-state materials. RK-ROSE data were modeled by using PLS multivariate regression, which showed a high correlation between the signal decay profile and average degrees of acetylation and crystallinity index. In CHAPTER III, it was systematically investigated the effects of particle size/ granulometry on the acidolysis of  $\beta$ -chitin (BCH) aiming the preparation of  $\beta$ -chitin nanowhiskers (CWH). The results shown that several features of nanowhiskers can be accessed by choosing properly the average powder size of parent chitin. In CHAPTER IV, two samples of *N*-(2-hydroxy)-propyl-3-trimethylammonium, *O*-palmitoyl chitosan (DPCat) with different average degrees of quaternization named as DPCat35 ( $\overline{DQ} = 35\%$ ) and DPCat80 ( $\overline{DQ} = 80\%$ ), were successfully synthesized by reacting GTMAC with *O*-palmitoyl chitosan (DPCh) derivative ( $\overline{DS} = 12\%$ ). Such amphiphilic derivatives of chitosan were fully water-soluble and showed significant electrostatic stability enhancement of a self-assembly micellar nanostructure due to its positively-charged out-layer. *In vitro* mucoadhesive and cytotoxicity essays toward mouse healthy fibroblast cells (Balb/C 3T3), and human prostate cancer (DU145) and liver cancer (HepG2/C3A) cell lines revealed that the biological properties of DPCat derivatives were strongly dependent on  $\overline{DQ}$ . Additionally, DPCat35 had better interactions with the biological tissue and with mucin glycoproteins at pH 7.4. These DPCat derivatives were further used in CHAPTER V as nanocarriers of clotrimazole (CLT-NPs) for the topical treatment of vulvovaginal candidiasis (VVC). The nanosystem featured pH-independent sustained drug release up to 24 h, which affected both *in vitro* anti-*Candida* activity and cytotoxicity. The CLT-loaded nanostructured platform yielded favorable selectivity index values for a panel of standard strains and clinical isolates of *Candida* spp. and female genital tract cell lines (HEC-1-A, Ca Ski and HeLa), as compared to the free drug. CLT-NPs also improved *in vitro* drug permeability across HEC-1-A and Ca Ski cell monolayers, thus suggesting that the nanocarrier may provide higher mucosal tissue levels of the active compound. Overall, data support that CLT-NPs may be a valuable asset for the topical treatment of VVC. The authentic format of this document makes it especially useful as a starting point for the development of different research segments. In this way, alternative studies may broaden de focus and applicability of the materials and characterizations used here, extending the knowledge to distinct innovations.

**Keywords:** Solid-state NMR, time-domain NMR, morphology, chitosan, chitin nanowhiskers, positively-charged amphiphilic chitosan, nanoparticles, sustained release of antifungals, vulvovaginal candidiasis.



## LIST OF FIGURES

<b>Figure 1</b> – Idealized chemical structure of chitin / chitosan formed by GlcN and GlcNAc units at variable ratio. The numbers indicate the location of the respective carbons and hydrogens from each unit. ....	<b>21</b>
<b>Figure 2</b> – Schematic illustration of CPMG pulse sequence (a) and spin echo correction to the same phase (b). ....	<b>24</b>
<b>Figure 3</b> – Spectral line shape illustrative effect with and without $^1\text{H}$ dipolar decoupling and coupled to MAS with rotational sidebands ( $\nu_r < \Delta\nu$ ) and without ( $\nu_r > \Delta\nu$ ) (a); Schematic illustration of Cross- Polarization (CP) pulse sequence (b); Relationship between $T_a$ and $T_2^*$ on spectral line width (c). ....	<b>27</b>
<b>Figure 4</b> – Schematic illustration of DIPSHIFT pulse sequence (a) and simulated dipolar curves performed at different mobility rates ( $k$ ). ....	<b>28</b>
<b>Figure 5</b> - Schematic illustration of HETCOR pulse sequence. ....	<b>29</b>
<b>Figure 6</b> – Flowchart of all materials prepared accordingly to the proposal of each referred chapter. ....	<b>32</b>
<b>Figure 7</b> – Pictorial graphic of molecular energy of butane with respect to the dihedral angle, separated by transition states of torsion depicted by Newman projections (a); chains packaging influence from trans and gauche states and its illustrative effect on isotropic chemical shifts distributions (b). ....	<b>36</b>
<b>Figure 8</b> – Non-published results of $^{13}\text{C}$ CPMAS spectra ( $T_c = 3000 \mu\text{s}$ , $d_1 = 2 \text{ s}$ and $12 \text{ kHz}$ of spinning frequency) of cellulose samples with different average crystallinity indexes (CrI) calculated by means of C4 and C6 deconvoluted signals (a); and similarly, for C1 of starch samples (b).. ....	<b>36</b>
<b>Figure 9</b> – $^1\text{H}$ NMR spectrum of USAD Ch1x (a); Ch2x (b); Ch3x (c) with respect to the spectrum of depolymerized (3h and 6h) samples in $\text{D}_2\text{O}/\text{HCl}$ 1% (v/v), acquired at $85^\circ\text{C}$ . ....	<b>45</b>
<b>Figure 10</b> – Size-exclusion chromatogram (SEC) profiles of USAD Ch1x (a); Ch2x (b); Ch3x (c) with respect to the profile of depolymerized (3h and 6h) samples. ....	<b>46</b>
<b>Figure 11</b> – $^1\text{H}$ NMR spectrum of N-acetylated Ch samples, named as Ch60 (a); Ch45 (b); Ch35 (c); Ch25 (d); Ch15 (e) and Ch5 (f) in $\text{D}_2\text{O}/\text{HCl}$ 1% (v/v), acquired at $85^\circ\text{C}$ ....	<b>47</b>
<b>Figure 12</b> – $^1\text{H}$ NMR spectrum interval of N-acetylated Ch samples, named as Ch60 (a); Ch45 (b); Ch35 (c); Ch25 (d); Ch15 (e) and Ch5 (f), assigned to $H1'$ and $H1$ signals, used for determination of $\overline{DA}$ and $PA$ . ....	<b>48</b>
<b>Figure 13</b> – $^1\text{H}$ NMR spectrum interval of USAD Ch1x (a); Ch2x (b); Ch3x (c) with respect to the spectrum of depolymerized (3h and 6h) samples, assigned to $H1'$ and $H1$ signals, used for determination of $\overline{DA}$ and $PA$ . .....	<b>49</b>
<b>Figure 14</b> – XRD patterns of $\alpha$ - and $\beta$ Ch (a); Ch5-60 and $\beta$ Ch (b); USAD (Ch1x, Ch2x and Ch3x) and depolymerized (3h and 6h) Ch samples (c). ....	<b>50</b>
<b>Figure 15</b> – $^{13}\text{C}$ CPMAS spectra ( $d_1 = 2 \text{ s}$ and $12 \text{ kHz}$ of spinning frequency) profiles of Ch25 at variable $T_c$ values (1000 to 4000 $\mu\text{s}$ ) compared to $^{13}\text{C}$ DPMAS profile at the whole spectral range (a) covering the interval of C4, C5-C3, C6 and C2 signals (b); C1 (c) and $\text{CH}_3$ (d) signals. ....	<b>53</b>

<b>Figure 16</b> – CP build-ups for CH <sub>3</sub> and C=O groups of Ch25 (a); DIPSHIFT curves acquired from Ch25 (b); <sup>13</sup> CPMAS spectrum of α-, βCh and Ch5-60 (c); and relationship of N-acetylated Ch profiles at T <sub>c</sub> = 3000 μs, d1 = 2 s and 12 kHz of spinning frequency showing the conformational dependence of $\overline{DA}$ (d). ....	<b>55</b>
<b>Figure 17</b> – <sup>13</sup> C CPMAS spectra (T <sub>c</sub> = 3000 μs, d1 = 2 s and 12 kHz of spinning frequency) of USAD Ch1x (a); Ch2x (b) and Ch3x (c), with respect to depolymerized (3h and 6h) Ch samples. ....	<b>58</b>
<b>Figure 18</b> – <sup>13</sup> C CPMAS spectra of ChC sample showing the conformational dependence of carbon signals at variable T <sub>c</sub> values (50 to 4500 μs) (a); 2D HETCOR spectrum of ChC (b); Ch15 (c) and Ch45 (d), proving that even without C4 signal splitting, distinguished correlations can be taken regarding the same kind of protons.....	<b>59</b>
<b>Figure 19</b> – 2D HETCOR spectrum of αCh (a); βCh (b); Ch45 (c); Ch25 (d); Ch15 (e) and Ch5 (f).....	<b>60</b>
<b>Figure 20</b> – Peak deconvolution method applied on <sup>13</sup> C CPMAS spectra (T <sub>c</sub> = 3000 μs, d1 = 2 s and 12 kHz of spinning frequency) of αCh (a), βCh (b) and N-acetylated Ch5-60 (c) samples, to estimate the short- range molecular ordering from C4 and C6 signals, allowing the quantification of CrI <sub>CP</sub> .....	<b>61</b>
<b>Figure 21</b> – Peak deconvolution method applied on <sup>13</sup> C CPMAS spectra (T <sub>c</sub> = 3000 μs, d1 = 2 s and 12 kHz of spinning frequency) of Ch1x (a); Ch1x3h (b); Ch1x6h (c); Ch2x (d); Ch2x3h (e); Ch2x6h (f); Ch3x (g); Ch3x3h (h) and Ch3x6h (i) samples, to estimate the short-range molecular ordering from C4 and C6 signals, allowing the quantification of CrI <sub>CP</sub> .....	<b>62</b>
<b>Figure 22</b> – Crystallinity index calculated according to peak height (CrI <sub>1</sub> ) and amorphous subtraction (CrI <sub>2</sub> ) method from XRD patterns; average contribution of ordered domains from C4 and C6 signals on <sup>13</sup> C CPMAS spectra (CrI <sub>CP</sub> ), with respect to the DA <sub>CP</sub> of αCh, βCh, N-acetylated Ch5-60 (a); USAD and depolymerized Ch (3h and 6h) Ch (b) samples. ....	<b>63</b>
<b>Figure 23</b> – Profile of the components DA* and CrI* generated from calibration matrix, X (a); <sup>13</sup> CPMAS spectra profile relationship of βCh, Ch60 and Ch5 with the theoretical profiles of crystalline and amorphous Ch. These spectra were normalized by C1 signal area.....	<b>65</b>
<b>Figure 24</b> – Schematic illustration of MSE pulse sequence with phase cycling obtained by $\phi = 90^\circ xyxy$ (a); schematic illustration of RK-ROSE pulse sequence (b). Because MSE and RK-ROSE signals are sensitive to the magnetic dipolar interactions between the <sup>1</sup> H nuclei in the sample, the signal arising from rigid segments decay differently from those that present some molecular mobility. ....	<b>68</b>
<b>Figure 25</b> – A representative RK-ROSE signal decay fitting carried out from 0 to ~0.2 ms for each sample.....	<b>71</b>
<b>Figure 26</b> – Thermogravimetric (a; c; e; and g) and DTG (b; d; f and h) curves recorded under N <sub>2</sub> atmosphere.	<b>73</b>
<b>Figure 27</b> – RK-ROSE signal decays of αCh, βCh, Ch1x and Ch3x samples and DIPSHIFT curves of αCh used as representative profile of each related segment (a); DIPSHIFT curves of CH <sub>3</sub> group from αCh and βCh (b); Ch1x and Ch3x with respect of βCh profile (c). ....	<b>76</b>
<b>Figure 28</b> – DIPSHIFT curves from βCh (a), Ch60 (b), Ch45 (c), Ch35 (d), Ch15 (e) and Ch5 (f). ....	<b>79</b>

<b>Figure 29</b> – $^1\text{H}$ TD-NMR signal decays recorded using RK-ROSE pulse sequence of N-acetylated Ch and $\beta\text{Ch}$ samples used for PLS validation procedure (a); Correlation of $DA$ (b); $DA_{CP}$ (c); $CrI_{CP}$ (d); $CrI_1$ (e); $CrI_2$ (f) values measured using high-resolution NMR and XRD and predicted by the PLS regression model.....	<b>81</b>
<b>Figure 30</b> – Partial least squares PLS regression model from linear correlation between the predicted values of the residual of hydration (% m/m). $R^2 = 0.40$ and $RMSE = 1.91$ .....	<b>82</b>
<b>Figure 31</b> – SEM images of BCHS (a), BCHI (b) and BCHL (c); and TEM images of CWHS (d), CWHI (e) and CWHL (f). .....	<b>91</b>
<b>Figure 32</b> – AFM images of CWHL (a), CWHI (b) and CWHS (c) samples and corresponding histograms showing the length, width and aspect ratio distributions. ....	<b>92</b>
<b>Figure 33</b> – $^{13}\text{C}$ CPMAS spectra of $\beta$ -chitin (a), parent chitin samples BCHL, BCHI and BCHS (b) and the corresponding freeze-dried samples CWHL (c), CWHI (d) and CWHS (e).....	<b>93</b>
<b>Figure 34</b> – Peak deconvolution method applied on $^{13}\text{C}$ CPMAS spectra ( $T_c = 3000 \mu\text{s}$ ) of BCHL (a), CWHL (b), BCHI (c), CWHI (d), BCHS (e) and CWHS (f) samples, allowing the quantification of $CrI_{CP}$ . .....	<b>95</b>
<b>Figure 35</b> – DIPSHIFT curves of $\beta$ -chitin (a). The normalized amplitude signals ( $S(t_1)/S(t_0)$ ) were acquired during heteronuclear dipolar interaction free precession ( $t_1$ ) of first rotor spin cycle ( $t_r$ ); MSEFID signal decays of BCHS, BCHI, BCHL (b), CWHS, CWHI and CWHL samples (c); relationship of MSEFID and DIPSHIFT experiments of lyophilized samples and its parent chitin (d-f).....	<b>96</b>
<b>Figure 36</b> – X-ray diffraction patterns of BCh and WCh samples. ....	<b>99</b>
<b>Figure 37</b> – TG (a) and DTG (b) curves of BCH and CWH samples. ....	<b>100</b>
<b>Figure 38</b> – X-ray photoelectron spectroscopy of $\text{C}^* 1\text{s}$ binding energies from BCH to CWH samples (a-c). N 1s (b) and O 1s (c) of BCHL showed as a representative spectrum profile. ....	<b>101</b>
<b>Figure 39</b> – Rheological behavior of CWH suspensions verified through shear flow curves (a), frequency sweep (c) and temperature sweep measurements (c). The $T_2$ relaxation time was measured using CPMG technique as function of temperature (d).....	<b>103</b>
<b>Figure 40</b> – Schematic illustration of step-by-step synthesis of amphiphilic chitosan derivative. ....	<b>110</b>
<b>Figure 41</b> – $^1\text{H}$ NMR spectra of Ch (a), DPCh (b), DPCat35 (c) and DPCat80 (d) in $\text{D}_2\text{O}/\text{HCl}$ 1% (v/v) at $85^\circ\text{C}$ . .....	<b>117</b>
<b>Figure 42</b> – $^{13}\text{C}$ CPMAS spectra of DPCat80 (a) and DPCat35 (b) samples spinning at 12 kHz. ....	<b>119</b>
<b>Figure 43</b> – $^{15}\text{N}$ CPMAS spectra of DPCat35 (a) and DPCat80 (b) samples spinning at 12 kHz; FTIR spectra of Ch and derivatives (c). ....	<b>120</b>
<b>Figure 44</b> – $^1\text{H}$ NMR signal decay profiles recorded by MSEFID pulse sequence (a), thermogravimetric and (b) and DTG curves of Ch, DPCh, DPCat35 and DPCat80 (c). ....	<b>122</b>
<b>Figure 45</b> – Aqueous solubility (a), zeta potential (b), specific conductivity as function of concentration of DPCh, DPCat35 and DPCat80 (d) and hydrodynamic size as function of pH.....	<b>125</b>

<b>Figure 46</b> – Hydrodynamic size distribution of DPCh and DPCat35 derivatives recorded by DLS experiment. The results are presented as function of volume (a,d), number (b,e) and intensity (c,f). .....	<b>127</b>
<b>Figure 47</b> – Water contact angles of Ch (a), DPCh (b) and DPCat35 (c) samples compressed into pellets .....	<b>129</b>
<b>Figure 48</b> – Maximum mucoadhesion (detachment) force (N) of Ch, DPCh, DPCat35 and DPCat80 from porcine intestine, used as biological tissue model. The level of significance of $p < 0.05$ was determined applying the Tukey’s test. ....	<b>130</b>
<b>Figure 49</b> – Average hydrodynamic size (bars) and zeta potential (dots) of DPCat35 (grey) and DPCat80 (black) at pH 5.5 (a) and 7.4 (b). ....	<b>132</b>
<b>Figure 50</b> – Concentration-response curves with DPCat35 (a) and DPCat80 (b) samples against Balb/C, DU 145 and HepG2/C3A cell lines. The screening of the samples using three cell lines to assess the cytotoxicity has been taken after 72h incubation. The viability of the negative control (untreated cells) was considered 100%, while the positive control with sepantonium bromide led to cell death (viability near 0%). Continuous lines represent log-logistic regression curves. ....	<b>133</b>
<b>Figure 51</b> – Procedure scheme of the in vitro biological assays. ....	<b>143</b>
<b>Figure 52</b> – Hydrodynamic size distribution by intensity of empty NPs and CLT-NPs (a); representative TEM images of CLT-NPs obtained at magnification 200 nm (b) and 100 nm (c). ....	<b>144</b>
<b>Figure 53</b> – Experiments were conducted in acetate buffer (pH = 4.3) and PBS (pH = 6.8). Dissolution profiles of CLT are included for comparison purposes. ....	<b>146</b>
<b>Figure 54</b> – Cell viability of CLT-NPs and free CLT to HEC-1-A (a), Ca Ski (b) and HeLa (c) cell lines as a function of concentration (expressed in total CLT content). Values are reported as mean $\pm$ SD ( $n = 3$ ). Continuous lines represent log-logistic regression curves. ....	<b>149</b>
<b>Figure 55</b> – Drug permeability and association to cell monolayers of free CLT and CLT-NPs. Cumulative drug permeability profile for free CLT, CLT-NPs and empty NPs physically mixed with CLT (NPs(+CLT)) across Ca Ski (a) and HEC-1-A (b) cell monolayers. Values of $P_{app}$ values (c) and associated drug (d) with cell monolayers for free CLT, CLT-NPs and NPs (+CLT). Results are presented as mean $\pm$ SD ( $n = 3$ ). (*) and (**) denote values of $p < 0.05$ and $p < 0.01$ , respectively. ....	<b>152</b>
<b>Figure A1</b> – XRD resulted profile of $\alpha$ Ch (a); $\beta$ Ch (b); Ch60 (c); Ch45 (d); Ch35 (e); Ch25 (f); Ch15 (g) and Ch5 (h) samples after the subtraction of amorphous contribution. The $L_{020}$ and $L_{110}$ values were obtained from <i>FWHM</i> by peak deconvolution. ....	<b>184</b>
<b>Figure A2</b> – XRD resulted profile of USAD Ch1x (a); Ch2x (b); Ch3x (c) with respect to the resulted profile of depolymerized (3h and 6h) samples, after the subtraction of amorphous contribution. The $L_{020}$ and $L_{110}$ values were obtained from <i>FWHM</i> by peak deconvolution. ....	<b>185</b>
<b>Figure B1</b> – XRD resulted profile of BCHL and CWHL (a); BCHI and CWHI (b); BCHS and CWSH (c) samples after the subtraction of amorphous contribution. The $L_{020}$ and $L_{110}$ values were obtained from <i>FWHM</i> by peak deconvolution. ....	<b>186</b>

## LIST OF TABLES

<b>Table 1</b> - Values of average degree of acetylation ( $\overline{DA}$ ), pattern of acetylation (PA), average molecular weight ( $\overline{M}$ ) and average degree of polymerization ( $\overline{DP}$ ) .....	<b>44</b>
<b>Table 2</b> - Crystallite lattice dimension from peaks at $2\theta \approx 8^\circ$ - $11^\circ$ ( $L_{020}$ ) and $19$ - $21^\circ$ ( $L_{110}$ ), and crystallinity index ( $CrI_1$ and $CrI_2$ ) estimated by different methods applied on XRD patterns. ....	<b>52</b>
<b>Table 3</b> - Values of average degree of acetylation ( $\overline{DA}_{CP}$ ) and crystallinity index estimated from C4 and C6 signal resonance of $^{13}C$ CPMAS ( $T_C = 3000 \mu s$ , $d1 = 2 s$ and $12 kHz$ of spinning frequency) spectra profiles ( $CrI_{CP}$ ) .....	<b>54</b>
<b>Table 4</b> - Concentration of the components $DA^*$ and $CrI^*$ and its correlation obtained by applying the SVD method on the regions 120-67, 120-40, 90-67 and 90-40 ppm from $^{13}C$ CPMAS spectra of <i>N</i> -acetylated Ch5-60 samples. ....	<b>64</b>
<b>Table 5</b> - Average molecular weight ( $\overline{M}$ ), average degree of polymerization ( $\overline{DP}$ ). The average degree of acetylation ( $\overline{DA}$ and $\overline{DA}_{CP}$ ), and crystallinity index ( $CrI_1$ , $CrI_2$ and $CrI_{CP}$ ) were used as structural and morphological calculated (reference) parameters for PLS analysis. ....	<b>70</b>
<b>Table 6</b> - Weight losses related to the thermal degradation of $\beta$ -chitin and Ch samples.....	<b>74</b>
<b>Table 7</b> - Rigid/mobile parameters from the corresponding segments of the polymers ( $T_{2r}$ , $T_{2m}$ , $v_m$ and $f_m$ )..	<b>78</b>
<b>Table 8</b> - Values of average degree of acetylation ( $\overline{DA}_{CP}$ ), viscosity average molecular weight ( $\overline{M}_v$ ), viscosity average degree of polymerization ( $\overline{DP}_v$ ), crystallinity index from $^{13}C$ CPMAS spectra profiles ( $CrI_{CP}$ ), rigid/mobile intermediate motion parameters ( $T_{2r}$ , $T_{2m}$ and $v_m$ and $f_m$ ) .....	<b>94</b>
<b>Table 9</b> - Crystallinity index ( $CrI_2$ ), apparent crystal dimension from hydrated peak at $2\theta \approx 8.2^\circ$ ( $L_{020}$ ) and $19.7^\circ$ ( $L_{110}$ ), temperatures and weight losses related to the thermal degradation of BCh and WCh samples. ....	<b>98</b>
<b>Table 10</b> - Distribution of surface functional groups of C1*, C2* and C3* signals and relative concentrations of carbon (C 1s), nitrogen (N 1s) and oxygen (O 1s) atoms. ....	<b>102</b>
<b>Table 11</b> - Average degrees of acetylation ( $\overline{DA}$ ), substitution ( $\overline{DS}$ ) and quaternization ( $\overline{DQ}$ ) determined by $^1H$ NMR. $\overline{DQ}$ was also determined by $^{15}N$ CPMAS and conductometric titration. ....	<b>118</b>
<b>Table 12</b> - Rigid/mobile components described as $T_{2r}$ and $T_{2m}$ , respectively, the mobile fraction parameter ( $f_m$ ) and shape parameter ( $v_m$ ) and the weight losses (WL) related to different degradation steps of the polymers. ....	<b>122</b>
<b>Table 13</b> - Quantitative data from the concentration-response curves for samples and cell lines used to access the cytotoxicity after 72 h incubation. ....	<b>133</b>

<b>Table 14</b> - <i>Candida</i> spp. strains used for testing the antifungal activity of CLT-NPs. ATCC strains and clinical samples used in this work were kindly provided from the Centre of Biological Engineering, University of Minho, Portugal. ....	<b>141</b>
<b>Table 15</b> - Average hydrodynamic size ( $D_h$ ), polydispersity index (PDI), zeta potential ( $\zeta$ ), AE% and LC% of NPs.....	<b>144</b>
<b>Table 16</b> - MIC and MFC of chitosan, DPCat35, DPCat80 and empty NPs. Results presented in $\mu\text{g mL}^{-1}$ (n = 3). .....	<b>147</b>
<b>Table 17</b> - Anti- <i>Candida</i> activity of free CLT and CLT-NPs. Results are presented as MIC and MFC values against ATCC strains and vaginal isolates of <i>Candida</i> species. Results are presented in $\mu\text{g mL}^{-1}$ of CLT (n = 3). The azole (FLC) resistance profile for each strain is also shown for reference and defined as susceptible (S; MIC $\leq 8 \mu\text{g mL}^{-1}$ ); dose-dependent susceptibility (S-DD; MIC = 16-32 $\mu\text{g mL}^{-1}$ ); or resistant (R; MIC $\geq 64 \mu\text{g mL}^{-1}$ ).....	<b>148</b>
<b>Table 18</b> - <i>SI</i> and <i>RSI</i> values for free CLT and CLT-NPs. <i>RSI</i> values denoting at least 2-fold reduction or 2-fold increase in <i>SI</i> of CLT-NPs as compared to the free drug are highlighted in red and blue, respectively. ....	<b>150</b>

## LIST OF ABBREVIATIONS AND ACRONYMS

AE	Association efficiency
AFM	Atomic Force Microscopy
ATCC	American Type Culture Collection
$\alpha$ Ch	Alfa-Chitin
Balb/C 3T3	Mouse healthy fibroblast cell line
BE	Binding Energy
$\beta$ Ch or BCH	Beta-Chitin
CAC	Critical Aggregation Concentration
Ca Ski	Epithelial (cervical) cell line of female genital tract
CC <sub>50</sub>	Concentration to reduce cell viability by 50%
Ch or ChC	Chitosan
CLT	Clotrimazole
CLT-NPs	Clotrimazole-loaded nanoparticles
CPMAS	Cross-Polarization Magic-Angle Spinning
CPMG	Carr Purcell Meiboom Gill
<i>CrI</i>	Crystallinity index
CWH	Chitin Whiskers
$\overline{DA}$	Average degree of <i>N</i> -acetylation
DEC	<sup>1</sup> H Dipolar Decoupling
DMEM	Dulbecco's Modified Eagle Medium
DMSO	Dimethyl sulfoxide
DIPSHIFT	Dipolar Chemical Shift Correlation
DLS	Dynamic Light Scattering
DTG	Derivative of the thermogravimetric curve
DPCat	<i>N</i> -(2-hydroxy)-propyl-3-trimethylammonium, <i>O</i> -palmitoyl chitosan
DPCh	<i>O</i> -palmitoyl chitosan
DPMAS	Direct Polarization Magic-Angle Spinning
$\overline{DP}_v$	Viscosity average degree of polymerization
$\overline{DP}_w$	Weight average degree of polymerization
$\overline{DQ}$	Average degree of quaternization
$\overline{DS}$	Average degree of substitution

DU145	Human prostate cancer cell line
EDTA	Ethylenediaminetetraacetic acid
ELS	Electrophoretic Light Scattering
FBS	Fetal bovine serum
FDA	Food and Drug Administration
FID	Free Induction Decay
FLC	Fluconazole
FS-LG	Frequency-switched Lee-Goldburg
FTIR	Fourier Transform Infrared Spectroscopy
FTP	Freeze - pump out – thaw deacetylation process
FWHM	Full width at half-maximum
GlcN	2-amino-2-deoxy- $\beta$ -D-glucopyranose or D-glucosamine
GlcNAc	2-acetamido-2-deoxy- $\beta$ -D-glucopyranose or <i>N</i> -acetyl-D-glucosamine
GRAS	Generally Recognized as Safe
GTMAC	Glycidyltrimethylammonium chloride
HEC-1-A	Epithelial (endometrial) cell line of female genital tract
HeLa	Epithelial (cervical) cell line of female genital tract
HepG2/C3A	Human liver cancer cell line
HBSS	Hank's balanced salt solution
HETCOR	Heteronuclear Correlation
HMB	Hexamethylbenzene
HPDEC	High Power Heteronuclear Decoupling
HPLC-UV	High Pressure Liquid Chromatography with UV detection
LC	Loading capacity
MFC	Minimal Fungicidal Concentration
MIC	Minimum Inhibitory Concentration
MOPS	3-( <i>N</i> -morpholino)propanesulfonic acid sodium salt
MSE	Magic Sandwich Solid-Echoes
MTT	3-(4,5-dimethylthiazol-2-yl)-2,5-diphenyltetrazolium
$\bar{M}_v$	viscosity average molecular weight
$\bar{M}_w$	weight average molecular weight
NPs	Nanoparticles
PA	Pattern of acetylation

$P_{app}$	Apparent permeability coefficient
PDI	Polydispersity index
PGM	Porcine gastric mucin
PLS	Partial Least Square
PMLG	Phase Modulated Lee-Goldburg
RK-ROSE	Rhim and Kessemeier - Radiofrequency Optimized Solid-Echo
RPMI 1640	Growth medium Roswell Park Memorial Institute
RSI	Relative selectivity index
SDA	Sabouraud dextrose agar
SE	Solid-Echo pulse senquence
SEC	Size-Exclusion Chromatography
SEM	Scanning Electron Microscopy
SCF	Solid component of fats
SI	Selectivity index
SSNMR	High-Resolution Solid-State Nuclear Magnetic Resonance Spectroscopy
SVD	Singular Value Decomposition
TEER	Transepithelial Electrical Resistance
TEM	Transmission Electron Microscopy
TD-NMR	Time-Domain Nuclear Magnetic Resonance Relaxometry
TGA	Thermogravimetric analysis
TPP	Sodium tripolyphosphate
TPPM	Heteronuclear Two-Phase Pulse Modulation
USAD	Ultrasound-assisted deacetylation
VVC	Vulvovaginal candidiasis
XPS	X-ray Photoelectron Spectroscopy
XRD	X-ray Diffraction
WL	Weight loss



## LIST OF SYMBOLS

$A$	Diffusion area from 12-well semipermeable polyester membrane support
$B_0$	Static magnetic field
$B_1$	Pulsed magnetic field
$B_{dip}$	Dipolar magnetic field
$C_0$	Initial concentration of a given polymer or CLT
C/N/O 1s	Carbon/ nitrogen/ oxygen electronic 1s orbital
$\gamma$	Gyromagnetic ratio
$\dot{\gamma}$	Shear rate
$G'$	Storage modulus
$G''$	Loss modulus
d1	Last delay
$D_h$	Average hydrodynamic size
$DQ$	Anisotropic chemical shift
$dt$	Dead time
$\delta$	Isotropic chemical shift
$\Delta B_0$	Non-homogeneity contribution from $B_0$
$\Delta\nu_{dip}$	Dipolar spin interaction
$\Delta\nu_{DQ}$	Spin interaction referred to anisotropic chemical shift
$\Delta Q$	Total amount of permeated CLT
$\zeta$	Zeta potential
$f_m$	Mobile-part fraction of $^1\text{H}$ signal decay
$f_r$	Rigid-part fraction of $^1\text{H}$ signal decay
$\mathcal{H}_{dip}$	Hamiltonian function that describes the energy from dipolar interactions
$\mathcal{H}_{DQ}$	Hamiltonian function that describes the energy from anisotropic chemical shift
$I$	NMR signal integral from high-resolution spectrum
$[\eta]$	Intrinsic viscosity
$\eta$	Dynamic viscosity
$\eta_0$	Zero shear viscosity
$\eta_{rel}$	Relative viscosity
$\eta_{sp}$	Specific viscosity

$\theta$	Flip angle between $M_0$ and $M_z$ after applying $B_1$
$2\theta$	X-ray scattering angle
$L_{hkl}$	Apparent crystallite dimensions
$L/w$	Aspect ratio (length per width)
$\vec{\mu}$	Nuclear magnetic momentum
$M_0$	Resulting magnetization across $B_0$
$M_z$	Longitudinal axis referred to the orientation of spin vectors during precession
$\nu$	Ultrasonic frequency in Hz
$\nu_r$	Rotor spinning frequency in Hz
$\sigma$	Shear stress
$\tau$	Free evolution time
$t$	Total cell permeability experiment time
$t_1$	Time registered for heteronuclear dipolar interaction
$T_1$	Longitudinal relaxation time
$T_{1\rho}$	Longitudinal relaxation time in the rotating frame
$T_2$	Transversal relaxation time
$T_2^*$	Transversal relaxation time with the contribution of $\Delta B_0$
$T_{2m}$	Transversal relaxation time of mobile segments
$T_{2r}$	Transversal relaxation time of rigid segments
$T_a$	Acquisition time
$t_c$	Correlation time
$T_c$	Contact time
$T_{CH}$	Cross-polarization time
$T_{MAX}$	Temperature of maximum weight loss
$T_{onset}$	Onset temperature
$t_p$	Pulse time for flip angle
$T_r$	Magnetization recovery time
$t_r$	Rotor spinning time
$u_m$	Shape parameter
$F$	normalized function from Bernoullian statistics
$\omega$	Angular frequency in $\text{rad s}^{-1}$
$\omega_0$	Larmor angular frequency in $\text{rad s}^{-1}$
$\omega_{sw}$	Oscillatory frequency-sweep

# CONTENTS

<b>1</b>	<b>INTRODUCTION</b> .....	<b>21</b>
<b>1.1</b>	<b>CHITOSAN: A BRIEF OVERVIEW</b> .....	<b>21</b>
<b>1.2</b>	<b>SOLID-STATE NUCLEAR MAGNETIC RESONANCE: BASIC PRINCIPLES</b> .....	<b>23</b>
1.2.1	Time-domain Relaxometry.....	23
1.2.2	High-resolution One-dimensional Spectroscopy .....	25
1.2.3	High-resolution Two-dimensional Spectroscopy .....	27
<b>2</b>	<b>GENERAL OBJECTIVES</b> .....	<b>30</b>
<b>3</b>	<b>DEVELOPMENT AND RELATIONSHIP AMONG THE STUDIES</b> .....	<b>32</b>
<b>CHAPTER I</b>		
<b>EVALUATION OF CHITOSAN CRYSTALLINITY: A HIGH-RESOLUTION SSNMR SPECTROSCOPY APPROACH</b> .....		
<b>34</b>		
<b>3.1.1.</b>	<b>THE MORPHOLOGICAL ISSUE AND HOW SSNMR CAN BE USEFUL</b> .....	<b>34</b>
<b>3.1.2.</b>	<b>MATERIALS AND METHODS</b> .....	<b>37</b>
3.1.2.1.	Ultrasound-assisted deacetylation of $\beta$ -Chitin .....	37
3.1.2.2.	Depolymerization of Chitosan .....	38
3.1.2.3.	N-Acetylation of Chitosan .....	38
<b>3.1.3.</b>	<b>CHARACTERIZATIONS</b> .....	<b>39</b>
3.1.3.1.	High-resolution $^1\text{H}$ NMR spectroscopy.....	39
3.1.3.2.	Average molecular weight and degree of polymerization.....	40
3.1.3.3.	X-ray diffraction (XRD).....	41
3.1.3.4.	SSNMR: $^{13}\text{C}$ CPMAS, DIPSHIFT and HETCOR techniques .....	42
3.1.3.5.	Multivariate analysis.....	43
<b>3.1.4.</b>	<b>RESULTS AND DISCUSSION</b> .....	<b>43</b>
3.1.4.1.	Structure and long-range molecular ordering .....	43
3.1.4.2.	Conformation and short-range molecular ordering .....	53
<b>3.1.5.</b>	<b>CONCLUSIONS</b> .....	<b>65</b>
<b>CHAPTER II</b>		
<b>FAST-FORWARD APPROACH OF TD-NMR RELAXOMETRY FOR SOLID-STATE CHEMISTRY OF CHITOSAN</b> .....		
<b>67</b>		
<b>3.2.1.</b>	<b><math>^1\text{H}</math> TD-NMR SIGNAL DECAY AS A TOOL TO RECOGNIZE AND EVALUATE PROPERTIES</b> .....	<b>67</b>
<b>3.2.2.</b>	<b>MATERIALS AND METHODS</b> .....	<b>69</b>
3.2.2.1.	Structural and morphological calculated parameters .....	69
<b>3.2.3.</b>	<b>CHARACTERIZATIONS</b> .....	<b>70</b>
3.2.3.1.	Thermogravimetric analysis (TGA) .....	70
3.2.3.2.	TD-NMR relaxometry: RK-ROSE technique .....	71
3.2.3.3.	Multivariate analysis.....	72
<b>3.2.4.</b>	<b>RESULTS AND DISCUSSION</b> .....	<b>72</b>
3.2.4.1.	Thermal behavior of side and main-chains on solid-state .....	72
3.2.4.2.	Internal mobility of side and main-chains on solid-state .....	75
<b>3.2.5.</b>	<b>CONCLUSIONS</b> .....	<b>83</b>
<b>CHAPTER III</b>		
<b>INSIGHT INTO PHYSICOCHEMICAL AND MORPHOLOGICAL PROPERTIES OF AQUEOUS BETA-CHITIN NANOWHISKERS: A HIGH- AND LOW-FIELD NMR APPROACH</b> .....		
<b>84</b>		
<b>3.3.1.</b>	<b>PREDICTING PERFORMANCE BY CONTROLLING THE REACTION SETTINGS</b> .....	<b>84</b>

<b>3.3.2. MATERIALS AND METHODS .....</b>	<b>87</b>
3.3.2.1. Preparation of $\beta$ -chitin suspensions .....	87
<b>3.3.3. CHARACTERIZATIONS .....</b>	<b>87</b>
3.3.3.1. Scanning electron microscopy (SEM).....	87
3.3.3.2. Transmission electron microscopy (TEM).....	88
3.3.3.3. Atomic force microscopy (AFM).....	88
3.3.3.4. TD-NMR relaxometry: MSEFID and CPMG techniques .....	88
3.3.3.5. X-ray photoelectron spectroscopy (XPS).....	89
3.3.3.6. Electrophoretic light scattering (ELS).....	89
3.3.3.7. Rheometric measurements.....	90
<b>3.3.4. RESULTS AND DISCUSSION.....</b>	<b>90</b>
3.3.4.1. Micrographs of chitin nanowhiskers.....	90
3.3.4.2. Structural and morphological features .....	92
3.3.4.3. Surface charge and functional groups.....	100
3.3.4.4. Rheological and relaxation behavior.....	102
<b>3.3.5. CONCLUSIONS .....</b>	<b>105</b>

#### **CHAPTER IV**

#### ***N*-(2-HYDROXY)-PROPYL-3-TRIMETHYLAMMONIUM, O-PALMITOYL CHITOSAN: SYNTHESIS, PHYSICOCHEMICAL AND BIOLOGICAL PROPERTIES .....**

**107**

<b>3.4.1. NOVEL SYNTHETIC STRATEGY FOR IMPROVING DESIRABLE APPLICATIONS .....</b>	<b>107</b>
<b>3.4.2. MATERIALS AND METHODS .....</b>	<b>109</b>
3.4.2.1. Synthesis of <i>O</i> -palmitoyl chitosan.....	109
3.4.2.2. Synthesis of <i>N</i> -(2-hydroxy)-propyl-3-trimethylammonium, <i>O</i> -palmitoyl chitosan.....	111
<b>3.4.3. CHARACTERIZATIONS .....</b>	<b>111</b>
3.4.3.1. Fourier transform infrared (FTIR) spectroscopy.....	111
3.4.3.2. High-resolution NMR: solution $^1\text{H}$ , solid-state $^{13}\text{C}$ and $^{15}\text{N}$ CPMAS.....	111
3.4.3.3. Conductometric titration .....	112
3.4.3.4. Aqueous solubility.....	113
3.4.3.5. Optical contact angle measurements .....	113
3.4.3.6. Critical aggregation concentration (CAC) .....	113
3.4.3.7. Dynamic and electrophoretic light scattering (DLS and ELS) .....	114
3.4.3.8. Mucoadhesion assessment.....	114
3.4.3.9. <i>In vitro</i> mucin interaction assay .....	114
3.4.3.10. <i>In vitro</i> cytotoxicity assay.....	115
3.4.3.11. Statistical analysis .....	115
<b>3.4.4. RESULTS AND DISCUSSION.....</b>	<b>116</b>
3.4.4.1. Spectroscopy and relaxometry characterization .....	116
3.4.4.2. Solution properties and wettability.....	124
3.4.4.3. Mucoadhesiveness and mucin interaction properties.....	129
3.4.4.4. Cytotoxicity assay using healthy and tumor cells.....	132
<b>3.4.5. CONCLUSIONS .....</b>	<b>134</b>

#### **CHAPTER V**

#### ***CLOTTRIMAZOLE-LOADED N*-(2-HYDROXY)-PROPYL-3-TRIMETHYLAMMONIUM, O-PALMITOYL CHITOSAN NANOPARTICLES FOR TOPICAL TREATMENT OF VULVOVAGINAL CANDIDIASIS .**

**136**

<b>3.5.1. SMART POLYMERS AGAINST INFECTIOUS DISEASE .....</b>	<b>136</b>
<b>3.5.2. MATERIALS AND METHODS .....</b>	<b>138</b>
3.5.2.1. Preparation and characterization of NPs .....	138
<b>3.5.3. CHARACTERIZATIONS .....</b>	<b>139</b>
3.5.3.1. <i>In vitro</i> drug release.....	139
3.5.3.2. <i>In vitro</i> susceptibility of <i>Candida</i> spp. ....	140

3.5.3.3.	<i>In vitro</i> cytotoxicity assay.....	141
3.5.3.4.	<i>In vitro</i> drug permeability and cell association.....	142
3.5.3.5.	Statistical analysis.....	143
<b>3.5.4.</b>	<b>RESULTS AND DISCUSSION.....</b>	<b>144</b>
3.5.4.1.	Physicochemical properties and drug release performance of NPs.....	144
3.5.4.2.	Susceptibility assay against <i>Candida</i> spp. ....	147
3.5.4.3.	Cytotoxicity and permeability to genital tract cell monolayers.....	149
<b>3.5.5.</b>	<b>CONCLUSIONS .....</b>	<b>152</b>
<b>4</b>	<b>FINAL REMARKS AND PERSPECTIVES .....</b>	<b>154</b>
<b>5</b>	<b>RESULTING PUBLISHED SCIENTIFIC ARTICLES .....</b>	<b>155</b>
	<b>REFERENCES .....</b>	<b>156</b>
	<b>APPENDIX A .....</b>	<b>184</b>
	<b>APPENDIX B.....</b>	<b>186</b>

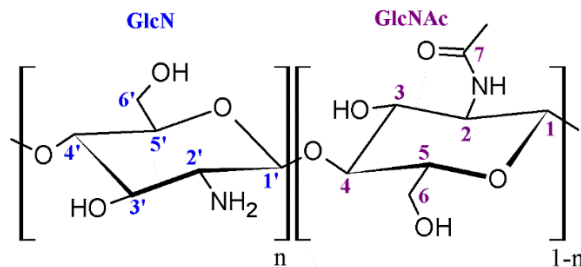


## 1 INTRODUCTION

### 1.1 Chitosan: a brief overview

Chitosan is a linear biopolymer constituted by 2-acetamido-2-deoxy-D-glycopyranose (GlcNAc) and 2-amino-2-deoxy-D-glycopyranose (GlcN) residues at variable proportions, sequentially linked by ( $\beta \rightarrow 4$ ) glycosidic bonds (Fig. 1). Its natural and most predominant form, however, is extensively made up by GlcNAc units as crystalline microfibrils, being designed as chitin, an aminopolysaccharide typically extracted from renewable sources, such as shellfish exoskeletons, arthropods cuticles and cocoons, larval membranes and cellular walls of fungi and algae (GONIL; SAJOMSANG, 2012; KAYA et al., 2017).

Figure 1 - Idealized chemical structure of chitin / chitosan formed by GlcN and GlcNAc units at variable ratio. The numbers indicate the location of the respective carbons and hydrogens from each unit.



Source: Own authorship.

The growing interest of the global scientific community in chitosan is due to its vast repertoire of properties, such as the polycationic character in acidic environment, antimicrobial, antioxidant and antitumor activity (VINSOVÁ; VAVRIKOVÁ, 2011), mucoadhesiveness, low cytotoxicity and biodegradability (DASH et al., 2011), which enables the preparation of films, scaffolds, membranes, hydrogels and nanomaterials (CROISIER; JÉRÔME, 2013; SHUKLA et al., 2013), aimed for different applications, such as food coating and preservation, biosensors, controlled and sustained release of drugs and bioactive agents, gene therapy and removal of toxic metals from aqueous solutions (HARISH PRASHANTH; THARANATHAN, 2007). Additionally, chitosan currently holds GRAS (generally recognized as safe) status, granted by the FDA (Food and Drug Administration) regulatory agency, for use in dietary supplements and curative excipients (GARCIA-FUENTES; ALONSO, 2012).

In order to improve specific functionalities and biological activities inherent to chitosan, such as solubility, mechanical performance, susceptibility to enzymatic degradation and mucoadhesiveness, chemical modifications are typically carried out on the nucleophilic sites formed by amino and hydroxyl groups, which enables the chain's functionalization and formation of derivatives or at least act as binding sites for chemical or electrostatical crosslinking agents (PAVINATTO et al., 2017). Despite that, studies have shown that several applications are also influenced by intrinsic characteristics of chitosan such as average molecular weight ( $\bar{M}$ ) (CHAE; JANG; NAH, 2005; RICHARDSON; KOLBE; DUNCAN, 1999; XING et al., 2005), number of GlcNAc units or average degree of acetylation ( $\bar{DA}$ ) (CHATELET; DAMOUR; DOMARD, 2001; HUANG; KHOR; LIM, 2004; SCHIPPER; VÅRUM; ARTURSSON, 1996), distribution of GlcNAc groups or parameter of acetylation ( $PA$ ) (AIBA, 1992; KUMIRSKA et al., 2009), chains packaging and crystallinity (GOPALAN NAIR; DUFRESNE, 2003; THAKHIEW; DEVAHASTIN; SOPONRONNARIT, 2013), surface area and particle size (DOTTO; PINTO, 2011; MIRMOHSENI et al., 2012), being all strongly dependent on the biomass source and processability (KURITA; SANNAN; IWAKURA, 1977), and also commonly related among each other (ARANAZ et al., 2009).

Chitin has three polymorphic structures described as  $\alpha$ -,  $\beta$ -,  $\gamma$ -. While the  $\alpha$ - and  $\gamma$ -allomorphs show similar chain packaging, the main differences remaining between the  $\alpha$ - and  $\beta$ -allomorphs are attributed to the lamellar disposal of polymeric sheets (KAYA et al., 2017), thus affecting the accessibility to small molecules. The extraction methods of  $\alpha$ -chitin, generally conducted from crustacean shells, follow different chemical (ACOSTA et al., 1993) or even enzymatic (WANG; CHIO, 1998) processes. Chemical methods involve demineralization, deproteinization and depigmentation, for the removal of carbonates (40-55%), proteins (25-40%) and pigments (< 1%) from biomass, respectively (NO; MEYERS, 1995). Although these steps are independent from the process step developed, the use of oxidizing agents and elevated temperatures also favor side reactions such as degradation of polymeric chains. On the other hand, the extraction of  $\beta$ -chitin requires only the deproteinization stage conducted under mild conditions, such as using a diluted alkaline medium at room temperature (LAVALL; ASSIS; CAMPANA-FILHO, 2007), which involves greater savings and use of reagents during the process steps, if compared to  $\alpha$ -chitin extraction. Even so, the commercial production of  $\beta$ -chitin on an industrial scale is much less explored compared to  $\alpha$ -chitin production (CAMPANA-FILHO et al., 2007).

The most common reaction developed in chitin polymorphs involves the heterogeneous thermochemical deacetylation in a strongly alkaline medium, which aims the hydrolysis of

acetamido groups and then producing chitosan. Therefore, the difference in crystallinity of chitins influences the accessibility to amorphous domains, which are more susceptible to the reaction significantly achieved in 30-50 minutes (LAMARQUE; VITON; DOMARD, 2004a). Distinguished methods have been proposed (ROGOVINA; AKOPOVA; VIKHOREVA, 1998; SAHU; GOSWAMI; BORA, 2009) in order to minimize simultaneous depolymerization, especially at high temperatures and long reaction periods (CHANG et al., 1997). Among these, one of the most effective method called freeze - pump out - thaw (FTP) (LAMARQUE et al., 2005), which basically consists of submitting a chitin suspension to successive cycles of freezing in liquid nitrogen and then perform the deacetylation for 60 minutes at 80-110 °C, allows the disruption of crystalline domains of chitin, leading to the formation of extensively deacetylated chitosan ( $\overline{DA} < 2\%$ ) with high weight average molecular weight ( $\overline{M}_w \approx 4,5 \cdot 10^5 \text{ g mol}^{-1}$ ). In this Thesis, it has been used the multistep Ultrasound-Assisted Deacetylation (USAD) process (FIAMINGO et al., 2016), that consists on the disruption of chitin packing domains and acetamido groups cleavage through the formation of cavitation bubbles with energy greater than interchain cohesion, added to sequential steps of acetate ions removal during three successive stages of ultrasonic deacetylation. In this modification, each step is developed in a short period (50 minutes) and reduced temperature (60 °C), as compared to FTP, thus generating chitosans with  $\overline{DA}$  ranged in 4-37 % and  $\overline{M}_w$  ranged in  $9.0 \times 10^5$  and  $1.2 \times 10^6 \text{ g mol}^{-1}$ . Nevertheless, heterogeneous deacetylation of  $\alpha$ - and  $\beta$ -chitin leads to form chitosans with crystallinity profile similar to that presented by  $\beta$ -chitin (CHO et al., 2000).

## *1.2 Solid-State Nuclear Magnetic Resonance: Basic Principles*

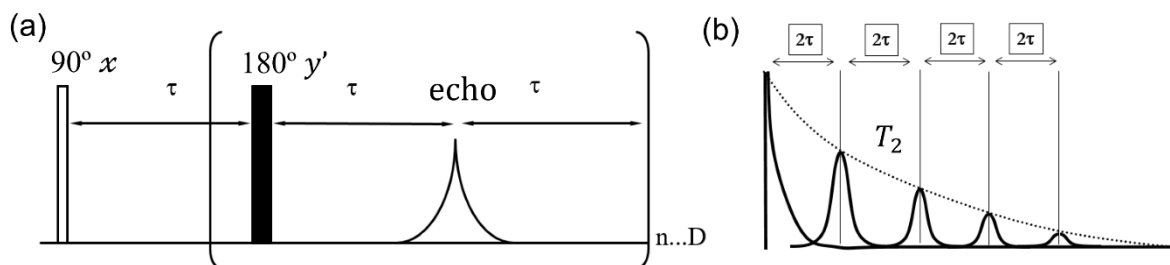
### *1.2.1 Time-domain Relaxometry*

The NMR phenomenon is the result achieved from the interactions between the nuclear magnetic moments ( $\vec{\mu}$ ) of nuclear spin submitted to a static magnetic field ( $B_0$ ), after applying a pulsed magnetic field ( $B_1$ ) irradiation under a certain angular frequency ( $\omega$ ). The  $B_0$  field splits the spins population (Zeeman levels) in which the relative excess at the lowest energy level leads to a resulting magnetization ( $M_0 = \Sigma \vec{\mu}$ ), and allows the precession of  $\mu$  vectors oriented along a longitudinal axis ( $M_0 = M_z$ ) at  $\omega_0$  (Larmor frequency). This frequency is proportional to the isotope specific gyromagnetic ratio ( $\gamma$ ) that possess an odd number of protons and/ or neutrons. The application of  $B_1$  radiofrequency (RF) with  $\omega_0 = \gamma B_0$ , under a

certain pulse time ( $t_p$ ) changes the orientation of  $M_0$  according to a flip angle  $\theta = \gamma B_1 t_p$ . Thus, after the pulse,  $M_0$  induces a freely decaying signal (Free Induction Decay, FID) during the longitudinal relaxation processes, referred to the return of the magnetization time to thermal equilibrium ( $T_1$ ) and transverse relaxation processes, regarding the loss of spins coherence in the  $xy$  plane ( $T_2$ ). In a perfectly homogeneous magnet, the NMR signal (FID) decays with  $T_2$ . However, for a solution or a liquid-state material with low viscosity, the NMR signal decay is governed by the effective relaxation time  $T_2^*$ , that has a greater contribution from the magnetic field non-homogeneity ( $\Delta B_0$ ) (COLNAGO; ANDRADE, 2017).

The  $T_2$  measurement is based on techniques of spin echo sequences. In order to eliminate the NMR signal interference from  $\Delta B_0$  and decrease the time-consumption for the analysis, the researchers Carr and Purcell proposed a method that consisting of a  $180^\circ$  pulse train separated by a certain free evolution time  $\tau$ , which generates an echo between these pulses. This procedure allowed the NMR signal to be acquired in a single pulse sequence, being not required to wait a longer recovery time ( $T_r \geq 5T_1$ ) between each echo (CARR; PURCELL, 1954). Later, Meiboom and Gill established a phase gap of  $90^\circ$  regarding the initial  $90^\circ$  pulse, applying the  $180^\circ$  pulse train on the  $y'$  axis (Fig. 2a). As a result, it was possible to eliminate the  $180^\circ$  pulse calibration imperfections and correct the phase of all echoes, providing a signal that decays with natural  $T_2$  of the sample (Fig. 2b) (MEIBOOM; GILL, 1958). This pulse sequence named as CPMG (Carr-Purcell-Meiboom-Gill) is to date the most used technique on relaxometry experiments.

Figure 2 – Schematic illustration of CPMG pulse sequence (a) and spin echo correction to the same phase (b).



Source: Own authorship.

The  $T_1$  and  $T_2$  relaxation times are dependent on the material viscosity or mobility of a given molecular component of the system. In colloidal dispersions or small molecules on low viscous fluids  $T_1 \geq T_2$ , due to the shorter time required for a given component to turnover its own symmetry axis (correlation time,  $t_c$ ). The gradual increase in viscosity leads to an increase

in  $t_c$  and a decrease in local field fluctuations at  $\omega_0$ , straightly contributing to the return of magnetization to  $M_0$ . The longitudinal relaxation efficiency, or relaxation rate  $1/T_1$ , reaches a maximum value in  $t_c\omega_0 \approx 1$  and, for higher intervals ( $t_c\omega_0 > 1$ ),  $T_1 > T_2$  for components with more restricted molecular motion, such as macromolecules and solid-state materials. Considering that the  $1/T_2$  relaxation rate has no maximum value and decreases as the molecular mobility decreases,  $T_1 \gg T_2$  especially in the solid-state and, for this cases, the acquisition time ( $T_a$ ) of the FID is kinetically-dependent and mostly modulated by  $T_2$  (GIL; GERALDES, 1987).

### 1.2.2 High-resolution One-dimensional Spectroscopy

The NMR signal dependency in frequency-domain spectroscopy ( $B_0 > 9$  T) with high field homogeneity ( $< 0.01$  ppm), lies in the response between the interaction of magnetic moments from nuclear spins with local magnetic fields from different physical sources, such as chemical shifts, J-coupling and dipolar coupling. Due to the fast and random movement of small molecules in low-viscous solutions, only the isotropic components of these interactions, such as the isotropic chemical shift and J-coupling are observed. However, due to the lower degree of freedom and spatial dependence of molecular segments in solid-state materials, the anisotropic chemical shift ( $\mathcal{DQ}$ ) and dipolar coupling interactions prevail, leading to a spectral broadening (LEVITT, 2008). As the quadrupolar interaction does not manifest in  $1/2$  spin, such as  $^1\text{H}$  and  $^{13}\text{C}$  nuclei, the description below won't highlight other spin quantum number interactions.

The heteronuclear dipolar interactions ( $^1\text{H}$ - $^{13}\text{C}$ ) are considered the primary sources of spectral broadening due to the natural abundance of  $^1\text{H}$  nuclei (high  $\gamma_H$ ), being the  $^{13}\text{C}$ - $^{13}\text{C}$  homonuclear dipolar coupling mostly insignificant due to the low binding probability between these nuclei (low  $\gamma_C$ ). Thus, the suppression of  $^1\text{H}$ - $^{13}\text{C}$  interaction usually involves a  $^1\text{H}$  Dipolar Decoupling (DEC) technique, which essentially consists of applying a continuous-wave and selective RF irradiation in order to minimize the local dipolar magnetic field ( $B_{dip}$ ) effect produced by the abundant nucleus ( $^1\text{H}$ ) (SARLES; COTTS, 1958). In this context, heteronuclear dipolar decoupling techniques have been proposed such as Two-Pulse Phase-Modulated (TPPM) (BENNETT et al., 1995) and Small Phase Incremental Alteration (Spinal-16) high power  $^1\text{H}$  decoupling (SINHA et al., 2005) have shown consistently more efficiency for correcting phase imperfections.

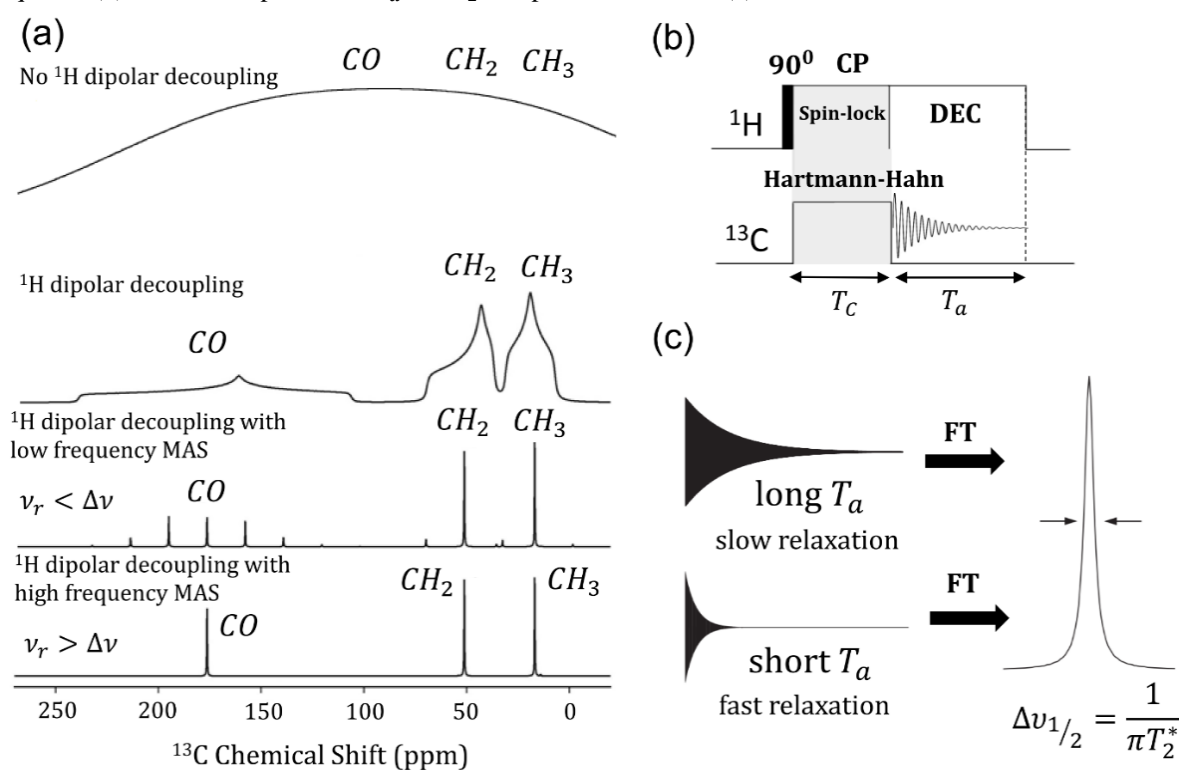
On the other hand, in order to minimize the  $^1\text{H}$ - $^{13}\text{C}$  dipolar interactions (ANDREW; BRADBURY; EADES, 1959; LOWE, 1959) and anisotropic chemical shifts, both responsible for the rotational sidebands to emerge (ANDREW; EADES, 1962), it is also performed the magic-angle spinning (MAS) as a coupled procedure. In this situation, the specific energies of these interactions, described by the Hamiltonians  $\mathcal{H}_{dip}$  and  $\mathcal{H}_{DQ}$ , which are proportional to the geometric factor  $(3\cos^2\theta - 1)$ , are both converged to zero by adjusting the sample's position at  $\theta = 54.74^\circ$  with respect to  $B_0$ . Thus, by submitting a given sample on this axis angle under a frequency spinning greater than the spin interaction ( $\nu_r > \Delta\nu$ ), the Hamiltonians will be only time-dependent and all internuclear vectors will have an average orientation modulated by the factor  $[\frac{1}{2}(\cos^2\theta - 1)]$  parallel to the referred rotational axis, being the spectral width reduced to an isotropic dependence. As  $\Delta\nu_{dip}$  is found ranging from 1 to 100 kHz and  $\Delta\nu_{DQ}$  from 1 to 10 kHz for  $B_0 \approx 10\text{ T}$ , it is usually applied MAS to suppress the anisotropic chemical shift interactions, coupled to DEC to suppress the  $^1\text{H}$ - $^{13}\text{C}$  dipolar interactions (DUER, 2002). All these passages are illustrated on Fig. 3a.

Due to the low natural abundance of  $^{13}\text{C}$  nuclei associated with low sensitivity to obtain the SSNMR signal ( $T_1 \gg T_2$ ), the excitation or direct polarization under magic-angle spinning (DPMAS) of this rare nuclei requires the accumulation of several spectra in order to improve the signal-to-noise ratio, which results in a high time-consuming analysis for a quantitative experiment. In this sense, the magnetization transfer method from an abundant nuclei ( $^1\text{H}$ ) to a rare one ( $^{13}\text{C}$ ), named as Cross Polarization Magic-Angle Spinning (CPMAS), enables a signal gain by a factor of  $\gamma_H/\gamma_C \approx 4$ , performing experiments around 10 times faster ( $T_{1H} \approx 10T_{1C}$ ). In this sense, to occur such polarization it is necessary to establish the Hartmann-Hahn matching requirement ( $\gamma_H B_{1H} = \gamma_C B_{1C}$ ), in which the  $B_1$  intensity is gradually adjusted until satisfy the  $\omega_H = \omega_C$  condition (spin-lock) (Fig. 3b) (PINES; GIBBY; WAUGH, 1973). However, as the polarization time ( $T_{CH}$ ) is straightly dependent on the heteronuclear dipolar interaction, the magnetization transfer or contact time ( $T_C$ ) varies accordingly to the internuclear distances and degree of freedom from different molecular segments, making CPMAS an intrinsically non-quantitative technique.

It should be noticed that an unidimensional  $^{13}\text{C}$  SSNMR spectra can be constitute by a series of sharp signals as much as compared to the isotropic chemical shift profile found in solution  $^{13}\text{C}$  NMR, if acquired from small to ordered materials (Fig. 3a). Taking into account that the isotropic chemical shift is also sensitive to local conformations, disordered materials can produce line broadening due to the wider distribution of possible conformations. In this

sense, the spectral line width resulted from non-crystallinity or amorphous domains of a given material is due to the local conformations, isomerism and packaging differences, being not related to anisotropy interactions and, consequently not suppressed by MAS even at  $\nu_r > \Delta\nu$  (DUER, 2002; SCHMIDT-ROHR; SPIESS, 1994). It is worth to note that  $T_2$  is inversely proportional to the signal width (Fig. 3c).

Figure 3 – Spectral line shape illustrative effect with and without  $^1\text{H}$  dipolar decoupling and coupled to MAS with rotational sidebands ( $\nu_r < \Delta\nu$ ) and without ( $\nu_r > \Delta\nu$ ) (a); Schematic illustration of Cross-Polarization (CP) pulse sequence (b); Relationship between  $T_a$  and  $T_2^*$  on spectral line width (c).



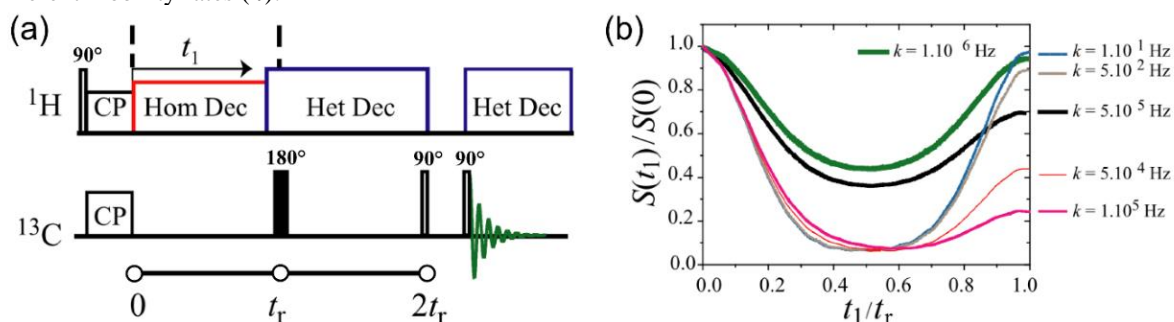
Source: Adapted from BERNARDINELLI et al., 2016.

### 1.2.3 High-resolution Two-dimensional Spectroscopy

Two-dimensional NMR (2D NMR) involves a set of techniques in which is possible to determine more complex structures usually appearing as overlapped signals, being at least defined one frequency-domain dimension. In case of 2D SSNMR, some techniques have been developed in order to study of the dynamics of molecular segments based on the spatial dependence of nuclear spin interactions (SCHMIDT-ROHR; SPIESS, 1994). Among different pulse sequences, it is especially useful the ones that explore the heteronuclear dipolar interactions, such as the Dipolar Chemical Shift Correlation (DIPSHIFT) (HONG et al., 2002; MUNOWITZ et al., 1981), which can estimate the relative mobility of chemical groups in an

intermediate regime ( $t_c \sim \mu\text{s}$  to  $\text{ms}$ ), internuclear distances and even activation energies (DEAZEVEDO et al., 2008; REICHERT et al., 2004). Additionally, it is also useful to evaluate the correlation between two heteronuclear spins, using the fast-spinning HETCOR technique (CARAVATTI; BRAUNSCHWEILER; ERNST, 1983; VAN ROSSUM; FÖRSTER; DE GROOT, 1997), which consists of a  $^1\text{H}$  NMR spectra in one dimension correlated with the a  $^{13}\text{C}$  NMR in a second dimension, providing valuable information regarding the heteronuclear spins proximity in the surrounding chemical environment (ANDO; ASAKURA, 1998). The following description brings an overview about the DIPSHIFT (Fig. 4) and HETCOR (Fig. 5) pulse sequences.

Figure 4 – Schematic illustration of DIPSHIFT pulse sequence (a) and simulated dipolar curves performed at different mobility rates ( $k$ ).



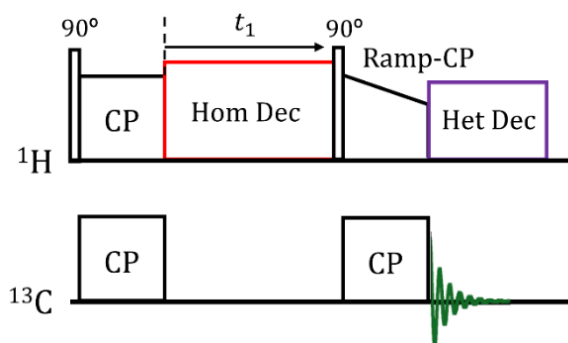
Source: Adapted from COBO, 2013.

According to the DIPSHIFT pulse sequence (Fig. 4a) (MUNOWITZ et al., 1981), after a first CP excitation ( $90^\circ$  pulse), the nuclear spins freely precess and the  $^{13}\text{C}$  magnetization evolves under the influence of the heteronuclear dipolar interaction during  $t_1$ . During this period, which varies from zero to the first rotational cycle ( $t_r$ ) of the rotor, a  $^1\text{H}$  dipolar decoupling sequence, such as the Frequency-Switched Lee-Goldburg (FS-LG) (BIELECKI et al., 1990) or Phase Modulated Lee-Goldburg (PMLG) (VINOGRADOV; MADHU; VEGA, 1999) is applied in order to suppress the  $^1\text{H}$ - $^1\text{H}$  interaction. Then, a  $180^\circ$  pulse is applied after the  $t_r$  period, followed by  $^1\text{H}$ - $^{13}\text{C}$  dipolar decoupling, such as TPPM (BENNETT et al., 1995) or Spinal-16 (SINHA et al., 2005) sequence carried on a second rotation cycle ( $2t_r$ ), which enables to refocus the isotropic chemical shift interaction in the  $^{13}\text{C}$  channel. After the  $2t_r$  period, the spin echo resulted from this refocus is modulated by the evolution of the  $^1\text{H}$ - $^{13}\text{C}$  interaction at each increment of  $t_1$ , accumulating phase due to this interaction. As consequence, the normalized signal amplitude  $S(t_1)$  referred to each chemical group (assigned on  $^{13}\text{C}$  CPMAS spectrum) decreases to a minimum in  $t_r/2$ , when the spin system accumulates less phase due to the beginning of a rotational echo. At the end of a first period, the accumulated

phase gradually decreases, leading to the formation of dipolar curves with variable amplitude (Fig. 4b). Thus, the smaller the amplitude of the resulting curve, the smaller the dipolar interaction and the greater the mobility rate ( $k$ ) for a given molecular segment (DEAZEVEDO et al., 2008). Higher mobility rates are also achieved when the recorded  $S(t_1)$  signal relatively decreases at the end of a cycle period, due to the loss of correlation between nuclei (Fig. 4b).

The heteronuclear correlation experiment HETCOR (Fig. 5), was designed to correlate  $^1\text{H}$  and  $^{13}\text{C}$  chemical shifts applying specific multiple-pulse sequences, that are performed to get narrow distribution signals as typically observed for isotropic chemical shifts on liquid-state experiments (CARAVATTI; BRAUNSCHWEILER; ERNST, 1983). The HETCOR pulse sequence consists of three periods, which sequentially includes the proton evolution, isotropic mixing and carbon detection. The evolution starts with a transverse  $^1\text{H}$  spin magnetization by a CP excitation ( $90^\circ$  pulse), followed by a homonuclear dipolar decoupling sequence, originally set by a multiple-pulse BLEW-12 (BURUM; LINDER; ERNST, 1981) or more recently using a FS-LG or PMLG pulse sequence (BIELECKI et al., 1990; VAN ROSSUM; FÖRSTER; DE GROOT, 1997; VINOGRADOV; MADHU; VEGA, 1999) during  $t_1$ . At the end of this period, the  $^1\text{H}$  NMR spectrum is recorded and the proton magnetization is restored by the  $90^\circ$  pulse. During the mixing period, it was originally set a windowless isotropic sequence (WIM-24) to optimize de RF power in order to retain the heteronuclear dipolar interactions (WEITEKAMP; GARBOW; PINES, 1982). However, as the CP magnetization transfer is highly sensitive to RF power at fast MAS, a better approach was found by setting a ramped-amplitude CP (RAMP-CP) to properly restore the Hartman-Hahn matching (METZ; ZILIOX; SMITH, 1996). The  $^{13}\text{C}$  detection is then carried by applying a  $^1\text{H}$ - $^{13}\text{C}$  dipolar decoupling, such as TPPM (BENNETT et al., 1995) or Spinal-16 (SINHA et al., 2005).

Figure 5 - Schematic illustration of HETCOR pulse sequence.



Source: Own authorship.

## 2 GENERAL OBJECTIVES

The main objective of this Thesis is to control the preparative condition for investigating the properties of chemically modified chitosans and the potential application of these materials in different research fields. For such a goal, different high- and low-NMR techniques were applied in order to elucidate intrinsic characteristics of chitins, chitosans and derivatives sometimes already verified through other methods. To fulfill the requirement of each specific objective, it was performed a series of characterizations, including non-spectroscopic and biological ones. In this sense, different studies were developed and sequentially presented in a clear and concise manner as possible, being divided into five distinguished Chapters, each one straightly related to some innovative proposal for a given research field, as briefly detailed:

CHAPTER I: Considering the strong relationship between *N*-acetylation and crystallinity of chitosan, its unclear dependence with molar masses, the lacking aspect of reliable quantification of *CrI* by XRD and the conformational influence on SSNMR spectra, this Chapter aims to propose a novel and straightforward approach to estimate the crystallinity through the short-range molecular ordering from chitin to chitosan. Samples possessing variable  $\overline{DA}$  and average weight average molecular weight ( $\overline{M}_w$ ) were produced and evaluated through  $^{13}\text{C}$  CPMAS SSNMR experiments, conducted as the main techniques, while DIPSHIFT and the HETCOR were used as auxiliary methods for signal assignments. The singular value decomposition (SVD) was applied as multivariate analysis for pattern recognition of analytical signs from  $^{13}\text{C}$  CPMAS spectra prior to cross-validate these components. The experimental steps were developed at Macromolecular Materials and Lignocellulosic Fibers Group laboratory (IQSC/USP) and NMR facilities at Embrapa Instrumentation, both at São Carlos, SP.

CHAPTER II: Knowing that none study had properly investigated the mutual dependence of  $\overline{DA}$  and crystallinity index (*CrI*) of Ch by using  $^1\text{H}$  TD-NMR relaxometry, this Chapter proposes the use of a novel solid-echo (SE) pulse sequence, named as Radiofrequency Optimized Solid-Echo (RK-ROSE), to evaluate both parameters in solid Ch samples. The aim of this work was to establish a Partial Least Square (PLS) regression model that would allow the prediction of  $\overline{DA}$  and *CrI* in different solid-state Ch samples based on a RK-ROSE signals. This method provides an additional approach with the advantages of easy operation, fast and minimum sample pre-treatment. The experimental steps were developed at Macromolecular

Materials and Lignocellulosic Fibers Group laboratory (IQSC/USP) and NMR facilities at Embrapa Instrumentation

CHAPTER III: The effect of the  $\beta$ -chitin particle size/ granulometry on the physicochemical properties of  $\beta$ -chitin nanocrystalline structures, *i. e.* nanowhiskers and nanocrystals (CWH) aqueous suspensions was investigated. CWH samples were prepared via acid hydrolysis of  $\beta$ -chitin and characterized in terms of morphology, surface properties, crystallinity and thermal stability. The molecular motions under intermediate-to-slow timescale were verified by Magic Sandwich Echo – Free induction decay ( $^1\text{H}$  MSEFID) pulse sequence and compared to the  $^1\text{H}$ - $^{13}\text{C}$  dipolar interaction curves for each molecular segment by DIPSHIFT experiment. The experimental steps were developed at Macromolecular Materials and Lignocellulosic Fibers Group laboratory (IQSC/USP), NMR facilities at Embrapa Instrumentation, Nanomaterials and Advanced Ceramics Group (IFSC/USP) and Electrochemical Materials and Electroanalytical Methods Group (IQSC/USP).

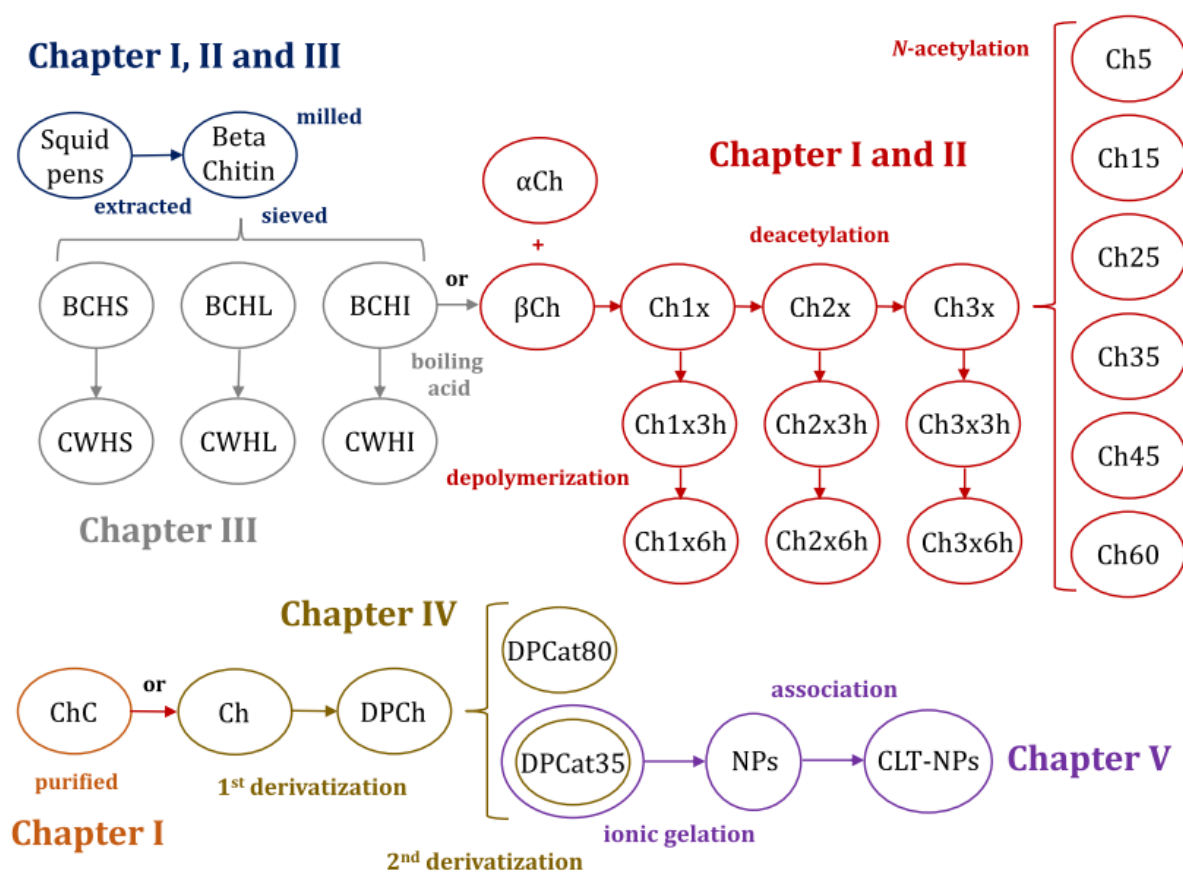
CHAPTER IV: Positively-charged amphiphilic chitosan derivative, named *N*-(2-hydroxy)-propyl-3-trimethylammonium, *O*-palmitoyl chitosan (DPCat), was synthesized in different reaction conditions to result in derivatives containing different contents of permanent and cationic charges. This Chapter focuses on the physicochemical and spectroscopy characterization of the polymer in solution and solid-state. The biological activities of derivatives were evaluated through mucoadhesiveness assessment, mucin interaction assays and cytotoxicity tests against healthy and cancer cell lines. The experimental steps were developed at Macromolecular Materials and Lignocellulosic Fibers Group laboratory (IQSC/USP), NMR facilities at Embrapa Instrumentation and Medicinal and Biological Chemistry Group (IQSC/USP).

CHAPTER V: The aim of this work is to further explore the range of biomedical applications of cationic DPCat, namely by assessing its potential for preparing clotrimazole-loaded nanoparticles (CLT-NPs) intended for the treatment of vulvovaginal candidiasis (VVC). NPs were characterized for relevant physicochemical, technological and *in vitro* biological (cytotoxicity against endometrial and cervical cell lines, anti-*Candida* activity and cell monolayer permeation/ association) properties pertinent to vaginal drug delivery and antifungal therapy. The experimental steps were developed at the Institute for Research and Innovation in Health (i3S) / National Institute of Biomedical Engineering (INEB)/ University of Porto (UP) in the city of Porto, Portugal.

### 3 DEVELOPMENT AND RELATIONSHIP AMONG THE STUDIES

The following flowchart (Fig. 6) illustrates the scheme of the materials' preparation for their use on each related chapter. Thus, in CHAPTERS I and II, chitosan samples were prepared by conducting the deacetylation (USAD) process (Ch1x, Ch2x and Ch3x), which was applied on  $\beta$ -chitin ( $\beta$ Ch or BCHI), extracted from squid pens, followed by depolymerization (Ch1x3h-6h, Ch2x3h-6h and Ch3x3h-6h) and *N*-acetylation (Ch5-60) processes. Commercial ChC (or Ch) and alfa-chitin ( $\alpha$ Ch) samples were also employed. In CHAPTER III, milled and sieved  $\beta$ -chitin at different powdered diameters (BCHS, BCHL and BCHI) were used for the preparation of chitin nanowhiskers/ nanocrystals (CWHS, CWHL and CWHI) through boiling acidolysis reaction. In CHAPTER IV, different chitosan derivatives (DPCh, DPCat35 and DPCat80) were prepared by consecutive functionalizations, being choose one of these (DPCat35) to prepare nanoparticles (NPs) by ionic gelation process for loading the antifungal clotrimazole (CLT) aiming for topical use against *Candida* spp. in CHAPTER V.

Figure 6 – Flowchart of all materials prepared accordingly to the proposal of each referred chapter.



Source: Own authorship.

The initial Research Project aimed the preparation of chitins, chitosans and amphiphilic chitosan derivatives and the proper investigation of physicochemical properties through TD-NMR techniques. However, some findings related to the variation of structure and morphology proved to be even more promising considering the unprecedented perspective and scientific contribution to the NMR and polysaccharide research fields. In this sense, new approaches were given to the development of this Thesis through the investigation of these properties by different SSNMR techniques performed at high and low magnetic fields.

The joint assessment between both variables, *i. e.* structure and morphology of chitosans, was investigated in CHAPTERS I and II, throughout high-resolution techniques in the former and time-domain in the latter. The main concept resulted from these first chapters were further used in CHAPTER III, in order to evaluate the influence of the particle size/granulometry on sieved and milled powdered  $\beta$ -chitins to the CWH samples, as a third variable rarely addressed in the literature. While CHAPTERS I and II are straightly connected to the state-of-the-art in order to validate SSNMR techniques within the analysed samples, CHAPTER III, on the other hand, focus on the characterization of novel nanomaterials mostly aimed to the application as polymeric reinforcement, which are especially useful for Tissue Engeneering research field. As shown in Fig. 6, the entire set of samples used for the development of CHAPTERS I, II and III originates from the same raw material: squid pens from *Dorytheuthis* spp.

Despite following the same trend as CHAPTER III, CHAPTER IV addresses concepts of high and low field SSNMR in novel chitosan derivatives, however it was mostly focused on the structure-property relationship of interest to the Biopharmaceutic research field, aimed for the application as drug release nanocarriers. The chitosan derivatives prepared in CHAPTER IV were finally used in CHAPTER V, which refers entirely to the preparation biomaterials for the association and release of antifungal for topical treatment of vulvovaginal candidiasis (VVC). It is worth to highlight that the parent chitosan used in the CHAPTERS IV and V was also used in CHAPTER I for structure and morphology comparison purposes.

## CHAPTER I

### *Evaluation of chitosan crystallinity: A high-resolution SSNMR spectroscopy approach*

Original source: **Carbohydrate Polymers**, Elsevier (FACCHINATTO, W. M. et al., 2020a)

#### *3.1.1. The morphological issue and how SSNMR can be useful*

Chitosan exhibit polymorphic forms designed in three crystal types named as  $\alpha$ ,  $\beta$ ,  $\gamma$  in function of the packing and polarities of adjacent chains in successive sheets (ZHOU et al., 2011). The different allomorphs account for the different intersheet accessibility to small molecules and crystallinity, which is on turn, strongly related to the solubility (KURITA; KAMIYA; NISHIMURA, 1991; SOGIAS; KHUTORYANSKIY; WILLIAMS, 2010), swelling behavior (GUIBAL, 2004; GUPTA; JABRAIL, 2006; SAITO et al., 2000), sorption kinetics of toxic metal ions in aqueous solutions (MILOT et al., 1998; PIRON; DOMARD, 1998) and reactivity (KURITA et al., 1994; LAMARQUE; VITON; DOMARD, 2004b). Additionally, several studies describe that besides polymorphism, the  $\overline{DA}$  acts as an important structural feature partially controlling the crystallinity and related properties, such as hydrophilicity (GUPTA; JABRAIL, 2006), water-sorption capacity (IOELOVICH, 2014) and susceptibility to enzymatic degradation (CARDOZO et al., 2019). Indeed, the lowest enzymatic degradation rates has been achieved for  $\overline{DA} < 15\%$  (FRANCIS SUH; MATTHEW, 2000), being also desirable a partially *N*-deacetylation for higher probability to form a lysozyme-substrate complex (CHO et al., 2000; HIRANO; TSUCHIDA; NAGAO, 1989). Higher digestibility is achieved when  $\overline{DA}$  values are ranged in 40 % to 80 % with lesser probability for a random distribution of acetamido groups (AIBA, 1992; HIRANO; TSUCHIDA; NAGAO, 1989). Thus, the crystallinity increases with  $\overline{DA}$  and the crystalline regions grows on segments containing blocks of *N*-acetylated units (OGAWA; YUI, 1993).

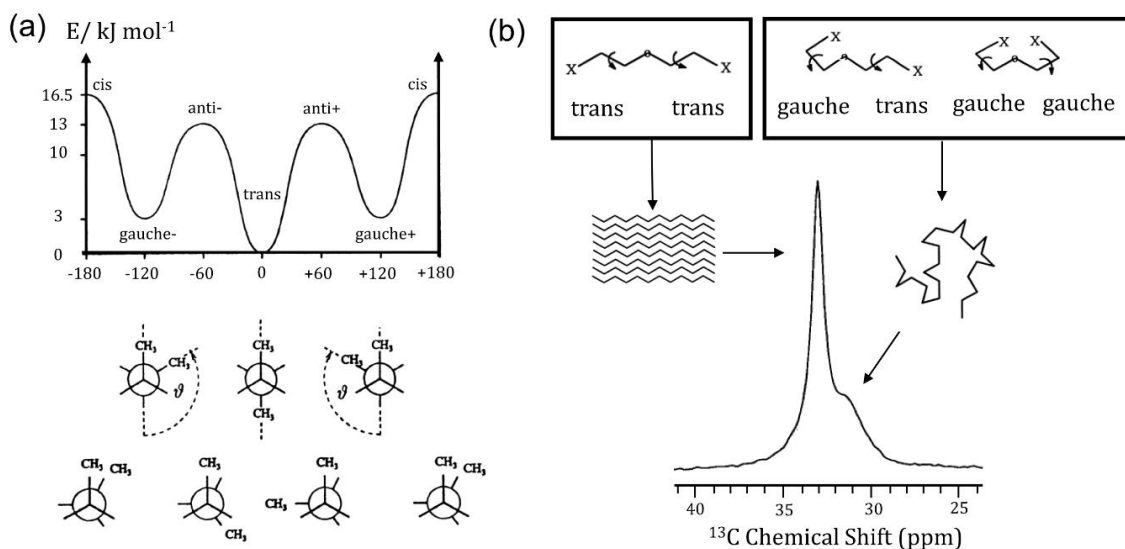
The crystallinity of polysaccharides has been evaluated by X-ray diffraction models and different spectroscopy techniques (ÅKERHOLM; HINTERSTOISSER; SALMÉN, 2004; PARK et al., 2010; SCHENZEL; FISCHER; BRENDLER, 2005). Currently, the Ch crystallinity has been quantified considering the long-range ordering on XRD patterns usually through the peak height (FOCHER et al., 1990; STRUSZCZYK, 1987) deconvolution methods (CHO et al., 2000) or based on subtraction of a diffraction pattern using one from an amorphous Ch as reference (OSORIO-MADRAZO et al., 2010). The first fails by not considering the

contribution of (110)<sub>a</sub> reflection from anhydrous allomorph near to the amorphous halo intensity at 16.0°, the second has overestimated the contribution of amorphous phase by fitting a cubic spline curve in the diffraction pattern, while the third proposes a laborious method for a routine evaluation of Ch crystallinity, using a totally amorphous samples which is usually not available. Studies has shown that for the same sample, the crystallinity index can also vary within a wide range from 57.0 to 93.0 % for chitin (FAN; SAITO; ISOGAI, 2008a, 2009) and from 40.0 to 80.0 % for chitosan (GRZĄBKA-ZASADZIŃSKA; AMIETSZAJEW; BORYSIK, 2017; PIRES; VILELA; AIROLDI, 2014; YUAN et al., 2011) depending on the calculation method. Consequently, the accurate estimative of crystallinity through XRD is considerable doubtful.

In this context, high-resolution solid-state nuclear magnetic resonance, SSNMR, spectroscopy has been one of the most used techniques due to the chemical shift dependence on local molecular conformations (TONELLI; SCHILLING, 1981). Because the local chain conformation (trans-gauche) changes the current electronic structure around <sup>13</sup>C nuclei, its nuclear magnetization become distinct allowing to distinguish between ordered and disordered populations (Fig. 7). For instance, <sup>13</sup>C CPMAS Solid-State NMR has been used to evaluate the fraction of interior-to-surface crystallites in cellulose (BERNARDINELLI et al., 2015; PARK et al., 2010; VIËTOR et al., 2002; WANG; HONG, 2016), starch (MUTUNGI et al., 2012; VILLAS-BOAS et al., 2020) and polyglycans (WEBSTER et al., 2006) usually referred as NMR crystallinity index. This can be typically achieved and widely applied using the C4 and C6 carbons from cellulose and C1 carbon from starch, which the splitting is directly associated to signals arising from ordered and disordered molecular segments. One should point out that NMR and X-ray crystalline index are not identical in the sense that in solid-state NMR it reflects the local conformation and population distribution, while in X-ray it is related to the long range order. However, they are close related in the sense that local order can be strongly influenced by long range order. In this sense, using NMR and X-ray diffraction together can be a valuable way of improving the information about the microstructure of chitosans.

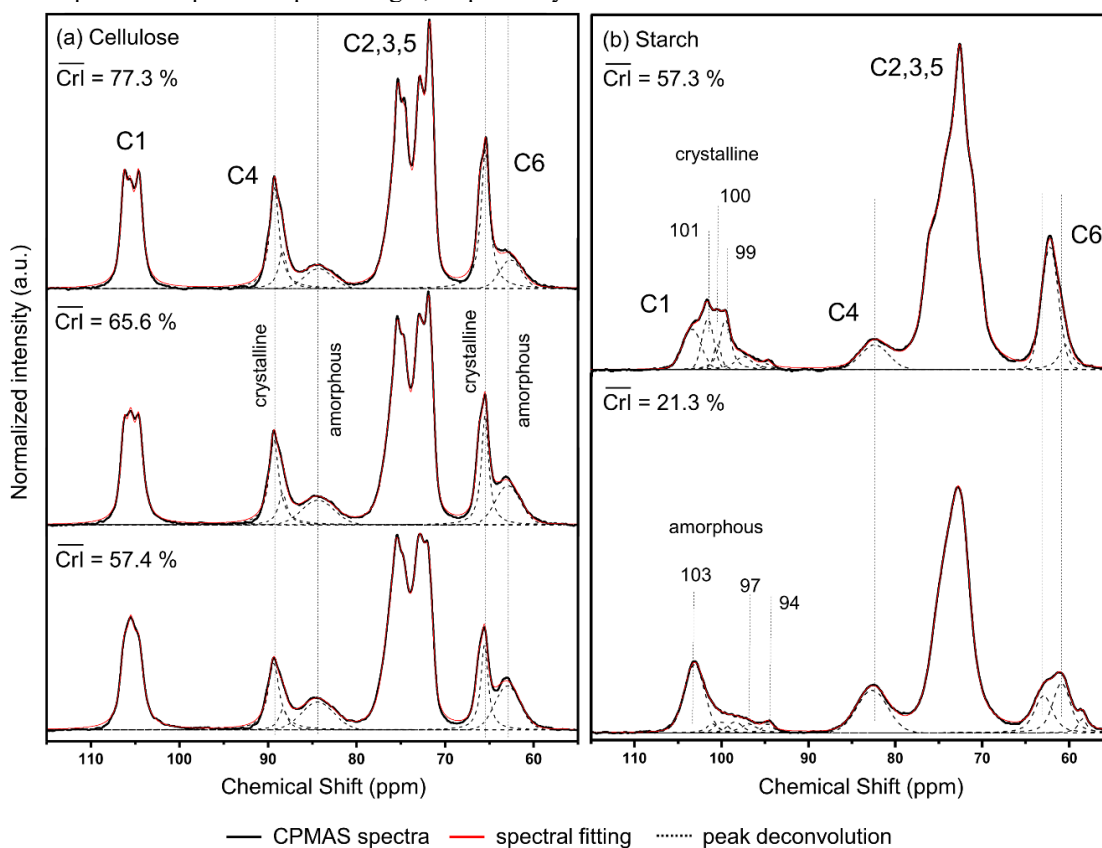
To illustrate the already known behavior of these biopolymers, *i.e.*, cellulose and starch, it was acquired the <sup>13</sup>C CPMAS spectra with different average crystallinity indexes ( $\overline{CrI}$ ) (Fig. 8). As observed, the signal shape and relative deconvoluted area describe the morphological changes achieved for each case.

Figure 7 – Pictorial graphic of molecular energy of butane with respect to the dihedral angle, separated by transition states of torsion depicted by Newman projections (a); chains packaging influence from trans and gauche states and its illustrative effect on isotropic chemical shifts distributions (b).



Source: Adapted from BORN & SPIESS, 1997.

Figure 8 – Non-published results of <sup>13</sup>C CPMAS spectra ( $T_c = 3000 \mu s$ ,  $d_1 = 2 s$  and  $12 kHz$  of spinning frequency) of cellulose samples with different average crystallinity indexes ( $\overline{CrI}$ ) calculated by means of C4 and C6 deconvoluted signals (a); and similarly, for C1 of starch samples (b). Spectra recorded on Bruker® Avance 400 spectrometer, using a Bruker 4-mm MAS double-resonance probe head, at 400.0 MHz (<sup>1</sup>H) and 100.5 MHz (<sup>13</sup>C) with 2.5  $\mu s$  and 4.0  $\mu s$  of  $\pi/2$  pulse length, respectively.



Source: Own authorship.

Despite the structural similarity with cellulose, a clear C4 signal split in  $^{13}\text{C}$  CPMAS spectra of Ch has been only observed in samples with low acetylated content (HEUX et al., 2000; SILVA et al., 2017a). This has been attributed to a greater mobility of amorphous region achieved through thermal treatment above 150 °C (FOCHER et al., 1990). The shape C1 and C4 signals of Ch salts have been also interpreted as consequence of twofold helical conformations (SAITÔ; TABETA; OGAWA, 1987), being highly sensitive to conformational changes on glycosidic linkages (HARISH PRASHANTH; KITTUR; THARANATHAN, 2002; TANNER et al., 1990). The signal split into doublets and sharp singlets were found on hydrated (tendom) and annealed chitosan forms, being influenced by chitin source, molecular weight and content of water molecules (SAITÔ; TABETA; OGAWA, 1987). However, the origin of this signal splitting is still controversy (FOCHER et al., 1992) and none study has satisfactory investigated the short-range ordering with the spectral shape variability of these carbon signals from different  $\overline{DA}$  and molar masses, without submitting Ch to any kind of physicochemical treatment.

### 3.1.2. *Materials and Methods*

Low molecular weight chitosan (ChC, 87 kDa,  $\overline{DA} \approx 5.0\%$ ) was obtained from fly larvae (Cheng Yue Plating® Co. Ltd. Chang, China) and purified according to the methodology described by SANTOS; BUKZEM; CAMPANA-FILHO (2016). The allomorph alfa-chitin ( $\alpha\text{Ch}$ ), obtained from shrimp shells, cellulose and starch samples (Sigma-Aldrich® Co. St. Louis, MO, USA), were used without further purification.

#### 3.1.2.1. *Ultrasound-assisted deacetylation of $\beta$ -Chitin*

The allomorph beta-chitin ( $\beta\text{Ch}$ ) was extracted from the squid pens (*Doryteuthis* spp.) (LAVALL; ASSIS; CAMPANA-FILHO, 2007), milled and sieved into powder sizes with average diameters ( $d$ ) ranged in  $0.125 < d < 0.425$  mm, then submitted to multistep ultrasound-assisted deacetylation process (USAD) to produce Ch samples with variable  $\overline{DA}$  (FIAMINGO et al., 2016). In brief, the  $\beta\text{Ch}/\text{NaOH}$  40% (w/w) aqueous suspension was placed in a jacked glass reactor ( $\theta_{\text{int}} = 3.5$  cm) and kept under magnetic stirring with a circulating thermostat at  $60 \pm 1$  °C, then sonicated with UP400S Hielscher® Sonifier ultrasonic device ( $\nu = 24$  kHz) coupled to  $\theta = 22$  mm stepped probe for pulsed irradiation. The deacetylation reaction was carried out

at 200 W for 50 min and then stopped by cooling and neutralization with HCl 3.0 mol L<sup>-1</sup>, followed by filtration under positive pressure through a 0.45 µm porous membrane (Millipore<sup>®</sup>, White SCWP). The resulting product, named as Ch1x, was freeze-dried at -45 °C for 24h (Liotop L101, Liobrás<sup>®</sup>). This process was sequentially applied to this sample at the same conditions to produce Ch2x and then similarly to produce Ch3x, an extensively deacetylated chitosan.

### 3.1.2.2. *Depolymerization of Chitosan*

Chitosans possessing different average molecular weights were prepared by submitting the samples Ch1x, Ch2x and Ch3x to homogeneous depolymerization via ultrasound treatment for 3h and 6h. Thus, 5.0 g of a given Ch was suspended in 500.0 mL of acetic acid 1.0 % (v/v) contained in a 1 L jacked glass reactor ( $\theta_{\text{int}} = 10$  cm) and subjected to ultrasound pulsed irradiation at 200 W ( $60 \pm 1$  °C) for the desired time by using the same operational parameters already described for deacetylation process. The products were neutralized by adding NaOH 0.1 mol L<sup>-1</sup>, filtered under positive pressure (0.45 µm) and then sequentially washed with ethanol 80 % (v/v) and deionized water. The resulting products were freeze-dried at -45 °C for 24 h and named as Chwxy, where “w” (1, 2 and 3) identify the parent Ch and “y” (3h and 6h) the time of ultrasound treatment.

### 3.1.2.3. *N-Acetylation of Chitosan*

Chitosans with a predicted and wide-ranged  $\overline{DA}$  were obtained by performing the homogeneous *N*-acetylation reaction onto Ch3x with acetic anhydride at molar ratios 0, 0.02, 0.20, 0.40, 0.60, 0.90 of anhydride/glucosamine, as similarly reported elsewhere (LAVERTU; DARRAS; BUSCHMANN, 2012; SORLIER et al., 2001). Thus, 0.5 g of Ch3x was suspended in 50.0 mL of acetic acid 1.0 % (v/v) and kept under mechanical stirring (500 rpm) in a double-walled cylindrical reactor at 25 °C for 24 h. In order to avoid the protonation of amino groups and prevent side reactions, such as *O*-acylation, it was added 40.0 mL of 1,2-propanediol to the reaction medium. The anhydride acid was slowly added and the reaction was interrupted by precipitation with NaOH 0.1 mol L<sup>-1</sup> after 24 h. The resulting solutions were filtered under positive pressure (0.45 µm), sequentially washed with ethanol 80 % (v/v) and deionized water,

and then freeze-dried at  $-45\text{ }^{\circ}\text{C}$  for 24 h. The products were named as Ch5, Ch15, Ch25, Ch35, Ch45 and Ch60, being each sample indicated next to the predicted  $\overline{DA}$  value (5-60%).

### 3.1.3. Characterizations

#### 3.1.3.1. High-resolution $^1\text{H}$ NMR spectroscopy

Chitosan samples were dissolved in  $\text{D}_2\text{O}/\text{HCl}$  1% (v/v), resulting in  $C_P = 10\text{ mg mL}^{-1}$ , then transferred to 5.0 mm NMR tubes. All  $^1\text{H}$  NMR spectra were acquired at  $85\text{ }^{\circ}\text{C}$  on a Bruker<sup>®</sup> Avance II HD ( $\nu = 600\text{ MHz}$ ), setting up the following pulse sequence parameters: 11  $\mu\text{s}$  for  $90^{\circ}$  pulse lengths, 6 s for recycle delay and 2 s for acquisition. A composite pulse was applied to suppress the signal from water hydrogens at 4.10 ppm by improving the signal-to-noise ratio of the samples. The  $\overline{DA}$  was calculated according to Eq. (1) (LAVERTU et al., 2003):

$$\overline{DA} (\%) = \left( \frac{I_{H1}}{I_{H1} + I_{H1'}} \right) \times 100 \quad (1)$$

where  $I_{H1}$  is the signal integral of  $H1$  hydrogens from anomeric carbon of GlcNAc units and  $I_{H1'}$  is the equivalent  $H1'$  hydrogens of GlcN. These samples were also characterized with respect to pattern of acetylation ( $PA$ ), as described by the Eq. (2) (WEINHOLD et al., 2009):

$$PA = \frac{F_{AD}}{2 \times F_{AA} + F_{AD}} + \frac{F_{AD}}{2 \times F_{DD} + F_{AD}} \quad (2)$$

where  $F_{AD}$ ,  $F_{AA}$  and  $F_{DD}$  are the normalized functions from Bernoullian statistics that are referred to the ratio of experimental area  $I_{AD} + I_{DA}$ ,  $I_{AA}$  and  $I_{DD}$  with the total area ( $I_T = I_{AD} + I_{DD} + I_{AA} + I_{DD}$ ), respectively, which one related to the probability of an adjacent neighbor residue to be a acetylated, A (GlcNAc), or an deacetylated, D (GlcN), unit. For  $PA = 2$ , 1 and 0 the distribution pattern is ideally alternate, random and block-wise throughout the polymer chain. The experimental area was obtained fitting Voigt functions on  $H1$  and  $H1'$  signals, using PeakFit<sup>™</sup> (v. 4.12) software for peak deconvolution processing.

### 3.1.3.2. Average molecular weight and degree of polymerization

The weight average molecular weight ( $\bar{M}_w$ ) of Ch samples were determined carrying measurements by size-exclusion chromatography (SEC) (FIAMINGO et al., 2016), whereas the viscosity average molecular weight ( $\bar{M}_v$ ) of chitin allomorphs were determined by means of capillary viscometry (CARDOZO et al., 2019).

The SEC measurements were conducted on Agilent<sup>®</sup> 1100 coupled to a refractive index detection module (RID-6A), pre-columns Shodex Ohpak<sup>®</sup> SB-G (50 x 6 mm) (10 $\mu$ )/ SB-803-HQ (8 mm DI x 300 mm) (6 $\mu$ )/ SB-805-HQ (8 mm DI x 300 mm) (13 $\mu$ ), stationary phase consisting of polyhydromethacrylate gel and mobile phase (eluent) constituted by 0.3 M acetic acid / 0.2 M sodium acetate buffer. Following, Ch solutions 1.0 mg mL<sup>-1</sup> were prepared in the same buffer and analyzed under the flow rate of 0.6 mL min<sup>-1</sup> at 35 °C. The  $\bar{M}_w$  values were obtained from the calibration curve constructed by monodisperse pullulan (708,000; 344,000; 200,000; 107,000; 47,100; 21,100; 9,600 and 5,900 g mol<sup>-1</sup>), cellobiose (343.2 g mol<sup>-1</sup>) and glucose (180.2 g mol<sup>-1</sup>) standards.

The viscometry analysis were performed in a glass capillary ( $\phi = 0.53$  mm) containing 15 mL of chitin dissolved in *N,N*-dimethylacetamide/5% LiCl (w/w) at low concentrations ( $1.2 < \eta_{rel} < 2.0$ ) using the AVS-360 viscometer coupled to an automatic burette (Schott-Geräte<sup>®</sup>, Germany) at  $25.00 \pm 0.01$  °C. The  $\bar{M}_v$  values were calculated from the parameters  $K' = 2.4 \times 10^{-4}$  L g<sup>-1</sup> and  $\alpha = 0.69$  and by means of intrinsic viscosities,  $[\eta]$ , according to Mark-Houwink-Sakurada equation, obtained from the extrapolation of reduced viscosity curves to infinite dilution.

The weight average degree of polymerization of Ch ( $\overline{DP}_w$ ) and viscosity average degree of polymerization of chitin allomorphs ( $\overline{DP}_v$ ) were calculated considering the relative amount of GlcNAc (203 g mol<sup>-1</sup>) and GlcN (161 g mol<sup>-1</sup>), as described by the Eq. (3):

$$\overline{DP} = \frac{\bar{M} \times 100}{(203 \times \overline{DA}) + [161 \times (100 - \overline{DA})]} \quad (3)$$

where  $\overline{DP}$  and  $\bar{M}$  are the average degree of polymerization and average molecular weight, respectively, each one properly describing the parameters  $\overline{DP}_w$ ,  $\overline{DP}_v$ ,  $\bar{M}_w$  and  $\bar{M}_v$ , in the whole set of samples.

### 3.1.3.3. X-ray diffraction (XRD)

The XRD patterns of chitin and chitosan samples were acquired in a Bruker® AXS D8 Advance diffractometer with a Cu anode coupled to Lynxeye® detector, setting up the acquisition mode as step scan and the operating parameters at 40 kV and 40 mA. The scanning measurements were performed applying the radiation  $\lambda_{K\alpha} = 1.548 \text{ \AA}$  with light scattering ranged in  $5^\circ < 2\theta < 50^\circ$  at  $5^\circ \text{ min}^{-1}$  of scan rate. The crystallinity index was estimated by employing the peak height method (FOCHER et al., 1990) and the amorphous subtraction method (OSORIO-MADRAZO et al., 2010) on XRD patterns, as described by Eq. (4) and (5), respectively:

$$CrI_1(\%) = \left( \frac{I_{(110)_h} - I_{am}}{I_{200}} \right) \times 100 \quad (4)$$

$$CrI_2(\%) = \left( \frac{A_{total} - A_{am}}{A_{total}} \right) \times 100 \quad (5)$$

where  $I_{(110)_h}$  is the diffraction peak intensity ( $2\theta \approx 20^\circ$ ) of the hydrated reflection (110)<sub>h</sub>;  $I_{am}$  is the amorphous halo peak ( $2\theta \approx 16^\circ$ );  $A_{am}$  is the amorphous scattering area obtained by fitting a cubic spline curve, which was subtracted from the total diffraction pattern area,  $A_{total}$ . This procedure was performed by PANanalytical™ X'pert high score Plus software. The widths at half-heights of the peak at  $2\theta \sim 19\text{-}21^\circ$  and  $\sim 8\text{-}11^\circ$ , corresponding to (110)<sub>h</sub> and (020)<sub>h</sub> reflection planes, respectively, were obtained by fitting Voigt functions prior to estimate the crystallite dimensions ( $L_{hkl}$ ), according to Scherrer equation (GOODRICH; WINTER, 2007; VILLAS-BOAS et al., 2020) described in Eq. (3.1.6):

$$L_{hkl} = \frac{(0.9)(\lambda_{K\alpha})}{(FWHM)_{hkl}(\cos\Theta)_{hkl}} \quad (6)$$

where  $FWHM$  is the full width at half-maximum of (110)<sub>h</sub> and (020)<sub>h</sub> reflections at  $2\theta$  of maximum intensity in radians. This procedure was performed using PeakFit™ (v. 4.12) software.

### 3.1.3.4. SSNMR: $^{13}\text{C}$ CPMAS, DIPSHIFT and HETCOR techniques

The SSNMR experiments were performed on a Bruker<sup>®</sup> Avance 400 spectrometer, using a Bruker 4-mm magic angle spinning (MAS) double-resonance probe head, at 400.0 MHz ( $^1\text{H}$ ) and 100.5 MHz ( $^{13}\text{C}$ ) with 2.5  $\mu\text{s}$  and 4.0  $\mu\text{s}$  of  $\pi/2$  pulse length, respectively. About 100 mg of powdered samples were packaged into zirconia rotors and all spectra were recorded at  $25 \pm 1$  °C of probe temperature. RF-ramped cross-polarization under magic angle spinning ( $^{13}\text{C}$  CPMAS) (METZ; ZILIOX; SMITH, 1996) and Spinal-16  $^1\text{H}$  decoupling (SINHA et al., 2005) performed with  $\gamma B_1/2\pi = 70$  kHz were applied for  $^{13}\text{C}$  signal acquisition. It was set 5 s of recycle delay, 2 s of last delay (d1), 40 ms of acquisition time and 1024 scans. Since the strength of the  $^1\text{H}$ - $^{13}\text{C}$  dipolar coupling depends on the internuclear distance and intermolecular mobility, the contact time ( $T_C$ ) was varied from 0.5 to 5.0 ms. This procedure was applied to achieve an optimal  $T_C$  for all carbon signals, making a better approach with a direct  $^{13}\text{C}$  polarization (DPMAS), which was recorded by the time-consuming high power  $^1\text{H}$  decoupling, HPDEC (d1 = 100 s) (KASAAI, M. R., 2010). The  $\overline{DA}_{CP}$  was calculated using the CPMAS spectra at optimal  $T_C$  as described by Eq. (7) (OTTØY; VÅRUM; SMIDSRØD, 1996):

$$\overline{DA}_{CP} (\%) = \left( \frac{I_{CH_3}}{I_{C1-C6}/6} \right) \times 100 \quad (7)$$

where  $I_{CH_3}$  is the signal integral of methyl carbons from GlcNAc units and  $I_{C1-C6}$  is the sum of integrals from carbon signals of glucopyranose ring.

The relative mobility from distinguish molecular segments was estimated applying DIPSHIFT technique (HONG et al., 2002; MUNOWITZ et al., 1981). In DIPSHIFT, each  $^{13}\text{C}$  signal in the  $^{13}\text{C}$  CPMAS spectrum has the amplitude modulated by C-H dipolar coupling to the neighbor protons. The experiment output is the modulation profile, which represents the intensity vs. the modulation evolution time  $t_1$  varying from 0 to one rotor cycle. Because the C-H dipolar coupling depend on the molecular mobility, the modulation profile is heavily dependent on the presence of molecular motions with rates higher than  $\sim 100$  kHz, making possible to distinguish molecular segments based on their mobility. The HETCOR spectra were recorded based on previous protocol (KONO, 2004). The hydrogen related spectra were recorded on the indirect frequency dimension F1, although  $^{13}\text{C}$  CPMAS spectra were acquired in the F2 dimension.  $T_C$  was set at 500  $\mu\text{s}$  to provide the necessary mixing time for correlation

of non-directly bonded  $^1\text{H}$  and  $^{13}\text{C}$  nuclei; the recycle delay was set at 2 s and 512 scans were accumulated. The  $^1\text{H}$ - $^1\text{H}$  dipolar interaction was successfully suppressed employing the frequency switched Lee-Goldburg (FS-LG) (BIELECKI et al., 1990) decoupling method during the proton chemical shift evolution and TPPM for proton decoupling during the  $^{13}\text{C}$  acquisition. All SSNMR spectra were acquired at  $12,000 \pm 2$  Hz and DIPSHIFT at  $6,000 \pm 2$  Hz spinning frequencies. The  $^{13}\text{C}$  and  $^1\text{H}$  chemical shifts were calibrated using hexamethylbenzene (HMB) at 17.3 ppm and L-alanine at 1.3 ppm, respectively. The acetylation and crystallinity information were extraction from  $^{13}\text{C}$  CPMAS spectra applying the deconvolution procedure carried through PeakFit<sup>TM</sup> (v. 4.12) software.

### 3.1.3.5. *Multivariate analysis*

The singular value decomposition (SVD) was used as a pattern recognition method applied on  $^{13}\text{C}$  CPMAS analytical signals in order to cross-validate these spectra profiles with the average degree of acetylation and crystallinity as distinguish components. Ch spectrum were normalized by C1 signal area and centralized according to the signal of maximum intensity (C5-C3). As described by FORATO; BERNARDES-FILHO; COLNAGO (1998), the spectra matrix  $E$  can be obtained by the product of the matrix of pure components  $E_p$  and the concentration matrix  $C$  of these components ( $E = E_p C$ ), being  $X$  the calibration matrix that defines the percent of correlation between the concentration of the components  $C$  and the analytical signal ( $C = XE$ ). The SVD was applied to decompose the information into singular value and orthogonal eigenvector matrices, leading to the inverse matrices  $E^{-1}$  and  $C^{-1}$ . This procedure sets to allow the calculation of  $X$  and the interpretation of the signals regarding the contribution of each component. The theoretical spectra of pure components, meaning as totally crystalline and amorphous Ch profile, were then generated applying the SVD to  $C^{-1}$ . This multivariate processing analysis was performed using GNU Octav<sup>TM</sup> software.

### 3.1.4. *Results and Discussion*

#### 3.1.4.1. *Structure and long-range molecular ordering*

Chitosans named Ch1x, Ch2x and Ch3x has been prepared through USAD multistep process, achieving similar  $\overline{DA}$  values from previous studies (FACCHINATTO et al., 2019;

FIAMINGO et al., 2016) with no significant variations on  $\overline{M}_w$  and, consequently, preserving the  $\overline{DP}_w$  during the reaction on hash alkaline medium as shown in Table 1. These results provided the necessary conditions for the sequential depolymerization procedure, starting from USAD Ch samples with similar chain lengths and then granting Ch with lower molar masses.

Table 1 - Values of average degree of acetylation ( $\overline{DA}$ ), pattern of acetylation (PA), average molecular weight ( $\overline{M}$ ) and average degree of polymerization ( $\overline{DP}$ ).

Sample	$\overline{DA}^a$ (%)	PA <sup>b</sup>	$\overline{M}^c \times 10^6$ (g mol <sup>-1</sup> )	$\overline{DP}^d$
$\alpha$ Ch	-	-	0.42 ± 0.01	2140
$\beta$ Ch	-	-	1.56 ± 0.03	7840
Ch1x	30.6 ± 3.3	1.15	1.02 ± 0.23	5867
Ch1x3h	33.8 ± 3.3	1.22	0.43 ± 0.07	2455
Ch1x6h	34.5 ± 4.9	1.25	0.19 ± 0.06	1083
Ch2x	12.0 ± 3.8	1.28	0.94 ± 0.14	5661
Ch2x3h	14.3 ± 2.9	1.30	0.30 ± 0.05	1796
Ch2x6h	12.9 ± 3.1	1.25	0.19 ± 0.04	1142
Ch3x	7.1 ± 0.7	1.23	0.97 ± 0.20	5884
Ch3x3h	6.9 ± 1.2	1.26	0.33 ± 0.05	2014
Ch3x6h	6.9 ± 1.0	1.22	0.15 ± 0.03	915
Ch60	59.4 ± 2.3	1.02	1.17 ± 0.19	6293
Ch45	43.5 ± 0.7	1.14	1.13 ± 0.17	6303
Ch35	33.9 ± 0.6	1.21	1.10 ± 0.17	6277
Ch25	23.8 ± 1.3	1.26	1.00 ± 0.16	5848
Ch15	15.2 ± 0.9	1.32	0.99 ± 0.14	5914
Ch5	4.8 ± 1.7	1.25	0.96 ± 0.13	5889

<sup>a</sup> Determined from <sup>1</sup>H NMR spectra by considering the relative contribution of  $H1'$  referred to hydrogens bonded to anomeric carbons of GlcNAc units;

<sup>b</sup> Determined from <sup>1</sup>H NMR spectra applying the Bernoullian statistics to  $H1'$  (GlcNAc) and  $H1$  (GlcN) signals;

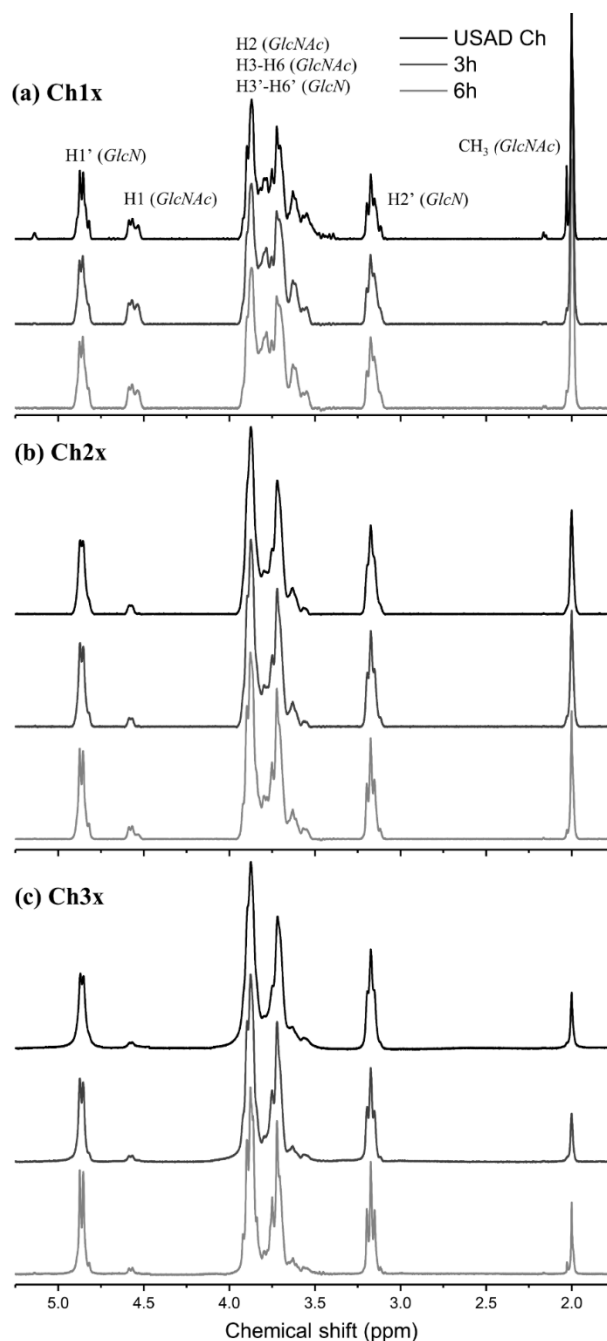
<sup>c</sup> Obtained from SEC calibration curve for chitosans ( $\overline{M}_w$ ) and by using Mark-Houwink-Sakurada equation with  $[\eta]$  values and the parameters  $K'$  and  $\alpha$  parameters for chitins ( $\overline{M}_v$ );

<sup>d</sup> Calculated by considering the  $\overline{M}$  and the relative amounts of GlcNAc and GlcN units on chitosans ( $\overline{DP}_w$ ) and chitins ( $\overline{DP}_v$ ).

Similarly, a recent study has submitted Ch to a sonication process at low concentrated acid medium (SAVITRI et al., 2014). Despite the great depolymerization efficiency achieved, the authors observed that such proposing method tends to break both residues at different rates, consequently leaving products with different  $\overline{DA}$  from parent Ch. Fortunately, as shown in Fig.

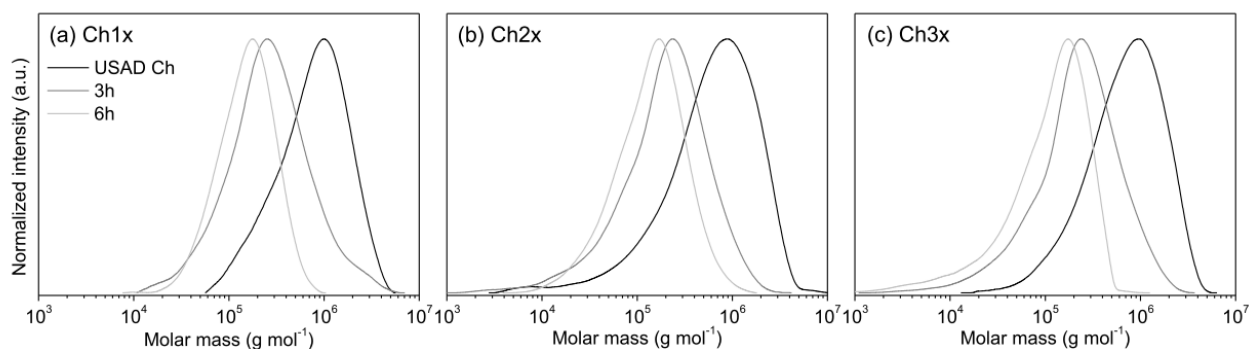
9, the  $^1\text{H}$  NMR spectrum of Ch samples reveals the depolymerizations proceeded efficiently without side reactions, and the overall chemical structure were essentially preserved at great extension after submitting these samples to each depolymerization step. This result confirms the successful cleavage of glycosidic bounds with no significant occurrence of undesirable deacetylation (Table 1), being also in agreement with the results from a established protocol in which Ch/ $\text{NaNO}_2$  ratios has been used (MAO et al., 2004).

Figure 9 -  $^1\text{H}$  NMR spectrum of USAD Ch1x (a); Ch2x (b); Ch3x (c) with respect to the spectrum of depolymerized (3h and 6h) samples in  $\text{D}_2\text{O}/\text{HCl}$  1% (v/v), acquired at  $85^\circ\text{C}$ .



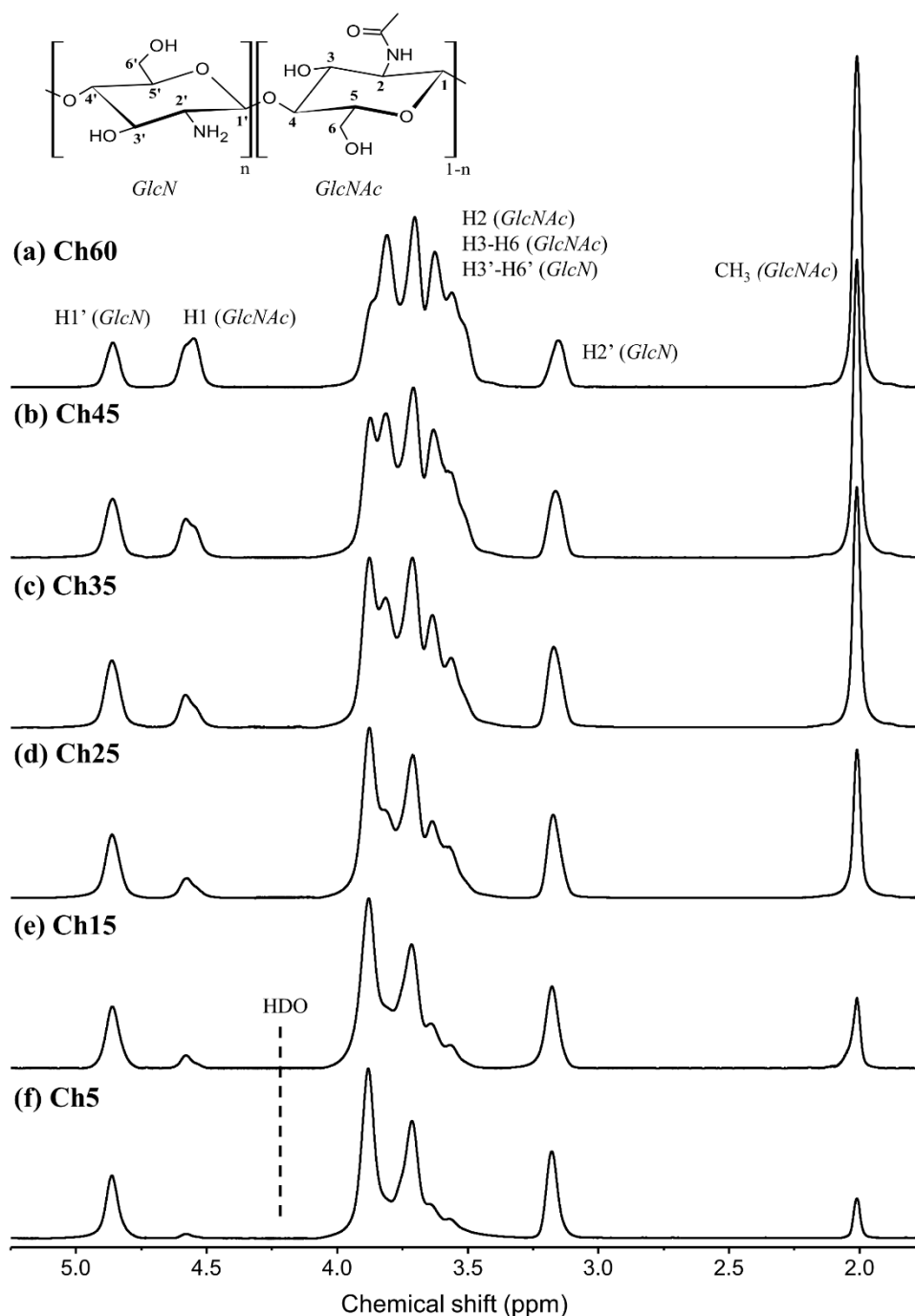
The pattern of molar masses distribution (Fig. 10) reveals the greater influence of first depolymerization with respect to the second one, which means that Ch1x, Ch2x and Ch3x with higher molar masses were more sensitive to depolymerization compared to Ch1x3h, Ch2x3h and Ch3x3h, similarly to results previously accomplished (MAO et al., 2004). The  $\overline{M}_w$  and  $\overline{DP}_w$  values (Table 1) also suggest that the chains cleavage slightly increases by decreasing the  $\overline{DA}$ .

Figure 10 - Size-exclusion chromatogram (SEC) profiles of USAD Ch1x (a); Ch2x (b); Ch3x (c) with respect to the profile of depolymerized (3h and 6h) samples.



The Ch3x sample was submitted to *N*-acetylation process achieving  $\overline{DA}$  values at very closer level with the expected ratios of anhydride/glucosamine (Table 1). No meaningful side reactions were detected and, considering the typical  $^1\text{H}$  NMR spectrum profiles presented by Ch5 to Ch60 (Fig. 11), the reactive conditions under acetic medium with 1,2-propanediol used as cosolvent avoided the *O*-acylation and favored the formation of *N*-acylated products (HIRANO; TSUCHIDA; NAGAO, 1989; VACHOUD; ZYDOWICZ; DOMARD, 1997). The slight variations on  $\overline{M}_w$  values ( $\sim 10^6 \text{ g mol}^{-1}$ ) are mainly ascribed to the gradual increment of acetamido moieties, once the  $\overline{DP}_w$  has just varied shortly in the range from  $\sim 5900$  to  $\sim 6300$  (Table 1). Thus, for practical concerns, it is reasonable to consider that it has no significant modifications, especially regarding the molecular weight of Ch backbone, from *N*-acylated samples, and the reaction medium were sufficiently mild to preserve the products with a negligible influence on chains lengths. Such result is consistent with the literature (KNAUL et al., 1998; KUBOTA; EGUCHI, 2005), in which the molecular weights of *N*-acylated Ch prepared under homogeneous conditions were no significantly affected.

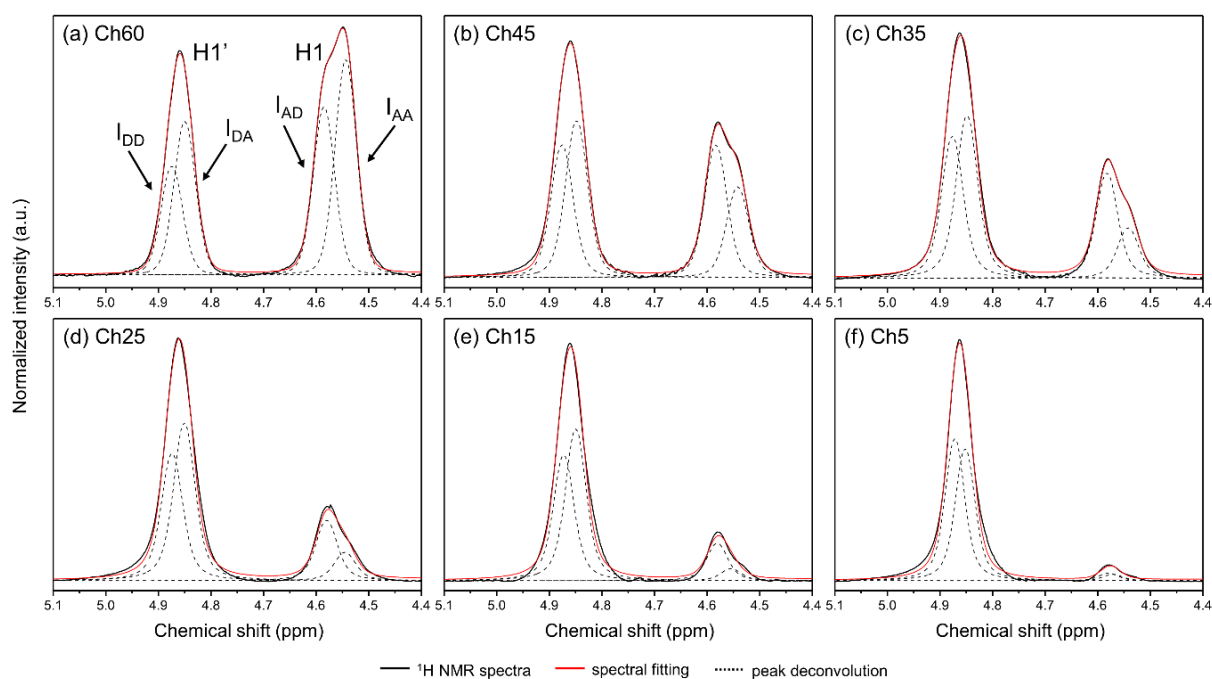
Figure 11 -  $^1\text{H}$  NMR spectrum of *N*-acetylated Ch samples, named as Ch60 (a); Ch45 (b); Ch35 (c); Ch25 (d); Ch15 (e) and Ch5 (f) in  $\text{D}_2\text{O}/\text{HCl}$  1% (v/v), acquired at 85 °C.



Despite this desirable feature, our main intent concerned to the preparation of *N*-acetylated Ch with a broader interval of  $\overline{DA}$  compared to the USAD Ch firstly prepared, granting a random-like distribution of acetamido moieties ( $PA \sim 1$ ) (LAVERTU; DARRAS; BUSCHMANN, 2012; SORLIER et al., 2001). As confirmed by the Bernoullian statistics applied on  $\text{H1}'$  and  $\text{H1}$  hydrogens signals (Fig. 12), the homogenous system ensured that the

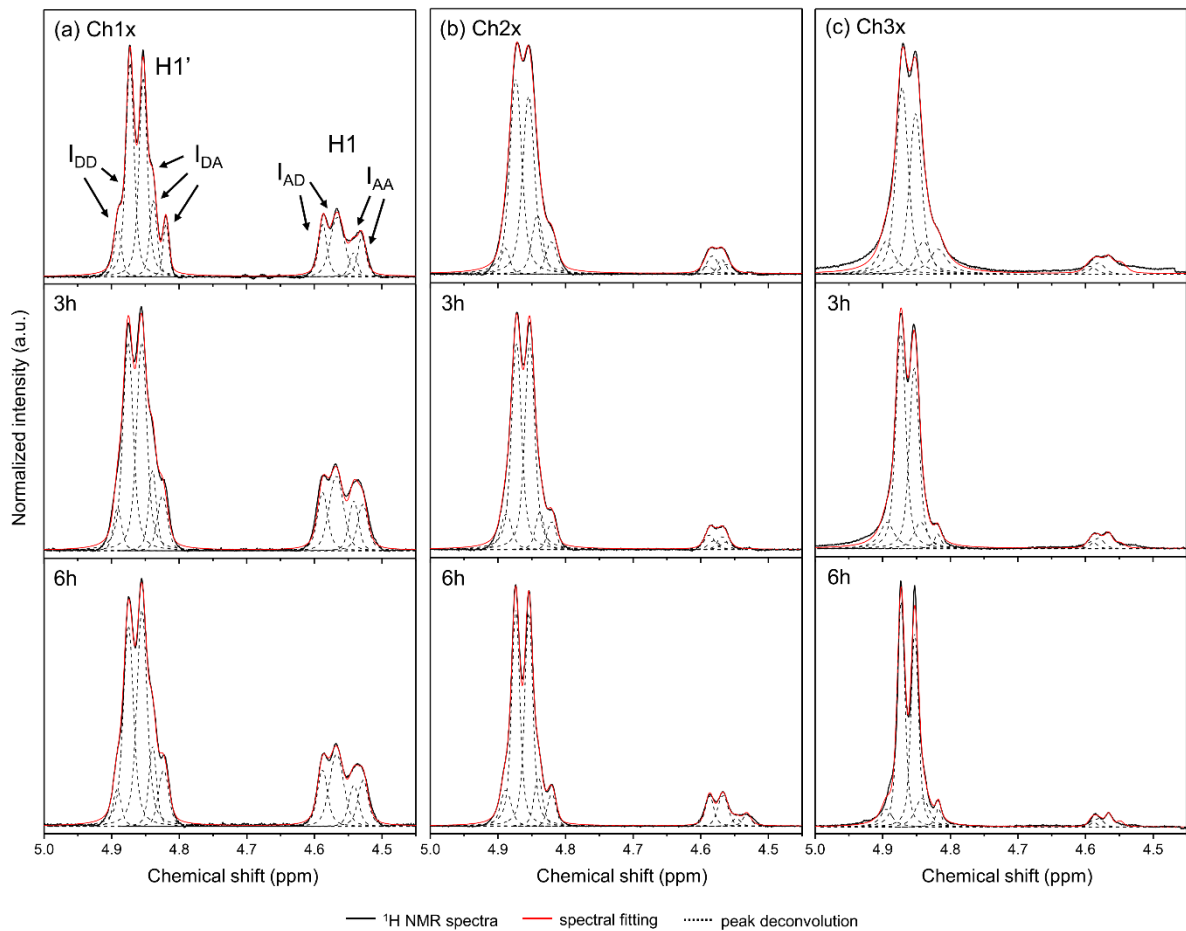
addition of acetate groups is mediated by the accessibility to sites that contain amino groups with lower steric hindrance between vicinal segments, preferentially choosing those with the greater gap from each acetamido as possible.

Figure 12 -  $^1\text{H}$  NMR spectrum interval of N-acetylated Ch samples, named as Ch60 (a); Ch45 (b); Ch35 (c); Ch25 (d); Ch15 (e) and Ch5 (f), assigned to  $H1'$  and  $H1$  signals, used for determination of  $\overline{DA}$  and  $PA$ .



Therefore, as listed in Table 1, the  $PA$  values reached about 1.0 to 1.3 for Ch, including the deacetylated and depolymerized samples (Fig. 13) prepared on heterogeneous medium. This occurrence is due to the slightly higher probability to have a frequency of GlcNAc-GlcNAc residues and then increased chances to form a block-wise distribution on heterogeneous conditions mainly at higher acetylation levels ( $\overline{DA} > 50\%$ ) (HIRANO; TSUCHIDA; NAGAO, 1989; VÅRUM et al., 1991). Nevertheless, Ch1x, Ch45 and Ch60 samples nearly accomplished the requirement for a random-like distribution.

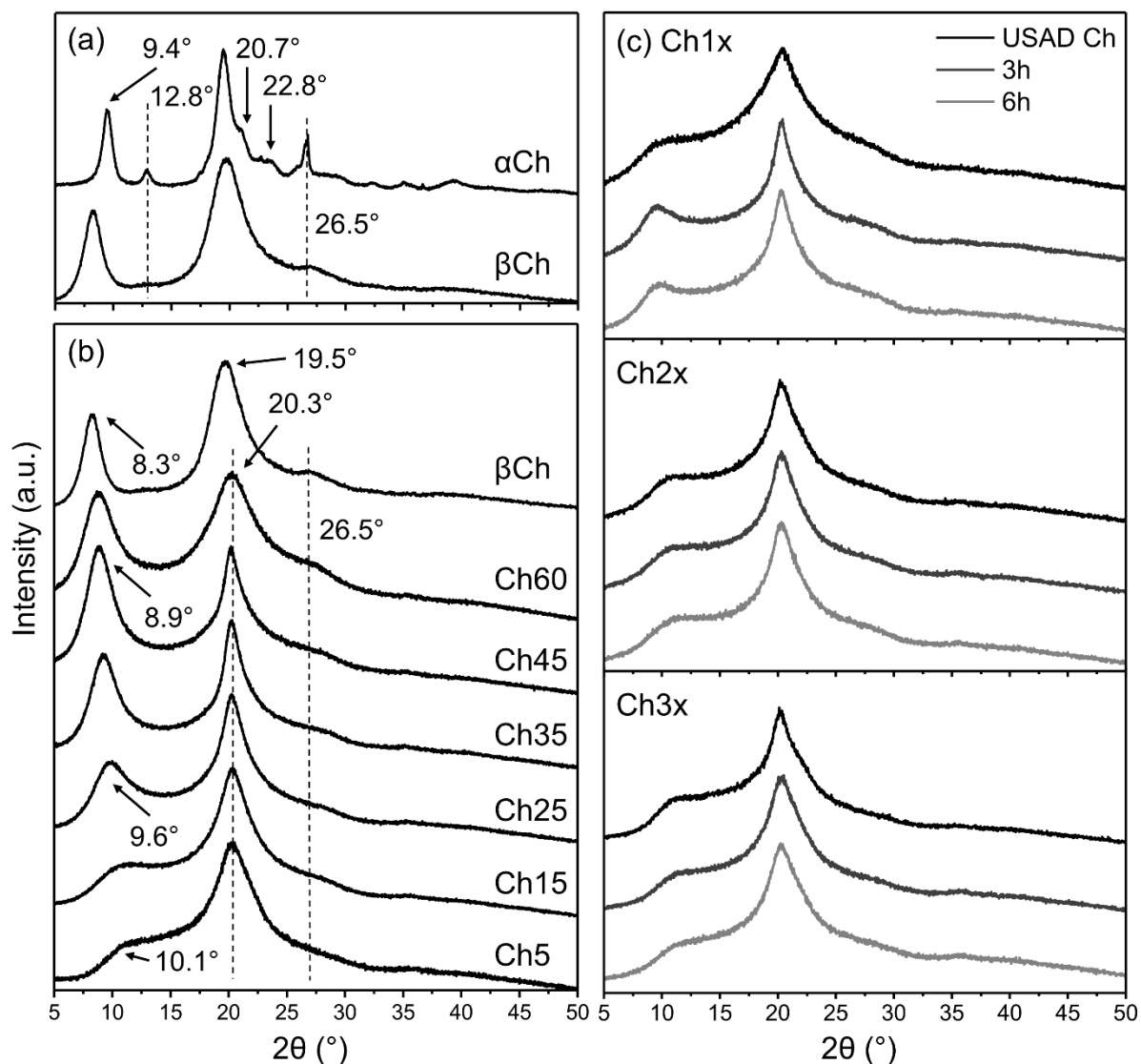
Figure 13 -  $^1\text{H}$  NMR spectrum interval of USAD Ch1x (a); Ch2x (b); Ch3x (c) with respect to the spectrum of depolymerized (3h and 6h) samples, assigned to  $H1'$  and  $H1$  signals, used for determination of  $\overline{DA}$  and  $PA$ .



Thus, the independent  $\overline{M}_w$  and  $\overline{DA}$  values with acetamido groups randomly distributed ( $PA \sim 1$ ) have been successfully achieved to evaluate the morphological feature from XRD patterns (Fig. 14). As illustrated in Fig. 14a, the diffractograms of chitins reveals the highly ordered pattern of  $\alpha\text{Ch}$ , that preserves the orthorhombic  $P2_12_12_1$  symmetry with antiparallel chains displacement (MINKE; BLACKWELL, 1978), compared to the typical profile of hydrated  $\beta\text{Ch}$  allomorph that reveals a monoclinic  $P2_1$  symmetry with parallel displacement and lower intersheet interaction across  $bc$  projection (GARDNER; BLACKWELL, 1975). The two diffraction peaks with the highest intensities comprising between  $2\theta \sim 8^\circ\text{-}11^\circ$  and  $19^\circ\text{-}21^\circ$  are mainly assigned to the hydrated crystalline planes  $(020)_h$  and  $(110)_h$ , respectively, whereas secondary peaks are predominantly evidenced on  $\alpha\text{Ch}$ . Such allomorph exhibits the peaks centered at  $13.8^\circ$  and  $22.8^\circ$  related to the anhydrous planes  $(110)_a$  and  $(120)_a$  reflections, respectively, while the peak at  $26.5^\circ$  which describes the  $(013)_a$  reflection are evidenced on

both chitins diffractograms (Fig. 14a) and seems to be related to  $\overline{DA}$ , once its relative intensity decreases from Ch60 to Ch5 (Fig. 14b).

Figure 14 - XRD patterns of  $\alpha$ - and  $\beta$ Ch (a); Ch5-60 and  $\beta$ Ch (b); USAD (Ch1x, Ch2x and Ch3x) and depolymerized (3h and 6h) Ch samples (c).



All Ch samples and  $\beta$ Ch (Fig. 14b,c) shows a broader peak at  $19^{\circ}$ - $21^{\circ}$ , hindering the  $(220)_h$  reflection at  $20.7^{\circ}$  that only clearly appears on  $\alpha$ Ch (OSORIO-MADRAZO et al., 2010). The absence of  $(110)_a$  reflection on Ch samples has been attributed to confirm the diffraction pattern of a hydrated (tendom) crystalline form. In such case, the hydrated Ch samples are stabilized by  $O3 \cdots O5$  hydrogen bonds and water-bridges between chains, which allows a twofold helical conformation to be preferentially formed (OKUYAMA et al., 1997; SIKORSKI; HORI; WADA, 2009)

Although single crystals of Ch have been identified with orthorhombic  $P2_12_12_1$  unit cell, the same symmetry found on  $\alpha$ Ch allomorph (CARTIER; DOMARD; CHANZY, 1990; SIKORSKI; HORI; WADA, 2009), an extensive crystalline disruption is provided by the high penetration of water molecules to produce Ch samples, which reduces the average crystallite sizes and leads to a structure expansion across  $b$  axis, due to the fact there are no intersheet hydrogen bonds between  $C(6_1)O \cdots HOC(6_2)$  along this axis (CHO et al., 2000). Nevertheless, the hydrated Ch preserves the  $N2 \cdots O6$  hydrogen bonds along  $b$  and then granting the intersheet parallel arrangement on  $bc$  projection (OKUYAMA et al., 1997).

The crystallite dimensions  $L_{020}$  and  $L_{110}$  from Ch samples, obtained by deconvolving the respective peaks (APPENDIX A), converged the values closer to those exhibited by  $\beta$ Ch (Table 2), consequently losing the structural compactness and then achieving a diffraction pattern more similar to such allomorph (SAITO et al., 1997). All the procedures involved on the preparation of Ch samples enabled this crystalline disruption and, consequently, shifted the peaks at  $8^\circ$ - $11^\circ$  and  $19^\circ$ - $21^\circ$  to higher scattering angles. The first one continuously shifts and decreases its relative intensity suggesting that the crystal structure was slightly distorted by decreasing the  $\overline{DA}$  (CHO et al., 2000; ZHANG et al., 2005), while the variability on  $19^\circ$ - $21^\circ$  peak width are possible ascribed to non-uniform deformations of crystallites (Fig. 14b) (GARVEY; PARKER; SIMON, 2005). Indeed, by lowering the peak intensity at  $8^\circ$ - $11^\circ$ , the hydrated  $(020)_h$  reflection should be closer to those exhibited by a completely amorphous pattern (OSORIO-MADRAZO et al., 2010), thus decreasing the regularity provided by interchain hydrogen bonds between  $C(7_3)=O \cdots HNC(2_1)$  and  $C(7_3)=O \cdots HOC(6_1)$  across  $a$  axis.

As observed in Fig. 14c, there are no significative variations on the diffraction patterns as function of  $\overline{M}_w$ , especially regarding the molar mass changes among samples with lower  $\overline{DA}$  (Ch2x and Ch3x). This result agrees with previous studies in which was found that the crystallinity is influenced by lowering the molar mass from Ch sample with  $\overline{DA} > 20\%$  (OGAWA; YUI, 1993; SAVITRI et al., 2014), similarly to the recorded for Ch1x ( $\overline{DA} \sim 30\%$ ) that shows few changes in the diffraction pattern compared to those from Ch1x3h and Ch1x6h.

Table 2 - Crystallite lattice dimension from peaks at  $2\theta \approx 8^\circ\text{-}11^\circ$  ( $L_{020}$ ) and  $19\text{-}21^\circ$  ( $L_{110}$ ), and crystallinity index ( $CrI_1$  and  $CrI_2$ ) estimated by different methods applied on XRD patterns.

Sample	$L_{020}^a$ (nm)	$L_{110}^a$ (nm)	$CrI_1^b$ (%)	$CrI_2^c$ (%)
$\alpha$ Ch	7.74	5.64	86.1	68.8
$\beta$ Ch	4.70	3.39	78.8	64.6
Ch1x	2.14	2.10	44.2	29.0
Ch1x3h	2.52	4.30	58.3	29.1
Ch1x6h	2.97	3.34	56.5	27.8
Ch2x	2.14	3.23	53.2	30.4
Ch2x3h	2.27	3.36	54.7	30.5
Ch2x6h	2.00	3.28	54.1	28.9
Ch3x	2.32	3.47	52.6	36.4
Ch3x3h	2.71	2.91	54.3	33.2
Ch3x6h	2.57	2.87	53.4	29.4
Ch60	2.97	2.48	48.6	48.0
Ch45	3.21	4.93	56.9	51.8
Ch35	3.21	5.12	61.5	45.3
Ch25	2.59	4.10	57.3	43.5
Ch15	2.20	3.31	53.1	44.0
Ch5	2.71	2.86	50.2	39.4

<sup>a</sup> Calculated through the *FHWM* of crystalline peaks, obtained through deconvolution processing from XRD patterns, using Scherrer equation.

<sup>b</sup> Calculated from XRD patterns by applying the peak height method.

<sup>c</sup> Calculated from XRD patterns by applying the amorphous scattering subtraction method.

The long-range ordering was estimated by means of crystallinity index applying two different methods ( $CrI_1$  and  $CrI_2$ ) of quantification on XRD patterns. The corresponding  $CrI_1$  and  $CrI_2$  values are listed on Table 2, showing that  $CrI_1 > CrI_2$  to almost all samples. However, distinct results of crystallinity index have been achieved for a given a sample, being evident the considerable influence of the method employed. Nevertheless, both values for each case tends to increase with  $\overline{DA}$  mainly on samples prepared in homogeneous conditions, except for Ch60, that revealed a slight decrease, and Ch35, that showed an unexpected increase on  $CrI_1$ . The deacetylated (USAD) and depolymerized Ch showed closer  $CrI_1$  values, which means that the straight relationship with  $\overline{DA}$  and crystallinity is not clearly observed on samples originally prepared in heterogeneous conditions. Additionally, a slight decrease on  $CrI_2$  values is only observed lowering the  $\overline{M}_w$  of Ch2x and Ch3x samples. Such discrepancy confirms the unsolved issue regarding the exact contribution of amorphous phase on scattering profile, as already

pointed out (IOELOVICH, 2014; OSORIO-MADRAZO et al., 2010), despite the possibility to carry similar tendencies through both methods mainly on products homogeneously prepared. In this sense, the accurate and reproductive determination of Ch crystallinity, even considering a wider structural variability, is largely affected by the processing steps of Ch preparation and XRD method, which is also not able to differentiate the molecular origin of the amorphous components.

### 3.1.4.2. Conformation and short-range molecular ordering

As it is well known the  $T_C$  dependence of the  $^{13}\text{C}$  CPMAS spectral profile arises from cross-polarization (CP) transfer rate, which depends on the dipolar coupling between the  $^{13}\text{C}$  and the neighbor  $^1\text{H}$  nuclei (METZ; ZILIOX; SMITH, 1996; TANNER et al., 1990). Thus, the  $^{13}\text{C}$  CPMAS spectra were initially acquired varying  $T_C$  to seek for an optimal condition that minimizes the signal dependence on the polarization transfer (KASAAI, 2010). This procedure was applied on the Ch25 sample due to the intermediate content of acetamido groups compared to the other samples. A set of  $^{13}\text{C}$  CPMAS spectra were acquired with different  $T_C$  and the spectral profile was compared to that of a quantitative  $^{13}\text{C}$  DPMAS spectrum as shown in Fig. 15. Therefore, with  $T_C = 3000 \mu\text{s}$ , the  $^{13}\text{C}$  CPMAS spectrum achieves a similar profile to the exhibited by the  $^{13}\text{C}$  DPMAS spectrum in the whole spectral range. All  $\overline{DA}_{CP}$  at  $3000 \mu\text{s}$  are listed on Table 3.

Figure 15 -  $^{13}\text{C}$  CPMAS spectra ( $d_1 = 2 \text{ s}$  and  $12 \text{ kHz}$  of spinning frequency) profiles of Ch25 at variable  $T_C$  values (1000 to 4000  $\mu\text{s}$ ) compared to  $^{13}\text{C}$  DPMAS profile at the whole spectral range (a) covering the interval of C4, C5-C3, C6 and C2 signals (b); C1 (c) and  $\text{CH}_3$  (d) signals.

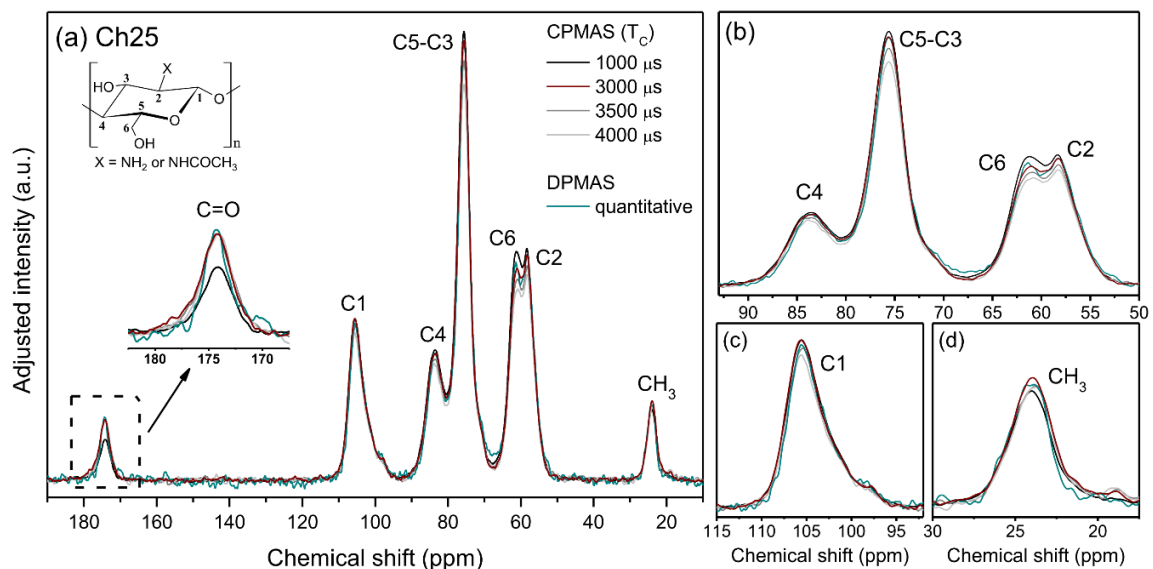


Table 3 - Values of average degree of acetylation ( $\overline{DA}_{CP}$ ) and crystallinity index estimated from C4 and C6 signal resonance of  $^{13}\text{C}$  CPMAS ( $T_C = 3000 \mu\text{s}$ ,  $d1 = 2 \text{ s}$  and  $12 \text{ kHz}$  of spinning frequency) spectra profiles ( $CrI_{CP}$ ).

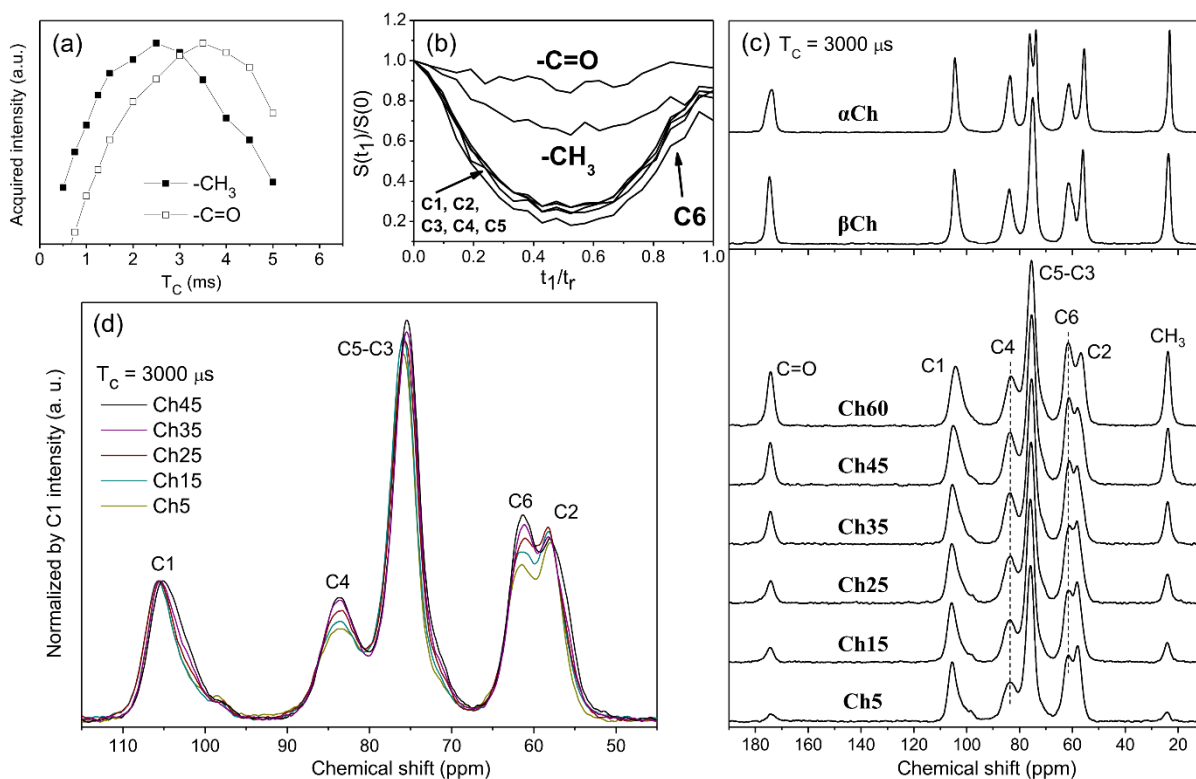
Sample	$\overline{DA}_{CP}$ <sup>a</sup> (%)	$CrI_{CP}$ <sup>b</sup> (%)	
		C4	C6
$\alpha\text{Ch}$	$87.9 \pm 3.9$	89.0	87.9
$\beta\text{Ch}$	$90.5 \pm 5.7$	82.1	80.7
Ch1x	$37.7 \pm 1.7$	54.7	56.9
Ch1x3h	$38.6 \pm 1.1$	55.7	56.3
Ch1x6h	$37.3 \pm 1.5$	53.6	57.9
Ch2x	$18.6 \pm 0.5$	46.9	47.0
Ch2x3h	$17.7 \pm 1.1$	45.2	48.5
Ch2x6h	$19.6 \pm 0.4$	46.9	47.3
Ch3x	$10.3 \pm 1.3$	35.8	38.3
Ch3x3h	$8.8 \pm 0.6$	35.7	39.5
Ch3x6h	$9.8 \pm 1.9$	36.7	38.6
Ch60	$59.3 \pm 3.5$	66.7	63.8
Ch45	$46.7 \pm 2.4$	59.8	61.5
Ch35	$38.8 \pm 1.33$	56.0	57.6
Ch25	$29.1 \pm 0.8$	50.2	51.8
Ch15	$18.3 \pm 1.5$	46.3	48.5
Ch5	$9.6 \pm 1.1$	34.7	37.4

<sup>a</sup> Determined from  $^{13}\text{C}$  CPMAS spectra by considering the relative contribution of methyl carbons with respect to glucopyranose ring carbons.

<sup>b</sup> Estimated by the relative area of ordered to disordered contribution on C4 and C6 signals of  $^{13}\text{C}$  CPMAS spectra using deconvolution method with Lorentzian and Gaussian functions, respectively.

Fig. 16a compares the  $^{13}\text{C}$  CPMAS signal intensity of  $\text{CH}_3$  and  $\text{C}=\text{O}$  groups as function of  $T_C$ . As expected, the  $\text{CH}_3$  signal shows faster CP build-up, due to three hydrogens direct bonded, and shorter decay time, due to the fast rotation around the C3 axis leading to a shorter relaxation time decay in rotating frame ( $T_{1\rho}$ ) (SAITÔ; TABETA; OGAWA, 1987). These results confirm that the best coincidence between the  $^{13}\text{C}$  CPMAS and the quantitative  $^{13}\text{C}$  DPMAS spectra is achieved at  $T_C = 3000 \mu\text{s}$ , once the signal integral ratio  $I_{\text{C}=\text{O}}/I_{\text{CH}_3} \sim 1$  reveals equivalent amount of both groups in the structure, as expected. Thus,  $^{13}\text{C}$  CPMAS with  $T_C = 3000 \mu\text{s}$  will be used here instead of the very time consuming  $^{13}\text{C}$  DPMAS spectra. However, it is important to point out that the chain mobility in the sample can change the optimal  $T_C$ , so such approach would only be possible if all samples have similar molecular mobility.

Figure 16 - CP build-ups for CH<sub>3</sub> and C=O groups of Ch25 (a); DIPSHIFT curves acquired from Ch25 (b); <sup>13</sup>CPMAS spectra of α-, βCh and Ch5-60 (c); and relationship of N-acetylated Ch profiles at T<sub>C</sub> = 3000 μs, d<sub>1</sub> = 2 s and 12 kHz of spinning frequency showing the conformational dependence of  $\overline{DA}$  (d).



The specific mobility along the molecular segments can be formally confirmed through the DIPSHIFT experiments. Such technique provides the access to the molecular mobility by monitoring the strength of the <sup>1</sup>H-<sup>13</sup>C dipolar interaction, which can be reduced by molecular motions. This is probed by applying a pulse sequence that modulates each <sup>13</sup>C signal in the <sup>13</sup>C CPMAS spectrum by a factor that depend on the dipolar coupling to its next neighbor <sup>1</sup>H nuclei during an evolution time  $t_1$ . The plot of the intensity of each <sup>13</sup>C signal as a function of  $t_1$  provide the so called DIPSHIFT curves, which have a “smile like” shape starting from a maximum value at  $t_1 = t_r$  reaching a minimum at  $t_1 = t_r/2$  and restoring to a value that depend on the  $T_2$  relaxation time of that specific carbon spin. The dependence of the DIPSHIFT curves on <sup>1</sup>H-<sup>13</sup>C dipolar interaction strength appears in the minimum intensity value reached at  $t_1 = t_r/2$  in such a way that higher is the dipolar interaction strength lower is the minimum intensity. Because molecular motions with rates higher than 10 kHz average out the dipolar interaction, this minimum value is increased for mobile segments. Slower motion, *i.e.*, with rates in the low kHz frequency scales, reduces the  $T_2$  relaxation time and show up in the DIPSHIFT curves as an intensity reduction at  $t_1 = t_r$  (DEAZEVEDO et al., 2008; MUNOWITZ et al., 1981).

As showed in Fig. 16b, the minimum intensity at  $t_1 = t_r/2$  achieved to C=O carbons is  $\sim 0.9$ , which is trivially associated to the lack of directly bonded  $^1\text{H}$ . Still the minimum intensity achieved by the  $\text{CH}_3$  carbon is  $\sim 0.7$ , which is closer to methyl carbons of L-alanine, confirming that the decrease of dipolar interaction is mainly consequence of the fast motion around its C3 symmetry axis. For carbons C1 to C5 the minimum intensity is  $\sim 0.25$ . This is a typical value obtained for CH carbons on glucose units of rigid carbohydrates (SIMMONS et al., 2016) pointing to a rigid backbone structure in the Ch sample. For rigid  $\text{CH}_2$  carbons the minimum intensity of the DIPSHIFT curves should reach  $\sim 0$ . This is not the case of the C6 signal, where the minimum intensity is  $\sim 0.2$ . This is associated to local motion of the  $\text{CH}_2\text{OH}$  side chain, which also decrease the  $T_2$  values and leads to a smaller final intensity at  $t_1 = t_r$  for the C6 carbons as compared to carbons C1-C5. All Ch samples showed similar DIPSHIFT profiles, showing that all samples have similar chain mobility. This information is important because it supports the use of the  $^{13}\text{C}$  CPMAS, instead of the quantitative, but very time consuming,  $^{13}\text{C}$  DPMAS spectra for evaluating the  $\overline{DA}$  and the NMR crystallinity of the samples.

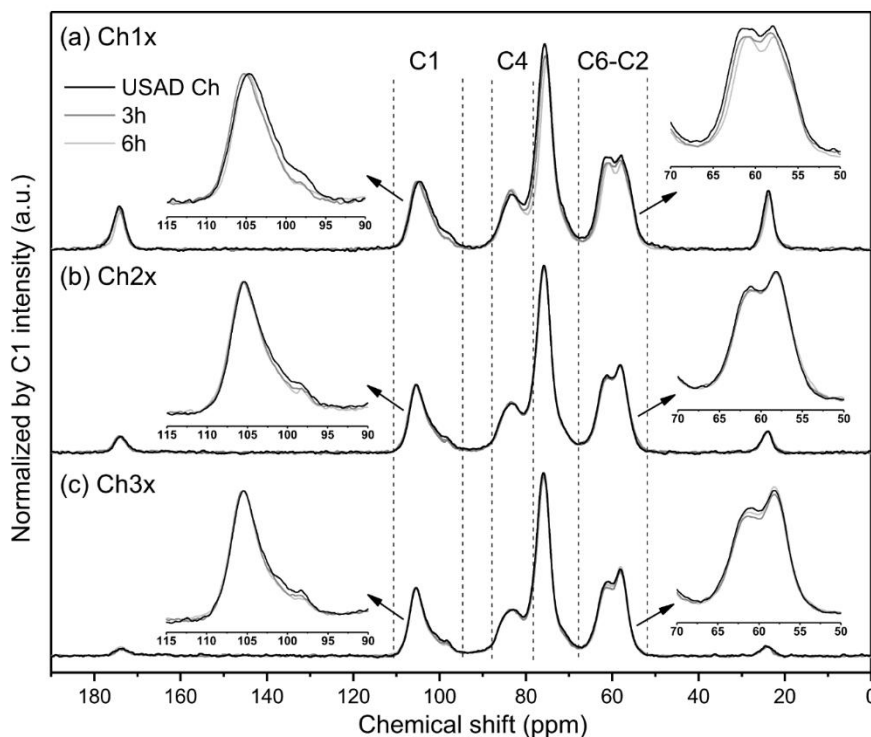
The  $^{13}\text{C}$  CPMAS spectra of acetylated Ch and chitin allomorphs are shown in Fig. 16c. Although  $\beta\text{Ch}$  reveals overlapped C5 and C3 signals, those are usually split on  $\alpha\text{Ch}$  leading to different chemical shifts, which indicates the main influence of packing and geometrical effects on polymeric chains (FOCHER et al., 1992; HEUX et al., 2000). Additionally, the asymmetrical shape of C=O from  $\alpha\text{Ch}$  are probably consequence of an inefficient removal of the strong dipolar interaction between the direct bonded quadrupolar  $^{14}\text{N}$  nucleus (TANNER et al., 1990). Indeed, such behaviors suggest higher density and homogeneity, due to the antiparallel arrangement of  $\alpha\text{Ch}$  chains, compared to the broad signals of  $\beta\text{Ch}$  and Ch samples that suggest lower homogeneity (Fig. 16c).

The profile of acetylated Ch samples follows the tendency assigned to C=O and  $\text{CH}_3$  signals, in accordance with  $\overline{DA}$  variation (Fig. 16c). A closer overview of this current region of the spectra, detached on Fig. 16d, shows that all resonances presented significant changes and specially C1, C4 and C6 signals clearly increases with  $\overline{DA}$ . The C4 signal in the  $^{13}\text{C}$  CPMAS spectra has been widely used to estimate the fraction between the internal (more ordered chain) and surface (more disordered) fibrils structures, which is usually referred as crystalline index (PARK et al., 2010). Similarly, it is reasonable to consider that those signals proportionally increase with Ch crystallinity. The spectral line shape is sensitive to the molecular conformation and content of ordered segments, being applicable a qualitative understanding based on  $\gamma$ -effect concept (BORN; SPIESS, 1997; TONELLI; SCHILLING, 1981). For this approach, it has to be firstly considered a molecular model building made by helical symmetry with a period of

10.34 Å across a fiber axis. Such model was properly used for explain the torsion angles of glycosidic linkages of Ch on  $^{13}\text{C}$  NMR data as complementary means to XRD by SAITÔ et al. (1987), and was formally detailed by OKUYAMA et al. (1997). This model includes two dihedral angles ( $\varphi$ ,  $\psi$ ) in the main-chain conformation represented by glycosidic C(1)-O1-C(4<sub>1</sub>) linkage, and a third dihedral angle ( $\chi$ ) at C(5)-C(6) that define the orientation of O6. Although  $\varphi$  and  $\psi$  are average stable with low degree of freedom, which is ensured by hydrogen bonds between O3 $\cdots$ O5,  $\chi$  can fall into three orientations at  $-60^\circ$ ,  $+60^\circ$  and  $180^\circ$ , satisfying the *gauche-gauche*, *gauche-trans* and *trans-gauche* conformations, respectively, with respect to C(4) (OKUYAMA et al., 1997). As already mentioned, it is well-accepted that O6 are not comprising on C(6<sub>1</sub>)O $\cdots$ HOC(6<sub>2</sub>) but still participates on C(7<sub>3</sub>)=O $\cdots$ HOC(6<sub>1</sub>) hydrogen bonds on  $\beta$ -forms, meaning that  $\overline{DA}$  actually affects the population of possible conformations of C(6)OH group. Therefore, we suppose that a wider distribution of these conformations is proportionally achieved by decreasing the  $\overline{DA}$  and so the population of this segments packed in a regular way. Consequently, the electronic structure around C(6) and C(4), located at two  $\sigma$ -bonds of distance, experiences different dipolar interactions, reflecting on those CP signals.

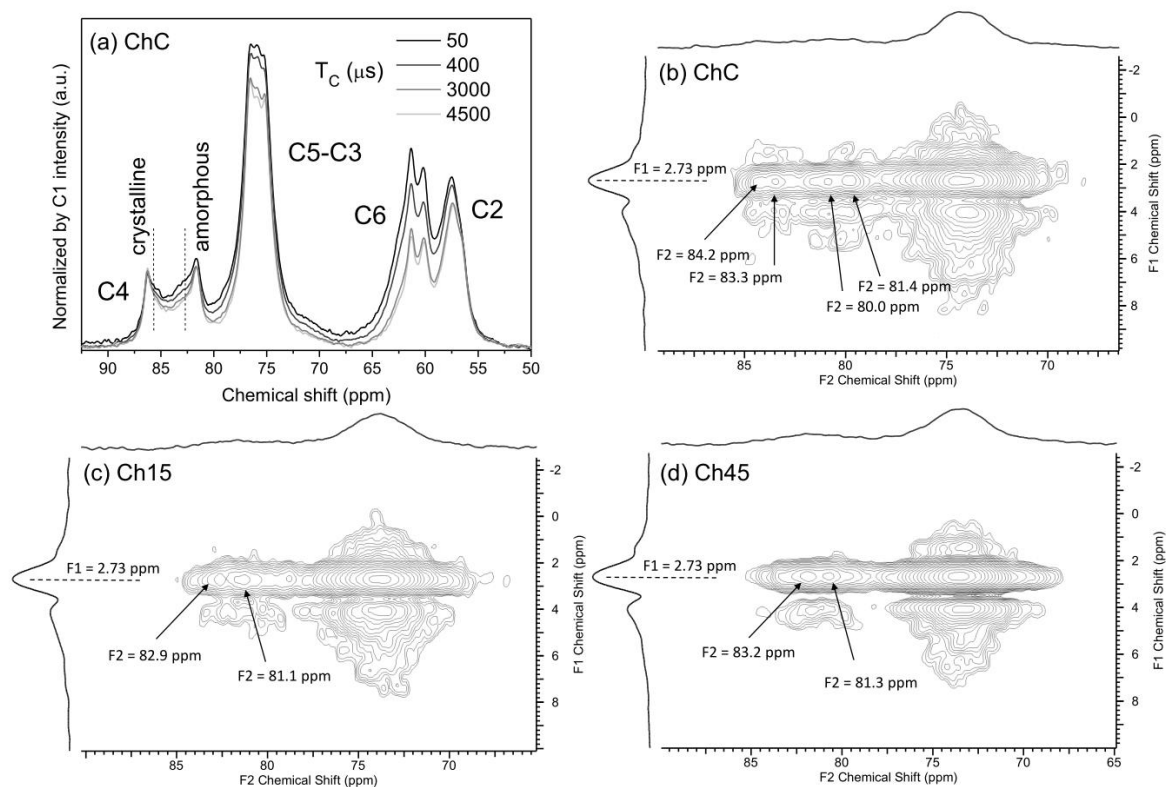
Differently from XRD data, the conformational refinement by CPMAS allows to observe slight variability on depolymerized Ch (Fig. 17). However, those are mainly assigned on C1 and C6 signals, showing no significant changes on C4. Considering that the depolymerization extensively undergoes on glycosidic linkages, this result confirms that C1 and C6 signals are quite sensitive to main-chain conformation specially on first depolymerization step, while C4 signal reveals great dependence with the  $\overline{DA}$  but none significative changes with molar masses. An exception regards to Ch1x that shows few changes on these related signals, probably ascribed to some packing influence that remains after heterogenous deacetylation of  $\beta$ Ch. According to studies (FOCHER et al., 1990; HEUX et al., 2000; SAITÔ; TABETA; OGAWA, 1987), the chains length dependence of C4 were only found at higher (annealing) temperatures, however such behavior was not formally ruled by the authors.

Figure 17 -  $^{13}\text{C}$  CPMAS spectra ( $T_C = 3000 \mu\text{s}$ ,  $d1 = 2 \text{ s}$  and  $12 \text{ kHz}$  of spinning frequency) of USAD Ch1x (a); Ch2x (b) and Ch3x (c), with respect to depolymerized (3h and 6h) Ch samples.



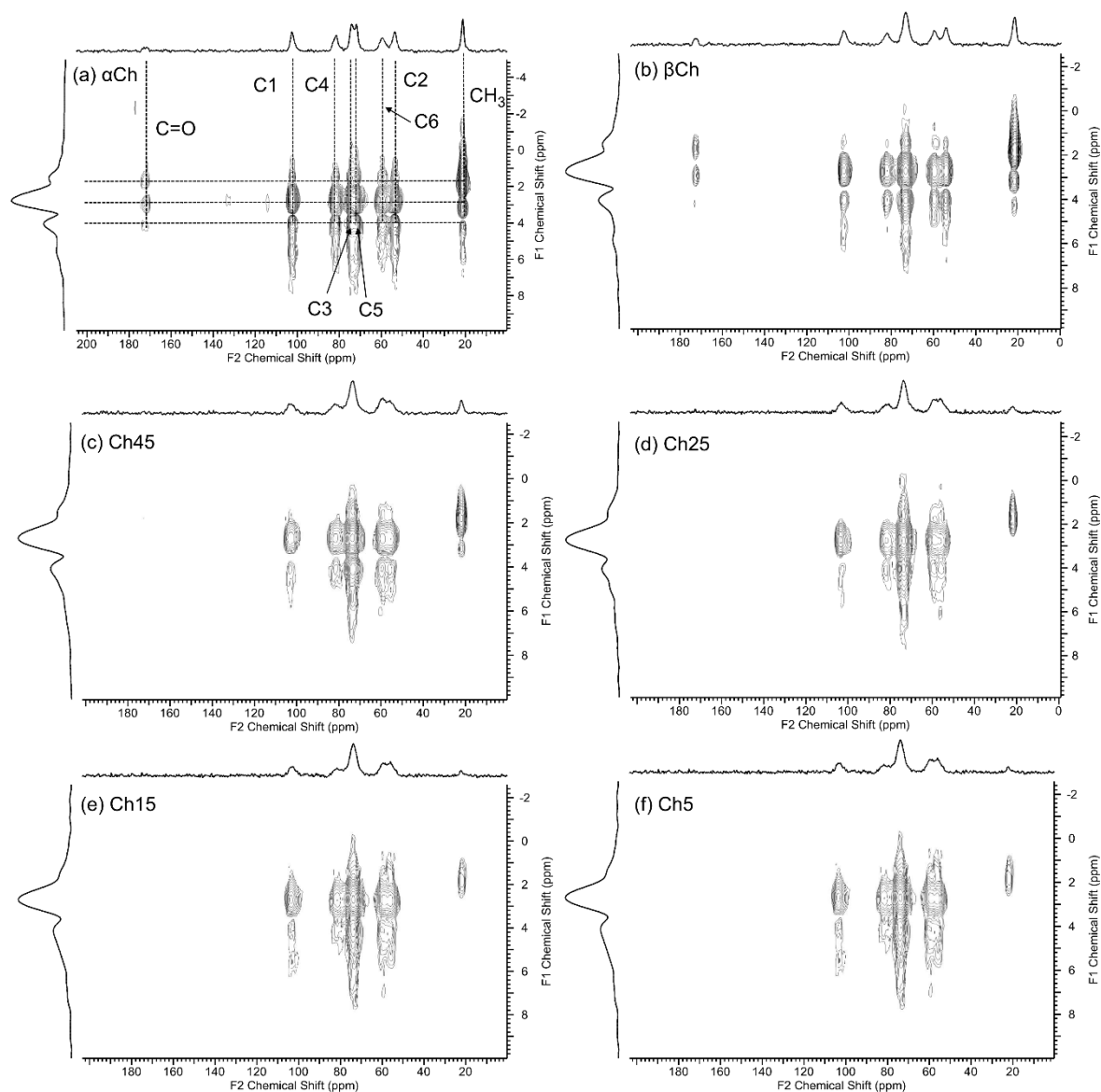
A proof of concept concerning the ordered and disordered contribution on C4 and C6 signals was carried by means of  $T_C$  ranged from 50 to 4500  $\mu\text{s}$  on ChC sample, which actually present splitted assignments for both signals (Fig. 18a). The spectral interval ranged in 95-50 ppm shows that each assigned C4 peak responds to dipolar interaction at differently CP rates. According to the C4 signal evolution profile, the downfield shifted C4 peak quickly recovers the magnetization even at shorter  $T_C$  (50  $\mu\text{s}$ ) compared to the upfield shifted peak, that requires longer  $T_C$  values to be totally polarized. Such behavior is typically ascribed to changes on molecular packing, once the spin diffusion is longer on amorphous phases, which have naturally lesser packed arrangement than the crystalline one (ANDO; ASAKURA, 1998). Each C4 peak can be properly described by such physical behavior, leading to distinguished chemical shifts for crystalline and amorphous domains, as expected by the  $\gamma$ -effect. In fact, and considering an wide distribution of  $\chi$  dihedral angles, the *trans* isomerism provides higher regularity and it is commonly downfield shifted, while *gauche* is associated to lesser regularity and it is upfield shifted (BORN; SPIESS, 1997), as confirmed by C4 signal of ChC. However, this behavior was not clearly evidenced on C6 split peaks, despite the influence  $\chi$  dihedral angles on C(6)OH conformation.

Figure 18 -  $^{13}\text{C}$  CPMAS spectra of ChC sample showing the conformational dependence of carbon signals at variable  $T_C$  values (50 to 4500  $\mu\text{s}$ ) (a); 2D HETCOR spectrum of ChC (b); Ch15 (c) and Ch45 (d), proving that even without C4 signal splitting, distinguished correlations can be taken regarding the same kind of protons.



Taking into account the whole set of results, it is reasonable to verify the correlations between nearby  $^1\text{H}$  nucleus from overlapped C4 signal of Ch samples. Thus, the 2D HETCOR spectra was carried to provide the heteronuclear correlation at distances higher than  $^1\text{H}$ - $^{13}\text{C}$  direct bonding (KONO, 2004). The C4 signal of ChC (Fig. 18b) revealed distinguished  $^{13}\text{C}$  chemical shifts (F2), each one referred to the same broad signal of aliphatic  $^1\text{H}$  nucleus (F1). Although all Ch samples have shown overlapped C4 signals, these have also achieved different  $^{13}\text{C}$  correlations with similar protons, as clearly observed on Ch15 (Fig. 18c) and Ch45 (Fig. 18d), which can be related to different populations of possible conformations. Heteronuclear correlations with protons from different chemical groups are also observed on chitin allomorphs and *N*-acetylated Ch (Fig. 19), as a consequence of longer mixing time.

Figure 19 - 2D HETCOR spectrum of  $\alpha$ Ch (a);  $\beta$ Ch (b); Ch45 (c); Ch25 (d); Ch15 (e) and Ch5 (f).



Given the dependency of C4 and C6 signals on conformational order, the peak deconvolution method was used to estimate the fraction between ordered (crystalline) and disordered (amorphous) content in the sample. The C4 and C6 signals were decomposed into Lorentzian and Gaussian functions for crystalline and amorphous contributions, respectively, according to non-linear quantification of individual states of order proposed by LARSSON; WICKHOLM; IVERSEN, (1997) for cellulose. The resulted peak deconvolution from the spectral region of interest of *N*-acetylated Ch and chitin allomorphs are shown in Fig. 20. For more reliable quantification, it was set an equal number of curves at the same chemical shift and *FWHM* to all samples, including for depolymerized Ch (Fig. 21). The estimative of

crystallinity index of C4 and C6 signals ( $CrI_{CP}$ ) is listed on Table 3 and, as observed, the content of ordered structures increases with  $\overline{DA}$ , being nearly constant by changing the molar masses.

Figure 20 - Peak deconvolution method applied on  $^{13}\text{C}$  CPMAS spectra ( $T_C = 3000 \mu\text{s}$ ,  $d1 = 2 \text{ s}$  and  $12 \text{ kHz}$  of spinning frequency) of  $\alpha\text{Ch}$  (a),  $\beta\text{Ch}$  (b) and N-acetylated Ch5-60 (c) samples, to estimate the short-range molecular ordering from C4 and C6 signals, allowing the quantification of  $CrI_{CP}$ .

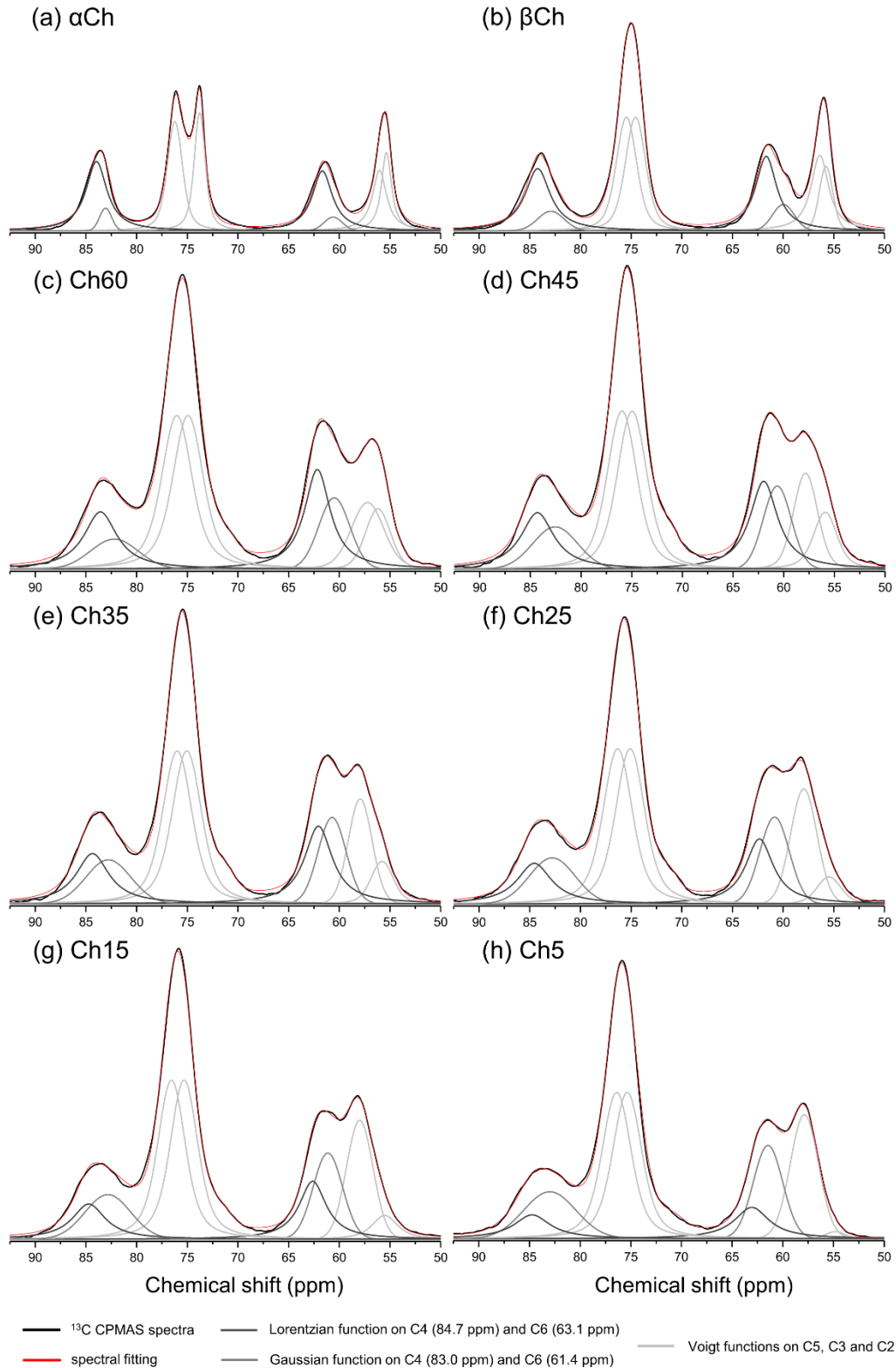
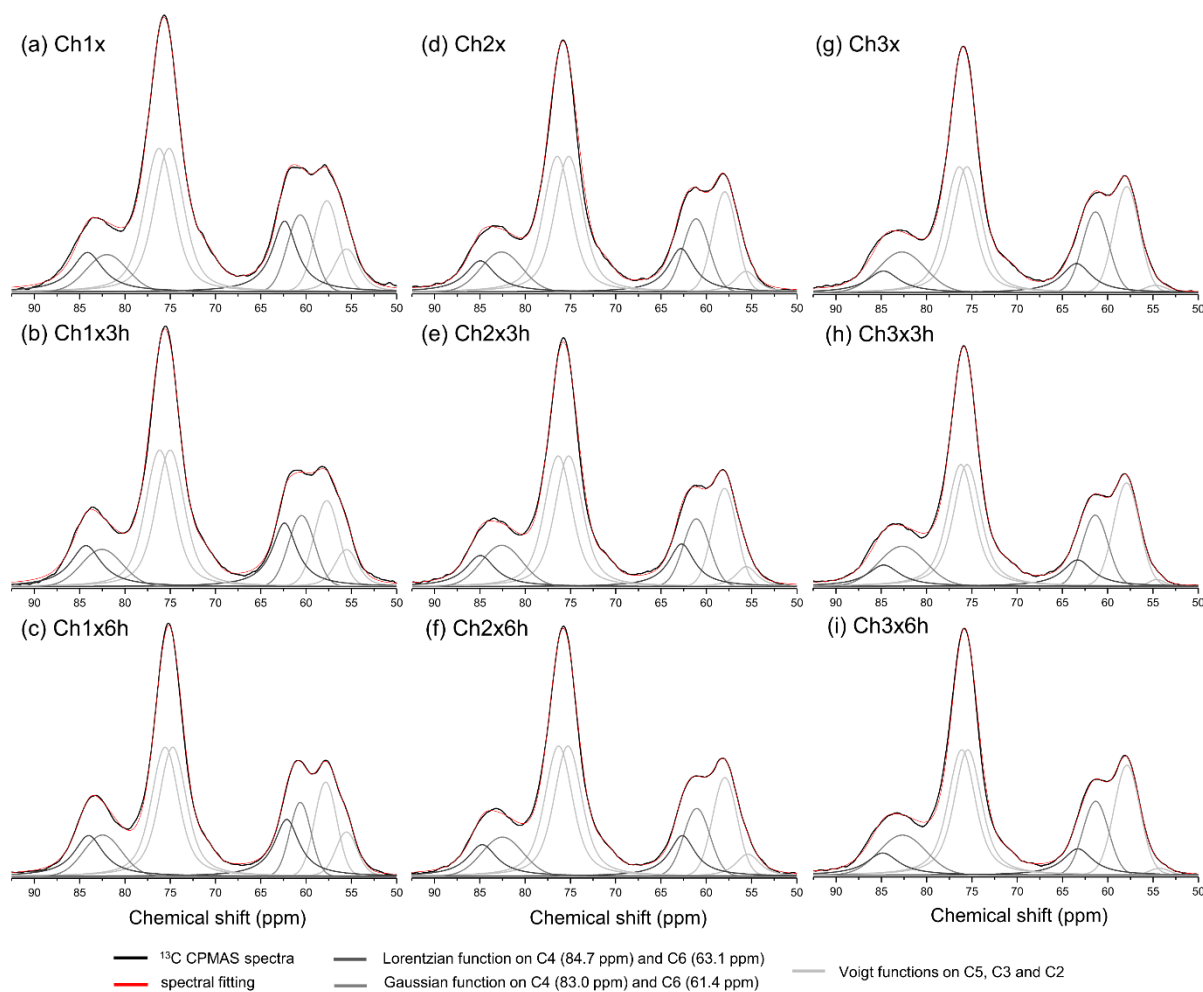
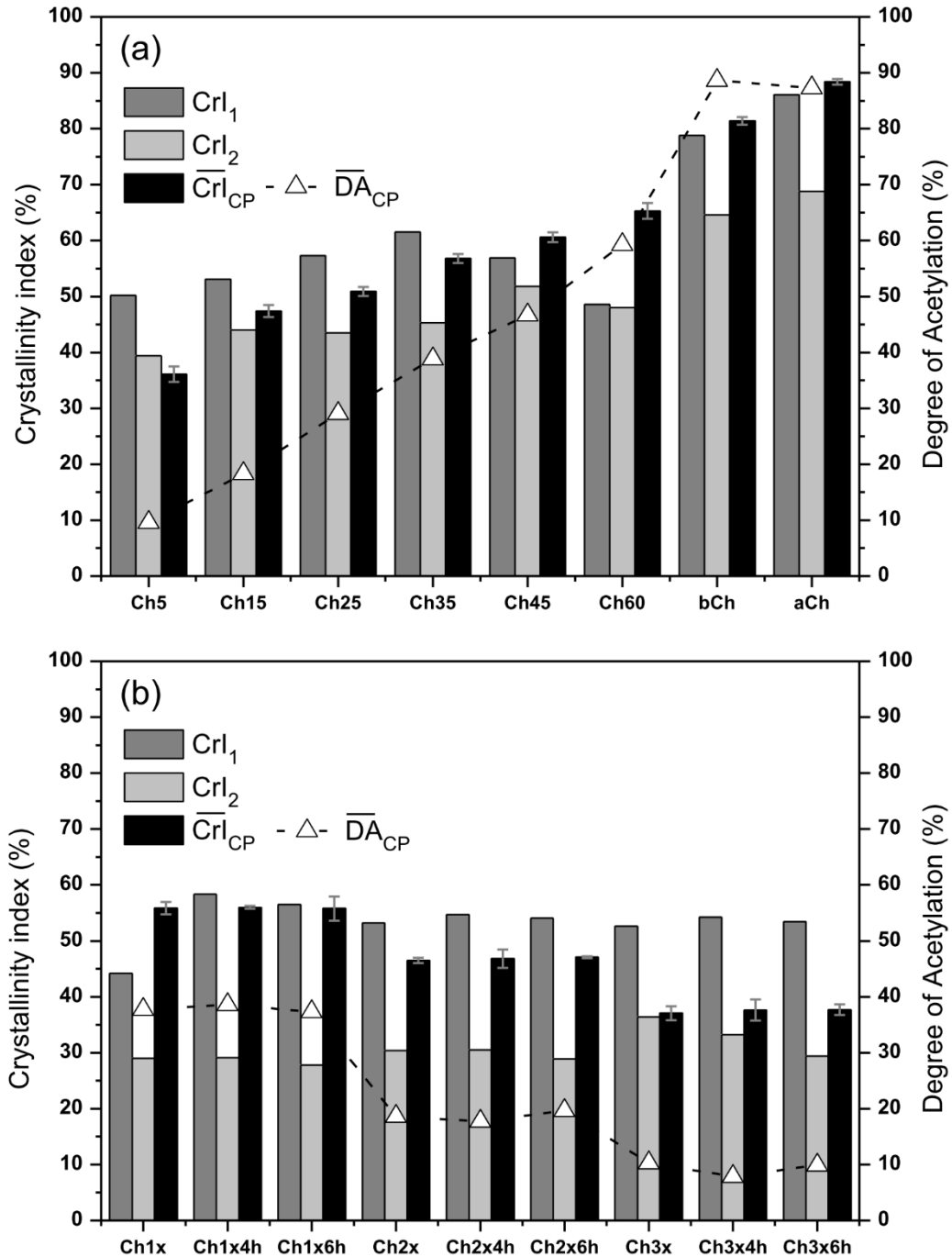


Figure 21 - Peak deconvolution method applied on  $^{13}\text{C}$  CPMAS spectra ( $T_C = 3000 \mu\text{s}$ ,  $d_1 = 2 \text{ s}$  and  $12 \text{ kHz}$  of spinning frequency) of Ch1x (a); Ch1x3h (b); Ch1x6h (c); Ch2x (d); Ch2x3h (e); Ch2x6h (f); Ch3x (g); Ch3x3h (h) and Ch3x6h (i) samples, to estimate the short-range molecular ordering from C4 and C6 signals, allowing the quantification of  $\overline{CrI}_{CP}$ .



A comparative analysis regarding the average crystallinity index obtained from C4 and C6 ( $\overline{CrI}_{CP}$ ) and the corresponding values calculated from XRD patterns with  $\overline{DA}_{CP}$  are shown in Fig. 22. The intrinsic dependence from structural and morphological features are considerably more evident through the proposing method employed on  $^{13}\text{C}$  CPMAS spectra, compared to the current methods from XRD. SSNMR should provide consistent results also avoiding problems with baseline determination, as commonly found on XRD methods. For instance, however, it is important to highlight that the physical origin remains different from each technique and the following results of short-range behavior (as probed in SSNMR) may not replace the long-range behavior (as probed in XRD) that attains the bulk for every case.

Figure 22 - Crystallinity index calculated according to peak height ( $CrI_1$ ) and amorphous subtraction ( $CrI_2$ ) method from XRD patterns; average contribution of ordered domains from C4 and C6 signals on  $^{13}\text{C}$  CPMAS spectra ( $\overline{CrI}_{CP}$ ), with respect to the  $\overline{DA}_{CP}$  of  $\alpha\text{Ch}$ ,  $\beta\text{Ch}$ , N-acetylated Ch5-60 (a); USAD and depolymerized Ch (3h and 6h) Ch (b) samples.



The multivariate SVD analysis (FORATO; BERNARDES-FILHO; COLNAGO, 1998) was also applied to the  $^{13}\text{C}$  CPMAS spectra of N-acetylated Ch using its predicted values of  $\overline{CrI}_{CP}$  and  $\overline{DA}_{CP}$ , in the same spectral range used for peak deconvolution (Fig. 20). The concentration of the components  $CrI^*$  and  $DA^*$  and its correlations with the predicted values were calculated from distinct intervals, as indicated in Table 4. Since the SVD method aims to

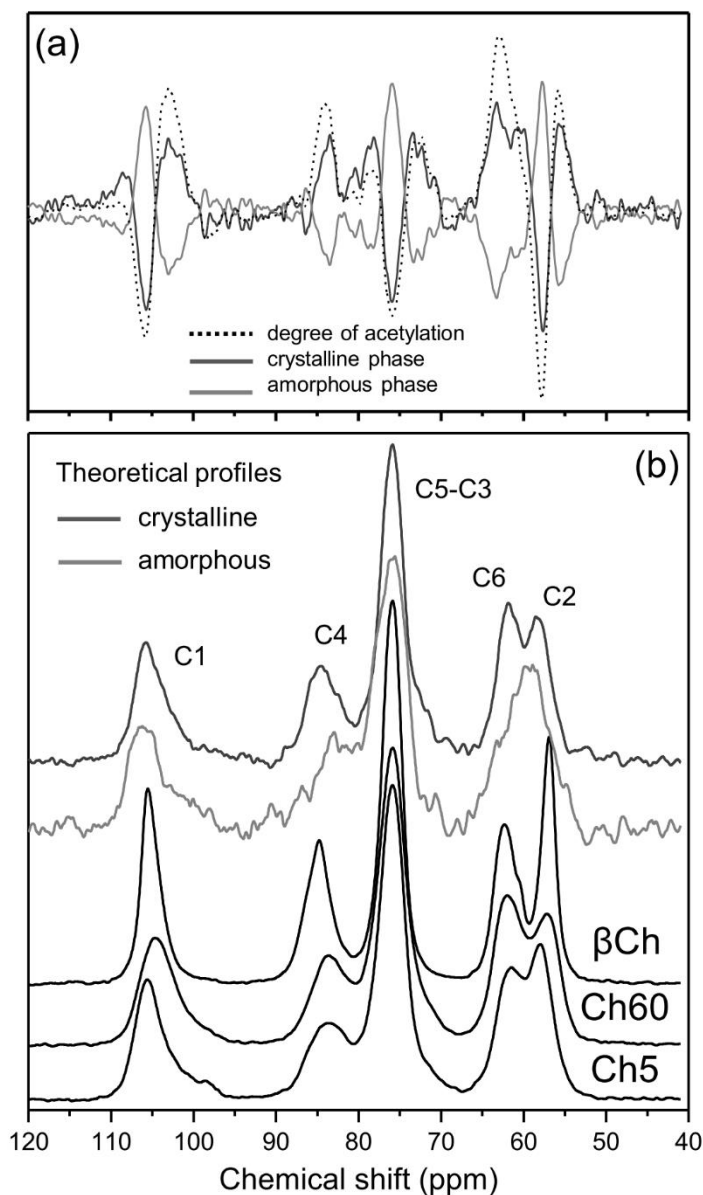
estimate the concentration of the components based on spectra profile changes, it was not possible to obtain a satisfactory correlation including the chitin allomorphs spectra in the set of samples due to the additional influence of intersheet packing. It can be noticed that all assigned regions are governed by both components, indicating that the concentration matrix is able to estimate  $CrI^*$  and  $\overline{DA}^*$  independently from  $CH_3$  and  $C=O$  signals, with an exception of  $\overline{DA}^*$  from 90-67 ppm region. In this sense, higher  $CrI^*$  correlation compared to  $\overline{DA}^*$  in 90-67 ppm interval highlights the major influence of short-range ordering, which essentially confirms the fundamental relevance of using C4 signal for structural analysis.

Table 4 - Concentration of the components  $DA^*$  and  $CrI^*$  and its correlation obtained by applying the SVD method on the regions 120-67, 120-40, 90-67 and 90-40 ppm from  $^{13}C$  CPMAS spectra of N-acetylated Ch5-60 samples.

Sample	$CrI^*(\%) / \text{ppm}$				$DA^*(\%) / \text{ppm}$			
	120-67	120-40	90-67	90-40	120-67	120-40	90-67	90-40
<b>Ch60</b>	56.7	57.3	54.3	56.2	50.3	54.4	29.0	51.6
<b>Ch45</b>	59.7	59.9	58.1	59.9	42.9	42.5	38.2	42.4
<b>Ch35</b>	53.1	53.9	51.6	54.1	33.4	35.3	27.2	35.6
<b>Ch25</b>	49.8	48.3	54.8	46.7	25.2	24.0	37.1	23.8
<b>Ch15</b>	43.6	44.0	44.3	43.8	15.7	16.6	17.6	16.7
<b>Ch5</b>	38.9	39.6	38.8	39.7	7.9	8.1	10.1	7.9
<b>Correlation</b>	0.934	0.938	0.882	0.921	0.993	0.998	0.766	0.994

The correlation of the components generated by the calibration matrix (Fig. 23a) indicate that both ones, *i. e.*  $CrI^*$  and  $\overline{DA}^*$ , coexist proportionally, as expected. Higher number of intersection points of these curves at 85-75 ppm further indicates that the local geometry between C4 and C6 is mediated by  $DA^*$ . In addition, the theoretical spectrum profile generated for pure components (Fig. 23b) suggests that the C4 signal tends to fit the exhibited by  $\beta$ Ch profile, evidencing the contribution regarding the chemical shift separation at distinguish C4 signal portions between the ordered and disordered structures. However, the clear distinction observed between  $\beta$ Ch and a fully crystalline profile indicates that the crystallinity of such allomorph is also dependent on how the chains are packaged, as already mentioned. This finding extends to  $\alpha$ Ch that even showing closer  $\overline{DA}_{CP}$  to  $\beta$ Ch (Table 3), the chains arrangement affects the  $\overline{CrI}_{CP}$  and, consequently, the spectral profile.

Figure 23 - Profile of the components  $DA^*$  and  $CrI^*$  generated from calibration matrix,  $X$  (a);  $^{13}C$ PMAS spectra profile relationship of  $\beta$ Ch, Ch60 and Ch5 with the theoretical profiles of crystalline and amorphous Ch. These spectra were normalized by C1 signal area.



### 3.1.5. Conclusions

In this CHAPTER I, chitosans (Ch) with variable degrees of *N*-acetylation and molar masses were successfully prepared on homogeneous conditions, all exhibiting random pattern of acetylation ( $PA \sim 1$ ). While acetylated Ch ( $\overline{DA}$  ranging as 5-60%) showed just slight variations of  $\overline{M}_w$ , the  $\overline{DA}$  values were mostly preserved after depolymerization of Ch ( $\overline{M}_w$  ranging as  $0.15\text{-}1.2 \times 10^6 \text{ g mol}^{-1}$ ).

The XRD pattern of Ch samples exhibited crystallite dimensions  $L_{020}$  and  $L_{110}$ , related to  $2\theta \sim 8^\circ$ - $11^\circ$  and  $19^\circ$ - $21^\circ$ , respectively, closer to those presented by  $\beta$ Ch. For all  $\beta$ -forms, the absence of anhydrous  $(110)_a$  plane on XRD pattern is straightly related to  $O3 \cdots O5$  hydrogen bonds that participates on the stabilization of twofold helical conformation by decreasing the  $\overline{DA}$ . Consequently, the amount of hydrogen bonds between  $C(7_3)=O \cdots HNC(2_1)$  and  $C(7_3)=O \cdots HOC(6_1)$  decreases, leading to typical diffraction pattern with lower crystallinity. Although the crystallinity indexes  $CrI_1$  and  $CrI_2$  proportionally increases with  $\overline{DA}$ , no significant changes were recorded varying the molar masses.

The  $^{13}C$  CPMAS spectra fitted closely the profile exhibited by DPMAS at  $T_C = 3000 \mu s$ . In fact, it was found that the C4 signal splitting strongly evidenced the CP rate variability of ordered and disordered conformations, which was confirmed by HETCOR experiments. The non-linear deconvolution of C4 and C6 signals showed a growing contribution of the crystalline content downfield shifted (Lozentzian curves), and some loss of magnetization upfield shifted (Gaussian curves) assigned to the amorphous content by increasing the  $\overline{DA}$ . Once the  $C(7_3)=O \cdots HOC(6_1)$  hydrogen bonds increases with  $\overline{DA}$ , lesser mobility of C(6)OH is allowed, probably leading the C(6)OH population to an growing contribution of trans conformation with respect do C(4).

The  $CrI_{CP}$  values proportionally increases with  $\overline{DA}$  but no significant changes were found as function of molar mass. High correlation with crystallinity was found using the peaks from 90-67 ppm and applying SVD analysis. Finally, according to the SVD multivariate analysis the spectra of pure crystalline and amorphous clearly illustrated that C4 signal is strongly related to crystallinity. Therefore, this work provided a novel approach of crystallinity index quantification of chitosans, extending the knowledge regarding to the origin of short-range molecular ordering, without requiring to external amorphous standards or exhibiting meaningful impact from molecular weight on C4 signal shape.

## CHAPTER II

### *Fast-forward approach of TD-NMR relaxometry for solid-state chemistry of chitosan*

Original source: **Carbohydrate Polymers**, Elsevier (FACCHINATTO, W. M. et al., 2020b)

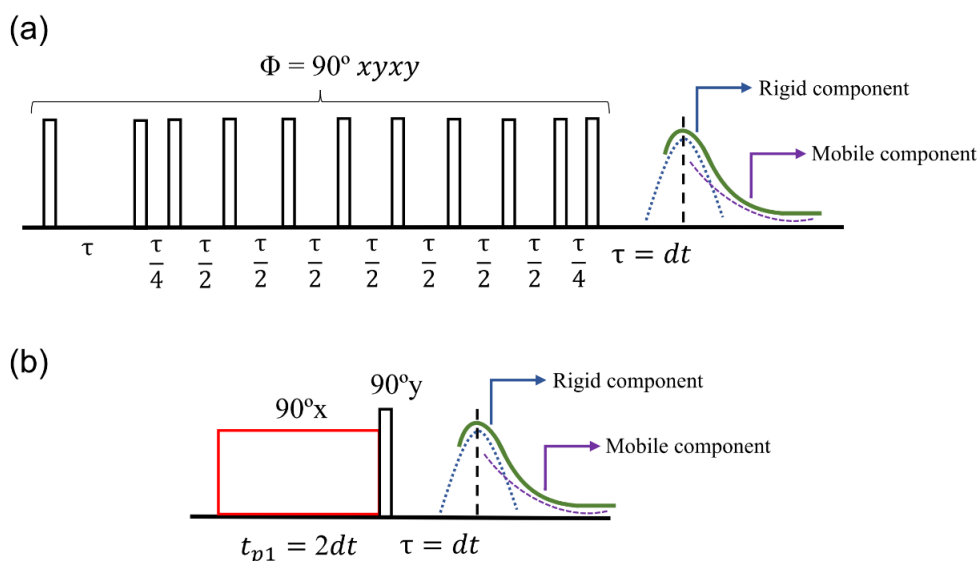
#### *3.2.1. $^1\text{H}$ TD-NMR signal decay as a tool to recognize and evaluate properties*

Although high-resolution NMR spectroscopy has a high potential as an analytical tool and has been used in almost all scientific fields, in the last decades several time-domain NMR (TD-NMR) methods, which are carried out in a considerable low-cost benchtop spectrometer, have been shown very useful for applications that do not require chemical shift resolution (COLNAGO et al., 2014).  $^1\text{H}$  TD-NMR applications include the analysis of agricultural and food products (AZEREDO et al., 2003; SANTOS et al., 2014a; WANG et al., 2016), pharmaceuticals (BRIGGS et al., 2019; ELIPE et al., 2016), petrochemicals (BARBOSA et al., 2013), monitoring *in situ* reactions (CABEÇA et al., 2011; GOMES et al., 2015), studies on stabilization and flocculation of polymers, surfactants and colloidal systems (COOPER et al., 2013), studies on microstructure, morphology and molecular dynamics in polymers (FARIA et al., 2020; SAALWÄCHTER, 2003; ZHANG; MIYOSHI; SUN, 2019), polymer gels (SAALWÄCHTER, 2007) and nanocomposites (SCHÄLER et al., 2015). TD-NMR has been also used to study chitosan coagulation (KOCK; COLNAGO, 2016) and as well as the interaction involving chitosan and paramagnetic ions (KOCK; MONARETTO; COLNAGO, 2017). Chitosans possessing different average degree of acetylation ( $\overline{DA}$ ) and molar masses have been also studied in acid medium according to its transverse relaxation time ( $T_2$ ) response to temperature, concentration and ionic strength (NOVOA-CARBALLAL; FERNANDEZ-MEGIA; RIGUERA, 2010). According to these authors, the flexibility of chitosan chains should increase with increasing  $\overline{DA}$ , as consequence of a reduced electrostatic behavior due to the decreasing content of protonated amino groups, which is in agreement with its dynamic viscosity behavior (RINAUDO; MILAS; LE DUNG, 1993).

TD-NMR applications can be based on the analyses of the relaxation times of liquids, entrapped liquids in heterogeneous materials or even in solid materials possessing chemical segments with higher mobility and, consequently, long transverse relaxation time  $T_2$  (COLNAGO et al., 2014; TODT et al., 2006). However, there are also many applications that are based on the  $^1\text{H}$  signal of rigid solid materials in which the strong dipolar homonuclear

interactions play the major role (DEMCO; FECHETE; BLÜMICH, 2003; FECHETE; DEMCO; BLÜMICH, 2003; MAUS; HERTLEIN; SAALWÄCHTER, 2006; SAALWÄCHTER, 2003). In most of these applications, it is necessary to use the so-called solid-echo experiments to recover the  $^1\text{H}$  signals, overcoming the probe dead time problem ( $dt$ ) (HAEBERLEN, 1976; RHIM; PINES; WAUGH, 1971). Nowadays, the commonly use solid-echo, known as Magic Sandwich Echoes (MSE) (MATSUI, 1992; PINES; RHIM; WAUGH, 1972; TAKEGOSHI; MCDOWELL, 1985), has been used to evaluate the crystallinity and dynamic process of synthetic polymers, rubbers (HANSEN; KRISTIANSEN; PEDERSEN, 1998; KRISTIANSEN; HANSEN; PEDERSEN, 1999; MAUS; HERTLEIN; SAALWÄCHTER, 2006; SAALWÄCHTER, 2007) and biopolymers (DIUK ANDRADE et al., 2018). It has been also used to study the rigidity/mobility of the polymers backbone and the side-chains that affect the crystalline/amorphous domains (MAUS; HERTLEIN; SAALWÄCHTER, 2006). This pulse sequence consists of a series of complex  $90^\circ$  pulses displaced at different phases separated by specific time intervals, which averages the homonuclear dipolar Hamiltonian to zero at the echo time generated by these pulses (Fig. 24a).

Figure 24 - Schematic illustration of MSE pulse sequence with phase cycling obtained by  $\phi = 90^\circ xyxy$  (a); schematic illustration of RK-ROSE pulse sequence (b). Because MSE and RK-ROSE signals are sensitive to the magnetic dipolar interactions between the  $^1\text{H}$  nuclei in the sample, the signal arising from rigid segments decay differently from those that present some molecular mobility.



Source: Own authorship

Thus, here we built up a version of the Rhim and Kessemeier (RK) experiment (RHIM; PINES; WAUGH, 1971), named as Radiofrequency Optimized Solid-Echo (RK-ROSE)

(GARCIA et al., 2019). However, it is worth to note that, in principle, any SE pulse sequence can be used for such a goal (HAEBERLEN, 1976; PINES; RHIM; WAUGH, 1972). One main aspect granted by RK-ROSE is the ability to refocus up to 99% of the magnetization at finite pulse power and dead time, being able to recover  $^1\text{H}$  signals from rigid segments at short echo times, without relying on an external calibration using multiple standard samples, as done to analyze the solid component of fats (SFC) (GARCIA et al., 2019). In fact, even for SFC that usually requires probe dead time shorter than 10  $\mu\text{s}$ , dead times around 1-2  $\mu\text{s}$  are needed for more rigid materials, such as solid polymers. Thus, RK-ROSE is able to overcome this probe limitation, potentially providing a more accurate determination of rigid components. According to the authors, it was possible to maximize the efficiency by adjusting the flip angle of the first  $90^\circ$  pulse with respect to the free acquisition time ( $\tau$ ) during the dead time of the equipment ( $t_{p1} = 2dt$ ) (Fig. 24b), consequently varying the echo generated after the second  $90^\circ$  pulse. The RK-ROSE is a much simpler sequence and shows similar efficiency to refocus the signal of solid components if compared to MSE pulse sequence.

Knowing that none study had properly investigated the mutual dependence of  $\overline{DA}$  and  $CrI$  by using TD-NMR relaxometry, this CHAPTER II proposes the use of solid-echo (SE) pulse sequence RK-ROSE to evaluate both parameters in solid Ch, based on the well-known behavior ascribed to the intrinsic mobility of hydrogens from methyl carbons on solid-state (CLEEMPUT et al., 1995; METZ; ZILIOX; SMITH, 1996). To achieve that, we realized firstly that the mutual influence of  $\overline{DA}$  and  $CrI$  would affect the  $^1\text{H}$  NMR signal due to the morphological dependence on the rigid/mobile components from variable structures. In a broader sense, the simultaneous measurement of degree of phase separation in, e.g., block copolymers by TD-NMR can be advantageous and applicable elsewhere, once the mobility of a given chemical group can be affected by the crystallization and mobility in different phases (MAUS; HERTLEIN; SAALWÄCHTER, 2006), being useful for possibly elucidate the structure and morphology relationship.

### 3.2.2. *Materials and Methods*

#### 3.2.2.1. *Structural and morphological calculated parameters*

All the reference parameters used in PLS regression model have been previously calculated and described on CHAPTER I (FACCHINATTO et al., 2020a). In this sense, Table

5 brings only the input values of average degree of acetylation ( $\overline{DA}$  and  $\overline{DA}_{CP}$ ), and crystallinity index ( $CrI_1$ ,  $CrI_2$  and  $CrI_{CP}$ ) used to predict and achieve such a goal.

Table 5 - Average molecular weight ( $\overline{M}$ ), average degree of polymerization ( $\overline{DP}$ ). The average degree of acetylation ( $\overline{DA}$  and  $\overline{DA}_{CP}$ ), and crystallinity index ( $CrI_1$ ,  $CrI_2$  and  $CrI_{CP}$ ) were used as structural and morphological calculated (reference) parameters for PLS analysis.

Sample	$\overline{M} \times 10^6$ (g mol <sup>-1</sup> )	$\overline{DP}$	$\overline{DA}$ (%)	$\overline{DA}_{CP}$ (%)	$CrI_1$ (%)	$CrI_2$ (%)	$CrI_{CP}$ (%)
$\alpha$ Ch			-	87.9 $\pm$ 3.9	86.1	68.8	89.0
$\beta$ Ch	0.42 $\pm$ 0.01	2140	-	90.5 $\pm$ 5.7	78.8	64.6	82.1
Ch1x	1.56 $\pm$ 0.03	7840	30.6 $\pm$ 3.3	37.7 $\pm$ 1.7	44.2	29.0	54.7
Ch1x3h	1.02 $\pm$ 0.23	5867	33.8 $\pm$ 3.3	38.6 $\pm$ 1.1	58.3	29.1	55.7
Ch1x6h	0.43 $\pm$ 0.07	2455	34.5 $\pm$ 4.9	37.3 $\pm$ 1.5	56.5	27.8	53.6
Ch2x	0.19 $\pm$ 0.06	1083	12.0 $\pm$ 3.8	18.6 $\pm$ 0.5	53.2	30.4	46.9
Ch2x3h	0.94 $\pm$ 0.14	5661	14.3 $\pm$ 2.9	17.7 $\pm$ 1.1	54.7	30.5	45.2
Ch2x6h	0.30 $\pm$ 0.05	1796	12.9 $\pm$ 3.1	19.6 $\pm$ 0.4	54.1	28.9	46.9
Ch3x	0.19 $\pm$ 0.04	1142	7.1 $\pm$ 0.7	10.3 $\pm$ 1.3	52.6	36.4	35.8
Ch3x3h	0.97 $\pm$ 0.20	5884	6.9 $\pm$ 1.2	8.8 $\pm$ 0.6	54.3	33.2	35.7
Ch3x6h	0.33 $\pm$ 0.05	2014	6.9 $\pm$ 1.0	9.8 $\pm$ 1.9	53.4	29.4	36.7
Ch60	0.15 $\pm$ 0.03	915	59.4 $\pm$ 2.3	17.7 $\pm$ 1.1	54.7	30.5	66.7
Ch45	1.17 $\pm$ 0.19	6293	43.5 $\pm$ 0.7	59.3 $\pm$ 3.5	48.6	48.0	59.8
Ch35	1.13 $\pm$ 0.17	6303	33.9 $\pm$ 0.6	46.7 $\pm$ 2.4	56.9	51.8	56.0
Ch25	1.10 $\pm$ 0.17	6277	23.8 $\pm$ 1.3	38.8 $\pm$ 1.33	61.5	45.3	50.2
Ch15	1.00 $\pm$ 0.16	5848	15.2 $\pm$ 0.9	29.1 $\pm$ 0.8	57.3	43.5	46.3
Ch5	0.99 $\pm$ 0.14	5914	4.8 $\pm$ 1.7	18.3 $\pm$ 1.5	53.1	44.0	34.7

### 3.2.3. Characterizations

#### 3.2.3.1. Thermogravimetric analysis (TGA)

The thermogravimetric profile was recorded using a Shimadzu RGA 50 equipment. Thus, about 8.0 mg of a given polymer was heated under nitrogen atmosphere at 50 mL min<sup>-1</sup> in the range 25-700 °C at 10 °C min<sup>-1</sup> (FACCHINATTO et al., 2019). All polymers were dried at 30 °C for 24 h, in order to avoid unintentional morphological changes (OGAWA; YUI; MIYA, 1992), and stored at room temperature with low and controlled humidity before conducting the analysis.

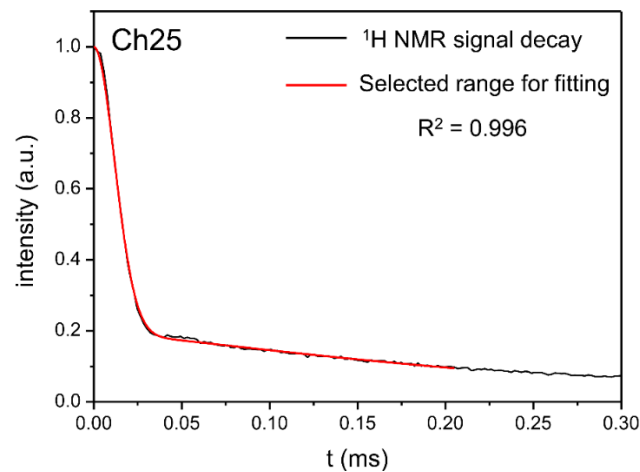
### 3.2.3.2. TD-NMR relaxometry: RK-ROSE technique

The  $^1\text{H}$  TD-NMR measurements were performed on a bench-top Minispec ND mq20 TD-NMR analyzer, Bruker<sup>®</sup> Germany, with a permanent magnet at  $^1\text{H}$  frequency of 19.9 MHz (0.47 T) and a 10-mm temperature-controlled probe-head at 25 °C. The signals were acquired using the Rhim and Kessemeier – Radiofrequency Optimized Solid-Echo (RK-ROSE) pulse sequence (GARCIA et al., 2019). All measurements were performed with dead time of 10  $\mu\text{s}$ ,  $\pi/2$  pulse length of 2.4  $\mu\text{s}$ , flip angle  $t_{px} = 22.2 \mu\text{s}$  and  $t_{py} = 2.98 \mu\text{s}$ , recycle delay of 5 s and acquisition time of 10 ms. The relative mobility of polymer chains was determined by decomposing the signal decay into rigid ( $T_{2r}$ ) and mobile ( $T_{2m}$ ) components as indicated by Eq. (8) (ALLER; PAGE, 1962; DERBYSHIRE et al., 2004; MAUS; HERTLEIN; SAALWÄCHTER, 2006).

$$\frac{FID(t)}{FID(0)} = f_r e^{-\left(\frac{t}{T_{2r}}\right)^2} \frac{\sin(bt)}{bt} + f_m e^{-\left(\frac{t}{T_{2m}}\right)^{v_m}} \quad (8)$$

where  $t$  is the experiment time;  $f_r$  and  $f_m$  are the rigid and mobile fractions parameters, respectively, being  $f_r = 1 - f_m$ ; and  $v_m$  is the shape parameter associated with the type of signal decay of the mobile components, which is associated to the degree of mobility of this component. The component  $\sin(bt)/bt$  was added to better adjust the exponential decay fitting, once Ch samples still have certain degree of order associated to the semi-crystalline character. The measurement was performed five times for each sample. Each experiment accumulated 512 scans and acquired 1000 echoes. The Fig. 25 shows the  $^1\text{H}$  NMR signal decay fitting with Eq. (8) that was carried out from 0 to  $\sim 0.2$  ms for each sample.

Figure 25 - A representative RK-ROSE signal decay fitting carried out from 0 to  $\sim 0.2$  ms for each sample.



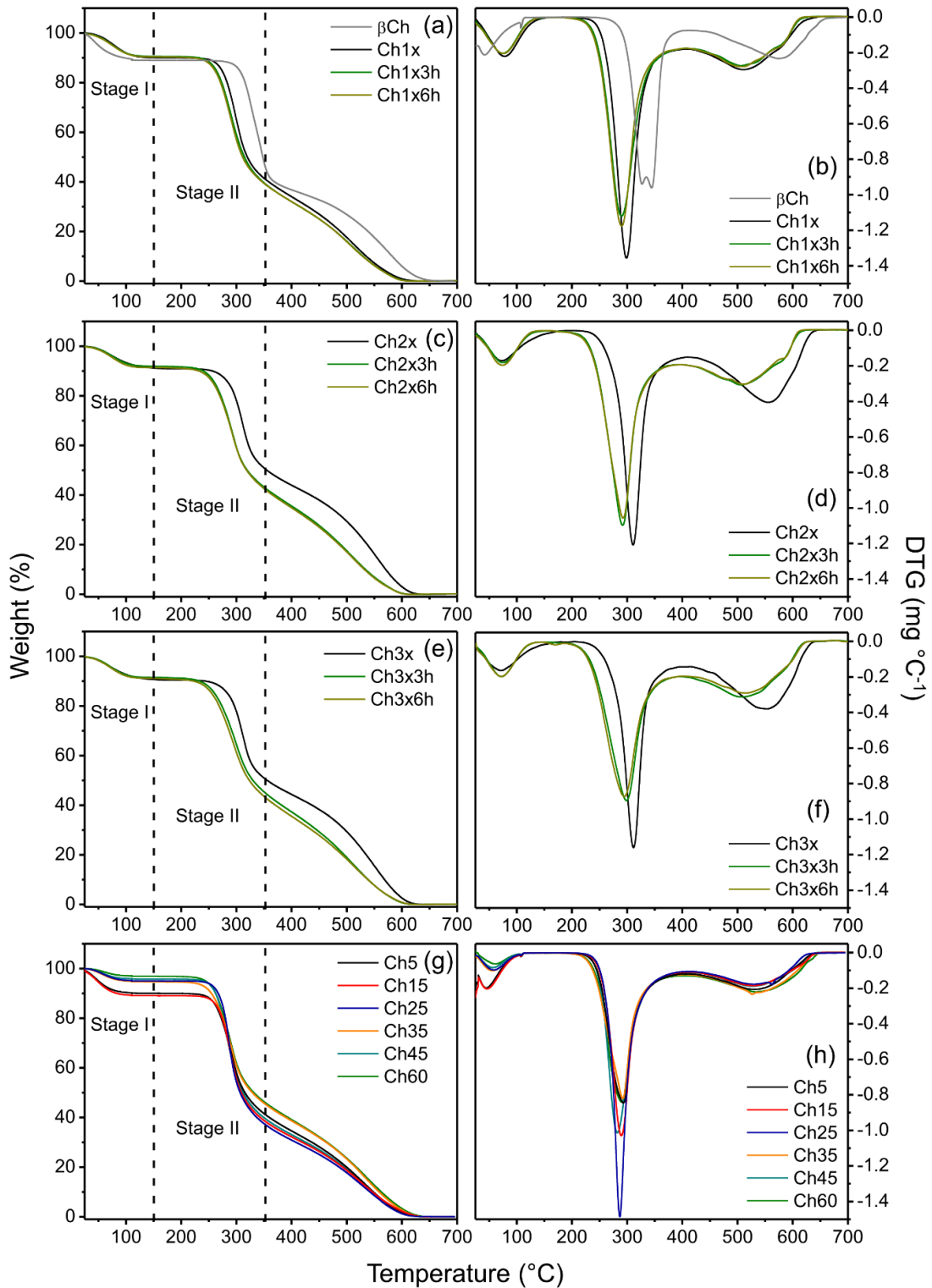
### 3.2.3.3. *Multivariate analysis*

The Partial Least Square (PLS) multivariate regression model (KOWALSKI; SEASHOLTZ, 1991) were built using the whole RK-ROSE data, as similarly attained for signal decays acquired from other TD-NMR pulse sequences (BIZZANI et al., 2020; PEREIRA et al., 2013; SANTOS et al., 2014a). Prior to the analysis, the signal decays were normalized and the regressions were constructed by separating the matrices into dependent variables (Y matrix) related to the reference parameters  $\overline{DA}$ ,  $\overline{DA}_{CP}$ ,  $CrI_1$ ,  $CrI_2$  and  $CrI_{CP}$ , and independent (predictors) variables (X matrix) related to the RK-ROSE data. For constructing the calibration data, the  $^1\text{H}$  NMR signal decay profiles from each Ch, including the samples issued from the USAD process and those 3 series of depolymerized samples and the *N*-acetylated samples produce from the homogeneous *N*-acetylation of Ch3x, and  $\beta\text{Ch}$ , were recorded. Additionally, the  $^1\text{H}$  NMR signal decay profiles from *N*-acetylated Ch samples and  $\beta\text{Ch}$  were recorded five times each one, totalizing 35 results to perform the validation step. The same procedure was applied to predict the residual of hydration, through the content of water molecules (residual hydration) calculated from TGA curves. The matrices were exploited and calculated by setting the algorithm singular value decomposition (SVD) (FORATO; BERNARDES-FILHO; COLNAGO, 1998). The PLS technique was carried out in MatLab<sup>®</sup> software (version R2017a The Mathworks Inc., Natick, MA, USA), using the PLS toolbox script.

### 3.2.4. *Results and Discussion*

#### 3.2.4.1. *Thermal behavior of side and main-chains on solid-state*

The thermal stability of  $\beta\text{Ch}$ , depolymerized and *N*-acetylated chitosan samples was studied by analyzing specific thermal events, which are recorded in the TG curves (Fig. 26). Although the TG curves display general similarity, two separate thermal events (Table 6) highlight the main differences among the chitosan samples, which may be attributed to their differences, structural as well as morphological.

Figure 26 - Thermogravimetric (a; c; e; and g) and DTG (b; d; f and h) curves recorded under N<sub>2</sub> atmosphere.

The first thermal event (25-150 °C) is attributed to the elimination of loosely-bound and weakly adsorbed water, corresponding to approximately 9% of the sample weight for most of the chitosan samples regardless of the  $\bar{M}_w$ . However, *N*-acetylated chitosan, namely samples

Ch60, Ch45, Ch35 and Ch25, presented lower water content as compared to any other chitosan sample, which may be attributed to increased hydrophobicity and compactness of these samples. While lesser mass loss variations on Stage I has been recorded within depolymerized Ch, as observed for USAD and *N*-acetylated samples, due to the  $\overline{DA}_{CP}$  (or  $\overline{DA}$ ) values (FACCHINATTO et al., 2019), such parameter presented meaningful influence regarding the water interaction on a broader interval of  $\overline{DA}_{CP}$ , achieving increased weight loss variability for *N*-acetylated Ch (~3-11%). In this case, the increasing ratio of GlcN/GlcNAc units has favored to stablish more hydrogen bonds between the amino groups and water molecules, as the GlcN units increase from Ch60 to Ch5, especially on Ch15 and Ch5. Indeed, although carbonyl groups are also able to form hydrogen bounds, it is actually mostly involved on intersheet interaction with hydroxyls nearly surrounded (CHO et al., 2000). An exceptional behavior is found for  $\beta$ Ch that reveals lower framework compactness (SAITO et al., 1997), enabling higher amount of entrapped water.

Table 6 - Weight losses related to the thermal degradation of  $\beta$ -chitin and Ch samples.

Sample	Stage I (25-150 °C)		Stage II (150-350 °C)	
	T <sub>MAX</sub> <sup>a</sup> (°C)	WL <sup>b</sup> (%)	T <sub>onset</sub> <sup>c</sup> (°C)	WL <sup>b</sup> (%)
$\beta$ Ch	41.2	11.1	334.6	43.4
Ch1x	77.6	9.3	298.6	50.0
Ch1x4h	74.2	9.3	290.4	51.5
Ch1x6h	74.2	9.3	290.4	51.5
Ch2x	71.7	8.6	312.1	41.3
Ch2x4h	71.7	8.6	291.7	49.3
Ch2x6h	71.7	8.6	291.7	49.3
Ch3x	70.1	8.9	311.4	40.5
Ch3x4h	71.1	8.9	298.0	46.5
Ch3x6h	71.1	8.9	294.6	48.4
Ch60	61.2	2.8	289.5	51.6
Ch45	55.9	3.7	281.0	56.8
Ch35	54.6	4.8	292.4	49.6
Ch25	54.6	4.4	286.3	59.4
Ch15	45.4	10.7	290.2	51.2
Ch5	45.4	9.3	292.8	49.0

<sup>a</sup> T<sub>MAX</sub> = temperature of maximum weight loss; <sup>b</sup> WL = weight loss; <sup>c</sup> T<sub>onset</sub> = onset temperature.

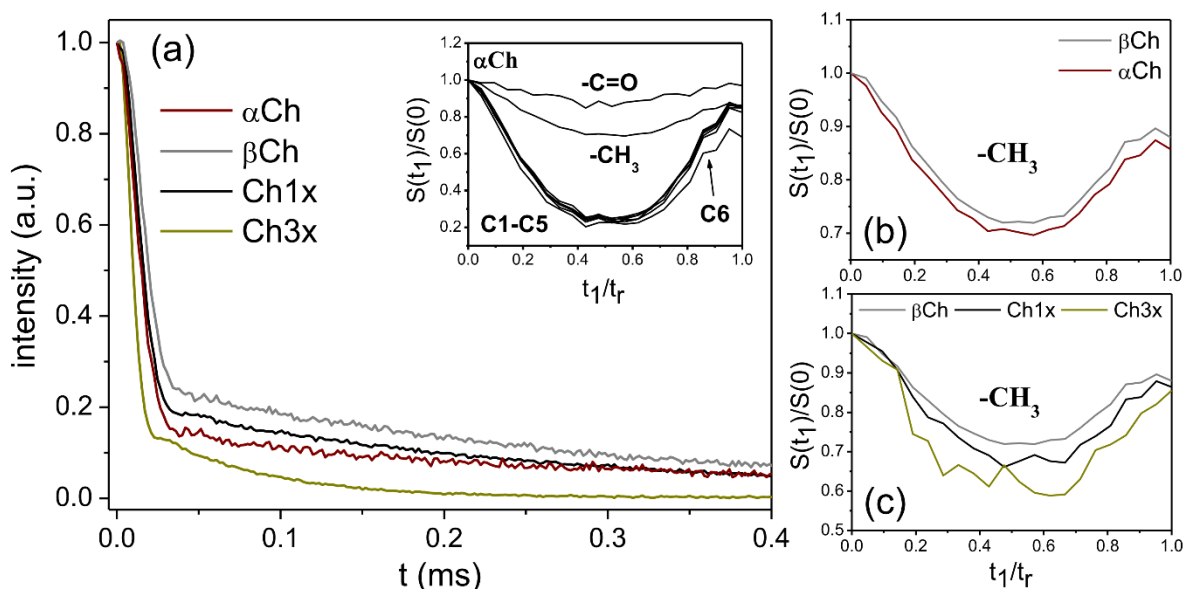
The second thermal event, observed in 150-350 °C, is attributed to the cleavage of bonds that lead the decomposition and elimination of lateral chains as volatile products. Concerning the Ch samples issued from the multistep ultrasound-assisted deacetylation of  $\beta$ -chitin and those resulting from controlled depolymerization, the main response to the furnished heat in this interval corresponds to an important loss of weight ( $\geq 40\%$ ) that starts in  $\approx 280^0 - 312\text{ }^\circ\text{C}$  (Table 6), depending on the molecular weight and average degree of acetylation (Fig. 26a-f) (FACCHINATTO et al., 2019; SANTOS; BUKZEM; CAMPANA-FILHO, 2016). Such results indicate that the heat absorption induces faster motion in short length chains due to its higher degree of freedom compared to larger ones, which present relatively more mobility restriction at the same temperature. The highly ordered arrangement of  $\beta$ Ch chains also implies in more stuck motion, thus resulting in higher  $T_{\text{onset}}$  (Table 6). However, the TG/DTG curves of the *N*-acetylated chitosan samples are practically coincident (Fig. 26g-h) and it is not observed any dependence of  $T_{\text{onset}}$  values on the average degree of acetylation ( $\overline{DA}_{CP}$ ). Indeed, such *N*-acetylated chitosans possess very similar  $\overline{M}_w$  values ( $\approx 1,000$  kDa), suggesting that changes on the content of GlcNAc units were not able to provoke significative influence during the heat absorption process.

### 3.2.4.2. *Internal mobility of side and main-chains on solid-state*

The  $^{13}\text{C}$  CPMAS and DIPSHIFT experiments were recorded for all polymers at  $T_c = 3.0$  ms in order to achieve the integral ratio  $I_{C=O}/I_{CH_3} \sim 1$ , related to C=O and  $\text{CH}_3$  resonance signals, respectively (CHAPTER I). DIPSHIFT technique is usually applied to estimate the molecular mobility due to the distinguished correlation time ( $t_c \sim \mu\text{s}$  to ms) exhibited by each molecular segment (DEAZEVEDO et al., 2008; MUNOWITZ et al., 1981). It is worth to recap out that the  $^{13}\text{C}$   $T_2$  relaxation is also present during the DIPSHIFT evolution time, and produces an exponential attenuation in the whole DIPSHIFT curve. As result, the stronger is the  $^1\text{H}$ - $^{13}\text{C}$  interaction, the lower is the amplitude at  $t_1 = t_r/2$ , while the shorter is the  $^{13}\text{C}$   $T_2$  the lower is the amplitude at  $t_1 = t_r$ . In this context, a representative DIPSHIFT analysis resulted from  $\alpha$ Ch is shown in Fig. 27a, revealing the main dynamic differences described by methyl, carbonyl and the other aliphatic carbons. The lower amplitude at  $t_r/2$  for the curves referred to C1-C6 indicates that the carbons from glucopyranose ring experiences stronger dipolar interaction, while carbonyl only weakly interact with nearby protons, due to the absence of  $^1\text{H}$  nuclei directly linked (FACCHINATTO et al., 2020a; SIMMONS et al., 2016). However, the

intermediate amplitude exhibited by methyl carbons, which resulted in  $S(t_1)/S(0) \sim 0.7$  at  $t_r/2$ , results from the partially averaging of the  $^1\text{H}$ - $^{13}\text{C}$  dipolar coupling, due to the intrinsic fast rotation of C-H bond around the  $\text{CH}_3$  C3 symmetry axis.

Figure 27 - RK-ROSE signal decays of  $\alpha\text{Ch}$ ,  $\beta\text{Ch}$ ,  $\text{Ch1x}$  and  $\text{Ch3x}$  samples and DIPSHIFT curves of  $\alpha\text{Ch}$  used as representative profile of each related segment (a); DIPSHIFT curves of  $\text{CH}_3$  group from  $\alpha\text{Ch}$  and  $\beta\text{Ch}$  (b);  $\text{Ch1x}$  and  $\text{Ch3x}$  with respect of  $\beta\text{Ch}$  profile (c).



The changes found on  $^1\text{H}$  NMR decay profiles (Fig. 27a) are associated to the structural and morphological variability within the samples. Concerning this aspect, the most important variation arising in the signal decay is ascribed to the methyl hydrogens (CLEEMPUT et al., 1995), also featuring the contribution of the residual hydration. Even storing the samples at close vessel with low and controlled humidity after drying at  $30^\circ\text{C}$  for 24 h, all samples still have an interstitial content of water molecules that are still detected by TGA. Knowing that submitting chitosan to higher temperatures or longer heating rates, it would certainly affect the overall morphology, as already recognized in the literature (FOCHER et al., 1990; OGAWA; YUI; MIYA, 1992), we considered advantageous to perform the RK-ROSE in samples exhibiting low residual hydration, instead of causing permanent changes in the crystallinity and then eventually compromise the prediction of this parameter through the PLS regression. Moreover, a closer view in the percent of hydration (Table 6), not only showed a lower variability compared to the wide interval of degree of acetylation, but also didn't increase according to the amount of methyl hydrogens of the samples. On the contrary, as the hydration is continuously reduced by increasing the degree of acetylation, we can infer that the

contribution of  $^1\text{H}$  nuclei from water molecules to the mobile-part of  $^1\text{H}$  NMR signal decay is also continuously reduced when increasing the content of methyl groups. Considering that most of the hydrogens from hydroxyl groups still participate in the hydrogen bond network (CHO et al., 2000), those mobilities are in average restricted. In this sense, methyl hydrogens and those from water molecules seems to be the most relevant  $^1\text{H}$  nuclei involved in the mobile fraction of  $^1\text{H}$  NMR signal decay, although other mobile hydrogens, such as hydrogen bond network, hydroxyl group, segments of polymer may also have some minor influence on the mobile fraction.

In this sense, the content of methyl groups, which are directly related to the content of GlcNAc units, is clearly affecting the relative intensity of the mobile-part signal, as revealed by Ch1x and Ch3x. In addition, the distinct  $^1\text{H}$  NMR signal decays may be associated to the chains packing, that displays differences on the local mobility (MAUS; HERTLEIN; SAALWÄCHTER, 2006), as demonstrated by the  $\alpha\text{Ch}$  and  $\beta\text{Ch}$  signal decay profiles. Even with similar and higher  $\overline{DA}_{CP}$  values, the specificity regarding the polymorphism of  $\alpha\text{Ch}$  and  $\beta\text{Ch}$  also implied on meaningful changes mainly on the mobile-part signal, being the one from a less densely packed  $\beta\text{Ch}$  allomorph showing improved contribution, and slower  $^1\text{H}$  signal decay, compared to the mobile-part signal of high densely packed  $\alpha\text{Ch}$ . The  $\alpha$ -chitin is composed by anti-parallel chains arrangement that allows higher number of intra and intersheet hydrogen bonds compared to  $\beta$ -chitin, in which the parallel chains arrangement leads to a weaker hydrogens bonds network and, consequently, providing a less densely packed material (CARDOZO et al., 2019). This is revealed in  $T_{2r}$  relaxation time which is inversely proportional to the second moment of the dipolar field distribution and consequently to the average distance between the  $^1\text{H}$  nuclei (SAALWÄCHTER, 2007; VAN VLECK, 1948). Unfortunately, the quantitative estimation of the dipolar second moment from TD-NMR, which could lead to the estimation of the local  $^1\text{H}$  density, is biased by signal distortions due to the echo acquisition, which is even more severe for RK-ROSE where magnitude mode signals are acquired (GARCIA et al., 2019; MAUS; HERTLEIN; SAALWÄCHTER, 2006). However, the observed proportionality in the signal decay times of the rigid and mobile component is modulated by the local chain packing.

As listed in Table 7, the rigid-part signal,  $T_{2r}$  just varied shortly in the interval from 10 to 21  $\mu\text{s}$  as compared to  $T_{2m}$  that is ranged from  $\sim 85$  to  $\sim 340$   $\mu\text{s}$  for all polymers. It is also important to highlight that no significant variation on  $T_{2r}$  and  $T_{2m}$  with respect to  $\overline{M}_w$  was registered. The mobile fraction parameter,  $f_m$ , showed an increasing tendency with  $\overline{DA}_{CP}$  (or

$\overline{DA}$ , Table 5) values, which confirm the mainly influence from methyl carbons from acetamido moieties of GlcNAc units as the chemical segment responsible for the mobility of Ch in solid-state. However, it should be pointed out that beside the average values of  $f_m$  are proportional to the amount of methyl carbons, it could not quantitatively estimate the average degree of acetylation, as already mentioned.

Table 7 - Rigid/mobile parameters from the corresponding segments of the polymers ( $T_{2r}$ ,  $T_{2m}$ ,  $v_m$  and  $f_m$ ).

Sample	$T_{2r}^a$ ( $\mu\text{s}$ )	$T_{2m}^a$ ( $\mu\text{s}$ )	$v_m^b$	$f_m^b$ (%)
$\alpha\text{Ch}$	$19.6 \pm 0.1$	$301 \pm 7$	$1.00 \pm 0.01$	$20.1 \pm 0.3$
$\beta\text{Ch}$	$16.2 \pm 0.1$	$334 \pm 8$	$1.00 \pm 0.04$	$45.4 \pm 0.9$
Ch1x	$16.2 \pm 0.1$	$241 \pm 3$	$1.01 \pm 0.05$	$24.1 \pm 0.6$
Ch1x3h	$16.8 \pm 0.1$	$234 \pm 5$	$1.00 \pm 0.03$	$26.7 \pm 0.8$
Ch1x6h	$16.7 \pm 0.1$	$237 \pm 7$	$1.02 \pm 0.02$	$26 \pm 1$
Ch2x	$21.5 \pm 0.1$	$212 \pm 5$	$1.6 \pm 0.5$	$18.1 \pm 0.9$
Ch2x3h	$19.2 \pm 0.1$	$206 \pm 10$	$1.2 \pm 0.2$	$19.3 \pm 0.8$
Ch2x6h	$19.3 \pm 0.1$	$204 \pm 10$	$1.3 \pm 0.2$	$17.7 \pm 0.4$
Ch3x	$10.7 \pm 0.1$	$87 \pm 1$	$1.16 \pm 0.04$	$8.7 \pm 0.3$
Ch3x3h	$11.5 \pm 0.1$	$93 \pm 4$	$1.1 \pm 0.2$	$9.1 \pm 0.5$
Ch3x6h	$12.1 \pm 0.1$	$89 \pm 3$	$1.2 \pm 0.2$	$9.7 \pm 0.2$
Ch60	$13.9 \pm 0.1$	$204 \pm 1$	$1.0 \pm 0.1$	$43.1 \pm 0.9$
Ch45	$13.6 \pm 0.1$	$235 \pm 7$	$1.00 \pm 0.06$	$36.7 \pm 0.6$
Ch35	$13.2 \pm 0.1$	$175 \pm 6$	$1.3 \pm 0.1$	$27.4 \pm 0.5$
Ch25	$13.2 \pm 0.1$	$165 \pm 6$	$1.02 \pm 0.05$	$18.9 \pm 0.7$
Ch15	$13.4 \pm 0.1$	$152 \pm 6$	$1.3 \pm 0.1$	$13.5 \pm 0.6$
Ch5	$12.8 \pm 0.1$	$134 \pm 9$	$1.00 \pm 0.07$	$9.8 \pm 0.9$

<sup>a</sup> Relaxation time of the transverse components of magnetization ( $M_{xy}$ ) from rigid-part ( $T_{2r}$ ) and mobile-part ( $T_{2m}$ ) signals of the polymers, calculated from  $^1\text{H}$  NMR signal decay profiles recorded by RK-ROSE method.

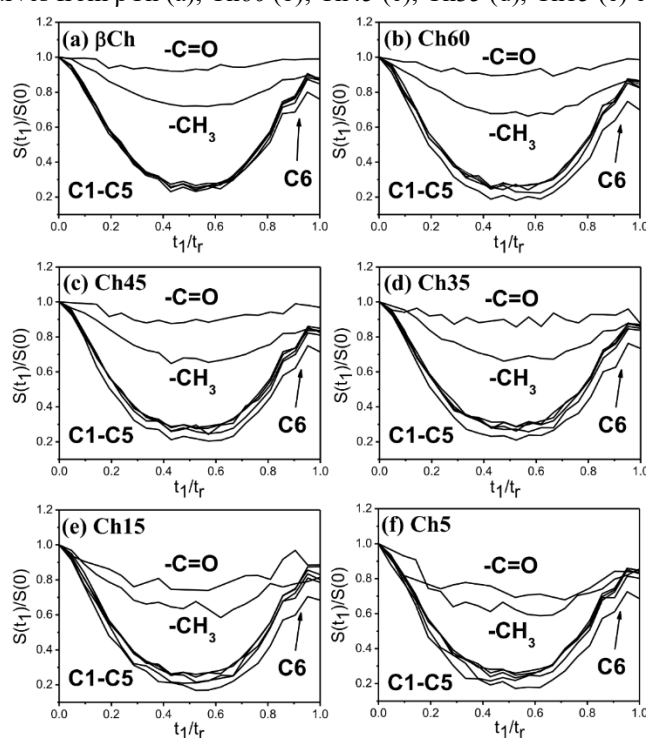
<sup>b</sup> Shape parameter ( $v_m$ ) and mobile fraction parameter ( $f_m$ ) also obtained from  $^1\text{H}$  NMR signal decay profiles.

Following similar tendency recorded by  $^1\text{H}$  NMR signal, Fig. 27b reveals slightly differences between the DIPSHIFT curves of methyl carbons from  $\alpha\text{Ch}$  and  $\beta\text{Ch}$ . In these cases, the amplitude achieved by  $\alpha\text{Ch}$  is slightly lower in the whole interval ( $0 < t_1/t_r < 1$ ) as compared to the amplitude exhibited by  $\beta\text{Ch}$ . This short variation could be explained by changes on the polymorphism. Thus, the higher  $^1\text{H}$  density around the methyl groups in the more densely packed allomorph ( $\alpha\text{Ch}$ ) possibly lead to a shorter  $^{13}\text{C}$   $T_2$  and enhance the attenuation of the whole DIPSHIFT curve as observed in Fig 27b, which is in agreement with the considerations made for methyl hydrogens (Fig. 27a). Despite that, it should be highlighted

that such argument has great impact on a qualitative point of view, although it does not preclude the quantitative differences achieved by  $T_{2m}$  for these polymers, being reasonable to consider the same meaning for similar behaviors. Additionally, considering the differences exhibited by methyl carbons from Ch samples with respect to  $\beta\text{Ch}$  (Fig. 27c), it can also be observed slight differences according to the content of methyl carbons, *i. e.*  $\overline{DA}_{CP}$ . However, such consideration should be carefully made considering that the decay of the DIPSHIFT curves reflects the local average mobility of the methyl groups and, to some extent, the local chain packing, but not the absolute amount of the methyl groups in the samples. Taken this into consideration, the minimum amplitude of the DIPSHIFT curves are in qualitative agreement with the  $T_{2r}$  (Table 7) and, consequently, with the packing behavior expected for the samples.

The DIPSHIFT curves recorded from *N*-acetylated Ch (Fig. 28) exhibited similar profile from those described by  $\beta\text{Ch}$  (Fig. 28a). Nevertheless, these results revealed that the curves referred to C1-C6 carbons may present slight influence upon the structural variability (Fig. 28b-f). Thus, while the C1-C6 curves from  $\beta\text{Ch}$  (and  $\alpha\text{Ch}$ ) are clearly overlapped, C6 curve present a higher deep compared to those backbone carbons. This is again in agreement with the lower packing for  $\beta\text{Ch}$  samples, which is expected to make the side chain C6 carbon more mobile in this samples. However, none reliable differentiation can be concluded on the profiles of DIPSHIFT curves regarding the influence of  $\overline{DA}_{CP}$ , or even observed upon  $\overline{M}_w$ , similarly to the  $T_{2m}$  values achieved for depolymerized Ch.

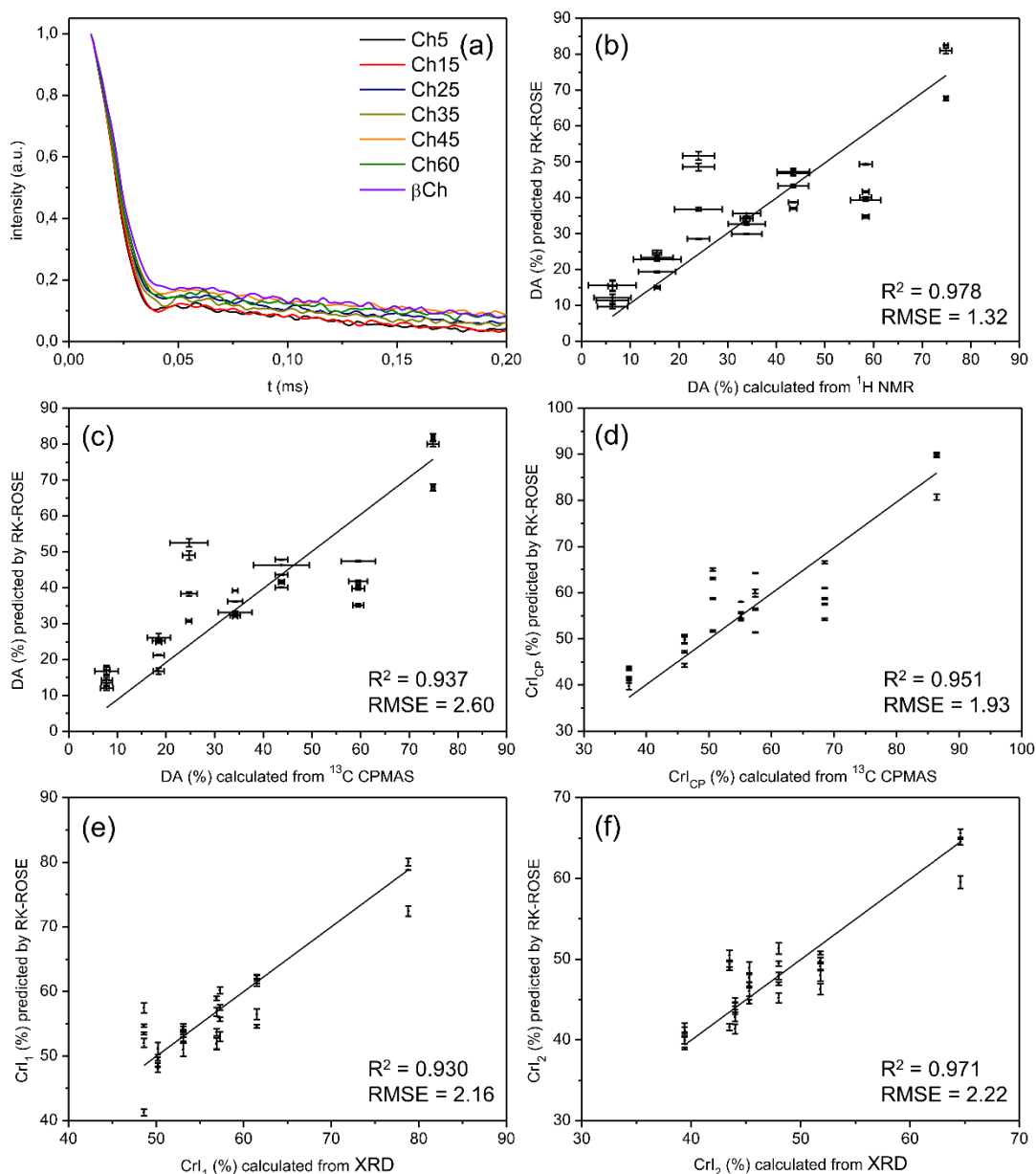
Figure 28 - DIPSHIFT curves from  $\beta\text{Ch}$  (a), Ch60 (b), Ch45 (c), Ch35 (d), Ch15 (e) e Ch5 (f).



Considering that the  $T_{2m}$  and  $f_m$  cannot properly estimate the average degree of acetylation and crystallinity index of Ch (Table 5) in at least a similar quantitative level as obtained from the conventional methods, the use of full RK-ROSE data, as an analytical input profile through PLS regression model, was able to recognize the whole variability recorded on fast and slow signal decaying, once the rigid-part signal has not been counted yet within the overall contribution to these Ch features. This model is commonly used to find the fundamental relations between two matrices (X and Y), *i.e.*, a latent variable approach to modeling the covariance structures in these two spaces. In this way, the PLS model were able to recognize the whole variability recorded on RK-ROSE data, finding the fast and slow decaying variables. The PLS validation step was applied to predict the measured parameters  $\overline{DA}$ ,  $\overline{DA}_{CP}$ ,  $CrI_1$ ,  $CrI_2$  and  $CrI_{CP}$ , which enabled to build up the response curves and thus obtain the predicted parameters (Fig. 29). In this sense, once the PLS model has been calibrated, one coefficient array with same length of RK-ROSE data is obtained. This coefficient array is used for multiplication by each variable of a new  $^1\text{H}$  NMR signal decay. Hence, the resultant array is summed with the Y average value, thus obtaining the predicted value (KOWALSKI; SEASHOLTZ, 1991). It is important to highlight, as already mentioned, that it was not possible to obtain the average degree of acetylation neither the crystallinity index from  $T_{2m}$ , but both were successfully predicted through the PLS model.

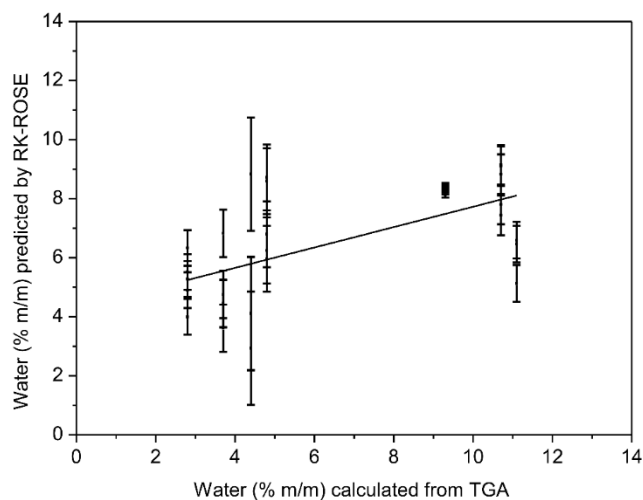
The results confirm that the PLS model demonstrate the straight relationship within these measured parameters, regarding the tendency visually described by the mobile-part of  $^1\text{H}$  NMR signal decay. The coefficient of determination was high for the parameters tested ( $R^2 > 0.93$ ), and the root mean square error (RMSE) showed low variations. These findings provide good evidence that RK-ROSE are sufficiently accurate to predict the average degree of acetylation and crystallinity index of Ch (CARVALHO et al., 2019; PEREIRA et al., 2013). Such outstanding correlation indicates that the predicted Ch features can be independently achieved by performing the cross-validation with the measured parameters, thus decomposing the information accordingly to the desired predict parameter.

Figure 29 -  $^1\text{H}$  TD-NMR signal decays recorded using RK-ROSE pulse sequence of N-acetylated Ch and  $\beta\text{Ch}$  samples used for PLS validation procedure (a); Correlation of  $\overline{DA}$  (b);  $\overline{DA}_{CP}$  (c);  $CrI_{CP}$  (d);  $CrI_1$  (e);  $CrI_2$  (f) values measured using high-resolution NMR and XRD and predicted by the PLS regression model.



On the other way, knowing that the residual hydration still participates on the  $^1\text{H}$  NMR signal decay, due to the remaining  $^1\text{H}$  nuclei from water molecules, it was also carried the PLS model for the weight loss (% m/m) values of weakly adsorbed water listed in Table 6. As revealed by the linear regression shown in Fig. 30, it was obtained very low correlation within the residual hydration and RK-ROSE data ( $R^2 > 0.40$ ). This result corroborates the previous discussion regarding the reduced influence of  $^1\text{H}$  nuclei from water molecules by increasing the average degree of acetylation.

Figure 30 - Partial least squares PLS regression model from linear correlation between the predicted values of the residual of hydration (% m/m).  $R^2= 0.40$  and  $RMSE = 1.91$ .



The main advantage of using PLS with TD-NMR data is to avoid co-linearity problems permitting to work with a number of variables that is greater than the number of samples. In this sense, PLS models can be used to calibrate parameters even with the presence of interference analytes, such as the residual content of hydration in our case. These characteristics allows to apply the PLS model on TD-NMR data in order to achieve a fast (less than 1 min) and non-invasive resolution (BIZZANI et al., 2017; CARVALHO et al., 2019; COIMBRA et al., 2020; PEREIRA et al., 2013; SANTOS et al., 2014a).

It is worth to mention that any Solid-Echo pulse sequence could be used in our approach. Indeed, it is known that the more robust mixed-MSE pulse sequence produces echoes with lesser signal distortion and better phase behavior. However, we should also point that, despite the contrast among the signal decays used to distinguish the different components, the quantification using PLS model is done based on the relative weights, so it can be done in magnitude mode acquisition and should not be highly sensitive to signal distortion. For short dead time probes, as is our case, RK-ROSE usually provide similar  $^1\text{H}$ - $^1\text{H}$  refocusing efficiency as mixed-MSE, but slightly better signal-to-noise because the use of shorter echo times and less pulses. For longer dead time probes, RK-ROSE can provide a better refocusing and signal-to-noise as compared to mixed-MSE (GARCIA et al., 2019). Thus, due to the specificity of the PLS analysis, RK-ROSE seems to be an adequate method for using here.

Therefore, the solid-state TD-NMR relaxometry can bring reliable information concerning to the prediction of degree of acetylation and crystallinity index of Ch by applying the PLS model, thus providing an additional method from others commonly chosen for these purposes, also through a cost-effective equipment.

### 3.2.5. Conclusions

In this CHAPTER II, *N*-acetylated and depolymerized chitosan (Ch) samples possessing different average degree of acetylation, crystallinity and molecular weight were analyzed using the RK-ROSE pulse sequence in a TD-NMR relaxometry experiment. It was provided a new approach in which was possible to identify and assign the major contribution referred to the changes of mobile-part signal recorded. Although the direct determination of degree of acetylation and crystallinity of chitosan from  $^1\text{H}$  NMR signal decay was not achieved, we propose the best conditions to guarantee that the contribution of  $^1\text{H}$  nuclei from other sources were minimized. Thus, it was performed some preliminary experiments such as TGA and DIPSHIFT to quantify the residual hydration, that remained at lower percentage among the samples, and to make sure that the only methyl groups from chitosan structure has a distinct  $^1\text{H}$ - $^{13}\text{C}$  dipolar interaction strength and intrinsic fast rotation compared the other carbons. The mobile fraction contribution assigned in the  $^1\text{H}$  NMR signal decay tends to grow by increasing the degree of acetylation, due to the presence of methyl groups. However,  $T_{2m}$  also indicates that some diverging values can be explained by slight changes in the C-H rotational dynamic inside the polymeric network, due to the differences regarding the crystallinity. The PLS regression model was applied to calibrate, validate and predict the parameters  $\overline{DA}$ ,  $\overline{DA}_{CP}$ ,  $CrI_1$ ,  $CrI_2$  and  $CrI_{CP}$  within the RK-ROSE data, assuring results with high coefficient of determination ( $R^2 > 0.93$ ).

In general, TD-NMR signal decay can be advantageous on predicting the tendency of structural and morphological features of powdered Ch at low time-consuming analyses, once the average degree of acetylation is the major aspect that controls the crystallinity of Ch with non-significant influence regarding molar masses. By performing the RK-ROSE pulse sequence, we could provide a first overview of the most important Ch features with reliable results that can support the conventional methods currently applied for obtain the degree of acetylation and crystallinity index, which in turn could be useful for distinguish Ch samples with similar  $\overline{DA}$  and perhaps different crystallinities, or even Ch with  $\overline{DA}$  completely different. We do consider that for complex systems such as Ch a multi technique approach will be always required, but having a fast-forward and non-destructive approach would be important to identity interesting systems for further investigations with more specialized methods.

## CHAPTER III

### *Insight into physicochemical and morphological properties of aqueous beta-chitin nanowhiskers: a high- and low-field NMR approach*

#### *3.3.1. Predicting performance by controlling the reaction settings*

Chitin, a semicrystalline polysaccharide, is abundantly found in highly crystalline fibrils arrangement at outstanding nanometer level (2.5 to 25 nm) (HASSAINIA; SATHA; BOU, 2018; KAYA et al., 2017). It has been widely used in several applications as biosensors and especially in biomedical field, which includes sutures, wound healing gauges and drug delivery vehicles. This remarkable potential is straightly related to its biocompatibility, biodegradability and nontoxicity character of chitin, in addition to optical properties and the ability to form films, hydrogels/aerogels, beads, scaffolds and nanomaterials (DUAN et al., 2018; SHAMSHINA; BERTON; ROGERS, 2019).

Chitin whiskers (CWH) are nanocrystalline structures generally prepared by chemically removing the amorphous regions of crude chitin through acid hydrolysis (LI et al., 2019; LIN; HUANG; DUFRESNE, 2012; ZENG et al., 2012). These nanostructures have attracted enormous attention for diverse applications including foodstuff, water treatment, photoelectronic devices (IFUKU; SAIMOTO, 2012; LIN; HUANG; DUFRESNE, 2012; ZENG et al., 2012), lightweight foams for food, pharmaceutical and cosmetics (HUANG et al., 2018) and for optically transparent materials such as contact lenses and wearable devices (HONG et al., 2018).

The physicochemical and biological properties of chitin whiskers are deeply related to the chitin sources and extraction methods (GOPALAN NAIR; DUFRESNE, 2003; MORIN; DUFRESNE, 2002). As the amorphous domains are more accessible to the acid than crystalline domains, the hydrolysis of the former is much faster, due to the tighter molecular arrangement of the latter, which prevents the accessibility to reactive sites. Additionally, the acid hydrolysis and the swelling behavior depends on the chains packaging and crystallinity regarding to the  $\alpha$ - and  $\beta$ -allomorphs. In case of  $\alpha$ -chitin, the antiparallel arrangement of the chains is tightly held by higher amount of intra and intersheet hydrogen bonds between acetamido and hydroxyls groups, when compared to  $\beta$ -chitin parallel arrangement. Thus,  $\beta$ -chitin shows greater flexibility and permeability to solvent molecules, being easier to hydrate than  $\alpha$ -chitin

(CARDOZO et al., 2019; DUAN et al., 2018). Alternative and upgrading strategies have also been successfully developed to produce well-dispersed chitin nanostructure suspensions to prevent the aggregation of the fibers (FAN; SAITO; ISOGAI, 2008a, 2009; IFUKU et al., 2009, 2011; KADOKAWA et al., 2011; KOSE; KONDO, 2011; LU et al., 2013; MUSHI et al., 2019; RIEHLE et al., 2019; WU et al., 2014).

The wide range of asymmetrical geometries usually displays different dynamics on aqueous suspensions specially at higher concentrations, when nanocrystals prepared from polysaccharides exhibit liquid crystalline behavior (LIN; HUANG; DUFRESNE, 2012; REVOL; MARCHESSAULT, 1993). Several factors can affect the liquid crystallinity and stiffness such as dispersity, surface charge and ionic strength, also showing strong dependence with flow alignment once the isotropy, anisotropy and biphasic behavior of chitin crystallites and fibrils suspensions reveal considerable dependence with shear rate and viscoelasticity (JOÃO et al., 2017; LI; REVOL; MARCHESSAULT, 1996).

In recent years, advances in low-field NMR techniques have provided valuable information with respect to the viscosity of colloids and polymeric solutions. Recent studies on colloidal aqueous dispersions of biomaterials (BELOTTI et al., 2010; OTONI et al., 2018) have been discussed through low-field NMR, achieving reliable data compared to conventional techniques. Such ones concern to the interfacial interaction of distinguished components, which can be probed by relaxation time of hydrogens from water in the first monolayer of adsorbed molecules on the substrate (COOPER et al., 2013). Thus, the viscosity is inversely proportional to solvent relaxation time, revealing important aspects of structure and molecular mobility. Although the liquid crystallinity of chitins has been reported, only few studies have discussed comprehensive observations of viscosity and rheological phenomenon ranging the effects of concentration, pH and temperature (LI et al., 2019). The mobility of polymeric chains on solid-state can be probed by  $^1\text{H}$  low-field NMR. The NMR signal is highly dependent on molecular mobility, bringing information on the mobility contrast among different groups and residues that can be associated to morphological feature of the samples (HANSEN; KRISTIANSEN; PEDERSEN, 1998; KRISTIANSEN; HANSEN; PEDERSEN, 1999; MAUS; HERTLEIN; SAALWÄCHTER, 2006; SAALWÄCHTER, 2007). Indeed, we've recently demonstrated that the mobile fraction was mostly associated with the methyl hydrogens, which might be explained by the intrinsic fast rotation of the C-H bond around the  $\text{CH}_3$   $\text{C}_3$  symmetry axis, being also affected by the sample's crystallinity (FACCHINATTO et al., 2020b). Since the degree of acetylation recorded for  $\alpha$ - and  $\beta$ -chitin are very similar, the difference between  $T_{2m}$  mainly

expresses the packing density. Thus, the less densely packed  $\beta$ -allomorph showed higher  $T_{2m}$  as compared to  $\alpha$ -allomorph that is more densely packed and, consequently more crystalline.

Since the diffusion-controlled nature of acid hydrolysis employed to produce chitin nanostructures is undertaken in heterogenous solutions, the hydrolytic kinetics is probably affected by the average powder size of chitin. Thus, the swelling behavior and consequently the acid permeability would be affected by the average powder size of chitin particles and so the accessibility to different portions of amorphous and crystalline domains. Consequently, the average size of chitin particles could mediate the consumption rate of amorphous and crystalline contributions and, as far as we know, none study has properly investigated this issue as one of the primary variables for a reproducible preparation of chitin nanostructure suspensions.

This CHAPTER III presents a NMR spectroscopic approach to investigate the effect of the  $\beta$ -chitin particle size on the physicochemical properties of CWH aqueous suspensions. Firstly, CWH samples were prepared via acid hydrolysis of  $\beta$ -chitin and characterized in terms of morphology, surface properties, average degree of acetylation ( $\overline{DA}$ ), average degree of polymerization ( $\overline{DP}_v$ ), crystallinity and thermal stability. The variations on molecular conformations of CWH were evaluated by  $^{13}\text{C}$  CPMAS spectra (FACCHINATTO et al., 2020a; HEUX et al., 2000). The rheological behavior of CWH aqueous suspensions was analyzed by using a rotational rheometer and the results were related to the low-field time-domain (TD) NMR transverse relaxation ( $T_2$ ) data, obtained with CPMG (CARR; PURCELL, 1954; MEIBOOM; GILL, 1958) pulse sequence. Furthermore, the molecular motions under intermediate-to-slow timescale were verified by Magic Sandwich Echo – Free induction decay ( $^1\text{H}$  MSEFID) pulse sequence (MAUS; HERTLEIN; SAALWÄCHTER, 2006) and compared to the  $^1\text{H}$ - $^{13}\text{C}$  dipolar interaction DIPSHIFT experiment (MUNOWITZ et al., 1981). All polymers were characterized accordingly to its geometrical feature through SEM, TEM including sizes distribution by AFM images. The crystallinity, crystal dimensions and thermal decomposition profile were provided by XRD and TGA analysis, while the surface stability of colloidal suspensions and the influence on surface functional groups were evaluated by zeta potential ( $\zeta$ ) and XPS, respectively (TAKETA et al., 2018).

### 3.3.2. Materials and Methods

#### 3.3.2.1. Preparation of $\beta$ -chitin suspensions

Initially, the allomorph  $\beta$ -chitin, extracted from squid pens (*Doryteuthis spp.*) (CHAPTER I and II). The product was then milled using a knife mill fitted with a 1 mm-sized, grinded and sieved into different powder fractions with average diameters ( $d$ ), ranging as  $d < 0.125$  mm, between 0.125-0.425 mm and  $d > 0.425$  mm, named as BCHS, BCHI and BCHL, for smaller, intermediate and larger powder sizes, respectively.  $\beta$ -chitin whiskers suspensions were prepared by carrying out acid hydrolysis according to a modified methodology proposed by GOPALAN NAIR; DUFRESNE (2003). Briefly, 5 g of  $\beta$ -chitin particles were suspended in 150 mL of 3 M HCl and then heated at 90°C under stirring for 3h. After the hydrolysis, the suspension was chilled with water and centrifuged for 10 min at 8000 rpm to remove the excess acid. This process was repeated five times and then the suspension was dialyzed against distilled water using dialysis membrane (cut off 12 kDa) for 3 days until pH  $\sim 7$  be reached. The resulting suspension of dialysis process was treated using a disperser UltraTurrax (IKA, D125 Basic, USA) for 5 min at 19,000 rpm and aliquots of 150 mL were sonicated for 3 min using a UP400S Hielscher Sonifier ultrasonic device ( $\nu = 24$  kHz) coupled to a 22 mm stepped probe, with pulsed irradiation (0.5) and ultrasound power set to 200 W. After that, the concentration of  $\beta$ -chitin whiskers in the colloidal suspensions was determined by freeze-drying, then adjusted with distilled water to  $20.0 \pm 0.5$  mg of chitin whiskers/g suspension by using the disperser at 19,000 rpm for 5 min, and sonicated again for 3 min to allow uniform dispersion. The resulting suspensions were named as CWHS, CWHI and CWHL, where “S”, “I” and “L” refer to the average particle size of BCH that was submitted to acidolysis, standing for small, intermediate and large particles sizes, respectively. The CWH suspensions were kept at 6-10 °C until further characterizations.

### 3.3.3. Characterizations

#### 3.3.3.1. Scanning electron microscopy (SEM)

The morphology of BCH samples was evaluated by scanning electron microscopy (SEM, JEOL JSM-6510) with an acceleration voltage of 5 kV. The samples were coated with 15 nm

of gold particles by using an automatic sputter coater SCD050 (Leica) under vacuum (GONZAGA et al., 2021).

### 3.3.3.2. *Transmission electron microscopy (TEM)*

The morphology of CWH samples was evaluated by transmission electron microscopy (TEM, FEI Tecnai G2F20) with an acceleration voltage of 200 kV. A drop of diluted CWH aqueous suspension (1/100 (w/w)) was deposited on a Cu microgrid (300 mesh), allowed to dry and then negatively stained with a 3% (w/w) solution of uranyl acetate and dried at room temperature.

### 3.3.3.3. *Atomic force microscopy (AFM)*

The AFM experiments were carried out with Shimadzu SPM-9600 equipment. A drop of diluted CWH aqueous suspension (1/100 (w/w)) was deposited onto a cleaved mica surface and air-dried. Then, AFM images were obtained at room temperature in intermittent non-contact mode by using a monolithic silicon cantilever with a curvature radius of less than 10 nm and a spring constant of  $48 \text{ N m}^{-1}$  at a scan rate of 1 Hz. The dimensions of whiskers were determined from AFM images by using the open-source Gwyddion<sup>TM</sup> software version 2.53. At least 100 random chitin nanocrystals were evaluated to determine their average length and diameter.

### 3.3.3.4. *TD-NMR relaxometry: MSEFID and CPMG techniques*

<sup>1</sup>H TD-NMR measurements were performed on a 20 MHz spectrometer Minispec mq20 bench-top pulsed NMR analyzer, Bruker Analytic, equipped with a permanent magnet and a 10-mm temperature-controlled probe-head. The determination of  $T_2$  relaxation times was performed using a CPMG (CARR; PURCELL, 1954; MEIBOOM; GILL, 1958) pulse sequence on CWH suspension samples ( $C_p = 20 \text{ wt } \%$ ,  $\text{pH} \approx 7.0$ ), in the temperature range of 20 - 100 °C with 10 °C step rate, recycle delay of 5 s,  $\tau$  of 0.1 ms. For all the analyses, 512 scans were accumulated and 1000 echoes were acquired. Receiver gain and flip angles of  $\pi/2$  and  $\pi$  pulse width were optimized for each temperature.

To estimate the mobility contrast among the molecular moieties of BCH and freeze-dried CWH samples, dipolar refocused echoes provided by the Magic Sandwich Echo method

(MSEFID) (MAUS; HERTLEIN; SAALWÄCHTER, 2006) was performed with 1024 scans, echo time of 0.1 ms and 2 s of recycle delay. Because the MSEFID signal is sensible to the magnetic dipolar interactions among the  $^1\text{H}$  nuclei in the sample, the signal arising from rigid segments decay differently from those that present molecular mobility with rates higher than the  $^1\text{H}$ - $^1\text{H}$  dipolar coupling. Indeed, considering a two mode molecular mobility model, one can estimate the relative mobility among molecular segment by fitting the MSEFID, as discussed in CHAPTER II and described by Eq. (8) (FACCHINATTO et al., 2020b).

### 3.3.3.5. X-ray photoelectron spectroscopy (XPS)

The elemental surface composition of BCH and lyophilized CWH samples were performed by X-ray photoelectron spectroscopy on a XPS spectrometer Scienta Omicron ESCA+, coupled with a hemispheric analyser EAC2000 for higher performances and a scanning monochromated Al  $K\alpha$  radiation as excitation source, with  $h\nu = 1486.7$  eV, 50 W and spot size of 200  $\mu\text{m}$ , as previously described (TAKETA et al., 2018). The ultra-high vacuum chamber was operating at  $10^{-9}$  Pa during the analysis and the XPS spectra were recorded at constant pass energy of 50 eV with energy step of 0.5 eV. The binding energies (BEs) of C 1s, N 1s and O 1s were determined with respect to the surface normal and evaluated using BE =  $284.6 \pm 0.1$  eV of C 1s spectra as reference. The argon bombardment of ion beam was performed over sweeping 200  $\mu\text{m} \times 700 \mu\text{m}$  of sample area, with analyzer workfunction of 4.5 eV and 20 nA of ion gun emission. The evaluation of subcomponents based on previous reported position (BE) and *FWHM* (KOSTOV et al., 2018; OH et al., 2013; WANG et al., 2012) were obtained applying the peak fitting deconvolution procedure with Voigt functions, by using PeakFit<sup>TM</sup> software version 4.12.

### 3.3.3.6. Electrophoretic light scattering (ELS)

Diluted aqueous suspensions of CWH samples ( $C_p \approx 10^{-3}$  wt % in deionized water) were carry out the ELS aiming to measure its electrophoretic mobility, often converted to zeta potential ( $\zeta$ ). The measurements were performed in a Zetasizer Nano ZS (Malvern Instruments<sup>®</sup>, Worcestershire, UK) equipped with laser beam of He-Ne at 633 nm, by means the Laser Doppler Micro-electrophoresis technique. The acquisition was automatically repeated multiple times until reach a monomodal profile for accurately values of  $\zeta$ . The values of zeta

potential was obtained applying the Smoluchowski equation (XU, 1993). The analysis reproductivity was verified with respect to KCl standard solution ( $\zeta = 61.8 \pm 7.68$  mV).

### 3.3.3.7. *Rheometric measurements*

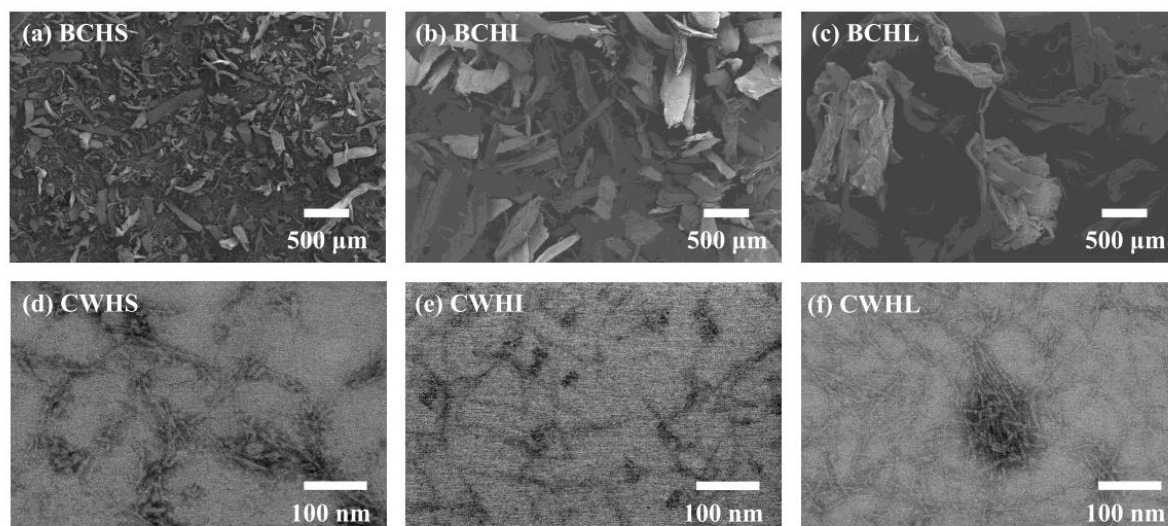
The rheological flow and oscillatory behavior of aqueous CWH suspension samples ( $C_p = 20$  wt %,  $\text{pH} \approx 7.0$ ) were performed by means of a controlled stress rheometer TA Instrument AR 1000N, equipped with a cone-plate geometry ( $2^\circ$ , diameter = 20 mm) with gap adjusted to maximize the values of storage modulus ( $G'$ ) regarding the loss modulus ( $G''$ ) and a solvent trap to avoid water evaporation, according to previously described by FACCHINATTO et al. (2019). Thus, as preliminary measurements, the zero-shear viscosity ( $\eta_0$ ) was determined from the steady shear flow curves ranged in  $0.1 < \dot{\gamma} < 1000$   $\text{s}^{-1}$ , and the linear viscoelastic region was determined by means of stress-sweep oscillatory measurements in the range  $0.1 < \tau < 500$  Pa at 1.0 Hz allowing the moduli determination regardless the strain amplitude. The mechanical moduli dependence was recorded from oscillatory frequency-sweep measurement ranged in  $0.1 < \omega_{sw} < 100$   $\text{rad s}^{-1}$  at constant shear stress  $\tau = 4.8$  Pa. These experiments were carried out at  $25.0 \pm 0.1$  °C. The temperature-sweep measurement was applied to evaluate the viscoelastic behavior from 20 to 80 °C at 1.0 Hz,  $6.5$  °C  $\text{min}^{-1}$  and  $\tau = 4.8$  Pa. All analyses were performed in triplicate.

## 3.3.4. *Results and Discussion*

### 3.3.4.1. *Micrographs of chitin nanowhiskers*

The effect of  $\beta$ -chitin (BCH) powder sizes on the preparation of chitin whiskers (WCh) suspensions by acid hydrolysis was investigated through SEM measurements (Fig 31a-c), while TEM measurements (Fig. 31d-f) were carried out for evaluate the CWH morphology. The micrographs indicate that all chitin whiskers samples exhibited individual needle-like nanoparticles and some aggregates. The presence of aggregates can be attributed to the high surface area of nanocrystals, which favors the occurrence of hydrogen bond involving the polymer chains during the removal of the dispersing medium for TEM assay (NETO et al., 2013).

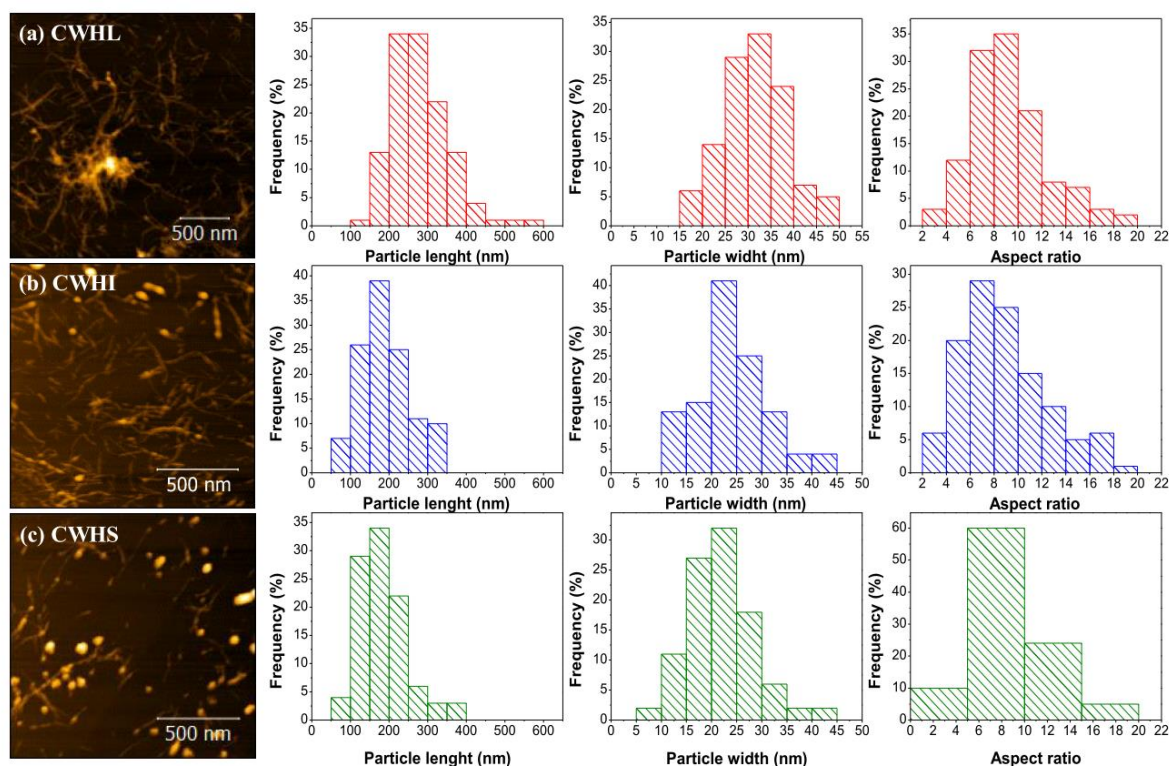
Figure 31 - SEM images of BCHS (a), BCHI (b) and BCHL (c); and TEM images of CWHS (d), CWHI (e) and CWHL (f).



AFM images (Fig. 32) reveal the presence of needle-like crystals aggregates as well as spherical shape nanoparticles in CWHI and CWHS suspensions. The dimensions of chitin nanocrystals were calculated showing that the average diameters were noticeably affected by the average particle size from parent BCH submitted to acidolysis. As can be seen in Fig. 32a, CWHL sample exhibited needle-like crystals with length ( $L$ ), width ( $w$ ) and aspect ratio ( $L/w$ ) ranging as 100-600 nm, 15-50 nm, and 2-20, respectively. However, the effect of acidolysis on BCH fraction possessing lower average particle size (BCHI and BCHS) resulted in nanocrystals displaying average length predominantly in the range of 100-350 nm, in CWHI and CWHS samples (Fig. 2b-c), while no significant differences among them can be observed regarding CWHL sample in terms of particle width and aspect ratio. Additionally, the number of spherical particles with diameters predominantly in the range 20-60 nm progressively increased with decreasing of powder size of the parent BCH. In this sense, the predominance of non-spherical shape nanocrystals can be understood as a direct consequence of the surface area exposure. Smaller particles intrinsically have higher surface/bulk ratio being more susceptible to acidolysis. Such behavior leads to form particles with nanocrystal geometry also with higher surface/bulk ratio as possible, *i.e.* spherical shape. This concept consequently explains the tendency of decreasing the amount of spherical particles obtained from higher average particle sizes of BCH, once nanowiskers or needle-like shape actually present a typical geometry with intrinsically lower surface/bulk ratio than the spherical shape. Indeed, the particle length and

width distribution mainly reveal the influence regarding the relative contribution of these distinct shapes on the average dimension.

Figure 32 - AFM images of CWHL (a), CWHI (b) and CWHS (c) samples and corresponding histograms showing the length, width and aspect ratio distributions.

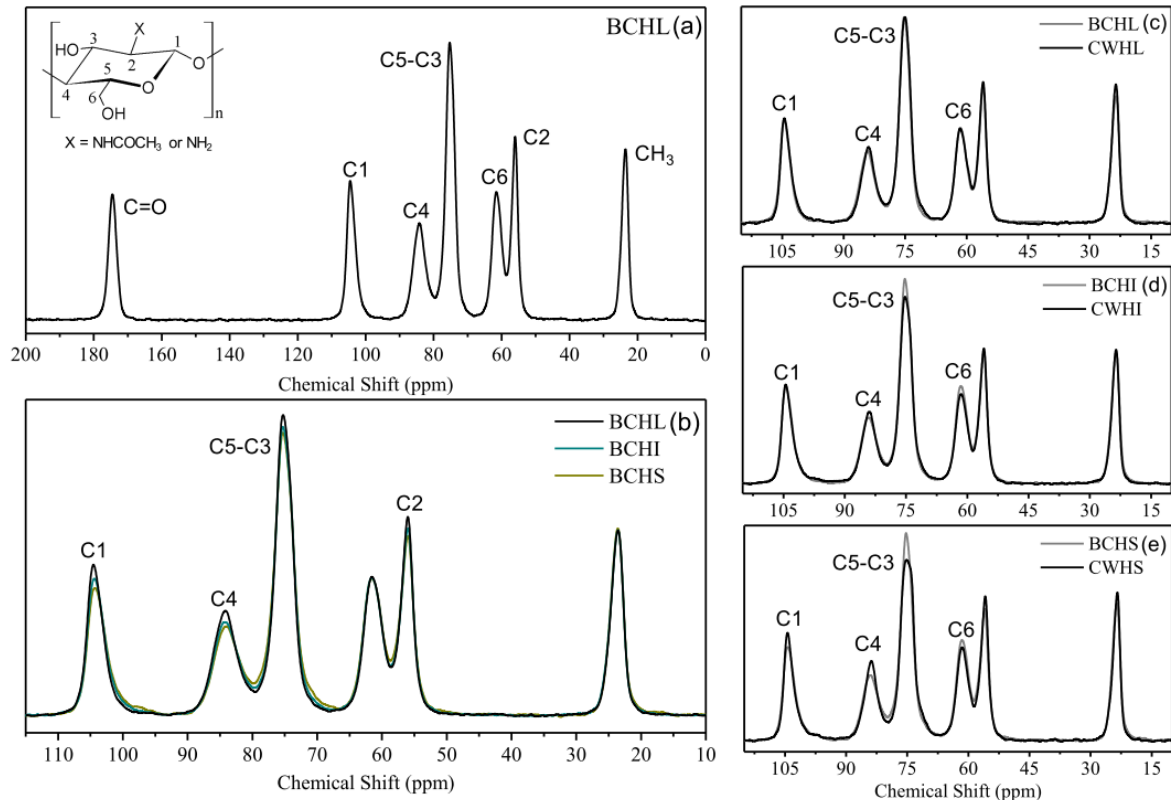


### 3.3.4.2. Structural and morphological features

The  $^{13}\text{C}$  CPMAS spectra of BCHL is shown in Fig. 33a as a  $\beta$ -chitin representative spectrum profile. The  $\overline{DA}_{CP}$  (Eq. (7)) of BCH and CWH samples are listed in Table 8 and, as observed, the average content of GlcNAc units remained almost unchanged after carrying out the acidolysis. In contrast, the significant decrease of  $\overline{M}_v$  shows that the hydrolysis of glycosidic bonds resulted in remarkable depolymerization, as confirmed by  $\overline{DP}_v$  values (Table 8). The  $\overline{M}_v$  of BCH are  $\geq 10^6 \text{ g mol}^{-1}$ , whereas the acidolysis led to  $\overline{M}_v \approx 10^4 \text{ g mol}^{-1}$  in the case of CWH. Moreover, it should be considered a meaningful effect from average powder size (granulometry) to the acid accessibility on glycosidic linkages. As the powder size decreases, the more effective is the cleavage of BCH polymeric chains. In this sense,  $\overline{M}_v$  of CWHL, CWHI and CWHS reached over 1.21, 1.08 and 0.70 % of the  $\overline{M}_v$  value obtained from BCHL, BCHI

and BCHS, respectively. It is important to notice that the grinding procedure also affects the  $\bar{M}_v$ , which is explained by the elevated temperature friction reached between the blades inside the mill (DELEZUK; PAVINATTO; CAMPANA-FILHO, 2019).

Figure 333 -  $^{13}\text{C}$  CPMAS spectra of  $\beta$ -chitin (a), parent chitin samples BCHL, BCHI and BCHS (b) and the corresponding freeze-dried samples CWHL (c), CWHI (d) and CWHS (e).



As revealed by the  $^{13}\text{C}$  CPMAS spectra profile on Fig. 33b-e, some of the corresponding carbon signal assignments of BCH with the corresponding CWH samples achieved varied shape, which is mainly due to the acidolysis effect on the chain's conformation (FACCHINATTO et al., 2020a). As shown in Fig. 33b, the signal shape assigned to C5-C3, C4, C2 and C1 of BCH samples is straight related to the local geometry from the intersheet spatial disposal. Noticeably, such conformational changes have no significant effect regarding the molar mass (FACCHINATTO et al., 2020a; HEUX et al., 2000; OTTØY; VÅRUM; SMIDSRØD, 1996). CWH samples (Fig. 33c-e) also reveal similar behavior in C5-C3, C6, C4 and C1 signals if compared to the parent BCH. As the reactivity on heterogeneous medium is mediated by the accessibility of the soluble reagent to the swelled solid particles, the intersheet hydrogen bonds should be greatly affected, modifying the overall conformation. Thus, slight variations regarding C3 and C6 signals could be partially related to conformational changes in

such reactive site, since it is directly linked to hydroxyls groups, which are responsible for setting those intersheet bindings, partially disrupted during the acydolysis. Because more disorder chains are expected to be present in the surface of the internal structures, it is reasonable to infer that the smaller the powder size of parent chitin, the higher the surface area available for acid hydrolysis, as observed from BCHL to WCHL samples (Fig. 33c), BCHI to WCHI (Fig. 33d) and BCHS to CWHS samples (Fig. 33e) with respect to this related carbon signals. The acid reactivity on heterogeneous medium was mediated by solid particle accessibility, leading products with great morphological variability, as discussed in the previous section.

Table 8 - Values of average degree of acetylation ( $\overline{DA}_{CP}$ ), viscosity average molecular weight ( $\overline{M}_v$ ), viscosity average degree of polymerization ( $\overline{DP}_v$ ), crystallinity index from  $^{13}\text{C}$  CPMAS spectra profiles ( $\overline{CrI}_{CP}$ ), rigid/mobile intermediate motion parameters ( $T_{2r}$ ,  $T_{2m}$  and  $v_m$  and  $f_m$ )

Samp.	$\overline{DA}_{CP}$ <sup>a</sup> (%)	$\overline{M}_v$ <sup>b</sup> × 10 <sup>4</sup> (g mol <sup>-1</sup> )	$\overline{DP}_v$ <sup>c</sup> × 10 <sup>2</sup>	$\overline{CrI}_{CP}$ <sup>d</sup> (%)	$T_{2r}$ <sup>e</sup> (μs)	$T_{2m}$ <sup>e</sup> (μs)	$v_m$ <sup>e</sup>	$f_m$ <sup>e</sup>
BCHL	89 ± 5	207 ± 14	104 ± 7	84 ± 2	18.4 ± 0.1	201 ± 4	1.40 ± 0.04	43 ± 1
BCHI	91 ± 6	156 ± 3	78 ± 2	83 ± 2	17.7 ± 0.8	254 ± 3	1.27 ± 0.02	45.1 ± 0.7
BCHS	91 ± 5	106 ± 4	53 ± 2	81 ± 1	19.4 ± 0.1	325 ± 7	1.05 ± 0.04	47.7 ± 0.2
CWHL	87 ± 6	2.49 ± 0.05	1.26 ± 0.02	86 ± 3	19.2 ± 0.2	290 ± 1	1.00 ± 0.05	41.9 ± 0.5
CWHI	88 ± 5	1.69 ± 0.10	0.85 ± 0.06	85 ± 3	20.2 ± 0.2	292 ± 1	1.03 ± 0.06	42.3 ± 0.7
CWHS	88 ± 6	0.73 ± 0.04	0.37 ± 0.02	87 ± 3	20.9 ± 0.2	320 ± 2	1.00 ± 0.09	45.2 ± 0.4

<sup>a</sup> Determined from  $^{13}\text{C}$  CPMAS spectra;

<sup>b</sup> Determined from the  $[\eta]$  values by using Mark-Houwink-Sakurada equation;

<sup>c</sup> Calculated according to the values of  $\overline{M}_v$  and  $\overline{DA}_{CP}$ ;

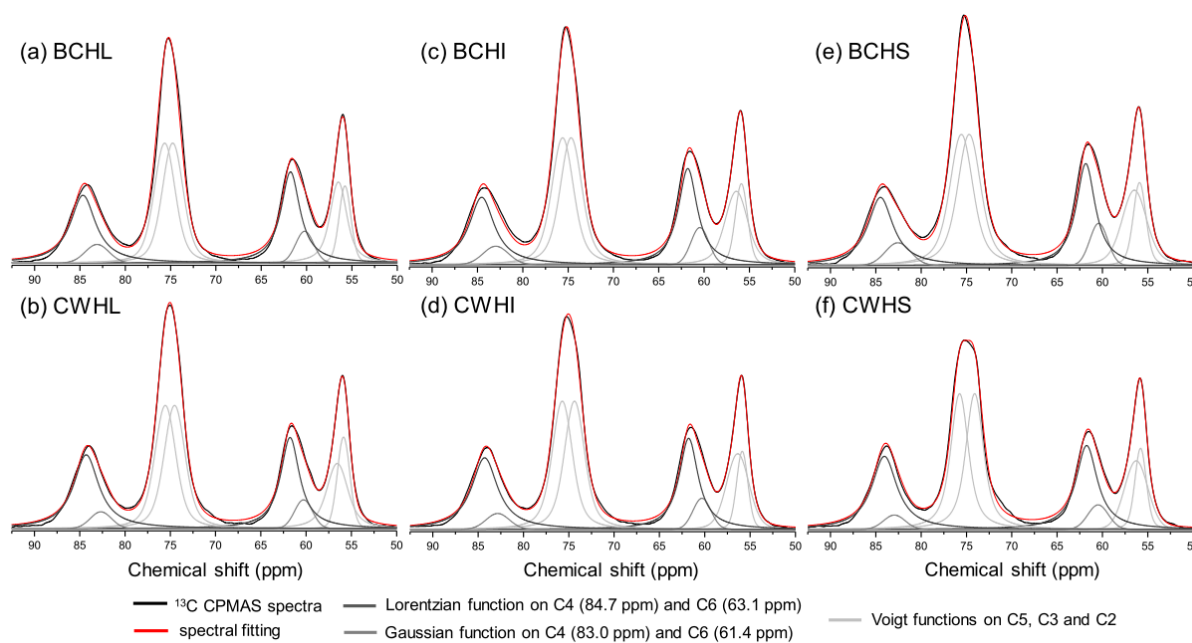
<sup>d</sup> Crystallinity index calculated from C4 and C6 resonance signals of  $^{13}\text{C}$  CPMAS spectra profile

<sup>e</sup> Rigid-part ( $T_{2r}$ ), mobile-part segments ( $T_{2m}$ ) and stretching parameter  $v_m$  and mobile fraction parameter  $f_m$ , calculated by MSEFID signal.

It was proposed on CHAPTER I the crystallinity index determination through the deconvolution procedure using C4/C6 carbons signals from  $^{13}\text{C}$  CPMAS spectra (Fig. 34) (FACCHINATTO et al., 2020a). The short-range molecular ordering, quantitatively evaluated by means of  $\overline{CrI}_{CP}$ , is shown in Table 8 for BCH and CWH samples. According to the study, the number of possible conformations between C4 and C6 are greatly affected by  $\overline{DA}_{CP}$  which proportionally increases with  $\overline{CrI}_{CP}$ . However, such values stay nearly unchanged regarding the effect of depolymerization with constant  $\overline{DA}_{CP}$ . These results partially explain the almost unchanged shape of C4 and C6 signals on  $^{13}\text{C}$  CPMAS spectra from CWH which respect to that from the parent BCH. Once the harsh acid conditions leave products with no meaningful

variability on  $\overline{DA}_{CP}$ , the  $\overline{CrI}_{CP}$  were only slightly affected, showing just a small increase from BCHL to CWHL and BCHI to CWHI (Table 8). On the other hand, the short-range molecular ordering seems to be more affected by decreasing the BCH particle size, which is corroborated by the  $\overline{CrI}_{CP}$  increase from BCHS to CWHS. More specifically, the drop in the relative intensity of the signal attributed the C4 carbons may be seen as a suggestion of the presence of two regions with distinct conformational order. Indeed, the degree of conformation disorder is mostly reflected in the inhomogeneous broadening of the signals, but the change in the fraction of disordered chain among the samples would lead to a lower relative intensity. Thus, the particle size might be included as secondary effect that can lead to short-range changes on the molecular arrangement, while the  $\overline{DA}_{CP}$  still holds the main influence on that.

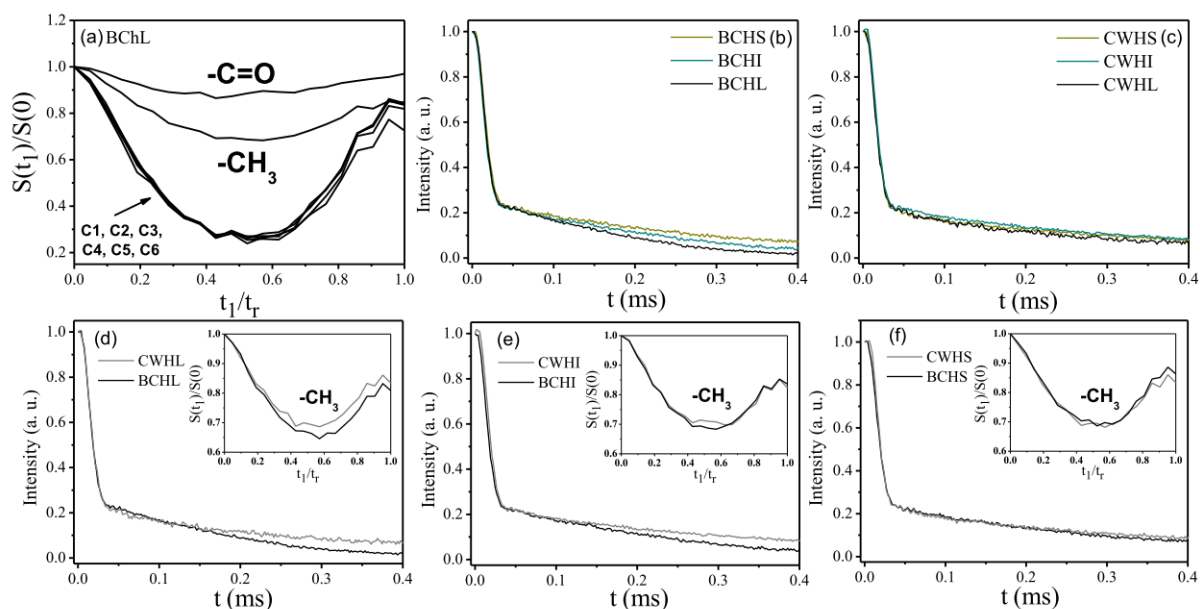
Figure 344 - Peak deconvolution method applied on  $^{13}\text{C}$  CPMAS spectra ( $T_C = 3000 \mu\text{s}$ ) of BCHL (a), CWHL (b), BCHI (c), CWHI (d), BCHS (e) and CWHS (f) samples, allowing the quantification of  $\overline{CrI}_{CP}$ .



The relative mobility of molecular segments of BCH and CWH samples were evaluated by DIPSHIFT and MSECID techniques (Fig. 35). DIPSHIFT is sensitive to motions in molecular segments with rates higher than the C-H dipolar coupling ( $\sim 10$  kHz). This is achieved by curves that represent the modulation of the spectral amplitudes by the evolution of the  $^{13}\text{C}$  magnetization by the  $^1\text{H}$ - $^{13}\text{C}$  dipolar interaction (DEAZEVEDO et al., 2008; MUNOWITZ et al., 1981). The resulting  $^1\text{H}$ - $^{13}\text{C}$  dipolar curves from each molecular segment of BCHL are presented in Fig. 35a as a representative profile. When  $t_1 = t_r$  is reached during the evolution time, the static  $^1\text{H}$ - $^{13}\text{C}$  dipolar interaction is refocused, meaning that it does not contribute

directly to the signal reduction. However, the  $^{13}\text{C}$   $T_2$  relaxation still produces an exponential attenuation of the signal, lowering the amplitude at  $t_1 = t_r$ . The shorter is  $T_2$ , the lower is the amplitude achieved.  $^{13}\text{C}$   $T_2$  relaxation in these systems is majorly produced by fluctuation on the  $^1\text{H}$ - $^{13}\text{C}$  dipolar interaction in the kHz frequency scales, so chemical groups that experiences lower interaction have longer  $^{13}\text{C}$   $T_2$ . This is the case of  $\text{CH}_3$ , because of the fast C3 rotations, and  $\text{C}=\text{O}$ , because of the absence of directly bonded  $^1\text{H}$ , which explain the behavior of the DIPSHIFT curves at  $t_1 = t_r$  (HONG et al., 2002; MUNOWITZ et al., 1981). The deepest amplitude from C1 to C6 are related to stronger  $^1\text{H}$ - $^{13}\text{C}$  dipolar interaction and thus restricted motion, while the lowest amplitude of carbonyl group means that there is no significative  $^1\text{H}$ - $^{13}\text{C}$  dipolar coupling due the absence of  $^1\text{H}$  nuclei directly linked and only weakly interact with nearby hydrogens (FACCHINATTO et al., 2020a; SIMMONS et al., 2016)

Figure 355 - DIPSHIFT curves of  $\beta$ -chitin (a). The normalized amplitude signals ( $S(t_1)/S(t_0)$ ) were acquired during heteronuclear dipolar interaction free precession ( $t_1$ ) of first rotor spin cycle ( $t_r$ ); MSEFID signal decays of BCHS, BCHI, BCHL (b), CWHs, CWHI and CWHL samples (c); relationship of MSEFID and DIPSHIFT experiments of lyophilized samples and its parent chitin (d-f).



The MSEFID curves are associated to the signal arising from  $^1\text{H}$  nuclei and it can be separated into fast and slow signal decays, referred to rigid/mobile fractions of polymeric chains (MAUS; HERTLEIN; SAALWÄCHTER, 2006). The quantitative information extracted from each  $^1\text{H}$  NMR signal decay profile BCH and CWH is shown in Table 8. The rigid-part signal,  $T_{2r}$ , typically decays within  $20 \mu\text{s}$ , corresponding to the Gaussian width associated the decay of the  $^1\text{H}$  magnetization (MAUS; HERTLEIN; SAALWÄCHTER, 2006). This was observed

for all samples, revealing that there is no significant molecular mobility on the glycosidic carbon, as similarly revealed by the DIPSHIFT curves (Table 8). In contrast, the major contribution on the mobile-part signal,  $T_{2m}$ , is partially ascribed to the  $^1\text{H}$  nuclei from methyl groups (CLEEMPUT et al., 1995) and those from residual water molecules, which is also in agreement with DIPSHIFT curve regarding the corresponding methyl carbon (FACCHINATTO et al., 2020b). Despite the  $T_{2m}$  values slight increase from BCHL to BCHS, this parameter does not follow such tendency among CWH samples (Table 8). Similarly to our previous findings in CHAPTER II (FACCHINATTO et al., 2020b), it was not possible to quantify the average degree of acetylation neither the crystallinity index directly from  $T_{2m}$  and  $f_m$  because both parameters simultaneously increase with the structural and morphological variability, including the less predominant influence of  $^1\text{H}$  nuclei from water molecules (residual of hydration). In this sense, the similarity observed in the mobile-part signal is modulated by the local chain packing, which means that the dynamic dependence of methyl hydrogens is slightly affected by intersheet packing and the fast rotation on C3 axis might be influenced by the surrounding spatial freedom of the powdered BCH particle. However, the  $^1\text{H}$  density estimated locally is biased by signal distortions due to the echo acquisition and, consequently, in this case such experiments are not sensible enough to predict the morphological specificities of CWH samples.

In addition, it is worth to mention that MSEFID were performed at 25 °C because chitin/chitosan are sensitive to temperature changes. Studies show that after submitting powdered chitin and/or chitosan to a thermal treatment, permanent changes occur in the morphology, thus affecting its crystallinity (FOCHER et al., 1990; OGAWA; YUI; MIYA, 1992). It is important to notice that the crystallinity and degree of acetylation were previously determined for the whole set of samples in the way that the morphology were carefully controlled and avoided as much as possible the influence of external variables, such as temperature. Hence, this feature was mostly dependent upon degree of acetylation (FACCHINATTO et al., 2020a). Indeed, a further study of microstructure modification with temperature can be done, but we thought the best decision to show the viability of the proposed approach would be its feasibility in standard systems as the low cost, benchtop and room temperature spectrometers.

The greater intersheet accessibility to small molecules and swelling behavior of  $\beta$ -chitin as compared to  $\alpha$ -chitin facilitate the crystallite surfaces to be reached, partially hydrolyzed and transferred to the medium as water-soluble fractions. Such explanation fits with the results indicated on Table 9. Even though the amorphous phase is relatively easier to be accessed than the crystalline one, the strong oxidative medium also affected the crystallites reducing its

average dimensions and, consequently, the  $CrI$  of CWH, both compared to the parent BCH. Thus, the long-range molecular ordering, obtained through XRD patterns, that regards to the chains packing are more affected if compared directly to the short-range ordering obtained through  $^{13}\text{C}$  CPMAS. Due to the tighter intersheet arrangement found on  $\alpha$ -chitin, the amorphous domains are considerably easier to be reached and removed than the crystallite surfaces, leading to a relative increase of  $CrI$  (GOODRICH; WINTER, 2007) or even a constant value if recrystallization occurs (FAN; SAITO; ISOGAI, 2008a). The peak deconvolution procedure performed on XRD patterns in order to calculate the crystal sizes on BHC and CWH samples are shown on APPENDIX B.

Table 9 - Crystallinity index ( $CrI_2$ ), apparent crystal dimension from hydrated peak at  $2\theta \approx 8.2^\circ$  ( $L_{020}$ ) and  $19.7^\circ$  ( $L_{110}$ ), temperatures and weight losses related to the thermal degradation of BCh and WCh samples.

Samp.	$CrI_2^a$ (%)	$L_{020}^b$ (nm)	$L_{110}^b$ (nm)	Stage I (25 - 150 °C)		Stage II (200 – 400 °C)	
				$T_{MAX}^c$ (°C)	WL <sup>d</sup> (%)	$T_{onset}^e$ (°C)	WL (%)
BCHL	71.2	4.66	3.28	86	9	307	51
BCHI	71.4	4.66	3.20	82	5	303	56
BCHS	61.1	4.63	3.05	82	5	295	62
CWHL	58.9	3.71	2.75	71	11	265	53
CWHI	48.8	3.43	2.24	71	11	245	57
CWHS	44.1	2.73	2.04	72	6	239	58

<sup>a</sup> Calculated considering the subtraction of amorphous contribution ( $A_{am}$ ) from the total diffraction pattern area ( $A_{tot}$ ).

<sup>b</sup> Calculated by using Scherrer equation on deconvoluted crystalline peaks of XRD patterns with Lorentzian functions.

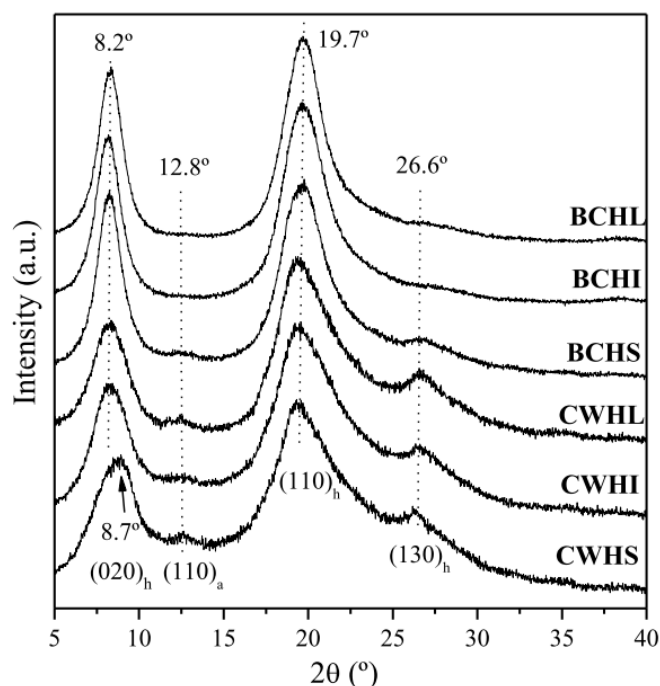
<sup>c</sup>  $T_{MAX}$  = temperature of maximum weight loss.

<sup>d</sup> WL = weight loss.

<sup>e</sup>  $T_{onset}$  = onset temperature.

The crystal sizes of  $(020)_h$  and  $(110)_h$  reflections corresponding to 010 and 100 planes of diffraction spots located in  $2\theta \approx 8.2^\circ$  and  $19.7^\circ$  peaks (Fig. 36), respectively, also decreased after acid hydrolysis (Table 9), being similar to the case described in previous study (FAN; SAITO; ISOGAI, 2008b). However, the overall decrease of crystallinity and crystal sizes of CWH is dependent on the average particle size of powdered BCH. Thus, the smaller the size, the greater the access to the crystallites that are transferred to the bulk solution. Consequently, crystallite dimensions  $L_{020}$  and  $L_{110}$  are reduced from CWHL to CWHS, as indicated in Table 9.

Figure 366 - X-ray diffraction patterns of BCh and WCh samples.

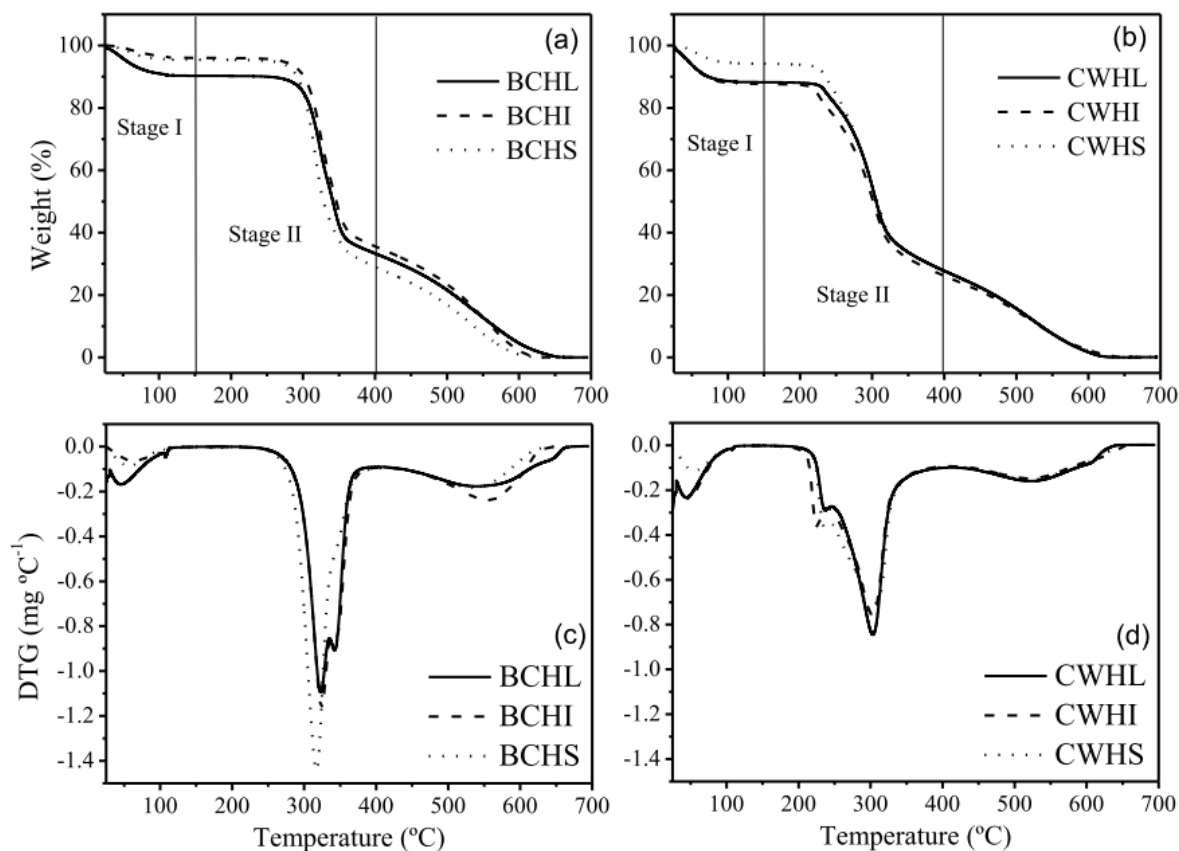


TGA was mainly used for the purpose of quantifying the residual hydration and the thermal stability of BCH and CWH samples through thermal decomposition curves, showed in Fig. 37. The TG main events can be visualized from two stages, which are assigned and listed in Table 9. In the first thermal decomposition stage (25-150 °C), the weight loss is attributed to the loosely bound water molecules that ranged from ~ 5 to 9 % in BChS to BChL (Fig. 37a), while the stage I of CWH samples also reveals similar tendency, ranging from ~ 6 to 11 % in CWHS to CWHL (Fig. 37b). Our preliminary intention was to correlate the average percentage of water in each chitin structure, and to recognize if there was some dependence between them. In this sense, our findings indicate that the content of water molecules didn't show huge changes. This tendency might be explained by the hydrated crystallites (Table 9), whose sizes reveal to be proportional to the retained water molecules content. It is important to notice that as the amount of water molecules doesn't changed drastically (Table 9), the  $^1\text{H}$  NMR signal decay profile (Fig. 35) are similarly affected in all cases in average, which is in accordance to CHAPTER II (FACCHINATTO et al., 2020b).

In the second thermal decomposition stage (200-400 °C), the  $T_{\text{onset}}$  is mainly attributed to the elimination of volatiles resulted from chitin structure decomposition (BRITTO; CAMPANA-FILHO; ASSIS, 2011). This second event is largely affected by chitin framework, leading to higher heat absorption, and thus its thermal stability, as molecular weight and

crystallinity of the samples increased, like observed through  $\bar{M}_v$  and  $CrI$  values, respectively (Table 8) (FACCHINATTO et al., 2019; SANTOS; BUKZEM; CAMPANA-FILHO, 2016).

Figure 37 - TG (a) and DTG (b) curves of BCH and CWH samples.

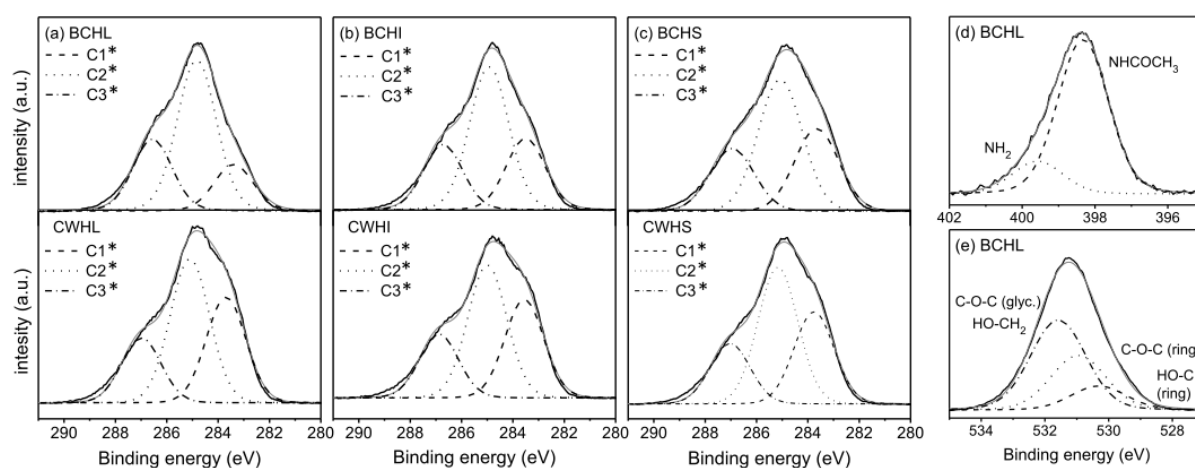


### 3.3.4.3. Surface charge and functional groups

The quantitative determination of surface composition and comparison between BCH and CWH samples were carried out by using XPS analysis (Fig. 38). The following description of peak deconvolution analysis has considered the experimental assignments with respect to theoretical atomic 1s binding energies with deviations from ideal C, N and O stoichiometry (KOSTOV et al., 2018). As shown in Fig. 38a-c, the spectra deconvolution allowed the carbon signals of C 1s orbital electrons to be classified into three distinct peak regions with bonding energies at 283.4, 284.3 and 286.5 eV, assigned as C1\*, C2\* and C3\*, respectively. This fitting procedure revealed that C1\* deconvoluted area attributed to C-C (sp<sup>3</sup>) and C=C (sp<sup>2</sup>) increases from BCH to the corresponding CWH sample, regarding the C2 (C-N/C-C) and C3 (C-O/C=O) signals (Table 10), which indicates the aliphatic surface replacement with hydrophobic

functional groups (WANG et al., 2012). Such result suggests that the significant stability enhancement of CWH nanostructures, confirmed by the zeta potential values (Table 10) on colloidal aqueous suspension, are successfully achieved by non-collapsed hydrophobic segments taking into account that high acetylated chitin samples usually aggregates itself into insoluble particles on aqueous medium. Additionally, the proportional increase of C1\* area from BCHL to BCHS also suggests that the hydrophobic content is continuously exposed by lowering the average particle size and increasing the surface area.

Figure 38 - X-ray photoelectron spectroscopy of C1\* 1s binding energies from BCH to CWH samples (a-c). N 1s (b) and O 1s (c) of BCHL showed as a representative spectrum profile.



The representative spectra of N 1s binding energy is shown in Fig. 38d. No significant difference was found with respect to the surface exposure of acetyl segments. According to previous studies, it is expected a dominant contribution of NHCOCH<sub>3</sub> group at 398.3 eV compared to NH<sub>2</sub> at 399.6 eV with significant less intense signal due to the higher content GlcNAc units (OH et al., 2013). The binding energy assigned to NH<sub>2</sub> was found shifted ~0.5 eV among BCH and WCH samples, which is possible attributed to NH<sub>3</sub><sup>+</sup> remaining structures (JIANG et al., 1997; TAKETA et al., 2018). Similarly, Fig. 38d shows representative spectra of O 1s binding energy which is also in agreement with reported spectra profiles (JIANG et al., 1997; KOSTOV et al., 2018).

Table 10 - Distribution of surface functional groups of C 1s signal and relative concentrations of carbon (C1 s), nitrogen (N 1s) and oxygen (O 1s) atoms.

Sample	C 1s <sup>a</sup> (%)			Atomic concentrations <sup>e</sup> (%)			$\zeta$ (mV)
	C1 <sup>*b</sup>	C2 <sup>*c</sup>	C3 <sup>*d</sup>	C 1s	N 1s	O 1s	
BCHL	17.3	56.0	26.7	40.6	7.0	52.4	-
BCHI	25.6	51.1	23.3	42.9	6.4	50.7	-
BCHS	29.9	47.5	22.6	43.7	6.4	49.9	-
CWHL	31.9	47.2	20.9	44.8	5.5	49.7	29.2 ± 1.6
CWHI	33.4	45.0	21.6	44.8	5.9	49.2	29.4 ± 2.0
CWHS	33.6	45.7	20.6	44.1	5.9	50.0	31.3 ± 3.0

<sup>a</sup> Deconvoluted regions from surface functional groups of C 1s signal, calculated by peak deconvolution of XPS spectra

<sup>b</sup> C-C (sp<sup>3</sup>) and C=C (sp<sup>2</sup>).

<sup>c</sup> C-O-C, C-OH, C-N-C, C-NH<sub>2</sub> and C-O-C=O.

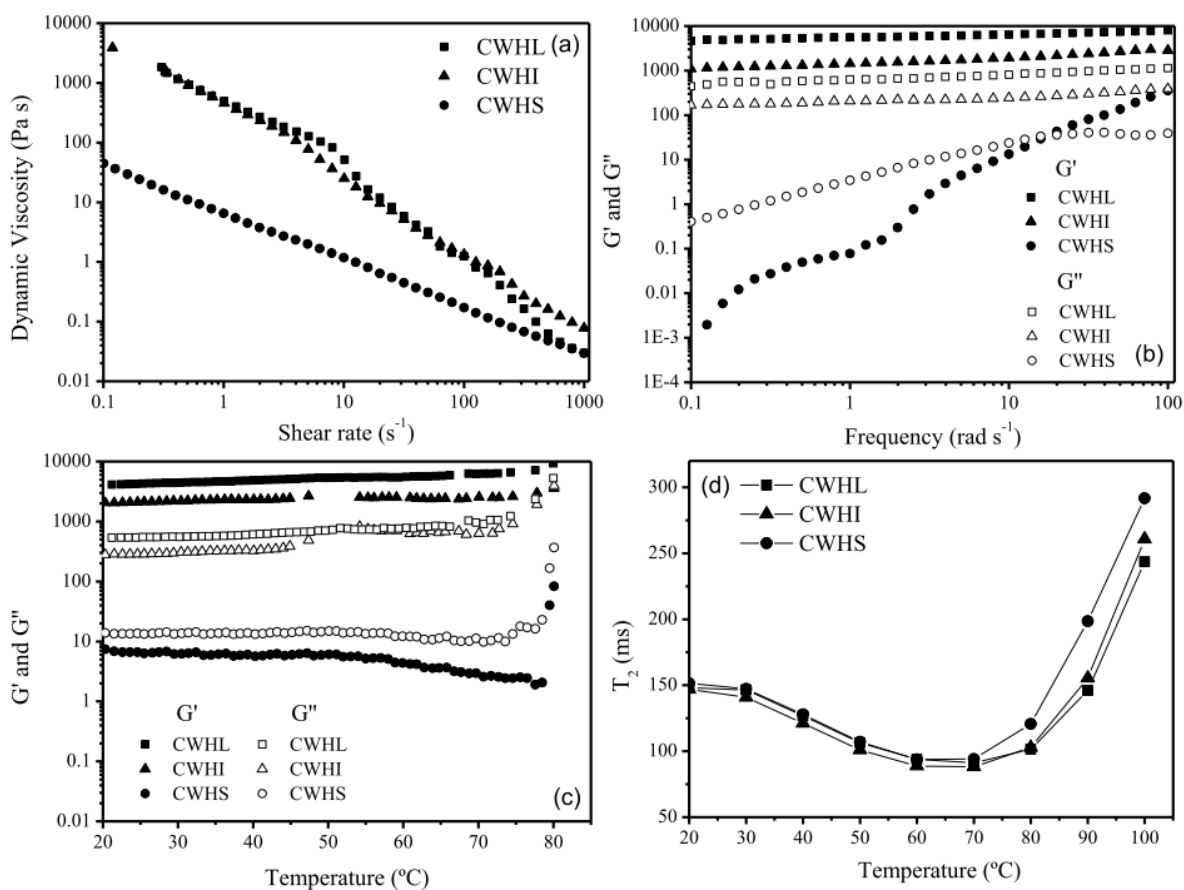
<sup>d</sup> C=O, O-C-O, N-C-O, N-C=O and N=C-O.

<sup>e</sup> Surface relative proportion of C 1s, N 1s (NHCOCH<sub>3</sub> and NH<sub>2</sub>) and O 1s (HO-CH<sub>2</sub>, HO-C and C-O-C from glycosidic bonds and glucopyranose rings).

#### 3.3.4.4. Rheological and relaxation behavior

The rheological behavior of CWH aqueous suspensions (Fig. 39a-c) and the  $T_2$  relaxation time as function of temperature (Fig. 39d) are highlighted in the following discussion. The curves of dynamic viscosity ( $\eta$ ) versus shear rate ( $\dot{\gamma}$ ) (Fig. 39a) show a decreasing viscosity with increasing shear stress, which characterizes a shear-thinning behavior that undergo from a random particle distribution to an organized orientation with the flow direction with increasing shear rate, achieving maximum plastic deformation at high shear rate values. According to previous studies (JOÃO et al., 2017; LI; REVOL; MARCHESSAULT, 1996), the flow properties of CWH suspensions, under influence of shear stress, has changed with respect to the concentration tested. Considering that the rheological measurements in the present study were carried out in high concentrated regime ( $C_p = 20$  wt %), the flow curves differs from the expected behavior of rod-like particles, that predominate at lower concentrations (< 9 wt %) and also exhibit a second Newtonian plateau resulting from the parallel alignment with the flow at high shear stress. Indeed, as the concentration increases, the influence of ellipsoid anisotropic domains in the biphasic region also increases (LEE; BRANT, 2002). Consequently, in this study the shear flow profiles are mainly dependent on the CWH length, width and aspect ratio at higher concentrations.

Figure 399 - Rheological behavior of CWH suspensions verified through shear flow curves (a), frequency sweep (c) and temperature sweep measurements (c). The  $T_2$  relaxation time was measured using CPMG technique as function of temperature (d).



The slower flow gradient presented by CWHS suspension (Fig. 39a) resulted in linear shear-thinning regime. This behavior typically remains from small particles that tumbling out with fast motion (faster stress response) (ACIERNO; COLLYER, 1996), which is possibly related to increased content of spherical nanoparticles, as well as reduced values of crystallite dimensions (Table 9) and molecular weight (Table 8). Analogously, CWHL and CWHI that are predominantly composed by needle-like nanocrystals with higher average sizes, showed faster flow gradient, which is in agreement to higher crystallite dimensions and molecular weights. Differently from CWHS flow profile, it is also observed a non-linear flow regime for CWHL and CWHI suspensions that are commonly described as three-regime flow curve, showing a shear-thinning behavior separated by a small increasing-viscosity over intermediate rates ( $10 s^{-1}$ ). This behavior is related to the increasing influence of anisotropic phase and indicates the formation of liquid crystalline domains (BERCEA; NAVARD, 2000; JOÃO et al., 2017; LI; REVOL; MARCHESSAULT, 1996).

The oscillatory sweep curves of CWH aqueous suspensions are shown in Fig. 39b-c. Almost no dependence of CWHL and CWHI on angular frequency is observed and the elastic shear modulus ( $G'$ ) values overcomes the viscous one ( $G''$ ) at the range explored (Fig. 39b). This viscoelastic behavior is attributed to a gel-like formation that is characterized by a rigid network. In contrast, the CWHS suspension reveals a liquid-like behavior ( $G'' > G'$ ) until reach  $\sim 16 \text{ rad s}^{-1}$  that indicates a transition to a solid-like one ( $G' > G''$ ) at higher frequencies, obeying the relation  $G' \approx \omega^2$  and  $G'' \approx \omega$ . These results show that the rheological measurements are affected by the hydrodynamics properties and structural parameters relationships such as particle geometry, according to previous studies (ISHII; SAITO; ISOGAI, 2011; TATSUMI; ISHIOKA; MATSUMOTO, 2002). These authors had demonstrated that the gel-like network structures are associated to strong attractive interactions and mainly ascribed to high aspect ratios of entangled fibrous particles, although rod-like particles suggest the formation of semiflexible network with a similar angular frequency profile achieved by CWHS suspension (Fig. 39b). Thus, it is possible to infer that the presence of whiskers displaying higher lengths implies in higher anisotropic phase contribution, which were found in the cases of the CWHL and CWHI suspensions, while the reduced presence of needle-like structures had shown greater impact on rheological behavior of CWHS suspension. Although the aspect ratio distribution, showed in Fig. 32, is not clearly distinguishable among the CWH samples, the rheological measurements assured that the nematic behavior prevails when anisotropic particles predominates, meaning that such a behavior is lesser important the higher the presence of spherical particles (REVOL; MARCHESSAULT, 1993).

Both moduli of CWHI and CWHL exhibit weak temperature dependence in the analyzed interval (Fig. 39c) due the fact that the particle vibrations and short-range rotational motions are largely restricted in these crystalline suspensions, as consequence of the fibrous network entanglements. Indeed, a thermo-induced rearrangement is only observed at higher temperatures ( $> 70 \text{ }^\circ\text{C}$ ), in which the heat energy favored the formation of new physical interaction connections. In the case of CWHS suspension, a slight and continuous drop of elastic modulus values starting over  $50 \text{ }^\circ\text{C}$  is a rheological behavior possibly associated with a plasticizing effect, that is typically observed in semicrystalline nanocomposites reinforced with chitin whiskers, such as poly(vinyl alcohol) (JUNKASEM et al., 2010), poly(ester-urethane) (ZENG et al., 2010) and phosphatidylcholine (NIKIFORIDIS; SCHOLTEN, 2015) at similar temperature range, but also found at higher values ( $> 200 \text{ }^\circ\text{C}$ ), for poly(caprolactone) (MORIN; DUFRESNE, 2002) and poly(styrene-*co*-butyl acrylate) (PAILLET; DUFRESNE, 2001). The significant elastic modulus drop reported in these studies is ascribed to a relaxation process

resulting from an anelastic manifestation of the glass-rubber transition, being this tensile property mainly function of chitin nanostructure concentration. In this present study, such anelastic relaxation process is manifested according to CWH nanostructure characteristics.

Despite there is no evidence of anelastic relaxation process on CWHI and CWHL through rheological measurements, the  $T_2$  relaxation time as function of temperature (Fig. 39d) suggests that such thermal-dependence mobility is also found in all analyzed suspensions. Differently from the transversal constant time parameter obtained in MSEFID measurement, the  $T_2$  of colloidal suspensions measure by CPMG provided reliable information about solvent interactions by means of its hydrogens on the surrounding environment (COOPER et al., 2013). Thus, the  $T_2$  reduction with increasing the temperature, which also fits in the described temperature interval of anelastic relaxation process, suggests an anisotropic motion of water molecules bonded at the polymeric particles surface, in response of a new intra- and inter-chain associations. As consequence, the water mobility is reduced leading the  $T_2$  relaxation time also to reduce (SIERRA-MARTÍN et al., 2005).

### 3.3.5. Conclusions

The  $\beta$ -chitin whiskers (CWH) were successfully prepared from different  $\beta$ -chitin (BCH) size fractions, ranging from  $d < 125$  nm (S) to  $d > 425$  nm (L), preserving the average degree of acetylation and showing straight structural and morphological dependence. According to zeta potential and XPS analyses, all CWH samples were stable on colloidal aqueous suspensions that was mainly attributed to the greater surface exposure of non-collapsed hydrophobic segments. Although needle-like crystals have predominated all over CWH samples, higher length, width and aspect ratio values were successfully achieved on CWHL while spherical nanoparticles were only found on CWHI and CWHS. Such influence is related to viscosity average molecular weights, crystallinity indexes and crystal dimensions values. Both structural and morphological relationship agree with flow gradient and viscoelastic behavior of CWH. In this sense, the rheological anisotropic response of liquid crystalline domains was evidenced on samples with strong network entanglement, *i.e.* CWHL and CWHI, while CWHS preserved a network with higher flexibility.

The useful tendencies regarding the powdered particle size and acidolysis accessibility were accomplished by different SSNMR techniques. Hydroxyl substituents responsible for setting those intersheet interactions are probably related to changes on the shape C3/C6 signals

on  $^{13}\text{C}$  CPMAS spectra from BCH to CWH samples and became more expressive by lowering the powdered particle diameter. Additionally, the particle size might be included as secondary effect that can lead to short-range changes on the molecular arrangement, considering that  $\overline{CrI}_{CP}$ , calculated by C4/C6 signals deconvolution procedure, slight increases from BCH to CWH. The major contribution on the mobile-part signal on MSECID signal decay profile,  $T_{2m}$ , is partially due to the  $^1\text{H}$  nuclei from methyl groups which was confirmed by  $^1\text{H}$ - $^{13}\text{C}$  dipolar interaction curve on DIPSHIFT experiment for the same methyl segment. The mobile component is modulated by the local chain packing BCH. However, the  $^1\text{H}$  NMR signal profile remains constant among CWH samples. No significant influence of water hydrogens on  $^1\text{H}$  NMR signal decay profile was found according to TG analysis, due to the attached and entrapped water molecules. In this sense, this study has shown that several features of chitin whiskers can be assessed by choosing properly the average powder size of parent chitin.

## CHAPTER IV

### *N*-(2-hydroxy)-propyl-3-trimethylammonium, *O*-palmitoyl chitosan: Synthesis, physicochemical and biological properties

Original source: **International Journal of Biological Macromolecules**, Elsevier  
(SILVA, D. S.; FACCHINATTO, W. M. et al., 2021)

#### 3.4.1. Novel synthetic strategy for improving desirable applications

Many studies have been focused on the production of amphiphilic chitosan derivatives aiming to form self-assembled structures for the encapsulation and sustainable release of hydrophobic drugs (MOTIEI et al., 2017). In particular, a number of well-defined core-shell architectures have been proposed as micellar nanocarriers, in which the hydrophobic domains have improved the drug protection against degradation in physiological environments, whereas the presence of the hydrophilic domains successfully trick the immune system recognition, improving the drug residence time and preventing the rapid *in vivo* clearance (HUO et al., 2011; QU et al., 2009). Indeed, previous studies have demonstrated that attaching hydrophilic segments onto hydrophobically modified chitosan allowed the development of carriers exhibiting increased loading capacity that improved the drug stability (LI et al., 2009; WORAPHATPHADUNG et al., 2016).

The sustainable release performance and bioavailability of drug delivery systems is enhanced through the adhesion onto mucus layer or to epithelial tissues. This property has been related to high cell uptake and prolonged therapeutic effects from different administration routes, resulting in cost-effective treatment. Nevertheless, the residence time and drug distribution are limited by the transmucosal ability, affecting the drug absorption efficiency under adequate levels (DAS NEVES et al., 2011). Despite the relevance of non-specific hydrophobic/ hydrophilic interactions, the strong electrostatic attraction between negatively charged regions from mucin glycoproteins and epithelial surfaces with the positively charged external layer of polymeric systems is a major contribution to improve the adhesion (ANDREWS; LAVERTY; JONES, 2009; SOSNIK; DAS NEVES; SARMENTO, 2014). In this sense, the advantageous polycationic character of chitosan naturally induces its mucoadhesiveness (SOGIAS; WILLIAMS; KHUTORYANSKIY, 2008). However, due to its limited solubility, restricted to acidic media, further chemical modifications on chitosan have been proposed aiming to improve the potential for transmucosal applications, which justifies

the balance of amphiphilic character and charged surfaces for promising mucoadhesive materials.

Several chitosan derivatives (WAYS; LAU; KHUTORYANSKIY, 2018) have been successfully designed to enhance the mucoadhesiveness and permeability of lipophilic drug through intestine (PRABAHARAN; GONG, 2008), buccal (LANGOTH et al., 2006) and vaginal mucosa (SANDRI et al., 2004). Among those promising platforms, *N,N,N*-trimethyl chitosan (TMC) has received considerable attention due to the presence of quaternized amino groups, which have permanent positive charges, resulting in higher water-solubility and improved mucoadhesiveness as compared to unmodified chitosan (NAZAR et al., 2011; SNYMAN; HAMMAN; KOTZE, 2003). TMC derivatives have achieved successful results in the transport rate of drugs and proteins across Caco-2 cell monolayers by decreasing the transepithelial electrical resistance (TEER) (KOTZÉ et al., 1997) and were effective on cellular uptake of loaded nanoparticles (SAYIN et al., 2009). However, its cytotoxicity has been evaluated as straightly dependent on the average degree of quaternization ( $\overline{DQ}$ ), which expresses the average content of quaternized amino groups, and on the distribution of positive charges in the polymeric chains (JINTAPATTANAKIT et al., 2008; SAJOMSANG et al., 2009). Similarly, the water-soluble quaternized derivative named as hydroxypropyltrimethyl ammonium chloride chitosan (HACC) was evaluated regarding its biological properties as a promising cationic microbistatic agent, being effective against *S. aureus*, *E. coli* and *C. albicans* (QIN et al., 2004). The dependence of antibacterial and antifungal activities with  $\overline{DQ}$  has also been studied, showing that higher inhibition capacity was developed by the higher content of quaternized amino groups (PENG et al., 2010; SHAGDAROVA et al., 2019). According to these authors, the HACC completely inhibited the growth of mycelial fungi when  $\overline{DQ} = 53\%$  (SHAGDAROVA et al., 2019), while it was previously rated as slightly cytotoxic to osteogenic cells when  $\overline{DQ} = 44\%$  (PENG et al., 2010).

A recent study on the synthesis of *N*-substituted HACC, named as QCat, reported the influence of reactions conditions on the derivative characteristics and properties, showing that it developed full water-solubility at  $\overline{DQ} > 40.0\%$  (SANTOS; BUKZEM; CAMPANA-FILHO, 2016). These cationic derivatives of chitosan were blended with different amounts of poly( $\epsilon$ -caprolactone) and electrospun to yield nonwovens displaying different morphology and physicochemical properties according to the  $\overline{DQ}$ . Moreover, such nonwovens were non-cytotoxic toward neonatal human dermal fibroblast (HDFn) cells, except for that one composed by a highly quaternized cationic derivative ( $\overline{DQ} = 71.1\%$ ) (SANTOS et al., 2018).

Several studies have shown that hydrophobic derivatives of chitosan are suitable candidates for encapsulation of poorly water-soluble drugs targeted to cancer therapy (SHANMUGANATHAN et al., 2019). Accordingly, a recent study shown that the 3,6-*O,O'*-dimyristoylchitosan with degree of substitution ( $\overline{DS}$ ) ranging as 6 % - 12% was effective in improving the solubility of paclitaxel (SILVA et al., 2017b) and camptothecin (SILVA et al., 2017a), showing higher permeability on Caco-2 and HT29-MTX intestinal epithelial cells as compared to unmodified chitosan. Taking into account the physicochemical properties and biological activities of cationic and hydrophobic chitosan derivatives, an amphiphilic derivative, namely *N*-(2-hydroxy)-propyl-3-trimethylammonium, 3,6-*O,O'*-dimyristoyl chitosan, was used to encapsulate curcumin (SILVA et al., 2018). However, a detailed physicochemical and biological study has not been developed regarding the major effects on its hydrodynamics, mucoadhesiveness and cytotoxicity profile on variable degrees of quaternization.

In this context, the CHAPTER IV focus on the synthesis of positively-charged amphiphilic chitosan derivative, named *N*-(2-hydroxy)-propyl-3-trimethylammonium, *O*-palmitoyl chitosan (DPCat), in different reaction conditions to result in derivatives containing different contents of positive charges. This work focuses on the synthesis of DPCat and their structural characterization by using high resolution  $^1\text{H}$ , solid-state  $^{13}\text{C}/^{15}\text{N}$  NMR and FTIR spectroscopy. The polymers were characterized according to its mobile-part  $^1\text{H}$  signal decay profile acquired by TD-NMR relaxometry experiments (FACCHINATTO et al., 2020b), thermogravimetric profile (TGA) and wettability recorded by means of optical contact angle. The solution properties, such as water solubility, zeta potential, average size and critical aggregation concentration, are also discussed. The biological activities of derivatives were evaluated through mucoadhesiveness assessment, mucin interaction assays and cytotoxicity tests against healthy cell line Balb/C 3T3, human prostate cancer (DU145) and liver cancer (HepG2/C3A) cell lines.

### 3.4.2. *Materials and Methods*

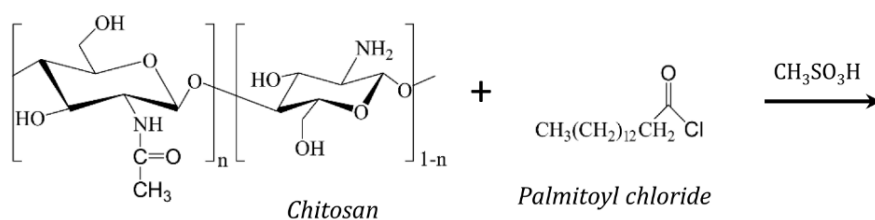
#### 3.4.2.1. *Synthesis of O-palmitoyl chitosan*

The *O*-palmitoyl chitosan derivative (DPCh) was synthesized by reacting Ch (ChC from CHAPTER I) with palmitoyl chloride in presence of  $\text{MeSO}_3\text{H}$  as previously reported (SILVA

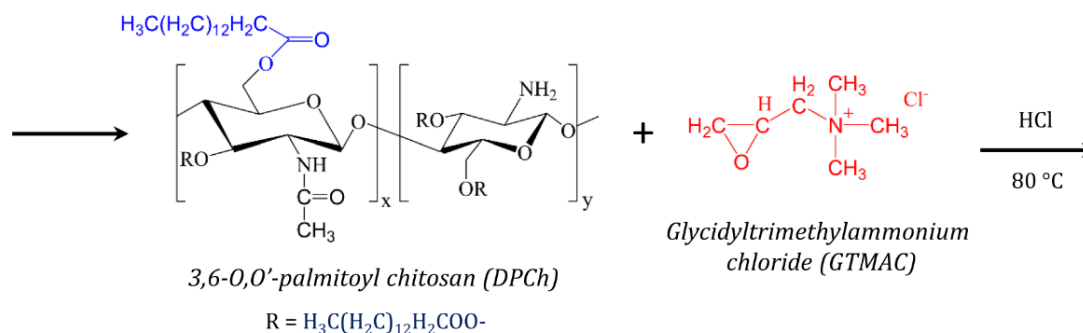
et al., 2017b). Briefly, 1.0 g of Ch sample was dissolved in 25.0 mL of MeSO<sub>3</sub>H upon stirring for 1 h at room temperature. Following, palmitoyl chloride was then added to Ch solution at molar ratio 13:1 and the reaction medium was kept under mechanical stirring for 1 h at room temperature. About 500 mL of distilled water at 4°C was added to the reaction medium and the resulting suspension was neutralized with aqueous NaHCO<sub>3</sub> 5 % (w/v), centrifuged, and the precipitate was thoroughly washed with distilled water. The product was submitted to Soxhlet-extraction for 12 h with chloroform, dried in a vacuum oven at 25 °C for 24 h and named as DPCh. The following description of the synthesis's steps used to produce the chitosan derivatives is schematically presented in Fig. 40.

Figure 40 – Schematic illustration of step-by-step synthesis of amphiphilic chitosan derivative.

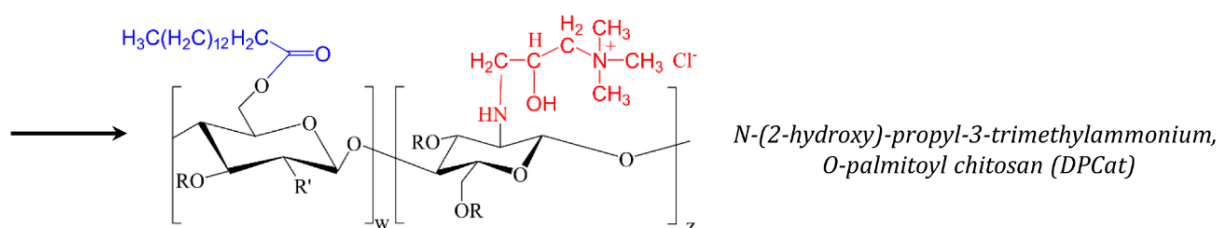
### 1<sup>st</sup> derivatization



### 2<sup>nd</sup> derivatization



### Positively charged amphiphilic chitosan derivative



Source: Own authorship

### 3.4.2.2. *Synthesis of N-(2-hydroxy)-propyl-3-trimethylammonium, O-palmitoyl chitosan*

The quaternization of 3,6-*O,O'*-dipalmitoyl chitosan (DPCh) was carried out based on the method proposed by RUIHUA et al. (2012). In brief, 1.0 g of DPCh was dissolved in 60 mL of aqueous acetic acid 1 % (v/v) and GTMAC was added dropwise to the polymer solution. Two molar ratios of GTMAC:DPCh were employed, namely 3.4:1 to 5.7:1, to result in DPCat derivatives possessing different average degrees of quaternization. The reaction was carried out for 8 h at 80 °C and then an excess of acetone was added to the reaction medium to result in the precipitation of the derivative, which was filtered and then submitted to Soxhlet-extraction for 6 h with acetone, as described by FACCHINATTO et al. (2016). The resulting DPCat derivatives (Fig. 40) were dried at 30 °C for 12 h and stored under reduced humidity until further use.

### 3.4.3. *Characterizations*

#### 3.4.3.1. *Fourier transform infrared (FTIR) spectroscopy*

Infrared spectra were recorded on an IRAffinity-1 Shimadzu® spectrometer. The powdered samples and KBr were previously dried in vacuum over 60 °C for 8 h, then mixed at 1:100 of mass ratio (sample:KBr) and compressed into pellet form. The IR spectra were acquired in the range of 4000–400 cm<sup>-1</sup> by accumulating at least 32 scans with resolution of 4 cm<sup>-1</sup>.

#### 3.4.3.2. *High-resolution NMR: solution <sup>1</sup>H, solid-state <sup>13</sup>C and <sup>15</sup>N CPMAS*

The <sup>1</sup>H NMR spectra were acquired using a Bruker® Avance III spectrometer (ν = 600 MHz for <sup>1</sup>H nuclei), as already described in CHAPTER I. The average degree of substitution ( $\overline{DS}$ ) of DPCh was calculated according to Eq. (9) (SILVA et al., 2017b):

$$\overline{DS} (\%) = \left( \frac{I_{CH_3}/3}{I_{H_2-H_6}/6} \right) \times 100 \quad (9)$$

where,  $I_{CH_3}$  is the signal integral of methyl hydrogens assigned to palmitoyl substituent ( $\approx 0.8$  ppm), while  $I_{H_2-H_6}$  is the signal integral of hydrogens from glucopyranose ring. The average degree of quaternization ( $\overline{DQ}$ ) of DPCat was calculated according to Eq. (10) (DESBRIÈRES; MARTINEZ; RINAUDO, 1996).

$$\overline{DQ} (\%) = \left( \frac{I_{H1'}}{I_{H1'} + I_{H1}} \right) \times 100 \quad (10)$$

where,  $I_{H1'}$  is the signal integral of the anomeric hydrogen from *N*-substituted *GlcN* units ( $\approx 5.5$  ppm) while  $I_{H1}$  is the signal integral of the anomeric hydrogen bonded to unsubstituted *GlcN* units ( $\approx 5.0$  ppm).

Solid-state  $^{13}\text{C}$  and  $^{15}\text{N}$  CPMAS experiments were performed on a Bruker<sup>®</sup> Avance 400 spectrometer using a Bruker 4-mm magical angle spinning (MAS) at 12 kHz in a double-resonance probe-head  $\nu = 100.5$  MHz ( $^{13}\text{C}$ ), 40.5 MHz ( $^{15}\text{N}$ ) and 400.0 MHz ( $^1\text{H}$ ). The experiments were performed using  $90^\circ$  pulse of of 4.0  $\mu\text{s}$  ( $^{13}\text{C}$ ), 5.5  $\mu\text{s}$  ( $^{15}\text{N}$ ) and 2.5  $\mu\text{s}$  ( $^1\text{H}$ ) were applied for the spin-lock cross-polarization transfer, with last delay of 5.0 s, 3.0 ms of contact time, 70 kHz for Spinal-16  $^1\text{H}$  (SINHA et al., 2005) decoupling and recycle delay of 5 s. The chemical shift of  $^{13}\text{C}$  and  $^{15}\text{N}$  CPMAS spectra were calibrated with the external standards hexamethylbenzene (HMB) and glycine (Gly), respectively. The  $\overline{DQ}$  of DPCat was estimated by fitting Voight functions on  $^{15}\text{N}$  spectra, using PeakFit<sup>TM</sup> (v. 4.12) software for peak deconvolution processing.

### 3.4.3.3. Conductometric titration

The average degree of quaternization ( $\overline{DQ}$ ) of DPCat was also determined by dosing the  $\text{Cl}^-$  counter-ions titrated with standardized 0.017 mol L<sup>-1</sup> aqueous  $\text{AgNO}_3$  solution (CHO et al., 2006). Thus, 0.1 g of DPCat sample was dissolved in 100 mL of deionized water and the solution conductivity was measured using a Handylab LF1 conductivimeter (Schott- Gerate<sup>®</sup>, Germany) as function of  $\text{AgNO}_3$  solution added at  $25 \pm 0.01$  °C. The  $\overline{DQ}$  of DPCat was calculated from the titration curves according to Eq. (11) (SANTOS; BUKZEM; CAMPANA-FILHO, 2016).

$$\overline{DQ} (\%) = \left( \frac{1.7 \times 10^{-5} V_{AgNO_3}}{((m - (1.7 \times 10^{-5} V_{AgNO_3} \times 113.0) / (203.0 \times \overline{DA}) + (161.0 \times (1 - \overline{DA}))) (1 - \overline{DA}))} \right) \times 100 \quad (11)$$

where,  $V_{AgNO_3}$  (mL) is the volume of standard solution added to reach the equivalent point;  $m$  (g) is the amount of dried DPCat; 113.0, 203.0 and 161.0  $\text{g mol}^{-1}$  are the molar mass of GTMAC, *GlcNAc* and *GlcN* units, respectively. The  $\overline{DQ}$  obtained through this method considers the previous determination of  $\overline{DA}$  from  $^1\text{H NMR}$  spectrum.

#### 3.4.3.4. Aqueous solubility

The aqueous solubility of Ch and derivatives as function of pH was estimated from transmittance (T%) measurements of polymer solution using a UV/Vis spectrophotometer (Shimadzu<sup>®</sup>, UV 3600) at  $\lambda = 600$  nm (FACCHINATTO et al., 2019; KUBOTA et al., 2000). Thus, the samples were dissolved in HCl 0.1  $\text{mol L}^{-1}$  to result in  $C_p = 1.0$   $\text{mg mL}^{-1}$  and the transmittance (T%) was sequentially recorded after the dropwise addition of NaOH 0.1  $\text{mol L}^{-1}$  solution. A given sample was considered insoluble when  $T (\%) < 70\%$ , taking the HCl solution transmittance as reference.

#### 3.4.3.5. Optical contact angle measurements

The contact angles measurements were conducted applying water droplets with a micro syringe attached to the apparatus OCA15, Dataphysics Instruments<sup>®</sup> Co. Ltd, Germany, on the surface of the polymers comprised into pellets (TABRIZ et al., 2019). Thus, the hydrophilicity/hydrophobicity nature of the polymers was analyzed through a high-performance CCD camera that captured the 1 to 3 seconds as soon as the water droplet ( $\sim 5$   $\mu\text{L}$ ) was placed on the surface of the polymeric substrate. The average of different contact angles was calculated by means of both sides of the drop.

#### 3.4.3.6. Critical aggregation concentration (CAC)

The CAC of DPCh and DPCat derivatives was determined on a Consort<sup>®</sup> C863 conductometer (Spain), through measurements of solution conductivity in acetic acid 0.1  $\text{mol L}^{-1}$  (KHAN; SHAH, 2008; SILVA et al., 2018). Thus, the conductivity of these polymer

solutions was recorded as function of concentration  $C_p$  ranged from  $10^{-6}$  mg mL<sup>-1</sup> to 1.0 mg mL<sup>-1</sup> under continuous stirring at 25 °C.

#### 3.4.3.7. *Dynamic and electrophoretic light scattering (DLS and ELS)*

The average surface charge and hydrodynamic size of Ch and derivatives were recorded using a Zetasizer Nano ZS (Malvern Instruments®, Worcestershire, UK) equipped with laser beam of He-Ne at 633 nm through measurements of zeta potential and dynamic light scattering (DLS), respectively. The samples were dissolved in HCl 0.1 mol L<sup>-1</sup> to result in  $C_p = 1.0$  mg mL<sup>-1</sup> and then diluted 1 to 100 times in NaCl  $10^{-2}$  mol L<sup>-1</sup> (FACCHINATTO, 2016). The pH of the polymer solution was adjusted with NaOH 0.1 mol L<sup>-1</sup> solution added dropwise. The acquisition of data was automatically repeated multiple times until reach a stable profile upon the pH variation.

#### 3.4.3.8. *Mucoadhesion assessment*

The mucoadhesiveness of Ch and derivatives was evaluated using porcine gastric mucin (PGM) as the mucosal model (BONI et al., 2018) in a TA-XT plus texture analyser (Stable Micro Systems, Surrey, UK). The biological tissue was carefully cleaned, cut, hydrated with phosphate buffer (pH 7.4) at 37 °C and fastened to the analyser platform. The samples were attached to the upper movable cylindrical probe (diameter 10.0 mm), using double side adhesive tape (Scotch®, 3M™). The measurement was triggered to begin when the upper probe started to record the resistance force of mucosal tissue. The contact was kept for 120 s with no force applied during this time, then the detachment force (N) was registered by raising the probe at constant speed of 0.5 mm s<sup>-1</sup>.

#### 3.4.3.9. *In vitro mucin interaction assay*

The interaction between the mucin surface and samples at  $C_p$  values above CAC was performed under healthy and tumour conditions of simulated gastrointestinal fluid, based on previous study (ANDREANI et al., 2015). Thus, the PGM was dispersed in aqueous solutions and the pH was adjusted through dropwise additions of HCl 0.1 mol L<sup>-1</sup> and NaOH 0.1 mol L<sup>-1</sup>. Following, 300 µL of DPCat solutions (pH = 7.0) were added to 900 µL of PGM solution

with stock solution of 100, 150 and 250  $\mu\text{g mL}^{-1}$ , which was homogenized and incubated for 1 h at 37 °C. The average hydrodynamic size and zeta potential of the polymers were determined in Zetasizer Nano ZS (Malvern Instruments<sup>®</sup>, Worcestershire, UK) and the results were compared to the condition without PGM. The analyses were performed in triplicate for each polymer and concentration.

#### 3.4.3.10. *In vitro* cytotoxicity assay

Human prostate cancer (DU145), liver cancer (HepG2/C3A) and mouse fibroblast (Balb/C 3T3 clone A31) cell lines were cultivated in flasks at 5% CO<sub>2</sub> atmosphere incubator and 90% humidity using DMEM medium (Cultilab, Campinas, Brazil), supplemented with 3.5 mg mL<sup>-1</sup> of glucose, 1.5 mg mL<sup>-1</sup> of NaHCO<sub>3</sub>, 10% (v/v) of FBS and 1% (v/v) of penicillin/streptomycin solution (SAIDEL et al., 2017). Cell passage was performed using a trypsin/EDTA 1% (m/v) solution and the resulted pellet was formed by centrifugation and resuspended in the medium. Cell viability experiments were carried out using MTT colorimetric assay (SAIDEL et al., 2017). Briefly, 100  $\mu\text{L}$  of cell suspension ( $10^5$  cells mL<sup>-1</sup>) was transferred to 96-wells plates and incubated for 24 h in 5% CO<sub>2</sub> atmosphere incubator and 90% humidity. Then, the medium was removed and the DPCat samples were added at concentration  $C_p = 15, 150$  and  $1,500 \mu\text{g mL}^{-1}$  and incubated for 72 h. After incubation, the supernatant was substituted by MTT solution ( $1.0 \text{ mg mL}^{-1}$ ) and cells were incubated for 3 h. The MTT was removed and 100  $\mu\text{L}$  of DMSO was added for solubilization. The absorbance (570 nm) was measured using a plate reader (Synergy HT Multi-Mode Microplate Reader, BioTek<sup>®</sup> Instruments). Culture medium with DMSO 0.5 % (v/v) was used as negative control, while YM155 ( $1.0 \mu\text{mol L}^{-1}$ ) was used as positive control. Half-maximal cytotoxic concentration ( $CC_{50}$ ) values were calculated by log-logistic regression of viability vs. concentration data using Prism 8 (GraphPad, San Diego, CA, USA). Two independent assays were conducted in quintuplicate.

#### 3.4.3.11. *Statistical analysis*

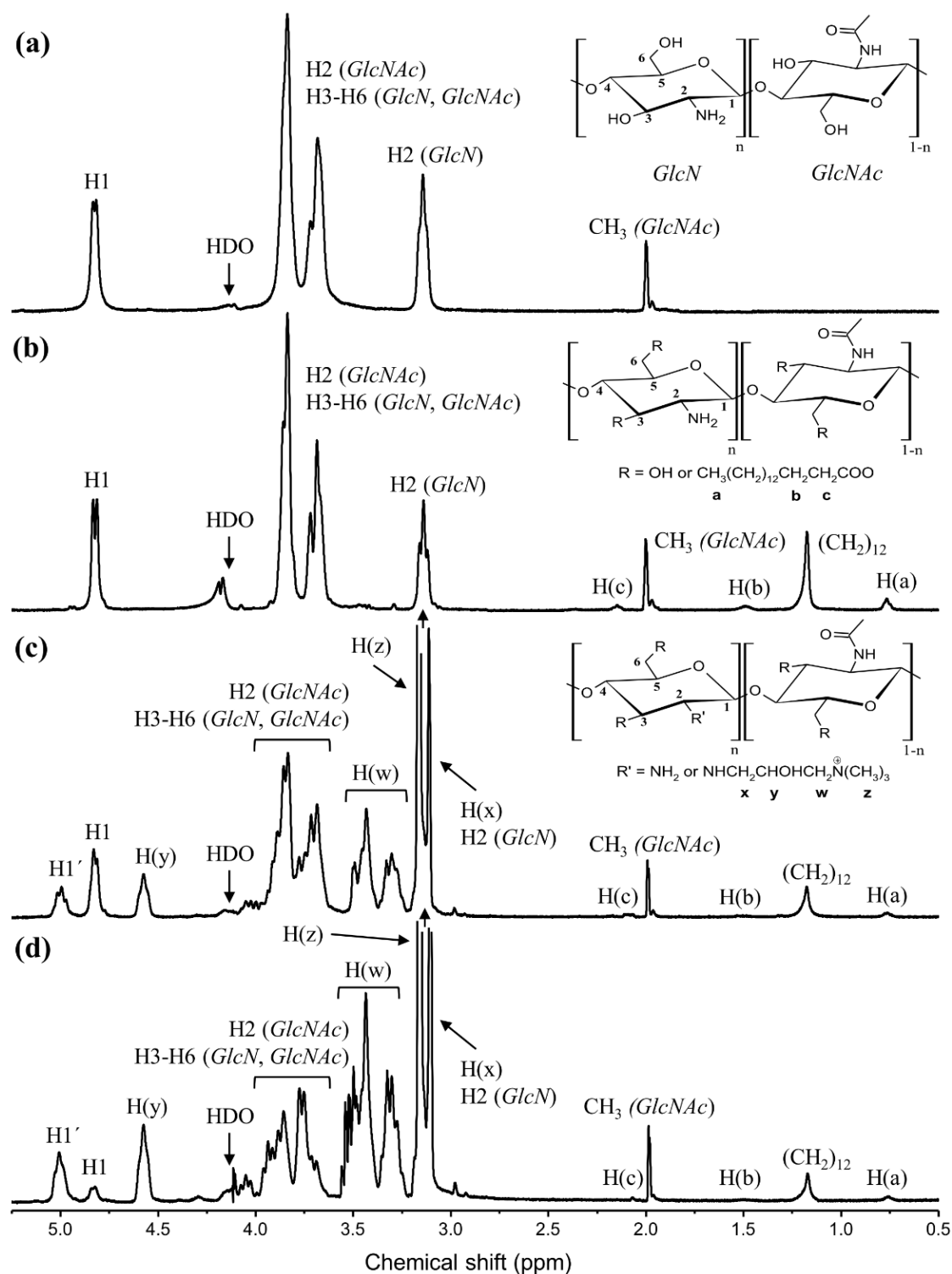
The experiments were performed in triplicate and the results were expressed as mean  $\pm$  standard deviation (SD). One-way ANOVA analysis was carried out and the significance level of different groups was set at probability of  $p < 0.05$ , determined by using Tukey's comparison test on GraphPadPrism<sup>™</sup> software (San Diego, CA, USA).

### 3.4.4. Results and Discussion

#### 3.4.4.1. Spectroscopy and relaxometry characterization

The structural modifications resulting from the acylation of Ch to prepare DPCh and the quaternization of DPCh, which produced DPCat, are evidenced by comparing  $^1\text{H}$  NMR spectra of Ch (Fig. 41a) and its derivatives (Fig. 41b-d). The  $^1\text{H}$  NMR spectrum of Ch exhibits signals at 2.0 and 3.2 ppm, which are assigned to methyl hydrogens of GlcNAc units and to the hydrogen H2 of GlcN units, respectively, whereas the overlapped signals in the interval 3.5-4.0 ppm are attributed to hydrogens H2 of GlcNAc and H3-H6 from GlcNAc and GlcN units. The signal at 4.8 ppm is related to the hydrogen bonded to the anomeric carbon C1 of GlcN and, due to the low average degree of acetylation ( $\overline{DA} \approx 5.0\%$ ), the H1 of GlcNAc is not observed (FACCHINATTO et al., 2019).

The  $^1\text{H}$  NMR spectrum of DPCh (Fig. 41b) shows additional characteristic signals related to palmitoyl moieties at 1.2, 1.5 and 2.1 ppm corresponding the overlapped hydrogen signals of methylene carbons and two down-field shifted signals also assigned to methylene, respectively (BADAWY et al., 2005). The signal at 0.8 ppm, corresponding to the hydrogens of terminal methyl group, was used to determine the average degree of substitution ( $\overline{DS} \approx 12.0\%$ ). The data show that the insertion of palmitoyl groups occurred mostly onto hydroxyl groups located at C3 and C6 carbons of the chitosan units, evidencing the predominant occurrence of *O*-acylation (GUTHRIE, 1978). Such predominance is also indirectly confirmed by the negligible hydrogen signal observed at 4.9 ppm, which is related to a modified chemical environment nearby C1 of substituted GlcN units (DESBRIÈRES; MARTINEZ; RINAUDO, 1996). It is important to notice that even occurring partial *N*-acylation at short extension, it doesn't cause meaningful disturbance on the final expected properties of this chitosan derivative, once the overall substituted sites still leads to a low  $\overline{DS}$ . In addition, it seems that even being possible, it is highly unlikely that a given GlcN residue would be favorable to become a reactive site for a second *O*-substitution instead of another one completely available, considering the steric hindrance from palmitoyl moieties and the fundamental thermodynamic issues that drives to the major formation of more stable products. In this sense, we agree that would be better to describe such substitution simply as *O*-palmitoyl.

Figure 41 -  $^1\text{H}$  NMR spectra of Ch (a), DPCh (b), DPCat35 (c) and DPCat80 (d) in  $\text{D}_2\text{O}/\text{HCl}$  1% (v/v) at  $85^\circ\text{C}$ .

The quaternization step is evidenced mainly by the occurrence of the additional signal in  $^1\text{H}$  NMR spectra (Fig. 1c-d) of DPCat samples at 3.3 ppm, which is referred to methylene hydrogens of secondary amino group ( $-\text{NHCH}_2-$ ), confirming that the reaction occurred at the amino groups. Additionally, the quaternization is also probed through the sharp signal at 3.2 ppm

that is related to methyl hydrogens of quaternary ammonium group,  $-N^+(\text{CH}_3)_3$ , which are overlapped with H2 of GlcN. The hydrogen signal of the anomeric carbon (C1) changed upon the chemical modifications at C2, which led to the arising signals at 5.0 and 4.6 ppm of substituted GlcN units (Fig. 41c-d) (FACCHINATTO et al., 2019; SANTOS; BUKZEM; CAMPANA-FILHO, 2016). The average degree of quaternization ( $\overline{DQ}$ ) was determined from  $^1\text{H}$  NMR spectra and assuming that the *N*-substitution predominated due to the higher nucleophilicity of amino groups in acid medium, preventing *O*-substitution (RUIHUA et al., 2012) and then resulting in  $\overline{DQ} \approx 35.0\%$  and  $\overline{DQ} \approx 80.0\%$ . These values of  $\overline{DQ}$  were used to identify the samples as DPCat35 (Fig. 41c) and DPCat80 (Fig. 41d). Similar  $\overline{DQ}$  values were found by carrying out the conductometric titration of DPCat samples (Table 11).

Table 11 - Average degrees of acetylation ( $\overline{DA}$ ), substitution ( $\overline{DS}$ ) and quaternization ( $\overline{DQ}$ ) determined by  $^1\text{H}$  NMR  $\overline{DQ}$  was also determined by  $^{15}\text{N}$  CPMAS and conductometric titration.

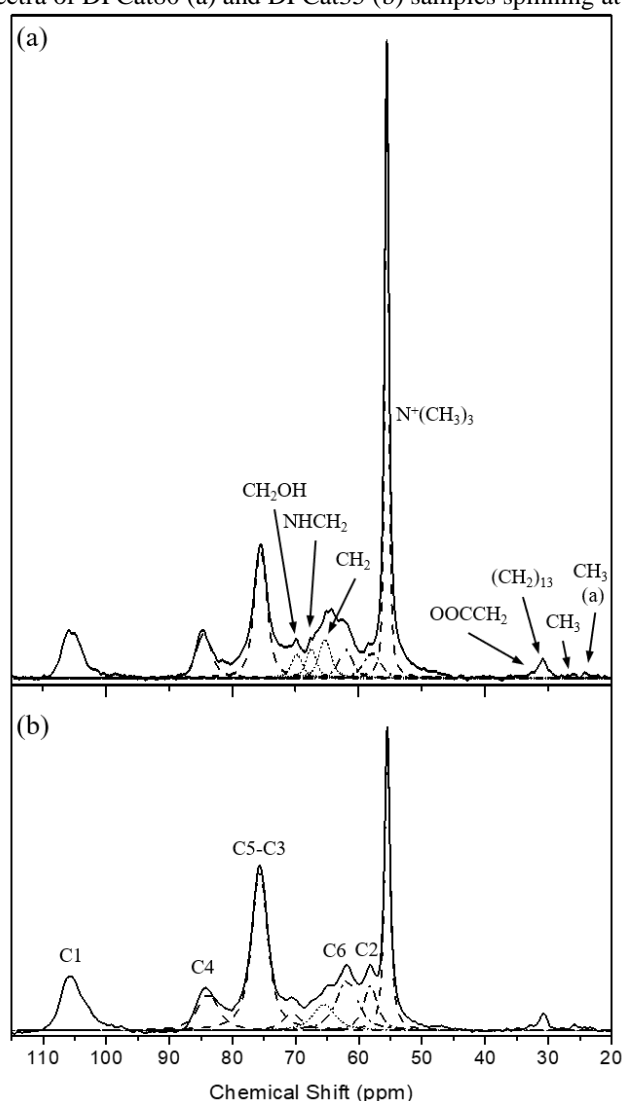
Samples	$\overline{DA}$ (%)	$\overline{DS}$ (%)	$\overline{DQ}$ (%)			CAC $\times 10^{-6}$ (mg mL $^{-1}$ )
			$^1\text{H}$ NMR	$^{15}\text{N}$ CPMAS	Conductometric titration	
Ch	5.0	-	-	-	-	n.d.
DPCh	5.0	12.0	-	-	-	25,000
DPCat35	5.0	12.0	35.0	41.2	36.5	6.8
DPCat80	5.0	12.0	80.0	70.7	78.0	2.6

The  $^{13}\text{C}$  CPMAS spectra of DPCat samples are shown in Fig. 42. As observed on  $^1\text{H}$  NMR spectra, it is also possible to infer, using the  $^{13}\text{C}$  CPMAS spectra, that the chitosan backbone is preserved after the quaternization of DPCh with significant modification in the carbon resonance signals at 73-50 ppm. However, mainly because of the signal overlapping and owing to the low signal-to-noise ratio of carbonyl signal (SILVA et al., 2017a), the quantifications are in some way affected in this experiment. Indeed, once the methyl groups from acetamido, palmitoyl and methyl groups from  $-N^+(\text{CH}_3)_3$  substituents are upfield shifted and also completely overlapped in  $^{13}\text{C}$  CPMAS spectrum (Fig. 42) the quantification of each group to the structure of DPCat derivatives is at least biased. Hence, we considered that even applying the deconvolution procedure, the proper distinction of every single contribution and quantification of  $\overline{DA}$ ,  $\overline{DS}$  and  $\overline{DQ}$  would be doubtful, thus it was not performed.

The sharp and intense signal changes assigned to methyl carbons on  $-N^+(\text{CH}_3)_3$  groups at 56 ppm are related to the amount and highly mobile quaternized groups, but also to shorter relaxation times ( $T_1$ ) that leads to a less efficient cross polarization transfer between  $^1\text{H}$  and  $^{13}\text{C}$

nuclei of methyl groups. In this case, during the recovery of magnetization, the higher mobility of these methyl groups induces a significant decrease of dipolar coupling with the surrounding environment (FACCHINATTO et al., 2020a, 2020b). This spin interaction dependence is the also the main responsible for signal broadening, as well as the local chain packing that is affected by the conformation and overall morphology of the polymer (CARDOZO et al., 2019; FACCHINATTO et al., 2020a).

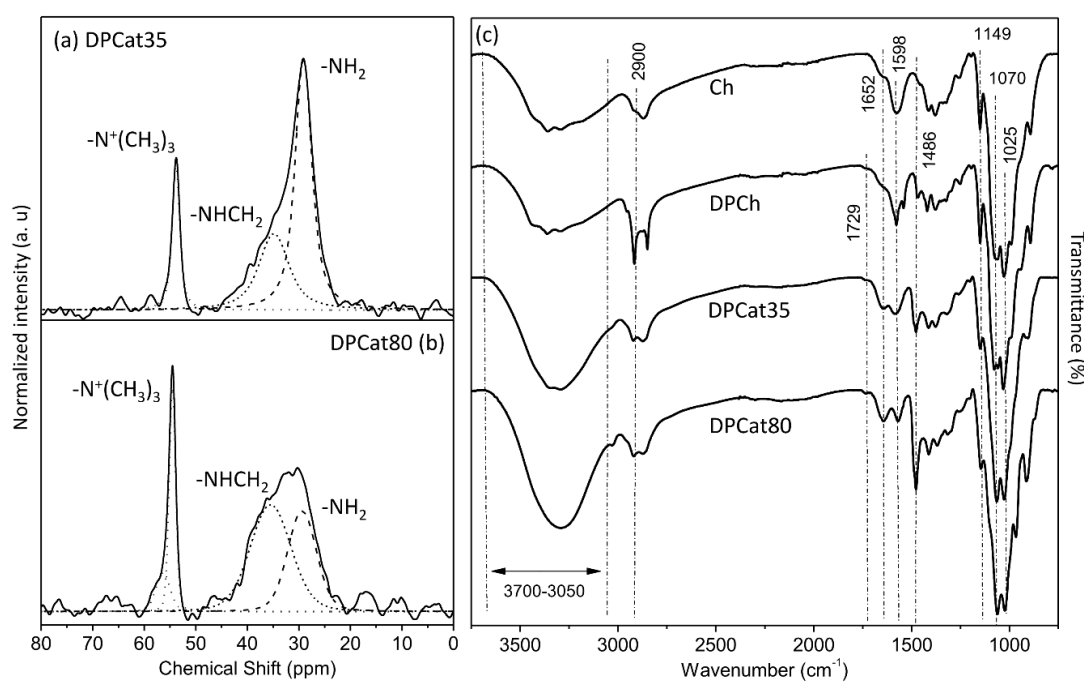
Figure 42 -  $^{13}\text{C}$  CPMAS spectra of DPCat80 (a) and DPCat35 (b) samples spinning at 12 kHz.



The  $^{15}\text{N}$  CPMAS was also performed to DPCat derivatives. Each  $^{15}\text{N}$  NMR spectrum, presented on Fig. 43a-b, shows mainly three nitrogen resonance signals, considering that the nitrogen signal of acetamido moieties was not detected. As observed in Fig. 42, these spectra show a similar tendency assigned to nitrogen at  $-\text{N}^+(\text{CH}_3)_3$  group, with weak dipolar coupling also due to the higher mobility of such group (SHON et al., 1991), compared do  $-\text{NH}_2$  and -

NHCH<sub>2</sub>-, that consequently leads to a sharper signal at 55 ppm. As -N<sup>+</sup>(CH<sub>3</sub>)<sub>3</sub> has no protons directly bonded to <sup>15</sup>N nuclei (weak dipolar interaction), and due to the high mobility of methyl groups directly linked, the magnetization recovery is straightly affected, making the cross-polarization less efficient. Differently from the higher polarization transfer found in C-H bonding of -N<sup>+</sup>(CH<sub>3</sub>)<sub>3</sub> as already mentioned, such interaction through N-C bonding allowed a better approach of  $\overline{DQ}$  (Table 11), considering the relative integral of -N<sup>+</sup>(CH<sub>3</sub>)<sub>3</sub> estimated through the deconvolution procedure from the overlapped signals of -NHCH<sub>2</sub> and -NH<sub>2</sub> at 50-20 ppm. As the gyromagnetic ratio value of <sup>15</sup>N nuclei is considerably lower than <sup>13</sup>C ( $\gamma_{15N} \ll \gamma_{13C}$ ), the signal assigned to the <sup>15</sup>N nuclei from acetamido groups, which comprises the lowest <sup>15</sup>N nuclei predominance, was underestimated because the one achieved similar order of magnitude of the noise arising from the spectrum baseline. However, and as indicated in Table 11 and Fig. 43a-b, the other <sup>15</sup>N nuclei are clearly distinguishable and were quantified applying the deconvolution procedure. One should point out that even being able to record the NH<sub>2</sub> signal from GlcN, the content of this group is straightly related to the extension of *N*-substitution, *i.e.* presence of -N<sup>+</sup>(CH<sub>3</sub>)<sub>3</sub> and NHCH<sub>2</sub> segments, and the  $\overline{DQ}$  was only estimated because we considered the  $\overline{DA}$  recorded from <sup>1</sup>H NMR spectrum. Therefore, the reaction conditions explored to introduce the cationic substituents into the DPCh chains not only favored the formation of a secondary amine, but almost exclusively led to *N*-substitution.

Figure 43 - <sup>15</sup>N CPMAS spectra of DPCat35 (a) and DPCat80 (b) samples spinning at 12 kHz; FTIR spectra of Ch and derivatives (c).



The FTIR spectra of chitosan and derivatives (Fig. 43c) exhibited several bands in common such as the intense and broad band at 3700-3050  $\text{cm}^{-1}$  assigned to the axial stretching of hydroxyl and amine groups, the weak band at 2900-2800  $\text{cm}^{-1}$  related to methyl and methylene symmetric and asymmetric stretchings (CRUZ et al., 2013) and the bands centred at 1129, 1070 and 1025  $\text{cm}^{-1}$  corresponding to angular deformation and stretching of C-O bending, mainly from GlcN units (BRUGNEROTTO et al., 2001). The low intensity band at 1729  $\text{cm}^{-1}$  in DPCh and DPCat spectra is attributed to axial deformation of carbonyl ester from *O*-acyl substituent (SILVA et al., 2017b). The sharp band at 1486  $\text{cm}^{-1}$  in the spectra of the DPCat is associated to C-H bending of  $-\text{N}^+(\text{CH}_3)_3$  group (CHO et al., 2006), and its relative intensity is in agreement with  $\overline{DQ}$  values (Table 11) as its contribution to the spectrum is higher in the one from DPCat80 as compared to DPCat35 spectrum. Significant modifications regarding the band at 1598  $\text{cm}^{-1}$  assigned to N-H bending of primary amine and at 1652  $\text{cm}^{-1}$ , from C=O stretching of secondary amine, are observed in the spectra of the DPCat derivatives. Thus, the relatively higher intensity of the former band in the spectra DPCat35 compared to Ch and DPCh confirms the conversion of a primary to a secondary amine due to the occurrence of *N*-substitution (SILVA et al., 2018; XIAO et al., 2012). Indeed, no evidence of chemical modifications at hydroxyl groups was found, which is confirmed by the occurrence of characteristic bands in the interval 1160  $\text{cm}^{-1}$  to 1120  $\text{cm}^{-1}$  (HUANG et al., 2014; SANTOS; BUKZEM; CAMPANA-FILHO, 2016).

The main dynamic behavior of the polymers was also assessed by analyzing  $^1\text{H}$  NMR signal decay profiles (Fig. 43a), similarly to the procedure used in CHAPTER II and III. In brief, due to the sensitivity of dipolar interactions with respect to the spin dynamics of the polymeric side-chains and backbone in solid-state, each curve can be decomposed into a faster decay (tenths of microseconds) related to the rigid components with stronger dipolar interactions, and longer decay from chemical segments of higher mobility. Such differences ascribed in the whole signal decay profile have been applied to evaluate the semicrystallinity of polymers (MAUS; HERTLEIN; SAALWÄCHTER, 2006), and to estimate the content of certain mobile molecular segments (CLEEMPUT et al., 1995). The mobile-part signal of  $^1\text{H}$  NMR decay profile is mainly attributed to the methyl hydrogens in solid-state, which consequently leads to lesser heteronuclear dipolar coupling with the surrounding chemical environment (METZ; ZILIOX; SMITH, 1996). In this sense, for chitosan and derivatives, the observed  $^1\text{H}$  NMR signal decay can be directly assigned to methyl groups of GlcNAc and to the palmitoyl and trimethylammonium substituents of DPCh and DPCat, respectively (FACCHINATTO et al., 2020b). Taking into account the relative content of methyl groups in

each polymeric structure, the mobile-part signal ( $T_{2m}$ ) listed in Table 12 was proportional to  $\overline{DA}$ ,  $\overline{DS}$  and  $\overline{DQ}$ , showing higher contribution for increasing content of substituents that possess methyl groups. The rigid-part signal ( $T_{2r}$ ) and the shape parameter ( $v_a$ ) were nearly constant, as observed for other polymeric structures (MAUS; HERTLEIN; SAALWÄCHTER, 2006) and for chitosan with variable  $\overline{DA}$  (FACCHINATTO et al., 2020b), except for DPCat80 derivative that featured an unusually higher value of  $T_{2r}$ . The mobile fraction parameter,  $f_m$  showed an increasing trend, although quantitative assessment of  $\overline{DA}$ ,  $\overline{DS}$  and  $\overline{DQ}$  was not possible because the estimation of local  $^1\text{H}$  density was distorted due to the echo acquisition (MAUS; HERTLEIN; SAALWÄCHTER, 2006).

Figure 44 –  $^1\text{H}$  NMR signal decay profiles recorded by MSEFID pulse sequence (a), thermogravimetric and (b) and DTG curves of Ch, DPCh, DPCat35 and DPCat80 (c).

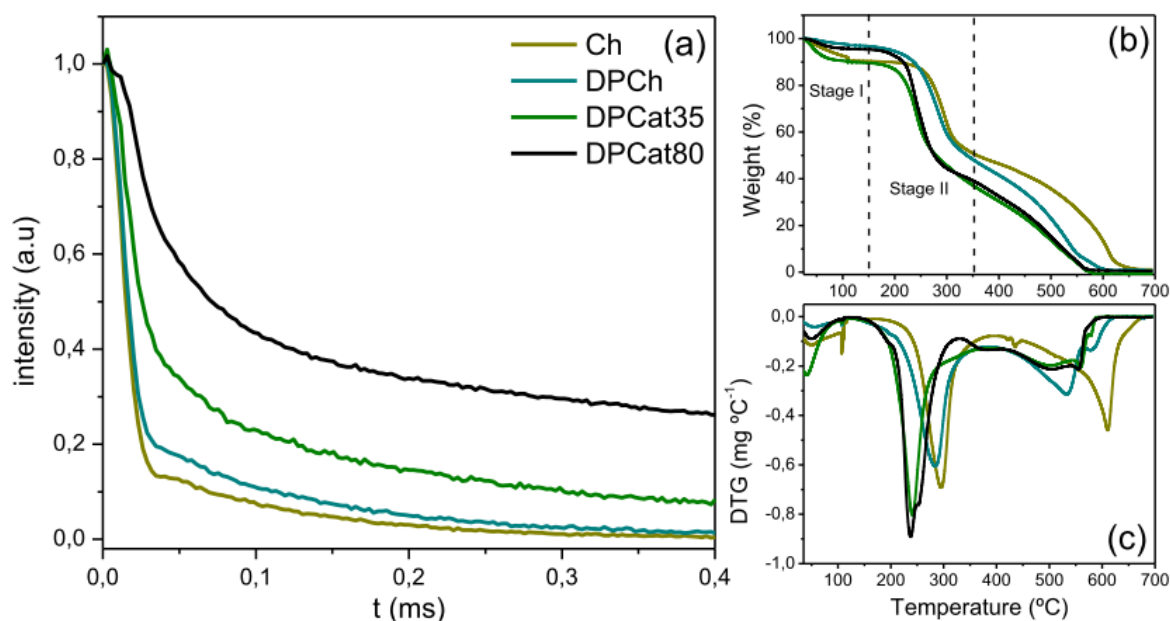


Table 12 - Rigid/mobile components described as  $T_{2r}$  and  $T_{2m}$ , respectively, the mobile fraction parameter ( $f_m$ ) and shape parameter ( $v_a$ ) and the weight losses (WL) related to different degradation steps of the polymers.

Samples	$^1\text{H}$ NMR signal decay				Stage I	Stage II	
	$T_{2r}^a$ ( $\mu\text{s}$ )	$T_{2m}^a$ ( $\mu\text{s}$ )	$v_m^a$	$f_m^a$	(25-150 °C)	(150-350 °C)	
					WL <sup>b</sup> (%)	$T_{onset}^c$ (°C)	WL <sup>d</sup> (%)
Ch	$16.4 \pm 0.1$	$130 \pm 3$	$1.18 \pm 0.03$	$9.6 \pm 0.5$	9.3	261.8	42.2
DPCh	$17.3 \pm 0.1$	$133 \pm 3$	$1.00 \pm 0.02$	$18 \pm 1$	2.7	238.7	44.8
DPCat35	$23.9 \pm 0.2$	$247 \pm 6$	$1.00 \pm 0.02$	$54 \pm 2$	9.8	216.9	26.5
DPCat80	$40.9 \pm 0.8$	$638 \pm 13$	$1.00 \pm 0.02$	$73 \pm 4$	3.8	219.3	35.4

<sup>a</sup> Calculated parameters from  $^1\text{H}$  NMR signal decay;

<sup>b</sup> Weight loss (WL) recorded from stage I assigned in the thermogravimetric response curve

<sup>c</sup> Onset temperature ( $T_{onset}$ ) referred to the maximum heat before polymeric chains cleavage;

<sup>d</sup> Weight loss (WL) recorded from stage II assigned in the thermogravimetric response curve.

Two different stages of temperature-dependent weight loss (WL%), namely Stage I and Stage II (Table 12) could be observed in the response TG curve (Figure 44b-c). The Stage I is attributed to weakly adsorbed water, while the larger weight loss on the Stage II is likely due to the occurrence of oxidative reactions and consequent elimination of volatiles. Thermal stability ( $T_{onset}$ ) successively decreased from chitosan to DPCat derivatives (Table 12). Indeed, as usually observed for other chemically-modified chitosans (FACCHINATTO et al., 2019; SANTOS; BUKZEM; CAMPANA-FILHO, 2016), for the successful binding be achieved on the reactive sites of chitosan, its necessary to cause an intersheet disruption, which induce to loss the former stability and compactness held by the hydrogen bonds network. The interchain long-range ordering is severely reduced, allowing the main and side chains to quicky response to furnished heat, once the faster chain motion is consequence of higher mobility freedom on lesser compact domains. Hence, as observed on Stage II (Figure 44b-c), such faster motion leads to an earlier cleavage and decomposition of main and side chains, markedly on lower  $T_{onset}$  (Table 12) as compared to unmodified chitosan. In this sense, it should be pointed out that the decrease of thermal stability on chitosan derivatives is straightly related to the intra- and interchain interactions.

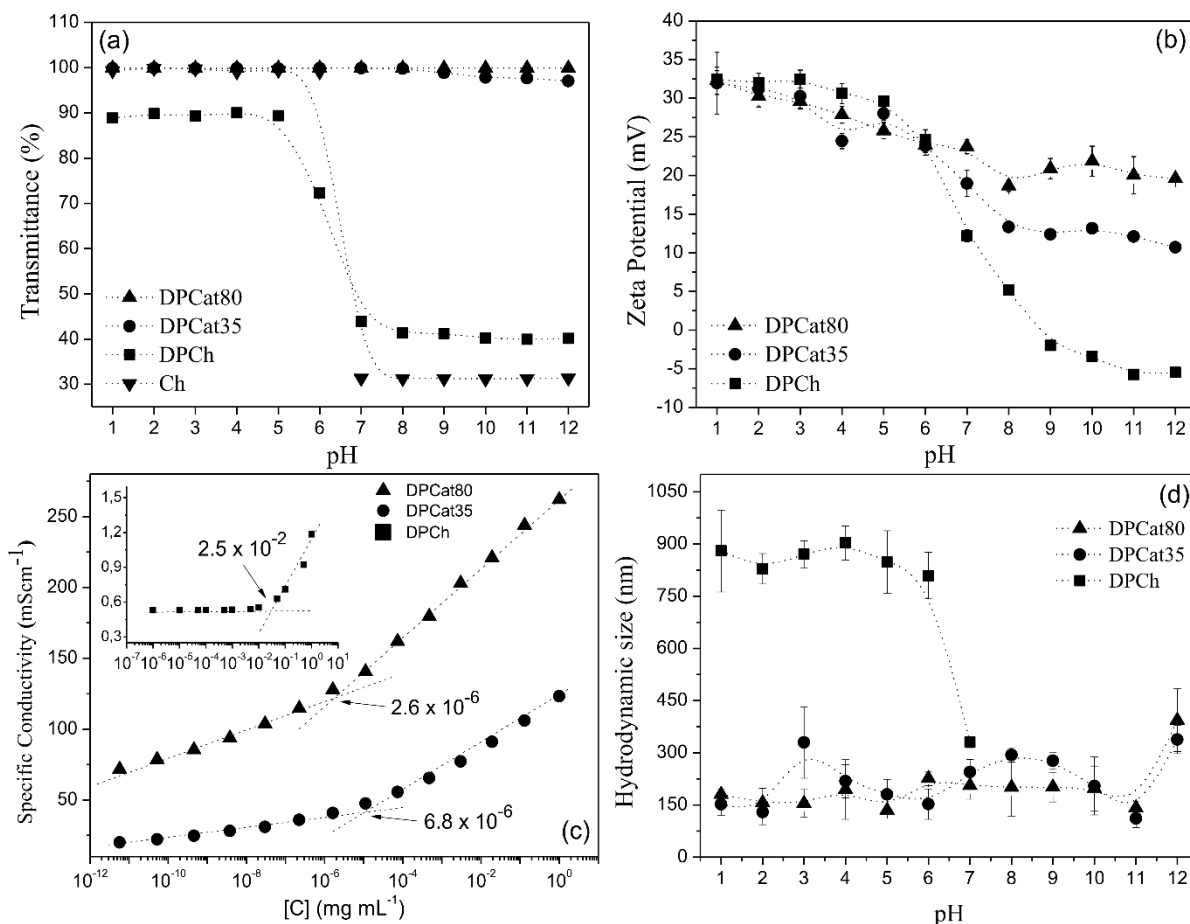
The major contribution of methyl groups was also indirectly confirmed by TG analysis. As the  $^1\text{H}$  NMR signal decay doesn't properly inform which  $^1\text{H}$  nuclei it is related to, the solid-state NMR analyses, namely Dipolar Chemical Shift Correlation (DIPSHIFT) experiment, has been previsouly performed (CHAPTER II) to fulfill this purpose (FACCHINATTO et al., 2020b), once the normalized DIPSHIFT curves reflects the local average mobility from distinct structure segments. As result, the weaker dipolar  $^1\text{H}$ - $^{13}\text{C}$  interaction on methyl groups leads to DIPSHIFT curves with higher amplitude, which might be explained by the intrinsic fast rotation of the C-H bond around the  $\text{CH}_3$  C3 symmetry axis. It was also confirmed that all C1-C6 carbons actually have no significant mobility and, consequently, none of each  $^1\text{H}$  nuclei directly linked. Hence, methyl hydrogens and those from water molecules, referred to the residual hydration assigned on Stage I of TGA curves, are the only relevant  $^1\text{H}$  nuclei involved in the mobile fraction of  $^1\text{H}$  NMR signal decay. Similarly to CHAPTER II achievements, the residual hydration didn't change as much as the content of methyl groups among the samples, with means that the weakly adsorbed water doesn't imply on significant effect on  $^1\text{H}$  NMR signal decay of chitosan and derivatives.

### 3.4.4.2. Solution properties and wettability

As shown in Fig. 45a, the transmittance (T%) values were as high as 90 % for all polymer solutions in acid medium ( $\text{pH} \leq 6$ ), indicating that the presence of positive charges, due to ammonium groups ( $-\text{NH}_3^+$ ) pertaining to GlcN units and to quaternary ammonium substituents ( $-\text{N}^+(\text{CH}_3)_3$ ), favored the complete solubilization of the polymers. In the case of DPCh, there are none quaternary ammonium substituents and the presence of palmitoyl moieties leads to a stronger hydrophobic character, while the neutralization of a significant part of its ammonium groups at  $\text{pH} \approx 6.0$  decreases the polymer charge density, decreasing its solubility as well as the solution transmittance. In neutral and mainly in alkaline media, most of the ammonium groups of GlcN units are neutralized and the transmittance of the solutions of Ch and DPCh decreased sharply, as a consequence of polymer aggregation, leading to polymer insolubility (SORLIER et al., 2001). In contrast, the DPCat35 and DPCat80 derivatives were fully soluble in the range  $1 \leq \text{pH} \leq 12$  as their solution transmittance were always very close to 100 %, which is attributed to their strong polycationic character due to the presence of numerous quaternary ammonium substituents, conferring a high content of positive charges to the polymer chains even in neutral and alkaline media.

The effect of the solution pH on the polymer charge density was evaluated by carrying out measurements of zeta potential (Fig. 45b). In acid medium, all polymers exhibited electrostatic stability as zeta potential values were higher than +25 mV due to the high positive charge density conferred by cationic sites, *i. e.* the ammonium groups ( $-\text{NH}_3^+$ ) of GlcN units (FACCHINATTO, 2016) and the quaternary ammonium substituents ( $-\text{N}^+(\text{CH}_3)_3$ ). However, in alkaline medium a drastic decrease of zeta potential was observed in the case of DPCh as most of its ammonium groups are neutralized at  $\text{pH} \approx 7.0$ , lowering the polymer charge density and its solubility, as already discussed. Such behavior suggests that even in acid medium the self-association of DPCh chains can be favored but the polymer remains soluble as long as enough positive charges, *i. e.* ammonium groups, are present in the polymer chains, assuring an extensive hydration. This discrete macromolecular association may be induced by the polymer segments of DPCh rich in palmitoyl moieties, constituting a hydrophobic core, while the hydrophilic shell, formed by polymer segments positively charged, prevents further aggregation. Although, when  $\text{pH} \geq 7.0$  the outer shell loses its positive charges and the polymer aggregation and insolubility are strongly favored.

Figure 45 - Aqueous solubility (a), zeta potential (b), specific conductivity as function of concentration of DPCh, DPCat35 and DPCat80 (d) and hydrodynamic size as function of pH.



In contrast, the zeta potential of DPCat35 and DPCat80 (Fig. 45b) decrease mildly upon increasing solution pH and from  $\text{pH} \geq 9.0$  a plateau is attained at approximately +12 mV and +20mV, respectively, showing that the higher the content of quaternary ammonium substituents the higher the zeta potential. Indeed, such results confirm the key role of quaternary ammonium substituents concerning the improved water-solubility and electrostatic stability of the DPCat as they are responsible for maintaining a high polymer charge density regardless of the solution pH. Such an improved stability of DPCat is a very important characteristic concerning its potential use as a platform for oral drug administration as the pH changes from neutral to slightly basic in the gastrointestinal mucosa (DESESSO; JACOBSON, 2001).

The macromolecular aggregation behavior of DPCh and DPCat derivatives was evaluated through the fast conductivity measurements of polymer solution as function of its concentration in aqueous medium (KHAN; SHAH, 2008). The specific conductivity versus polymer concentration curves (Fig. 45c) were treated to determine the critical aggregation concentration (CAC) of DPCh and DPCat derivatives (Table 11). The formation of a linear intersection

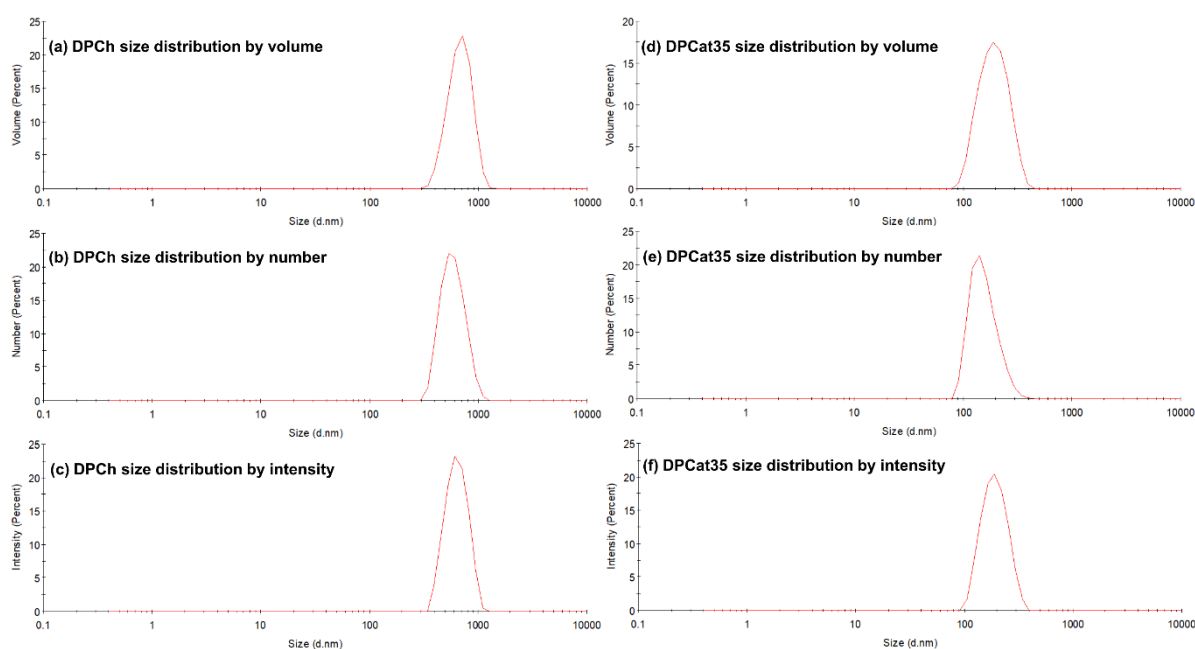
between two increasing tendencies as function of concentration (CAC) means that the recorded conductivity describes the changes in the polymer aggregation behavior, which are consequently held by the positively-charged moieties. Once the content the amphiphilic chains in the medium increases, the average distance among them goes down and the aggregation phenomenon takes place until reaches a critical concentration, when the medium becomes saturated with micelle-like structures. After that point, the fast conductivity increment occurs on a concentration interval in which the increased content of amphiphilic chains in the medium starts being less capable to thermodynamically stabilize itself into a micellar system (SILVA et al., 2017b). Thus, the excess of positively-charged moieties reflects on the higher conductivity because these charged groups are not held on the micellar out layer. Taking into account that the CAC achieved by DPCat derivatives are considerably lower than that of DPCh, it is reasonable to infer that the former is even more capable to form stable micelle-like structures at lower polymer concentration (FENG; DONG, 2006; HUO et al., 2011), while the latter continuously aggregates until reach higher concentrations, leading to structures in which much more amphiphilic chains are involved. Lower CAC is also advantageous to avoid physical dissociation (FENG; DONG, 2006). Such distinct behavior between these chitosan derivatives is deeply related to the quaternary ammonium substituents ( $-N^+(CH_3)_3$ ), as clearly evidenced by the specific conductivity values achieved (Fig. 45c). In this sense, as typically revealed by polyelectrolytes systems, the presence of positive charges is the main responsible for the electrostatic repulsion, consequently preventing the aggregation at high extension (SILVA et al., 2018; ŠTĚPÁNEK et al., 2001). As the content of positive charges increases, the electrostatic repulsion mostly reveals itself as the main driving mechanism to form micelle-like structures requiring considerably less content of amphiphilic chains, thus lowering the CAC of DPCat as compared to DPCh. Thus, owing to their very low CAC ( $2.6 \times 10^{-6} \text{ mg mL}^{-1} - 6.8 \times 10^{-6} \text{ mg mL}^{-1}$ ), both DPCat derivatives are potentially more suitable for development of nanostructured micelles as compared to DPCh aiming the encapsulation and release of hydrophobic drugs compared to DPCh.

The effect of solution pH on the average hydrodynamic size of DPCh and DPCat derivatives was evaluated by carrying out DLS measurements (Fig. 45d), which confirmed that these chitosan derivatives display very different behaviors that are strongly dependent on the chemical nature of their substituents. In acid medium ( $\text{pH} \leq 6.0$ ) the average hydrodynamic size of DPCh is much higher (700-1000 nm) than that of DPCat derivatives (150-350 nm), supporting the thesis that a moderate macromolecular association occurs in the former case, as already proposed. However, as the polymer solution attains  $\text{pH} \approx 7.0$  the DPCh chains lose most

of its positive charges, aggregation is strongly favored and the DLS measurements become very unstable. In the case of DPCat, in contrast, the high charge density prevents the occurrence of aggregation regardless of the solution pH.

As already discussed, the quaternary ammonium groups from both DPCat derivatives allow reaching a considerable reduced CAC due to the electrostatic repulsion that prevents larger micellar-like structures to be formed, as compared to the ones from DPCh. Hence, and considering an equivalent amount of soluble species in a given polymer concentration, it should be pointed out that the micelles made from DPCat leads to lower average sizes of these structures, while those from DPCh are relatively oversized. This consideration was confirmed by the average hydrodynamic size achieved by each derivative (Fig. 45d) and confirmed by the monomodal size distribution profile showed in Fig. 46. This data recorded from DLS experiment at  $\text{pH} \approx 2$  reveals that the distribution of the volume of each particle and number of species agree with the scattering intensity profile for both derivatives, which means that the average hydrodynamic size is representative in the whole analyzed content. Moreover, these size distribution curves also confirm that stable and larger micelle-like structures of DPCh are formed, once the distribution curves are located at higher size distribution interval, while small structures formed by DPCat chains are shifted to lower size distribution interval.

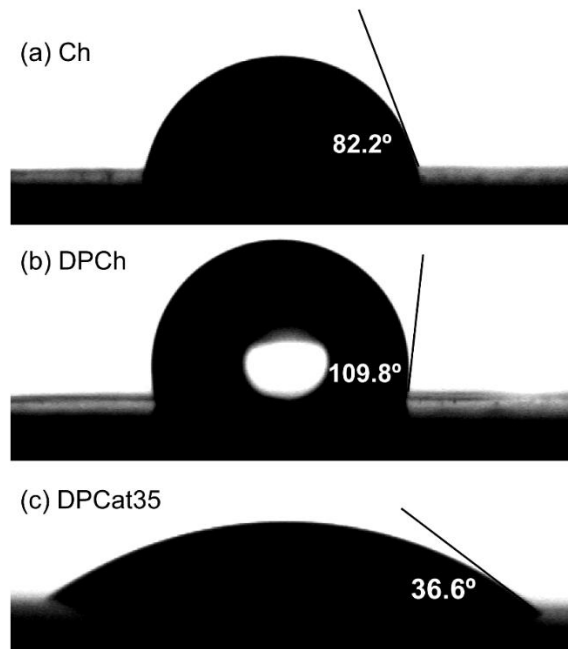
Figure 46 – Hydrodynamic size distribution of DPCh and DPCat35 derivatives recorded by DLS experiment. The results are presented as function of volume (a,d), number (b,e) and intensity (c,f).



The average hydrodynamic size values of DPCat derivatives, although varying in a relatively wide interval (120 nm – 420 nm) are inserted in a useful range concerning its potential application as a drug nanocarriers. Indeed, a drug platform presenting average size in the range 200-500 nm is the preferential choice for enhanced diffusion while those presenting smaller sizes (150-200 nm) are chosen to avoid rapid clearance and enhanced permeation and retention effect (EPR), whereas higher sizes usually lead to a slower transportation through the mucus layer (DAS NEVES et al., 2011).

The results of water contact angle recorded on the polymers compressed into pellets are shown in Fig. 47. This parameter provides important information about the chemical composition and microstructure through the wettability property on solid surfaces. Compared to the contact angle exhibited by Ch (82.2°) used as control (Fig. 47a), mainly attributed to the interaction between hydrophilic segments (amino and hydroxyl groups) with water molecules, the derivatives exhibited opposite behaviors between them as consequence of the hydrophilicity/hydrophobicity moisture ratio due to the relative changes on each functionalization step performed. As observed in Fig. 47b, the lesser wettability expected for DPCh derivative is confirmed by the enhanced contact angle (109.8°) as consequence of the added content of palmitoyl substituents, thus revealing higher hydrophobicity with respect to the control behavior (SILVA et al., 2017b). However, the result recorded for DPCat35 (36.6°), showed in Fig. 47c, reveals an outstanding improvement of wettability behavior due to the addition of the quaternized ammonium,  $-N^+(CH_3)_3$ , substituents (TABRIZ et al., 2019). Such group can highly enhance the hydrophilicity compared to the unmodified amino group because the permanent cationic charge induces a higher polarity which allows the interaction with more water molecules, also suppressing the overall contribution referred to the hydrophobic moieties. It was not possible to record the contact angle on DPCat80 pellet due to the faster wettability property (< 1 s), which agrees to the expected behavior once the content of cationic charges have been significantly enhanced compared to those exhibited by DPCat35.

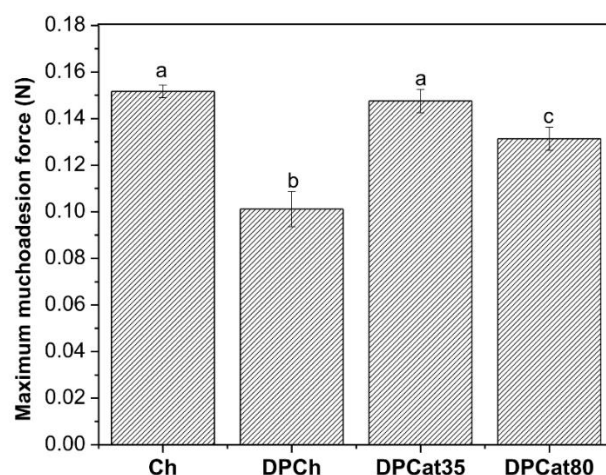
Figure 47 - Water contact angles of Ch (a), DPCh (b) and DPCat35 (c) samples compressed into pellets



#### 3.4.4.3. *Mucoadhesiveness and mucin interaction properties*

The detachment test has been carried out on potential mucoadhesive materials to estimate the maximal force required to detach them from a biological substrate (BONI et al., 2018). The complexity involved in the detachment force as a physical process is due to the mucoadhesive interaction and deformation properties that simultaneously occur in the interface between the material and the substrate (WAYS; LAU; KHUTORYANSKIY, 2018). In this study, the intestinal tissue was used as a model platform to mimic the physiological conditions in a simulated biological environment. The mucoadhesive capacity was estimated comparing indirect measures of the detachment force (N) applied individually, performed after carrying the mucoadhesion consolidation with equivalent contact stages, thus providing the maximum mucoadhesion force for each case (Fig. 48).

Figure 48 - Maximum mucoadhesion (detachment) force (N) of Ch, DPCh, DPCat35 and DPCat80 from porcine intestine, used as biological tissue model. The level of significance of  $p < 0.05$  was determined applying the Tukey's test.



A comparative analysis of Ch and DPCh reveals that the hydrophobic content related to palmitoyl moieties has decreased the mucoadhesive strength onto mucus layer. In fact, both polymers possess amino groups, which renders the macromolecules positively-charged, thus making the electrostatic behaviour as the main driving force for mucosal adhesion interaction with negatively-charged components (SOGIAS; WILLIAMS; KHUTORYANSKIY, 2008; WAYS; LAU; KHUTORYANSKIY, 2018). The secondary linkages with mucus layer are promoted by lower potential energy that sustain the interaction at shorter distances, which is essentially due to the hydrophobic moieties in DPCh, compared to the long-range interactions achieved by charged segments. Therefore, the higher hydrophobicity of DPCh resulted in lower hydration degree as compared to Ch, hindering the interpenetration of polymeric chains in the consolidation step of mucoadhesion (ANDREWS; LAVERTY; JONES, 2009). The palmitoyl chains have been previously reported as chitosan substituents in which the mucoadhesive performance has been increased only by including the hydrophilic glycol segment (BONFERONI et al., 2010). The bioadhesion of palmitoyl glycol chitosan on buccal mucosa could be also enhanced by increasing the polymer hydrophobicity by attaining higher degrees of palmitoylation (MARTIN et al., 2002). Nevertheless, even with such an increased amphiphilic character the authors highlighted that this derivative develops insolubility, depending on the degree of substitution (BONFERONI et al., 2010; MARTIN et al., 2002).

The introduction of quaternary ammonium group onto chitosan backbone has been associated to an increased permeability to hydration, stereochemical hindrance and mucoadhesiveness (RUIHUA et al., 2012; SONIA; SHARMA, 2011). Indeed, as shown in Fig. 48, both DPCat derivatives have enhanced the adhesion to mucosa as compared to DPCh, which

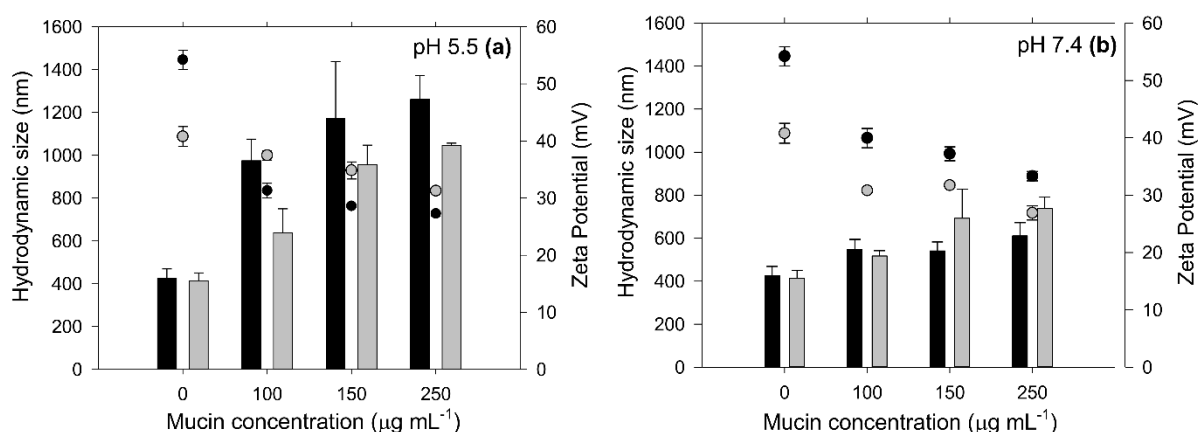
emphasizes the importance of positively-charged surface to engage higher efficiency to this process. However, the maximum mucoadhesion (detachment) force for DPCat35 was higher than DPCat80, which could be associated to the increase of hydration capacity and absorption of large amounts of water molecules by increasing the content of  $-N^+(CH_3)_3$  groups. Similar results were obtained with N,N,N-trimethylchitosan derivative, in which permanent quaternary ammonium groups are also present (NAZAR et al., 2011; SNYMAN; HAMMAN; KOTZE, 2003). In this case, the authors have observed an enhanced work of adhesion of TMC compared to unmodified chitosan with a degree of quaternization from 22.1 to 25.6 %, achieving lower performance at the interval between 48.8 – 61.3 % of quaternization. Indeed, the good mucoadhesive behavior is strongly related to higher levels of water-holding capacity (ANDREWS; LAVERTY; JONES, 2009). However, the excess of hydration, due to the increased electrostatic affinity of DPCat80 for water molecules and owing to its strong polycationic character, might hinder the penetration of polymer chains into mucus layer, thus decreasing the spreadability of polymer solution through the surface and, consequently, the mucoadhesiveness (ANDREWS; LAVERTY; JONES, 2009; NAZAR et al., 2011; SNYMAN; HAMMAN; KOTZE, 2003).

It is worth to mentioning that values of maximum detachment force for DPCat35 derivative did not differ significantly when compared to unmodified chitosan. In this sense, the apparent constant mucoadhesive property with respect to Ch has to be understood as a recovered property, once DPCat35 and DPCat80 were produced from a hydrophobically-modified chitosan, DPCh, that showed lower mucoadhesiveness. Thus, the permanent charged structure achieved by the second derivatization performed in this study reveals as an advantageous over the previous ones, due to the useful properties added and also recovered.

Mucin is formed by high molecular weight glycoproteins ( $10^6$ - $10^7$  Da) that are constituted by approximately 75% of oligosaccharides *O*-linked with proteins (BAFNA; KAUR; BATRA, 2010). The concentration of mucin has been related to the malignancy of several types of tumours, once cancer cells are responsible for high levels of mucins that are largely produced in acid microenvironment. Healthy and tumour tissues typically show similar intracellular pH, however the acidification of surrounding extracellular content has been associated to advanced tumour stages, which results in  $pH \approx 5.5$ . (DANHIER; FERON; PRÉAT, 2010). In this sense, considering that the interactions between a chitosan-based system with mucins are favoured in a slightly acid to neutral pH (SILVA et al., 2012), the self-assembly behavior of DPCat derivatives was investigated in pH 7.4 and 5.5 for simulating physiological and tumor microenvironment systems, respectively, in the presence of mucin.

As shown in Fig. 49, the hydrodynamic size increases with increasing mucin concentration. This behavior is mainly due to the electrostatic attractions involving the negative charges of carboxylate groups of the sialic acid on mucin and the positively-charged DPCat, which results in the adsorption of mucin on the polymeric surface. This adsorption phenomenon is enhanced in pH 5.5 (Fig. 49a) at equivalent mucin concentration measured in physiological medium (Fig. 49b), due to the presence of numerous ionized sialic acid residues (ANDREANI et al., 2015) and protonated amino groups of chitosan, as well as the permanent positive charges present in DPCat derivatives, leading to a stronger electrostatic attraction and favoring the formation of ionic complexes. As consequence, the charged double layer of such macrostructure decreases with mucin concentration, continuously leaving positively-charged groups less available on the surface and thus reducing the zeta potential values. Therefore, the DPCat mucoadhesiveness seems to be more efficient in acid medium, which highlights the major influence of electrostatic force in the consolidation of mucoadhesion process, being especially useful to target anti-cancer drugs in the acid microenvironment of tumoral sites (WAYS; LAU; KHUTORYANSKIY, 2018).

Figure 499 - Average hydrodynamic size (bars) and zeta potential (dots) of DPCat35 (grey) and DPCat80 (black) at pH 5.5 (a) and 7.4 (b).



#### 3.4.4.4. Cytotoxicity assay using healthy and tumor cells

The cell viability screening, aimed for safety administrations of DPCat derivatives, was performed to evaluate the cytotoxicity *in vitro* for HepG2/C3A and DU 145 as cancer epithelial cell lines from liver and prostate, respectively. It was conducted the same assay to a cell line of mouse fibroblast (Balb/C 3T3 clone A31) as healthy model line widely used to assess the toxic response for novel and known chemicals (SAIDEL et al., 2017). The results indicate that

DPCat35 is considerably more safe than DPCat80 as evidenced through the concentration-response curves (Fig. 50), which confirmed the lower cytotoxicity of DPCat35 as compared to DPCat80 to all cell lines, the latter being 13 times more cytotoxic for Balb/C 3T3. Such distinguished behavior is also evidenced in Table 13, according to  $CC_{50}$ , once DPCat35 didn't reach 50% of cell death for DU 145 or HepG2/C3A cells at the concentration interval tested.

Figure 50 - Concentration-response curves with DPCat35 (a) and DPCat80 (b) samples against Balb/C, DU 145 and HepG2/C3A cell lines. The screening of the samples using three cell lines to assess the cytotoxicity has been taken after 72h incubation. The viability of the negative control (untreated cells) was considered 100%, while the positive control with sepamongonium bromide led to cell death (viability near 0%). Continuous lines represent logistic regression curves.

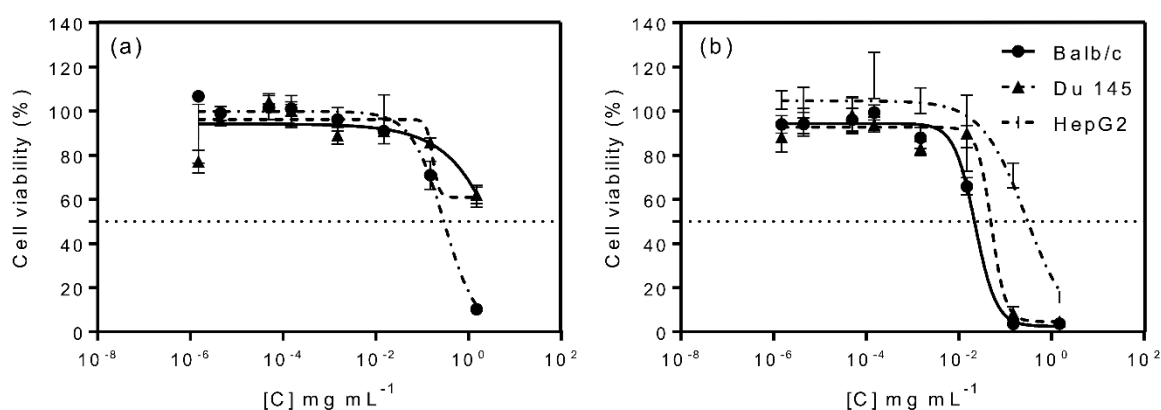


Table 13 - Quantitative data from the concentration-response curves for samples and cell lines used to assess the cytotoxicity after 72 h incubation.

Cell line	DPCat35	DPCat80
	$CC_{50} \pm SD$ ( $\mu\text{g mL}^{-1}$ )	$CC_{50} \pm SD$ ( $\mu\text{g mL}^{-1}$ )
	$R^2/Sy.x$	$R^2/Sy.x$
Balb/C 3T3	$295 \pm 21$ $0.963/5.760$	$22 \pm 2$ $0.985/4.810$
DU 145	NA	$50 \pm 17$ $0.956/8.540$
HepG2/C3A	NA	$277 \pm 34$ $0.934/8.760$

$CC_{50}$ : concentration necessary to reduce cell viability by 50% (half-maximal cytotoxic concentration); standard deviation (SD); non-linear fitting ( $R^2$ ); standard error of the fitting ( $Sy.x$ ). NA = inactive.

Our previous findings have revealed that hydrophobically-modified chitosan derivatives don't exhibit significant cytotoxicity against other cancer cell lines (SILVA et al., 2017b, 2017a), similarly revealed by DPCh, that showed inactive behavior (N.A.) in the initial cell viability screening array ( $15\text{-}1,500 \mu\text{g mL}^{-1}$ ) for all cell lines tested. Hence, in this study, the

major effects regarding the cell viability remain from positively-charged substituents. In fact, according to literature, quaternized chitosan derivatives have been associated to an increased cytotoxicity against different cell lines, which has been also related to the average content of permanent-charged groups available in the structure (JINTAPATTANAKIT et al., 2008; SAJOMSANG et al., 2009; SANTOS et al., 2018; XIAO et al., 2012). Drastically cell viability changes have been found when  $\overline{DQ}$  increases from 28.1 to 43.7 % (XIAO et al., 2012) or from 30 to 82 % (SAJOMSANG et al., 2009). In these studies, at lower  $\overline{DQ}$ , the  $CC_{50}$  values ranged as 150-500  $\mu\text{g mL}^{-1}$ , while at higher  $\overline{DQ}$ , the cell lines almost die at concentration higher than 50  $\mu\text{g mL}^{-1}$ . Moreover, we have found previously that quaternized chitosan derivative, namely N-(2-hydroxy)-propyl-3-trimethylammonium, 3,6-*O,O'*-dimyristoyl chitosan, DMCat, successfully improved the *in vitro* cell viability of curcumin-loaded nanoparticles toward Caco2/HT29-MTX cell lines compared to free curcumin, however empty nanoparticles exhibited  $CC_{50} \sim 50 \mu\text{g mL}^{-1}$  at  $\overline{DQ} = 35 \%$  against both cell lines (SILVA et al., 2018). In this sense, such results corroborate that DPCat35 derivative display similar or even higher cell viability as compared to other positively-charged chitosan approaches and has greatly improved the cell viability as compared to DMCat. Thus, DPCat35 has shown outstanding potential for further biomedical applications, especially for the development of nanosystems of drug delivery, in which the main concern is usually to hide hydrophobically drugs against the immune system recognition and to improve its efficiency, instead of adding some intrinsic and expressive cytotoxic effect with  $CC_{50}$  values at the same log of magnitude to those generally presented by antitumoral drugs (SILVA et al., 2017b, 2017a, 2018).

### 3.4.5. Conclusions

The conditions employed in the derivatizations aimed to introduce new functional groups in the chitosan backbone resulted predominantly in *O*-substitution when introducing palmitoyl groups to result in DPCh ( $\overline{DS} \approx 12.0 \%$ ), a hydrophobic derivative, and in *N*-substitution when introducing the quaternized moieties to DPCh to result in DPCat. The latter is an amphiphilic derivative displaying full water solubility at a wide pH range, the quaternization reaction being carried out at different reaction conditions to result in derivatives DPCat35 ( $\overline{DQ} \approx 35 \%$ ) and DPCat80 ( $\overline{DQ} \approx 80 \%$ ). The main structure of DPCat35 was confirmed by carrying out TD-NMR experiments and TG analysis. While the hydrodynamic size of DPCat derivatives ranged as 100 - 320 nm, a useful range for promising polymeric platforms to be used as drug

nanocarriers, the quaternary ammonium groups of such polymers enabled the exposure of a positively-charged surface, which maintains the electrostatic stability regardless of the solution pH as observed through zeta potential measurements. Such behavior displays a desirable feature for interaction with glycoproteins. Indeed, the positively-charged DPCat surface revealed to be the driving force that sustains the electrostatic attraction with the negatively-charged mucin moieties. In this sense, the mucoadhesive detachment test of DPCat35 showed increased adhesive interaction with the biological tissue model compared to DPCh and DPCat80. The DPCat35 was lesser cytotoxic against the healthy cell line model Balb/C 3T3 than DPCa80 and also showed inactivity against cancer cell lines DU 145 and HepG2/C3A. This cytotoxic profile is in agreement with similar already reported derivatives in which the cell viability is largely reduced by increasing the  $\overline{DQ}$  values. Therefore, the overall properties of DPCat35 make it a promising candidate for applications as a drug nanocarrier as compared to DPCat80.

## CHAPTER V

### *Clotrimazole-loaded N-(2-hydroxy)-propyl-3-trimethylammonium, O-palmitoyl chitosan nanoparticles for topical treatment of vulvovaginal candidiasis*

Original source: **Acta Biomaterialia**, Elsevier (FACCHINATTO, W. M. et al., 2021)

#### *3.5.1. Smart polymers against infectious disease*

Vulvovaginal candidiasis (VVC) is a common genital infection affecting one in every four women at least once during their lifetime (SOBEL, 2007). The disease is particularly prevalent in women of reproductive age and can be quite variable in severity, ranging from sporadic cases featuring mild local symptomatology that are readily solved by oral or topical treatment, to a chronic or recurrent infection that can be hard to manage with currently available drugs. Azoles have been the drug class of choice for treatment of VVC, but some challenges remain. For example, oral azoles (triazoles) are widely used, although topical azoles (imidazoles) can be as effective and avoid systemic side-effects (DAS NEVES et al., 2008). Azole-resistance is also an emerging issue, which can be particularly troublesome due to the relatively scarce availability of alternatives (WHALEY et al., 2017).

From a biopharmaceutical perspective, the use of topical azoles is also limited by the relatively unchanged panorama regarding vaginal formulation approaches that have been available to clinicians and women for managing VVC. Treatment with conventional products – mostly in the form of suppositories, creams or gels – is often associated with poor intravaginal retention and distribution, which restricts local drug availability and, thus, its efficacy (DAS NEVES et al., 2008). Leakage and messiness associated to the use of standard drug dosage forms further affect the willingness of women to fully adhere to treatment (PALMEIRA-DE-OLIVEIRA et al., 2015). Different formulations and drug delivery approaches have been proposed over the years for the vaginal administration of imidazoles (namely its most representative compound clotrimazole (CLT)), including the use of nanotechnology-based solutions. Nanosystems hold the potential to increase drug residence by promoting mucoadhesion, controlling drug release, reducing drug-associated toxicity or even enhancing the interactions between drug and pathogens (VANIĆ; ŠKALKO-BASNET, 2013). For instance, Santos *et al.* (SANTOS et al., 2013, 2014b) developed mucoadhesive CLT-loaded Eudragit® RS 100 capsules and showed their ability to provide sustained drug release and inhibit *Candida* spp. *in vitro*. In another study, Jøraholmen *et al.* (JØRAHOLMEN et al., 2014)

showed that coating CLT-loaded nano-liposomes with chitosan enhanced the ability of the drug to be retained in *ex vivo* vaginal mucosa. A similar effect was recently reported by Soriano-Ruiz *et al.* (SORIANO-RUIZ *et al.*, 2019) when using nanoemulsions to deliver CLT, as compared with commercial references. Gaurav *et al.* (GAURAV *et al.*, 2015) proposed an interesting hybrid nanocomplex comprising albumin-stabilized silver nanoparticles (NPs) coated with CLT included into  $\beta$ -cyclodextrin. Interestingly, this study showed the synergistic effect between CLT and silver NPs, which was able to reverse the drug-resistance profile in a limited number of *Candida* spp. strains.

Chitosan and its derivatives have attracted great interest for various biomedical applications owing to their typical mucoadhesiveness, biocompatibility and biodegradability, and have been widely used for the production of NPs for drug delivery purposes (NASKAR; SHARMA; KUOTSU, 2019; PAVINATTO *et al.*, 2017). The use of such nanocarriers for vaginal use has been documented, particularly for enhancing drug residence upon administration (MENG; STURGIS; YOUAN, 2011) or promoting mucosal permeation (SANDRI *et al.*, 2004). Thiolated chitosan nanoparticles were successfully applied for enhance tenofovir activity, showing non-cytotoxicity to vaginal floral species (MENG; STURGIS; YOUAN, 2011), while 5-methyl-pyrrolidinone chitosan has enhanced the mucoadhesive property and acyclovir permeation in vaginal environment (SANDRI *et al.*, 2004). Additionally, chitosan-coated liposomes formulations were successfully effective against vaginal infections (JØRAHOLMEN *et al.*, 2020). An additional interesting feature of chitosan-based NPs is their reported activity against both planktonic cells and biofilms of *Candida albicans* (DE CARVALHO *et al.*, 2019; ING *et al.*, 2012). However, chitosan and most of its derivatives are hydrophilic in nature and may not be suitable for incorporating highly hydrophobic drugs such as CLT (log P = 5.44; water solubility = 0.56 mg/L) (SAADATFAR *et al.*, 2018).

In order to address this issue, in our previous work, an amphiphilic chitosan derivative was synthesized and exhibited self-assembly aspect in water as well as high loading capacity of lipophilic drugs (SILVA *et al.*, 2017a). In particular, two derivatives displayed additional properties that could support their biomedical use: N-(2-hydroxy)-propyl-3-trimethylammonium, *O,O'*-dimyristoyl chitosan exhibited low cytotoxicity and the ability to promote cell permeation (SILVA *et al.*, 2018), while the permanent-charged amphiphilic chitosan derivative, DPCat (CHAPTER IV), improved mucoadhesiveness (SILVA *et al.*, 2021). The latter derivative also exhibited cytotoxicity that was dependent on its average degree of quaternization ( $\overline{DQ}$ ) (SILVA *et al.*, 2021). Additionally, such cationic amphiphilic chitosan derivatives are soluble over a broad range of pH, contrasting with the low solubility of chitosan

at pH values around six (SILVA et al., 2018, 2021). Furthermore, a previous study suggested that hydroxypropyltrimethylammonium chloride chitosan, a cationic derivative with permanent-charged ammonium groups, not only featured pH-independent solubility, but also showed improved antifungal activity as compared to chitosan (QIN; LI; GUO, 2020). The antimicrobial effect has been typically well correlated with the average degree of quaternization ( $\overline{DQ}$ ) such chitosan derivatives (QIN et al., 2004; SANTOS et al., 2018; SHAGDAROVA et al., 2019).

The aim of this CHAPTER V is to further explore the range of biomedical applications of DPCat, namely by assessing its potential for preparing CLT-loaded NPs intended for the treatment of VVC. The NPs were characterized with respect to its hydrodynamic size and surface charge density through dynamic and electrophoretic light scattering (DLS and ELS) analysis, respectively, and compared with the particle dimensions and morphology recorded by transmission electron microscopy (TEM). NPs were characterized for relevant *in vitro* biological (cytotoxicity, anti-*Candida* activity and cell monolayer permeation/association) properties pertinent to vaginal drug delivery and antifungal therapy. The cytotoxicity to female genital epithelial cells and permeability to cell-monolayer models were carried out using HEC-1-A endometrial cell line and Ca Ski cervical cell line, while the HeLa cervical cell line was additionally used only on cytotoxicity assays.

### 3.5.2. Materials and Methods

#### 3.5.2.1. Preparation and characterization of NPs

DPCat35 was selected for producing NPs due to its lower toxicity, as compared to DPCat80 (SILVA et al., 2021). NPs were prepared by ionic gelation in order to improve colloidal stability of the system in aqueous media (CALVO, P.; REMUNAN-LOPEZ, C.; VILA-JATO, J. L.; ALONSO, 1997). Briefly, 1.0 mL of TPP 1.0 mg mL<sup>-1</sup> aqueous solution was slowly added to 5.0 mL of DPCat35 at 2.0 mg mL<sup>-1</sup> in acetic acid 1.0% (v/v), and left under magnetic stirring (300 rpm) for 1 h at 25 °C. Drug-loaded NPs (CLT-NPs) were obtained by dispersing one milligram of CLT in the TPP solution using 100 µL dimethyl sulfoxide (DMSO) as water miscible solvent of CLT. In either case, the resulting suspension of NPs was centrifuged at 1,500 rpm using Amicon® Ultra-15 filters with 100 kDa cut-off for 10 min at 4

°C in order to remove the non-associated drug, washed three times and resuspended in deionized water.

The hydrodynamic diameter and zeta potential of NPs were determined by dynamic and electrophoretic light scattering, respectively, using a Zetasizer Nano ZS (Malvern Instruments, Malvern, UK). The morphology of the NPs was observed by transmission electron microscopy (TEM) using a JEM 1400 microscope (JEOL, Tokyo, Japan). Both procedures are described in CHAPTER IV

The amount of CLT (Acros Organics, New Jersey, NJ, USA) associated with NPs was determined by modifying a previously described HPLC-UV method (SOLICH et al., 2002). Chromatographic runs were performed by using a HPLC Merck-Hitachi 7000 equipment (Merck, NJ, USA) with a Xterra® column Symmetry® C<sub>18</sub> (5 μm, 100 Å porosity, 150 × 3.0 mm) from Waters (Milford, MA, USA) maintained at 25 °C. The mobile phase was composed by acetonitrile/0.1 % (v/v) trifluoroacetic acid at a 40:60 volume ratio and was used at a flow rate of 0.5 mL min<sup>-1</sup>. Sample injection volume was 10.0 μL and CLT was detected by UV at 254 nm, with a retention time of approximately 4.2 min. The drug was extracted under magnetic stirring (700 rpm) for 2 h and sonication for 30 min using a probe-type sonicator (Vibra-cell, Sonics Material INC. Danbury, CT, USA). Results of the amount of CLT recovered were used for the determination of association efficiency (AE%) and loading capacity (LC%), as described by Eq. (12) and (13).

$$AE (\%) = \frac{CLT_{recovered}}{CLT_{total}} \times 100 \quad (12)$$

$$LC (\%) = \frac{CLT_{recovered}}{\text{total weight of NPs}} \times 100 \quad (13)$$

### 3.5.3. Characterizations

#### 3.5.3.1. *In vitro* drug release

*In vitro* release studies were conducted in two different media in order to simulate the acidic environment typical of healthy women during reproductive age (pH = 3.5-4.5) and the

near neutral conditions that can occur during non-*Candida* dysbiosis, menopause or in the presence of semen (pH > 5) (DAS NEVES et al., 2014). The former medium was simulated by using 0.3 mol L<sup>-1</sup> acetic acid/0.2 mol L<sup>-1</sup> sodium acetate buffer solution (pH = 4.3), while the previous one was mimicked using a phosphate buffered saline solution (PBS, pH = 6.8). Poloxamer 407 at a concentration of 1 % (w/v) was added to both media to ensure sink conditions. The experiments were carried out by placing 5 mL of CLT-NPs (corresponding to 100 µg of CLT) inside a regenerated cellulose dialysis membrane tube (10 kDa MWCO cut-off, Thermo Scientific, Waltham, MA, USA) and allowing it to incubate in 40 mL of release medium under orbital shaking (100 rpm) at 37 °C. Aliquots (1.0 mL) were collected periodically between 15 min and 48 h, and replaced with fresh release medium. The amount of CLT released in the incubation medium was quantified using UV spectrophotometry (Perkin Elmer, Waltham, MA, USA, Lambda 35) at 254 nm based on a previously prepared calibration curve. Experiments were performed in triplicate.

### 3.5.3.2. *In vitro* susceptibility of *Candida* spp.

The *in vitro* activity of CLT-NPs against *Candida* spp. strains was evaluated according to the M27-A4 broth microdilution reference method from CLSI (CLSI: CLINICAL AND LABORATORY STANDARDS INSTITUTE, 2017). Empty NPs, free CLT and polymers were also tested for comparison purposes. Fungi were initially grown on Sabouraud dextrose agar (SDA) at 37 °C, 95% RH and 5% CO<sub>2</sub> for 24 h (48 h in the case of *C. parapsilosis* strains) before experiments. Various *Candida* spp. ATCC reference strains and clinical vaginal isolates, listed in Table 14 were dispersed in a sterile saline solution and diluted in Roswell Park Memorial Institute (RPMI) 1640 medium supplemented with MOPS (pH = 7.0) at a final concentration of 0.5-2.5 × 10<sup>3</sup> cells mL<sup>-1</sup> and further incubated with a 2-fold dilution series of CLT or tested NPs/materials in 96-well plates at 37 °C for 48 h. The minimum inhibitory concentration (MIC) was then determined and defined as the lowest concentration of CLT/material for which no fungal growth is observed upon visual inspection. The minimal fungicidal concentration (MFC) – corresponding to the lowest concentration at which at least 99% of the inoculum is killed – was also determined, as previously described (CANTÓN et al., 2003). Briefly, 20 µL of cell suspension collected from each well featuring no apparent growth was plated onto SDA in duplicate and incubated for 24 h (48 h in the case of *C. parapsilosis*)

at 37° C. Each drug/material concentration was tested in triplicate in three independent experiments.

Table 14 - *Candida* spp. strains used for testing the antifungal activity of CLT-NPs. ATCC strains and clinical samples used in this work were kindly provided from the Centre of Biological Engineering, University of Minho, Portugal.

Origin	Species	Reference	Isolation site
ATCC	<i>C. albicans</i>	90028	Blood
	<i>C. krusei</i>	6258	Sputum (bronchomycosis)
	<i>C. glabrata</i>	2001	Intestine (from feces)
	<i>C. tropicalis</i>	750D-5	Not available
	<i>C. parapsilosis</i>	22019	Intestine (celiac disease)
Clinical isolate	<i>C. albicans</i>	558234	Vagina
	<i>C. albicans</i>	569322	Vagina
	<i>C. krusei</i>	CPA/H/04	Vagina
	<i>C. krusei</i>	CPA 4/104	Vagina
	<i>C. glabrata</i>	534784	Vagina
	<i>C. tropicalis</i>	T2.2	Vagina
	<i>C. parapsilosis</i>	513143	Vagina

### 3.5.3.3. *In vitro* cytotoxicity assay.

The toxicity of free CLT and CLT-NPs to epithelial cell lines of female genital tract origin, namely HEC-1-A endometrial cells, Ca Ski cervical cells and HeLa cervical cells (all acquired from ATCC, Manassas, VA, USA), was determined using the resazurin reduction assay (PRÄBST et al., 2017). All cells were maintained in McCoy's 5A medium (HEC-1-A cells), RPMI 1640 medium (Ca Ski cells) or DMEM (HeLa cells) supplemented with 10% (v/v) fetal bovine serum, 100 U mL<sup>-1</sup> penicillin and 100 µg mL<sup>-1</sup> streptomycin 100 µg mL<sup>-1</sup> at 37°C, 95% RH and 5% CO<sub>2</sub>. In brief, 5,000 cells per well were seeded in 96-well plates in appropriate medium and incubated for 24 h. Serial dilutions of free CLT and CLT-NPs were then added to cells, which were allowed to incubate for an additional 48 h. Plain medium and 1% (w/v) Triton X-100 were also tested as positive and negative controls, respectively. Cells were washed twice with PBS and again incubated with resazurin 10 µg mL<sup>-1</sup> prepared in medium specific for each cell line for 3 h. Finally, 100 µL supernatant was transferred to an opaque 96-well plate and fluorescence was measured at 590/530 nm using a Synergy HT Multi-Mode plate reader (BioTek, Winooski, VT, USA). Each concentration was tested in quintuplicate in three

independent experiments.  $CC_{50}$  values for CLT-NPs and free CLT were calculated by log-logistic regression of viability vs. concentration data using Prism 8 (GraphPad, San Diego, CA, USA). The selectivity index ( $SI$ ) was also determined as the ratio between  $CC_{50}$  and MIC values of CLT-NPs or free CLT for a given human cell line and *Candida* spp. strain, respectively. Additionally, the relative selectivity index ( $RSI$ ) was considered as the ratio between  $SI$  values for CLT-NPs and free CLT.

#### 3.5.3.4. *In vitro* drug permeability and cell association

Two cell monolayer models based on either HEC-1-A cells or Ca Ski cells were generated and used to assess the ability of NPs to modulate drug permeation and cell association at the cervicovaginal epithelium, as previously described (DAS NEVES et al., 2013; DAS NEVES; SARMENTO, 2015). Briefly, cells were seeded on 12-well semipermeable polyester membrane supports (1  $\mu\text{m}$  porosity; Millicell<sup>®</sup>, Merck Millipore, Tullagreen, Ireland) pre-coated with rat tail collagen type I (10  $\mu\text{g cm}^{-2}$ ) at a density of  $3 \times 10^5$  cells  $\text{cm}^{-2}$ . Cell monolayers were allowed to form upon incubation for 7 days at 37 °C, 95% RH and 5%  $\text{CO}_2$ . Media were renewed every 2–3 days and the TEER was periodically measured using an EVOM2 epithelial voltohmmeter (World Precision Instruments, Sarasota, FL, USA) equipped with chopstick electrodes.

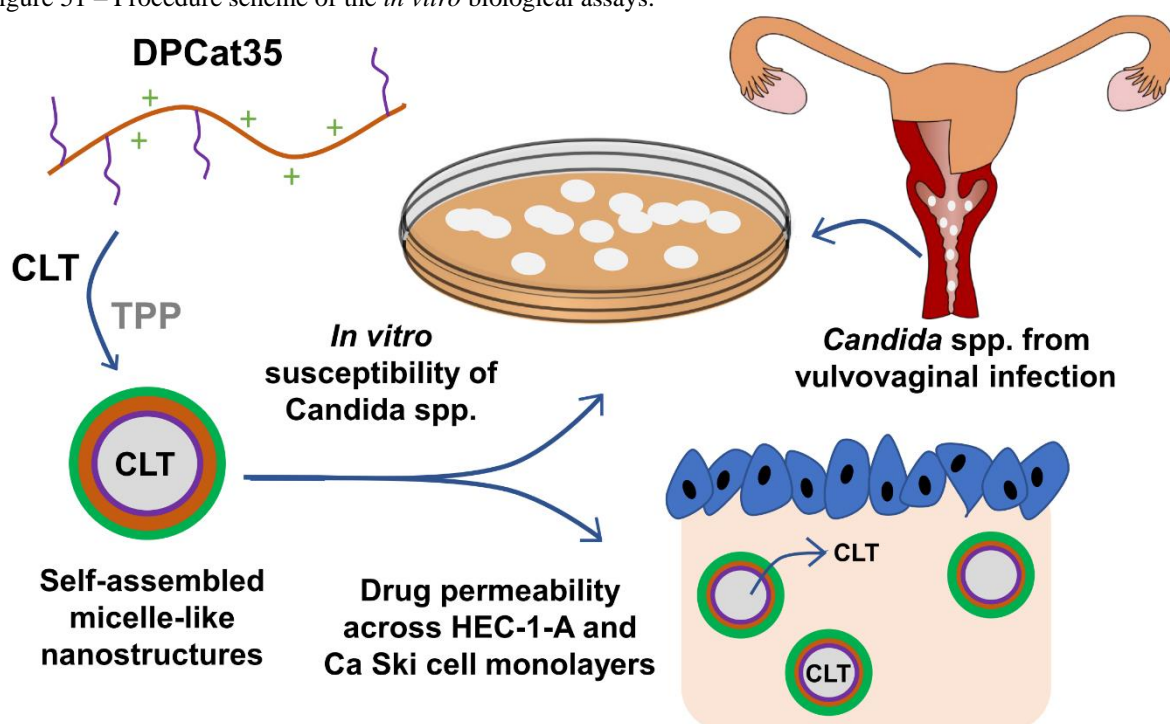
Permeability experiments were conducted using HBSS supplemented with 0.2% ( $w/v$ ) poloxamer 407 as medium in both apical (0.5 mL) and basolateral (1.5 mL) compartments in order to maintain sink conditions. CLT-NPs or free CLT were dispersed in the apical compartment medium at a final concentration of 20  $\mu\text{g mL}^{-1}$  (expressed in CLT content). DMSO at a concentration of 0.2 % ( $v/v$ ) was used in the case of free CLT in order to facilitate dispersion in HBSS. Drug permeability across cell monolayers was assessed by periodically collecting 0.5 mL of medium from the basolateral compartment up to 4 h of incubation at 37 °C under orbital shaking (100 rpm). Medium in the basolateral compartment was replaced after each collection and cell monolayer integrity during experiments was monitored by measuring TEER. Additionally, the membrane support containing cell monolayers was collected, washed briefly with PBS, incubated with acetonitrile, centrifuged (700 rpm, 15 min) and the supernatant collected for CLT extraction. All samples were analyzed spectrophotometrically at 254 nm for assessing drug content. The apparent permeability coefficient ( $P_{\text{app}}$ ) across cell monolayers was calculated according to Eq. (14):

$$P_{app} (cm s^{-1}) = \frac{\Delta Q}{A \times C_0 \times t} \quad (14)$$

where  $\Delta Q$  is the total amount of permeated CLT ( $\mu\text{g}$ ),  $A$  the diffusion area ( $\text{cm}^2$ ),  $C_0$  the initial concentration of CLT in the donor compartment ( $\mu\text{g cm}^{-3}$ ) and  $t$  is the total experiment time (s) (DAS NEVES; SARMENTO, 2015). All experiments were performed in triplicate.

Fig. 51 reveals a illustrative scheme of the *in vitro* biological assays conducted in this CHAPTER V.

Figure 51 – Procedure scheme of the *in vitro* biological assays.



Source: Own authorship.

### 3.5.3.5. Statistical analysis

Data are presented as mean  $\pm$  standard deviation (SD) from three independent experiments, unless otherwise stated. Comparison of results for permeability experiments was performed by one-way ANOVA with Tukey's post-hoc test using Prism 8. Values of  $p < 0.05$  were considered as denoting significance.

### 3.5.4. Results and Discussion

#### 3.5.4.1. Physicochemical properties and drug release performance of NPs

The ionic gelation method was performed using DPCat35 derivative with TPP as crosslinker in order to yield a polymeric suspension with increased colloidal stability. The experimental conditions employed granted that the hydrodynamic sizes of empty NPs fits in a nanoscale distribution, similarly to the accomplished for low molecular weight chitosan with  $\overline{DA} < 10.0\%$ , as reported elsewhere (CALVO, P.; REMUNAN-LOPEZ, C.; VILA-JATO, J. L.; ALONSO, 1997; FAN et al., 2012). Such procedure was repeated for loading CLT lipophilic molecules resulting in the CLT-NPs with similar monomodal size distribution profile compared to the empty NPs (Fig. 52a). As indicated in Table 15, the average hydrodynamic size ( $D_h$ ) also showed remarkably small PDI ( $< 0.2$ ). This result indicates the great advantage of a physical crosslinking to assembly nanostructures with narrow distribution. Sizes ranged in 200 to 500 nm are commonly preferential for enhanced diffusion through the mucus layer (DAS NEVES et al., 2011).

Figure 522 - Hydrodynamic size distribution by intensity of empty NPs and CLT-NPs (a); representative TEM images of CLT-NPs obtained at magnification 200 nm (b) and 100 nm (c).

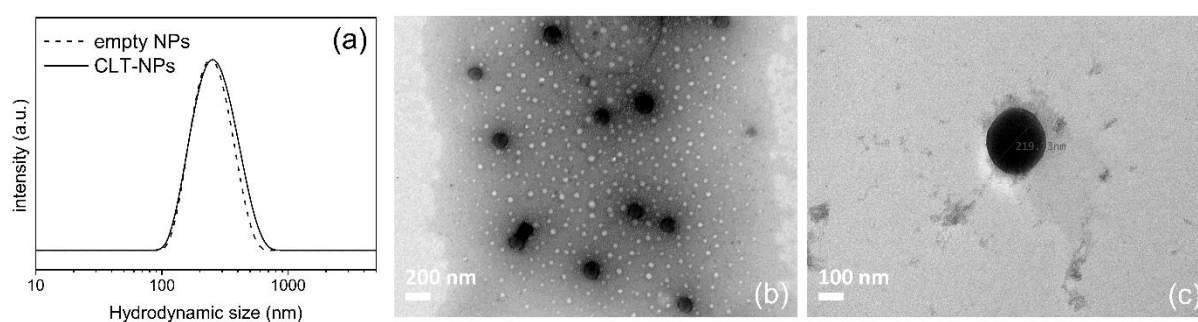


Table 15 - Average hydrodynamic size ( $D_h$ ), polydispersity index (PDI), zeta potential ( $\zeta$ ), AE% and LC% of NPs

Nanoparticles	Hydrodynamic diameter (nm)	PDI	Zeta potential (mV)	AE%	LC%
Empty NPs	$272 \pm 13$	$0.16 \pm 0.01$	$+26 \pm 1$	-	-
CLT-NPs	$279 \pm 19$	$0.18 \pm 0.01$	$+26 \pm 2$	$84 \pm 2$	$7 \pm 2$

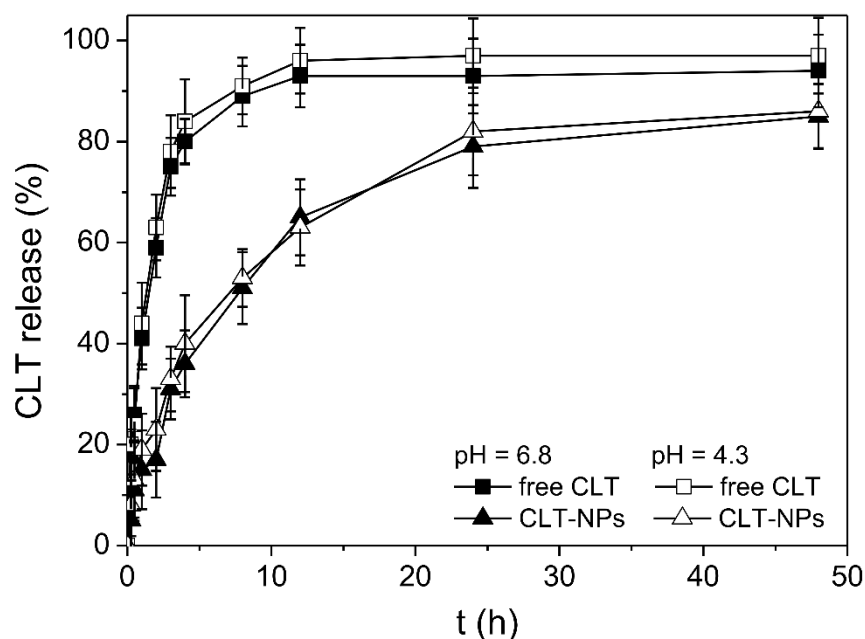
Taking into account such reproductive size distribution between empty and loaded NPs and the higher EE (%) of nanoparticles initially loaded with  $7 \pm 2$  % (w/w) of CLT (Table 15), it is reasonable to consider that the palmitoyl moieties are mostly hosted inside, being the main responsible for the hydrophobic interactions with the drug in the CLT-NPs core. In fact, the micellar-like disposal probably contributes to the colloidal stability until certain level, as noticed in previous studies (SILVA et al., 2017b, 2017a). These considerations regarding the general aspects of the CLT-NPs were confirmed through TEM images. As showed in Fig. 52b-c, the spherical shape assigned to the dark spots can be associated to an assembled micellar-like structure, although with smaller sizes than the former swollen CLT-NPs suspension. This behavior relies directly to the drying process that allows the analysis to be performed, which consequently shrinks the nanoparticles into smaller sizes (BOOTZ; VOGEL; SCHUBERT, 2004).

The electrostatic stability of the nanoparticles suspensions was evaluated by means of zeta potential, which highlights the average charge density remaining on the nanoparticle surface. As showed in Table 15, both empty and loaded NPs achieved positive zeta potential values ( $> 25$  mV), indicating that even in neutral medium the nanoparticles still have a positive out-layer mostly preserved due to the surface exposure of quaternary ammonium groups,  $-N^+(CH_3)_3$ , that exhibit permanent cationic charges. At pH  $\sim 7.0$ , the protonated ammonium groups from chitosan backbone are almost neutralized, which would lead to a completely surface discharge and aggregation of chains in the absence of  $-N^+(CH_3)_3$  groups, thus compromising the solubility and the overall nanocarrier performance. It is also important to notice that the introduction of CLT doesn't affect the zeta potential value, which means that the content and distribution of positive charges remains nearly the same after encapsulation. The localized neutralization of positive charges due to the ionic crosslink with negatively-charged TPP molecules is negligible, since it left several  $-N^+(CH_3)_3$  groups available. In fact, this achievement reveals to be one of the main advantages of performing the ionic gelation procedure, because the resulted zeta potential values are comparable to those achieved by the DPCat35 derivative itself in neutral media, as showed in CHAPTER IV, leading to no significant disruption of charged sites. Such electrostatic behavior that stays constant regardless the pH is a useful feature for designing new nanocarriers, once the pH of vaginal tract can be temporally elevated during a yeast infection, thus affecting the absorption of certain drugs (BOSKEY et al., 1999; ENSIGN; CONE; HANES, 2014).

Sequentially, the *in vitro* performance of CLT-NPs provides relevant information regarding their potential for vaginal drug delivery, namely in the context of VVC management.

One important property of nanocarriers relates to their ability to release active payload when placed in biorelevant aqueous media. Experiments were carried out under different pH in order to simulate different scenarios. Although VVC is not associated with changes to the acidic environment of the vagina, increasing pH may still be observed in cases of mixed infection or underlying dysbiosis (DAS NEVES et al., 2008). Drug release from CLT-NPs in acidic (pH = 4.3) or near neutral (pH = 6.8) media values was similar (Fig. 53). The release of CLT was sustained up to around 24 h, and it was nearly complete after 48 h, which – alongside the mucoadhesive behavior typical of cationic chitosan derivatives (WAYS; LAU; KHUTORYANSKIY, 2018) – could be regarded as an interesting feature for providing prolonged mucosal drug residence and enhancing the treatment of VVC following vaginal administration. This is in contrast with the rapid dissolution of free CLT (approximately 80% over 4 h). Moreover, drug release from CLT-NPs was considerably slower than for previously developed CLT-loaded liposomes and microemulsions (BACHHAV; PATRAVALE, 2009; JØRAHOLMEN et al., 2014), and comparable to that of Eudragit® RS 100 nanocapsules (SANTOS et al., 2014b).

Figure 53 – Experiments were conducted in acetate buffer (pH = 4.3) and PBS (pH = 6.8). Dissolution profiles of CLT are included for comparison purposes.



### 3.5.4.2. Susceptibility assay against *Candida* spp.

We assessed the impact of incorporating CLT into NPs in its ability to inhibit fungal growth using the clinically relevant M27-A4 method from CLSI. Preliminary experiments were conducted in order to screen for any potential intrinsic activity of polymers (Ch, DPCat35 and DPCat80) and empty NPs. Indeed, chitosan and several of its derivatives have been reported as possessing considerable antifungal activity (ALBURQUENQUE et al., 2010; PALMEIRA-DE-OLIVEIRA et al., 2010; PARK et al., 2008; TAYEL et al., 2010). However, chitosan was not able to inhibit the growth of different ATCC strains of *Candida* spp., while DPCat35, DPCat80 and empty NPs featured only mild activity, as showed in Table 16. The lack of activity of chitosan up to 1,024  $\mu\text{g mL}^{-1}$  is in line with MIC values typically found in the literature (GOY; BRITTO; ASSIS, 2009; VERLEE; MINCKE; STEVENS, 2017; VINSOVÁ; VAVRIKOVÁ, 2011) while the minor improvement in activity of DPCat35 and DPCat80 could be attributed to the incorporation of trimethylammonium groups in the chitosan backbone, as previously reported in the literature (HOQUE et al., 2016; QIN et al., 2004; QIN; LI; GUO, 2020; SHAGDAROVA et al., 2019). A trend towards slightly better activity of empty NPs as compared to DPCat35 (Table 16) may be related to the combined antifungal properties of the polymer and TPP (PALMEIRA-DE-OLIVEIRA et al., 2011) and/or the enhance exposure of trimethylammonium groups at the surface of nanosystems (ING et al., 2012).

Table 16 - MIC and MFC of chitosan, DPCat35, DPCat80 and empty NPs. Results presented in  $\mu\text{g mL}^{-1}$  (n = 3).

Strains	Chitosan		DPCat35		DPCat80		Empty NPs	
	MIC	MFC	MIC	MFC	MIC	MFC	MIC	MFC
<i>C. albicans</i> ATCC 90028	> 1024	> 1024	> 1024	> 1024	> 1024	> 1024	1024	>1024
<i>C. krusei</i> ATCC 6258	> 1024	> 1024	> 1024	> 1024	> 1024	> 1024	1024	1024
<i>C. glabrata</i> ATCC 2001	> 1024	> 1024	> 1024	> 1024	> 1024	> 1024	512	>1024
<i>C. tropicalis</i> ATCC 750	> 1024	> 1024	512	> 1024	256	> 1024	512	512
<i>C. parapsilosis</i> ATCC 22019	> 1024	> 1024	128	> 1024	128	> 1024	64	512

The activity of free CLT and CLT-NPs was then tested against an expanded panel of ATCC strains and clinical isolates of *Candida* spp. using the M27-A4 method. MIC and MFC

results are presented in Table 17. In general, the association of CLT to NPs led to an apparent decrease in activity, with a typical 2- to 8-fold increase in the values of MIC. Still, MIC values were equal or lower than  $8 \mu\text{g mL}^{-1}$  for 9 out of 12 strains/isolates and never above  $32 \mu\text{g mL}^{-1}$ , which seems to assure enough potency for use in the management of VVC (RICHTER et al., 2005). In the case of MFC, results were more variable and ranged from over 8-fold reduction (*C. albicans* 558234) to a 32-fold increase when comparing CLT-NPs to free CLT. Interestingly, MFC values for CLT-NPs never exceeded  $64 \mu\text{g mL}^{-1}$ , while free CLT was not able to fully inactivate two clinical isolates (*C. albicans* 558234 and *C. glabrata* 534784) even at the highest tested concentration.

Table 17 - Anti-Candida activity of free CLT and CLT-NPs. Results are presented as MIC and MFC values against ATCC strains and vaginal isolates of Candida species. Results are presented in  $\mu\text{g mL}^{-1}$  of CLT (n = 3). The azole (FLC) resistance profile for each strain is also shown for reference and defined as susceptible (S;  $\text{MIC} \leq 8 \mu\text{g mL}^{-1}$ ); dose-dependent susceptibility (S-DD;  $\text{MIC} = 16\text{-}32 \mu\text{g mL}^{-1}$ ); or resistant (R;  $\text{MIC} \geq 64 \mu\text{g mL}^{-1}$ ).

Strains	FLC susceptibility	CLT		CLT-NPs	
		MIC	MFC	MIC	MFC
<i>C. albicans</i> ATCC 90028	S	1	4	8	32
<i>C. krusei</i> ATCC 6258	S-DD	0.5	1	4	32
<i>C. glabrata</i> ATCC 2001	S-DD	2	8	32	64
<i>C. tropicalis</i> ATCC 750D-5	S	4	16	16	64
<i>C. parapsilosis</i> ATCC 22019	S	1	4	4	8
<i>C. albicans</i> 558234	R	4	> 256	8	32
<i>C. albicans</i> 569322	R	2	4	2	16
<i>C. krusei</i> CPA/H/04	R	1	4	8	32
<i>C. krusei</i> CPA 4/104	S-DD	2	4	4	16
<i>C. glabrata</i> 534784	S	2	> 256	8	32
<i>C. tropicalis</i> T2.2	R	2	8	16	64
<i>C. parapsilosis</i> 513143	S	1	> 16	4	8

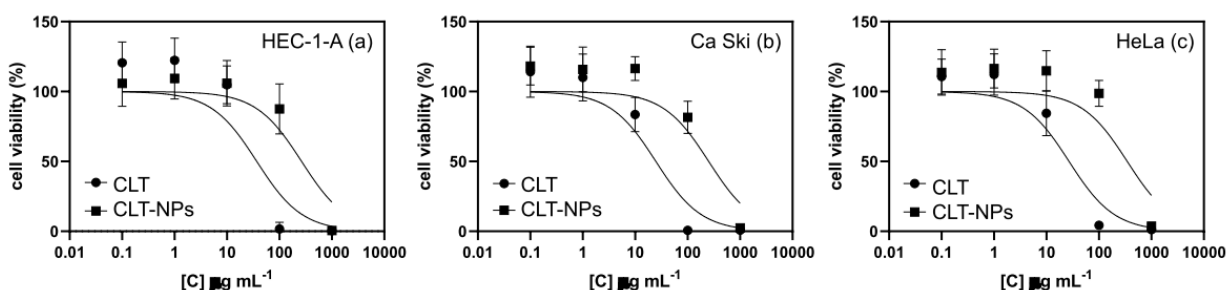
No correlation between susceptibility to CLT/CLT-NPs and fluconazole (FLC, Acros Organics) was apparent. Overall, the ability of NPs to provide prolonged release of CLT may be partially responsible for the increase in MIC values, since the available levels of drug that actually interact with yeast cells are decreased; however, given enough time for CLT to be fully released, the proposed nanosystem seems to be as effective as the free drug, if not more. Such ability to inactivate *Candida* spp. in the long run may be related with improved cell internalization of yeast cells as mediated by the nanocarrier (PENG et al., 2008). However, this

capability requires further investigation. From a practical point of view, these *in vitro* results suggest that higher doses of CLT-NPs may be necessary for effective treatment of VVC.

### 3.5.4.3. Cytotoxicity and permeability to genital tract cell monolayers

In order to attest the possible use of higher doses of CLT-NPs, we assessed their *in vitro* cytotoxicity against different cell lines of female genital tract origin. Cell viability was assessed using the resazurin reduction assay and viability vs. concentration plots (Fig. 54) were used to determine  $CC_{50}$  values. Curiously, CLT-NPs were shown to roughly reduce cytotoxicity by one log of magnitude as compared to free CLT. Mean values of  $CC_{50}$  for CLT-NPs were  $261 \pm 3 \mu\text{g mL}^{-1}$ ,  $245 \pm 7 \mu\text{g mL}^{-1}$  and  $359 \pm 13 \mu\text{g mL}^{-1}$  for HEC-1-A, Ca Ski and HeLa cell lines, respectively, as compared to  $37.6 \pm 0.6 \mu\text{g mL}^{-1}$ ,  $24.8 \pm 0.3 \mu\text{g mL}^{-1}$  and  $26.6 \pm 0.3 \mu\text{g mL}^{-1}$  for free CLT. Again, the ability of nanocarriers to prolong drug release and reduce the levels of free CLT available for interacting with cells may be responsible for such an apparent decrease in toxicity. These results are in accordance to our previous observations for an antiretroviral drug featuring considerable intrinsic cytotoxicity: when associated to poloxamer-modified polycaprolactone NPs,  $CC_{50}$  against Ca Ski (DAS NEVES et al., 2013), HEC-1-A and HeLa (DAS NEVES et al., 2012) cells were considerably increased even if overall higher intracellular drug concentrations were achieved.

Figure 54 - Cell viability of CLT-NPs and free CLT to HEC-1-A (a), Ca Ski (b) and HeLa (c) cell lines as a function of concentration (expressed in total CLT content). Values are reported as mean  $\pm$  SD ( $n = 3$ ). Continuous lines represent log-logistic regression curves.



The combined analysis of MIC and  $CC_{50}$ , expressed in terms of  $SI$  (Table 18), allows to better forecast whether CLT-NPs can be useful in the management of VVC, namely when compared to the performance of free CLT ( $RSI$ ). Values of  $SI$  were generally higher for CLT-NPs, the exception being *C. glabrata* ATCC 2001 for which CLT-NPs was slightly lower as compared to the free drug ( $RSI = 0.6-0.8$ ). As for the remaining *Candida* spp. strains/isolates,

CLT-NPs performed as good as free CLT or even better. Improvement in *SI* for nanocarriers was particularly striking in the case of some clinical isolate, namely FLC-resistant *C. albicans* 558234 (*RSI* = 3.6-6.4) and *C. albicans* 569322 (*RSI* = 7.1-12.9). These results appear to further support the potential of CLT-NPs for the treatment of *Candida* spp. involved in VVC.

Table 18 - *SI* and *RSI* values for free CLT and CLT-NPs. *RSI* values denoting at least 2-fold reduction or 2-fold increase in *SI* of CLT-NPs as compared to the free drug are highlighted in red and blue, respectively.

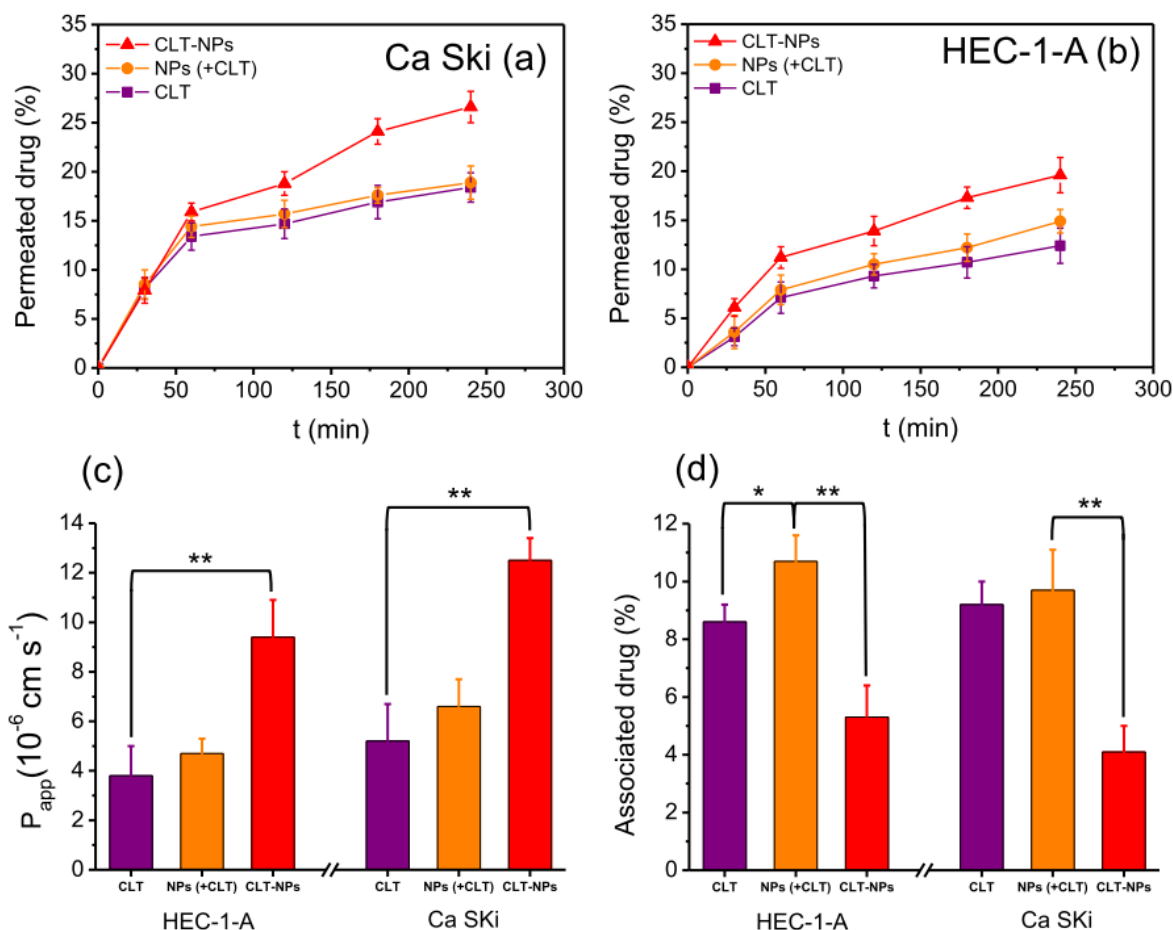
Strains	<i>SI</i> (CLT)			<i>SI</i> (CLT-NPs)			<i>RSI</i>		
	HEC-1-A	Ca Ski	HeLa	HEC-1-A	Ca Ski	HeLa	HEC-1-A	Ca Ski	HeLa
<i>C. albicans</i> ATCC 90028	37	24.8	26.9	33.1	31.5	43.3	0.9	1.3	1.6
<i>C. krusei</i> ATCC 6258	74	49.6	53.8	66.1	63.0	86.5	0.9	1.3	1.6
<i>C. glabrata</i> ATCC 2001	18.5	12.4	13.5	8.3	7.9	10.8	0.4	0.6	0.8
<i>C. tropicalis</i> ATCC 750D-5	9.3	6.2	6.7	16.5	15.8	21.6	1.8	2.5	3.2
<i>C. parapsilosis</i> ATCC 22019	37	24.8	26.9	66.1	63.0	86.5	1.8	2.5	3.2
<i>C. albicans</i> 558234	9.3	6.2	6.7	33.1	31.5	43.3	3.6	5.1	6.4
<i>C. albicans</i> 569322	18.5	12.4	13.5	132.3	126.1	173.1	7.1	10.2	12.9
<i>C. krusei</i> CPA/H/04	37	24.8	26.9	33.1	31.5	43.3	0.9	1.3	1.6
<i>C. krusei</i> CPA 4/104	18.5	12.4	13.5	66.1	63.0	86.5	3.6	5.1	6.4
<i>C. glabrata</i> 534784	18.5	12.4	13.5	33.1	31.5	43.3	1.8	2.5	3.2
<i>C. tropicalis</i> T2.2	18.5	12.4	13.5	16.5	15.8	21.6	0.9	1.3	1.6
<i>C. parapsilosis</i> 513143	37	24.8	26.9	66.1	63.0	86.5	1.8	2.5	3.2

Finally, and in order to predict the interaction of CLT-NPs with the vaginal mucosa, we tested the permeability and cell association of CLT using relevant Ca Ski and HEC-1-A cell monolayers. These models are easy to use and standardize, and have been shown useful in previous studies for understanding the ability of different drugs and carriers/formulations to cross and accumulate in the cervicovaginal epithelium (DAS NEVES; SARMENTO, 2015; GORODESKI, 1998; GRAMMEN; AUGUSTIJNS; BROUWERS, 2012; LI et al., 2011;

ZHANG et al., 2015). It should also be noted that these *in vitro* models have well-recognized limitations such as lack of the stratified cell structure, absence of mucus and microbiota, presence of increased amounts of a static fluid with nearly neutral pH in the apical side, which should be considered when interpreting results (MACHADO et al., 2015). Permeability of CLT across both models are presented in Fig. 55a-b. Ca Ski cell monolayers were generally more permeable than HEC-1-A cell monolayers, in accordance with previous work testing a hydrophobic drug and its nanocarriers (DAS NEVES; SARMENTO, 2015). When considering each model individually, CLT-NPs presented overall higher drug permeability as compared to free CLT in both models. It is worth to emphasize that this effect was only observed when CLT was associated to NPs rather than simply mixed, which suggests that permeation is likely to be mediated by enhanced drug dissolution and/or cytoadhesion, while the disruption of cell monolayer integrity and promotion of paracellular transport probably plays a minor role (SIEW et al., 2012). Supporting this possibility is the fact that we have recently shown that DPCat35 interacts strongly with porcine tissue and mucin, thus featuring high mucoadhesiveness (SILVA et al., 2021). Although the models used in this study do not produce mucus, such results reveal that NPs may be able to intimately adhere to epithelial surfaces. Also, TEER did not change significantly during all permeability experiments (data not shown), thus suggesting that the integrity of the cell monolayers was not affected.

Calculated  $P_{app}$  values presented in Fig. 55c further highlight the significant enhancement of drug permeability as mediated by CLT-NPs (roughly 2-fold in both models). These observations may be of significance for the treatment of VVC. Clinical infection by *Candida* spp. is associated with the ability of budding yeasts (non-pathogenic) to undergo dimorphic transition and invade the underlying epithelium (NAGLIK et al., 2011). Thus, antifungal drugs such as CLT should penetrate sufficiently the mucosa in order to reach the deeper ends of invasive hyphae in order to be effective (WÄCHTLER; WILSON; HUBE, 2011). Drug association with cell monolayers was significantly higher when CLT was used in the free form, with or without the presence of empty NPs (Fig. 55d). Although we could not distinguish the fraction of CLT that was actually internalized by epithelial cells after 4 h, it is likely that these results reflect the deposition of the drug due to its use in the form of a suspension.

Figure 55 - Drug permeability and association to cell monolayers of free CLT and CLT-NPs. Cumulative drug permeability profile for free CLT, CLT-NPs and empty NPs physically mixed with CLT (NPs(+CLT)) across Ca Ski (a) and HEC-1-A (b) cell monolayers. Values of  $P_{app}$  values (c) and associated drug (d) with cell monolayers for free CLT, CLT-NPs and NPs (+CLT). Results are presented as mean  $\pm$  SD ( $n = 3$ ). (\*) and (\*\*) denote values of  $p < 0.05$  and  $p < 0.01$ , respectively.



### 3.5.5. Conclusions

In this CHAPTER V, we successfully applied a permanent-charged amphiphilic chitosan derivative for producing CLT-loaded NPs, and assessed different *in vitro* properties relevant for their potential use in the treatment of VVC. Despite the amphiphilic nature of the polymer and the formation of self-assembled micelle-like nanostructures in water, varying out the TPP crosslinking was of key importance to produce stable nanocarriers. This association of CLT to NPs allowed obtaining a sustained release profile of the drug up to 24 h, which could be beneficial in terms of prolonging drug residence *in vivo*. The anti-*Candida* activity of CLT-NPs was generally lower than that of the free drug, but was counterbalanced by improved *in vitro* safety profiles. In fact, *SI* results were largely favorable to CLT-NPs, which could be translated into an improved therapeutic index as compared with free CLT. CLT-NPs also featured

promising behavior when tested in two different cell monolayer models, highlighting a potential role in improving tissue penetration by CLT and, presumably, better mucosal distribution and retention. However, complementary *in vivo* studies are needed in order to confirm such possibilities, and eventually allow the establishment of an *in vitro-in vivo* correlation.

#### 4 FINAL REMARKS AND PERSPECTIVES

The Chapters that compose this Thesis explored the use of different NMR, non-spectroscopy and biological techniques and chitosan-based materials in order to cover promising research fields. The authentic format of this document makes it especially useful as a starting point for the development of different research segments. In this way, the following suggestions concerns about alternative studies that may broaden the focus and applicability of the materials and characterization used in each Chapter.

An important property extensively addressed in works involving chitins, chitosans and derivatives refers to the degree of cross-linking. There is no consensus on the method of determination for those generally employing laborious procedures. For this reason, further studies may come to offer alternative methods for characterizing the degree of cross-linking via SSNMR, as addressed for the degree of acetylation and crystallinity. Chelation behavior and assymmetric membranes formation may also be explored as function of these chitosan features.

The effects on the average particle size of  $\beta$ -chitin whiskers can be investigated from new matrices polymeric composites, being solid-state and solution NMR possibly useful for further trend comparison. For instance, the incorporation of nanowhiskers and nanocrystals into new matrices by performing methodologies such as electrospinning and blowspinning. Moreover, such  $\beta$ -chitin nanowhiskers will be investigated as immunosensing platform, to explore the selectivity and sensitivity of different biomarkers.

New bioactives may be associated into the amphiphilic matrices of chitosan derivatives, outlining the most diverse objectives related to the research field of sustained drug release. The *in/ ex vivo* profile of these materials may also be carried in partnership with specialized institutions. In addition, it would be very interesting if such material were further studied using organoids or mini-organs, maybe reaching a next level of sustainable and ethical scientific experimentation.

## 5 RESULTING PUBLISHED SCIENTIFIC ARTICLES

During the Ph.D. development and until the date of this Thesis final submission, four articles specifically described as CHAPTERS I, II, IV and V, were published in peer-reviewed journals, as listed below.

- Evaluation of chitosan crystallinity: A high-resolution solid-state NMR spectroscopy approach. **Carbohydrate Polymers**, v. 250, p. 116891-1-116891-14, 2020;
- Fast-forward approach of time-domain NMR relaxometry for solid-state chemistry of chitosan. **Carbohydrate Polymers**, v. 256, p. 117576-1–117576-10, 2020;
- N-(2-hydroxy)-propyl-3-trimethylammonium, O-palmitoyl chitosan: Synthesis, physicochemical and biological properties. **International Journal of Biological Macromolecules**, v. 178, p. 558-568, 2021;
- Clotrimazole-loaded N-(2-hydroxy)-propyl-3-trimethylammonium, O-palmitoyl chitosan nanoparticles for topical treatment of vulvovaginal candidiasis. **Acta Biomaterialia**, v. 125, p. 312-321, 2021.

Additionally, other collaborative papers have been published, all using SSNMR as a tool for a wide-ranged characterization of chemically modified polymers:

- Self-aggregates of 3,6-O,O'-dimyristoylchitosan derivative are effective in enhancing the solubility and intestinal permeability of camptothecin. **Carbohydrate Polymers**, v. 177, p. 178–186, 2017;
- Bioproduction of N-acetyl-glucosamine from colloidal  $\alpha$ -chitin using an enzyme cocktail produced by *Aeromonas caviae* CHZ306. **World Journal of Microbiology and Biotechnology**, v. 35, n. 8, p. 114, 2019;
- Effect of amylolysis on the formation, the molecular, crystalline and thermal characteristics and the digestibility of retrograded starches. **International Journal of Biological Macromolecules**, v. 163, p. 1333–1343, 2020.
- Production of carbon nanofibers from PAN and lignin by solution blow spinning. **Journal of Polymer Research**, v. 28, p. 237-249, 2021.

## REFERENCES

- ACIERNO, D.; COLLYER, A. A. **Rheology and processing of liquid crystal polymers**. Glasgow: Springer Science, 1996. 331 p.
- ACOSTA, N.; JITINEZT, C.; BORAUT, V.; HERAS, A. Extraction and characterization of chitin from crustaceans. **Biomass and Bioenergy**, Oxford, v. 5, n. 2, p. 145–153, 1993.
- AIBA, S. Studies on chitosan: 4. Lysozymic hydrolysis of partially N-acetylated chitosans. **International Journal of Biological Macromolecules**, Amsterdam, v. 14, n. 4, p. 225–228, 1992.
- ÅKERHOLM, M.; HINTERSTOISSER, B.; SALMÉN, L. Characterization of the crystalline structure of cellulose using static and dynamic FT-IR spectroscopy. **Carbohydrate Research**, Oxford, v. 339, n. 3, p. 569–578, 2004.
- ALBURQUENQUE, C.; BUCAREY, S. A.; NEIRA-CARRILLO, A.; URZA, B.; HERMOSILLA, G.; TAPIA, C. V. Antifungal activity of low molecular weight chitosan against clinical isolates of *Candida* spp. **Medical Mycology**, Oxford, v. 48, n. 8, p. 1018–1023, 2010.
- ALLER, L. H.; PAGE, T. The abundance of the elements. **American Journal of Physics**, Melville, v. 30, n. 1, p. 79–79, 1962.
- ANDO, I.; ASAKURA, T. **Solid state NMR of polymers: studies in physical and theoretical chemistry**. Tokyo: Elsevier, 1998. 1017 p.
- ANDRADE, F. D.; NEWSON, W. R.; BERNARDINELLI, O. D.; RASHEED, F.; COBO, M. F.; PLIVELIC, T. S.; DE AZEVEDO, E. R.; KUKTAITE, R. An insight into molecular motions and phase composition of gliadin/glutenin glycerol blends studied by <sup>13</sup>C solid-state and <sup>1</sup>H time-domain NMR. **Journal of Polymer Science, Part B: polymer physics**, Hoboken, v. 56, n. 9, p. 739–750, 2018.
- ANDREANI, T.; MIZIARA, L.; LORENZÓN, E. N.; DE SOUZA, A. R.; KIILL, C. P.; FANGUEIRO, J. F.; GARCIA, M. L.; GREMIÃO, P. D.; SILVA, A. M.; SOUTO, E. B. Effect of mucoadhesive polymers on the in vitro performance of insulin-loaded silica nanoparticles: interactions with mucin and biomembrane models. **European Journal of Pharmaceutics and Biopharmaceutics**, Amsterdam, v. 93, p. 118–126, 2015.
- ANDREW, E. R.; BRADBURY, A.; EADES, R. G. Removal of dipolar broadening of nuclear magnetic resonance spectra of solids by specimen rotation. **Nature**, London, v. 183, n. 4678, p. 1802–1803, 1959.
- ANDREW, E. R.; EADES, R. G. Possibilities for high-resolution nuclear magnetic resonance spectra of crystals. **Discussions of the Faraday Society**, Cambridge, v. 34, n. 1, p. 38, 1962.
- ANDREWS, G. P.; LAVERTY, T. P.; JONES, D. S. Mucoadhesive polymeric platforms for controlled drug delivery. **European Journal of Pharmaceutics and Biopharmaceutics**, Amsterdam, v. 71, n. 3, p. 505–518, 2009.

ARANAZ, I.; MENGÍBAR, M.; HARRIS, R.; PAÑOS, I.; MIRALLES, B.; ACOSTA, N.; GALED, G.; HERAS, Á. Functional characterization of chitin and chitosan. **Current Chemical Biology**, Sharjah, v. 3, p. 203–230, 2009.

AZEREDO, R. B. V.; COLNAGO, L. A.; SOUZA, A. A.; ENGELSBERG, M. Continuous wave free precession: practical analytical tool for low-resolution nuclear magnetic resonance measurements. **Analytica Chimica Acta**, Amsterdam, v. 478, n. 2, p. 313–320, 2003.

BACHHAV, Y. G.; PATRAVALE, V. B. Microemulsion-based vaginal gel of clotrimazole: formulation, in vitro evaluation, and stability studies. **AAPS PharmSciTech**, New York, v. 10, n. 2, p. 476–481, 2009.

BADAWY, M. E. I.; RABEA, E. I.; ROGGE, T. M.; STEVENS, C. V.; STEURBAUT, W.; HÖFTE, M.; SMAGGHE, G. Fungicidal and insecticidal activity of O-acyl chitosan derivatives. **Polymer Bulletin**, Heidelberg, v. 54, n. 4–5, p. 279–289, 2005.

BAFNA, S.; KAUR, S.; BATRA, S. K. Membrane-bound mucins: the mechanistic basis for alterations in the growth and survival of cancer cells. **Oncogene**, London, v. 29, n. 20, p. 2893–2904, 2010.

BARBOSA, L. L.; KOCK, F. V. C.; SILVA, R. C.; FREITAS, J. C. C.; LACERDA, V.; CASTRO, E. V. R. Application of low-field NMR for the determination of physical properties of petroleum fractions. **Energy and Fuels**, Washington, v. 27, n. 2, p. 673–679, 2013.

BELOTTI, M.; MARTINELLI, A.; GIANFERRI, R.; BROSIO, E. A proton NMR relaxation study of water dynamics in bovine serum albumin nanoparticles. **Physical Chemistry Chemical Physics**, Cambridge, v. 12, n. 2, p. 516–522, 2010.

BENNETT, A. E.; RIENSTRA, C. M.; AUGER, M.; LAKSHMI, K. V.; GRIFFIN, R. G. Heteronuclear decoupling in rotating solids. **The Journal of Chemical Physics**, Melville, v. 103, n. 16, p. 6951–6958, 1995.

BERCEA, M.; NAVARD, P. Shear dynamics of aqueous suspensions of cellulose whiskers. **Macromolecules**, Washington, v. 33, n. 16, p. 6011–6016, 2000.

BERNARDINELLI, O. D.; LIMA, M. A.; REZENDE, C. A.; POLIKARPOV, I.; DE AZEVEDO, E. R. Quantitative <sup>13</sup>C MultiCP solid-state NMR as a tool for evaluation of cellulose crystallinity index measured directly inside sugarcane biomass. **Biotechnology for Biofuels**, London, v. 8, n. 1, p. 110, 2015.

BERNARDINELLI, O. D.; NOVOTNY, E. E.; DE AZEVEDO, E. R.; COLNAGO, L. A. Analyses of biomass products by nuclear magnetic resonance spectroscopy. *In*: VAZ JUNIOR, S. (ed.). **Analytical techniques and methods for biomass**. Berlin: Springer International Publishing, 2016. p. 143–172.

BIELECKI, A.; KOLBERT, A. C.; DE GROOT, H. J. M.; GRIFFIN, R. G.; LEVITT, M. H. Frequency-switched Lee-Goldburg sequences in solids. **Advances in Magnetic and Optical Resonance**, San Diego, v. 14, n. C, p. 111–124, 1990.

BIZZANI, M.; FLORES, D. W. M.; COLNAGO, L. A.; FERREIRA, M. D. Monitoring of soluble pectin content in orange juice by means of MIR and TD-NMR spectroscopy combined with machine learning. **Food Chemistry**, Amsterdam, v. 332, p. 127383-1-127383-7, 2020.

BIZZANI, M.; FLORES, D. W. M.; COLNAGO, L. A.; FERREIRA, M. D. Non-invasive spectroscopic methods to estimate orange firmness, peel thickness, and total pectin content. **Microchemical Journal**, Philadelphia, v. 133, p. 168–174, 2017.

BONFERONI, M. C.; SANDRI, G.; FERRARI, F.; ROSSI, S.; LARGHI, V.; ZAMBITO, Y.; CARAMELLA, C. Comparison of different in vitro and ex vivo methods to evaluate mucoadhesion of glycol-palmitoyl chitosan micelles. **Journal of Drug Delivery Science and Technology**, Amsterdam, v. 20, n. 6, p. 419–424, 2010.

BONI, F. I.; ALMEIDA, A.; LECHANTEUR, A.; SARMENTO, B.; CURY, B. S. F.; GREMIÃO, M. P. D. Mucoadhesive nanostructured polyelectrolytes complexes modulate the intestinal permeability of methotrexate. **European Journal of Pharmaceutical Sciences**, Amsterdam, v. 111, p. 73–82, 2018.

BOOTZ, A.; VOGEL, V.; SCHUBERT, D. Comparison of scanning electron microscopy , dynamic light scattering and analytical ultracentrifugation for the sizing of poly (butyl cyanoacrylate) nanoparticles. **European Journal of Pharmaceutics and Biopharmaceutics**, Amsterdam, v. 57, p. 369–375, 2004.

BORN, R.; SPIESS, H. W. *Ab initio* calculations of conformational effects on <sup>13</sup>C NMR spectra of amorphous polymers. In: SEELING, J. (ed.). **NMR basic principles and progress**. New York: Springer, 1997. p. 1–127.

BOSKEY, E. R.; TELSCH, K. M.; WHALEY, K. J.; MOENCH, T. R.; CONE, R. A. Acid production by vaginal flora *in vitro* is consistent with the rate and extent of vaginal acidification. **Infection and Immunity**, Washington, v. 67, n. 10, p. 5170–5175, 1999.

BRIGGS, K. T.; TARABAN, M. B.; WANG, W.; YU, Y. B. Nondestructive quantitative inspection of drug products using benchtop NMR relaxometry - the case of NovoMix® 30. **AAPS PharmSciTech**, New York, v. 20, n. 5, p. 189, 2019.

BRITTO, D.; CAMPANA-FILHO, S. P.; ASSIS, O. B. G. Role of the alkyl moiety and counter ions on the thermal stability of chitosan derivatives. **Journal of Applied Polymer Science**, Hoboken, v. 121, n. 2, p. 815–822, 2011.

BRUGNEROTTO, J.; LIZARDI, J.; GOYCOOLEA, F. M.; ARGUELLES-MONAL, W.; DESBRIÈRES, J.; RINAUDO, M. An infrared investigation in relation with chitin and chitosan characterization. **Polymer**, London, v. 42, n. 8, p. 3569–3580, 2001.

BURUM, D. P.; LINDER, M.; ERNST, R. R. Low-power multipulse line narrowing in solid-state NMR. **Journal of Magnetic Resonance**, Maryland Heights, v. 44, n. 1, p. 173–188, 1981.

- CABEÇA, L. F.; MARCONCINI, L. V.; MAMBRINI, G. P.; AZEREDO, R. B. V.; COLNAGO, L. A. Monitoring the transesterification reaction used in biodiesel production, with a low cost unilateral nuclear magnetic resonance sensor. **Energy and Fuels**, Washington, v. 25, n. 6, p. 2696–2701, 2011.
- CALVO, P.; REMUNAN-LOPEZ, C.; VILA-JATO, J. L.; ALONSO, M. J. Novel hydrophilic chitosan-polyethylene oxide nanoparticles as protein carriers. **Journal of Applied Polymer Science**, Hoboken, v. 63, n. 1, p. 125–132, 1997.
- CAMPANA-FILHO, S. P.; BRITTO, D.; CURTI, E.; ABREU, F. R.; CARDOSO, M. B.; MARCOS, V.; SIM, P. C.; GOY, R. C.; SIGNINI, R. Extração, estruturas e propriedades de  $\alpha$ - e  $\beta$ -quitina. **Química Nova**, São Paulo, v. 30, n. 3, p. 644–650, 2007.
- CANTÓN, E.; PEMÁN, J.; VIUDES, A.; QUINDÓS, G.; GOBERNADO, M.; ESPINEL-INGROFF, A. Minimum fungicidal concentrations of amphotericin B for bloodstream *Candida* species. **Diagnostic Microbiology and Infectious Disease**, Philadelphia, v. 45, n. 3, p. 203–206, 2003.
- CARAVATTI, P.; BRAUNSCHWEILER, L.; ERNST, R. R. Heteronuclear correlation spectroscopy in rotating solids. **Chemical Physics Letters**, Amsterdam, v. 100, n. 4, p. 305–310, 1983.
- CARDOZO, F. A.; FACCHINATTO, W. M.; COLNAGO, L. A.; CAMPANA-FILHO, S. P.; PESSOA, A. Bioproduction of N-acetyl-glucosamine from colloidal  $\alpha$ -chitin using an enzyme cocktail produced by *Aeromonas caviae* CHZ306. **World Journal of Microbiology and Biotechnology**, Dordrecht, v. 35, n. 8, p. 114, 2019.
- CARR, H. Y.; PURCELL, E. M. Effects of diffusion on free precession in nuclear magnetic resonance experiments. **Physical Review**, vol. 94, no. 3, p. 630–638, 1954.
- CARTIER, N.; DOMARD, A.; CHANZY, H. Single crystals of chitosan. **International Journal of Biological Macromolecules**, Amsterdam, v. 12, n. 5, p. 289–294, 1990.
- CARVALHO, L. C.; MORAIS, C. L. M.; LIMA, K. M. G.; TEIXEIRA, G. H. A. Assessment of macadamia kernel quality defects by means of near infrared spectroscopy (NIRS) and nuclear magnetic resonance (NMR). **Food Control**, Oxford, v. 106, p. 106695, 2019.
- CHAE, S. Y.; JANG, M-K.; NAH, J-W. Influence of molecular weight on oral absorption of water soluble chitosans. **Journal of Controlled Release**, Amsterdam, v. 102, n. 2, p. 383–394, 2005.
- CHANG, K. L. B.; TSAI, G.; LEE, J.; FU, W. R. Heterogeneous N-deacetylation of chitin in alkaline solution. **Carbohydrate Research**, Oxford, v. 303, n. 3, p. 327–332, 1997.
- CHATELET, C.; DAMOUR, O.; DOMARD, A. Influence of the degree of acetylation on some biological properties of chitosan films. **Biomaterials**, Amsterdam, v. 22, n. 3, p. 261–268, 2001.

CHO, J.; GRANT, J.; PIQUETTE-MILLER, M.; ALLEN, C. Synthesis and physicochemical and dynamic mechanical properties of a water-soluble chitosan derivative as a biomaterial. **Biomacromolecules**, Washington, v. 7, n. 10, p. 2845–2855, 2006.

CHO, Y-W.; JANG, J.; PARK, C. R.; KO, S-W. Preparation and solubility in acid and water of partially deacetylated chitins. **Biomacromolecules**, Washington, v. 1, n. 4, p. 609–614, 2000.

CLEEMPUT, M. V.; BUEKENHOUDT, A.; GERVEN, L. V.; HORSEWILL, A. J. Quantum and classical dynamics of a methyl group with tunneling frequency 3.4 MHz studied by low field NMR. **The Journal of Chemical Physics**, Melville, v. 103, n. 8, p. 2787–2794, 1995.

CLINICAL AND LABORATORY STANDARDS INSTITUTE. **Reference method for broth dilution antifungal susceptibility testing of yeasts**. 4. ed. Annapolis Junction: CLSI, 2017. 46 p.

COBO, M. F. **Exploração de técnicas de RMN dipolar e aproximações analíticas no estudo de reorientações de segmentos moleculares**. 2013. 203 f. Tese (Doutorado em Ciências) - Instituto de Física de São Carlos, Universidade de São Paulo, São Carlos, 2013.

COIMBRA, P. T.; BATHAZAR, C. F.; GUIMARÃES, J. T.; COUTINHO, N. M.; PIMENTEL, T. C.; CUCINELLI NETO, R. P.; ESMERINO, E. A.; FREITAS, M. Q.; SILVA, M. C.; TAVARES, M. I. B.; CRUZ, A. G. Detection of formaldehyde in raw milk by time domain nuclear magnetic resonance and chemometrics. **Food Control**, Oxford, v. 110, p. 107006, 2020.

COLNAGO, L. A.; ANDRADE, F. D.; SOUZA, A. A.; AZEREDO, R. B. V.; LIMA, A. A.; CERIONI, L. M.; OSÁN, T. M.; PUSIOL, D. J. Why is inline NMR rarely used as industrial sensor? Challenges and opportunities. **Journal of Chemical Engineering and Technology**, Chennai, v. 37, n. 2, p. 191–203, 2014.

COLNAGO, L. A.; ANDRADE, F. D. **RMN no domínio do tempo: fundamentos e aplicações offline e inline**. In: BIOTECNOLOGIA Aplicada à agro&Indústria. São Paulo: Editora Blucher, 2017. p. 439–470.

COOPER, C. L.; COSGROVE, T.; DUIJNEVELDT, J. S. V.; MURRAY, M.; PRESCOTT, S.W. The use of solvent relaxation NMR to study colloidal suspensions. **Soft Matter**, Cambridge, v. 9, n. 30, p. 7211–7228, 2013.

CROISIER, F.; JÉRÔME, C. Chitosan-based biomaterials for tissue engineering. **European Polymer Journal**, Oxford, v. 49, n. 4, p. 780–792, 2013.

CRUZ, R. A.; CATUNDA, T.; FACCHINATTO, W. M.; BALOGH, D. T.; FARIA, R. M. Absolute photoluminescence quantum efficiency of P3HT/CHCl<sub>3</sub> solution by thermal lens spectroscopy. **Synthetic Metals**, Lausanne, v. 163, p. 38–41, 2013.

DANHIER, F.; FERON, O.; PRÉAT, V. To exploit the tumor microenvironment: passive and active tumor targeting of nanocarriers for anti-cancer drug delivery. **Journal of Controlled Release**, Amsterdam, v. 148, n. 2, p. 135–146, 2010.

DAS NEVES, J.; ARAÚJO, F.; ANDRADE, F.; MICHIELS, J.; ARIËN, K. K.; VANHAM, G.; AMIJI, M.; BAHIA, M. F.; SARMENTO, B. *In vitro* and *ex vivo* evaluation of polymeric nanoparticles for vaginal and rectal delivery of the anti-HIV drug dapivirine. **Molecular Pharmaceutics**, Washington, v. 10, n. 7, p. 2793–2807, 2013.

DAS NEVES, J.; BAHIA, M. F.; AMIJI, M.; SARMENTO, B. Mucoadhesive nanomedicines: characterization and modulation of mucoadhesion at the nanoscale. **Expert Opinion on Drug Delivery**, Abingdon, v. 8, n. 8, p. 1085–1104, 2011.

DAS NEVES, J.; MICHIELS, J.; ARIËN, K. K.; VANHAM, G.; AMIJI, M.; BAHIA, M. F.; SARMENTO, B. Polymeric nanoparticles affect the intracellular delivery, antiretroviral activity and cytotoxicity of the microbicide drug candidate dapivirine. **Pharmaceutical Research**, New York, v. 29, n. 6, p. 1468–1484, 2012.

DAS NEVES, J.; PALMEIRA-DE-OLIVEIRA, R.; PALMEIRA-DE-OLIVEIRA, A.; RODRIGUES, F.; SARMENTO, B. Vaginal mucosa and drug delivery. *In*: KHUTORYANSKIY, V. V. (ed.). **Mucoadhesive materials and drug delivery systems**. New Jersey: John Wiley & Sons, 2014. p. 99–132.

DAS NEVES, J.; PINTO, E.; TEIXEIRA, B.; DIAS, G.; ROCHA, P.; CUNHA, T.; SANTOS, B.; AMARAL, M. H.; BAHIA, M. F. Local treatment of vulvovaginal candidosis: general and practical considerations. **Drugs**, Auckland, v. 68, n. 13, p. 1787–1802, 2008.

DAS NEVES, J.; SARMENTO, B. Precise engineering of dapivirine-loaded nanoparticles for the development of anti-HIV vaginal microbicides. **Acta Biomaterialia**, Amsterdam, v. 18, p. 77–87, 2015.

DASH, M.; CHIELLINI, F.; OTTENBRITE, R.M.; CHIELLINI, E. Chitosan—a versatile semi-synthetic polymer in biomedical applications. **Progress in Polymer Science**, London, v. 36, n. 8, p. 981–1014, 2011.

DE CARVALHO, F. G.; MAGALHÃES, T. C.; TEIXEIRA, N. M.; GONDIM, B. L. C.; CARLO, H. L.; DOS SANTOS, R. L.; DE OLIVEIRA, A. R.; DENADAI, Â. M. L. Synthesis and characterization of TPP/chitosan nanoparticles: Colloidal mechanism of reaction and antifungal effect on *C. albicans* biofilm formation. **Materials Science and Engineering C**, Amsterdam, v. 104, 2019.

DE AZEVEDO, E. R.; SAALWACHTER, K.; PASCUI, O.; DE SOUZA, A. A.; BONAGAMBA, T. J.; REICHERT, D. Intermediate motions as studied by solid-state separated local field NMR experiments. **Journal of Chemical Physics**, Melville, v. 128, n. 10, p. 104505-1-104505–12, 2008.

DELEZUK, J. A. M.; PAVINATTO, A.; CAMPANA-FILHO, S. P. Influence of the process parameters on  $\beta$ -chitin and  $\alpha$ -chitin extraction: probing about the grinding and particles size. **Materials Today: Proceedings**, Amsterdam, v. 14, p. 722–732, 2019.

DEMCO, D. E.; FECHETE, R.; BLÜMICH, B. Residual dipolar couplings of soft solids by accordion magic sandwich. **Chemical Physics Letters**, Amsterdam, v. 375, n. 3–4, p. 406–412, 2003.

DERBYSHIRE, W.; VAN DEN BOSCH, M.; VAN DUSSCHOTEN, D.; MACNAUGHTAN, W.; FARHAT, I. A.; HEMMINGA, M. A.; MITCHELL, J. R. Fitting of the beat pattern observed in NMR free-induction decay signals of concentrated carbohydrate-water solutions. **Journal of Magnetic Resonance**, Maryland Heights, v. 168, n. 2, p. 278–283, 2004.

DESBRIÈRES, J.; MARTINEZ, C.; RINAUDO, M. Hydrophobic derivatives of chitosan: characterization and rheological behaviour. **International Journal of Biological Macromolecules**, Amsterdam, v. 19, n. 1, p. 21–28, 1996.

DESESSO, J. M.; JACOBSON, C. F. Anatomical and physiological parameters affecting gastrointestinal absorption in humans and rats. **Food and Chemical Toxicology**, Oxford, v. 39, n. 3, p. 209–228, 2001.

DOTTO, G. L.; PINTO, L. A. A. Adsorption of food dyes onto chitosan: optimization process and kinetic. **Carbohydrate Polymers**, Oxford, v. 84, n. 1, p. 231–238, 2011.

DUAN, B.; HUANG, Y.; LU, A.; ZHANG, L. Recent advances in chitin based materials constructed via physical methods. **Progress in Polymer Science**, London, v. 82, p. 1–33, 2018.

DUER, M. J. **Solid-state NMR spectroscopy: principles and applications**. Cambridge: Blackwell Science, 2002. 587 p.

ELIPE, M. V. S.; LI, L.; NAGAPUDI, K.; KOOK, A.M.; COBAS, C.; IGLESIAS, I.; PENG, C. Application of <sup>19</sup>F time-domain NMR to measure content in fluorine-containing drug products. **Magnetic Resonance in Chemistry**, Oxford, v. 54, n. 6, p. 531–538, 2016.

ENSIGN, L. M.; CONE, R.; HANES, J. Nanoparticle-based drug delivery to the vagina: a review. **Journal of Controlled Release**, Amsterdam, v. 190, p. 500–514, 2014.

FACCHINATTO, W. M. **Preparação e caracterização de nanosuspensões e hidrogéis de N,O-metoxipoli (etilenoglicol)-g-quitosana para aplicação em sistemas de liberação de fármacos antitumorais**. 2016. 139 f. Dissertação (Mestrado em Físico-Química) - Instituto de Química de São Carlos, Universidade de São Paulo, São Carlos, 2016.

FACCHINATTO, W. M.; FIAMINGO, A.; SANTOS, D. M.; CAMPANA-FILHO, S. P. Characterization and physical-chemistry of methoxypoly(ethylene glycol)-g-chitosan. **International Journal of Biological Macromolecules**, Amsterdam, v. 124, p. 828–837, 2019.

FACCHINATTO, W. M.; GALANTE, J.; MESQUITA, L.; SILVA, D. S.; SANTOS, D. M. MORAES, T. B.; CAMPANA-FILHO, S. P.; COLNAGO, L. A.; SARMENTO, B.; DAS NEVES, J. Clotrimazole-loaded N-(2-hydroxy)-propyl-3-trimethylammonium, O-palmitoyl chitosan nanoparticles for topical treatment of vulvovaginal candidiasis. **Acta Biomaterialia**, Amsterdam, v. 125, p. 312–321, 2021.

FACCHINATTO, W. M.; GARCIA, R. H. S.; SANTOS, D. M.; FIAMINGO, A.; FLORES, D. W. M.; CAMPANA-FILHO, S. P.; DE AZEVEDO, E. R.; COLNAGO, L. A. Fast-forward approach of time-domain NMR relaxometry for solid-state chemistry of chitosan. **Carbohydrate Polymers**, Oxford, v. 256, p. 117576-1-117576–10, 2020.

FACCHINATTO, W. M.; SANTOS, D. M.; FIAMINGO, A.; BERNARDES-FILHO, R.; CAMPANA-FILHO, S. P.; DE AZEVEDO, E. R.; COLNAGO, L. A. Evaluation of chitosan crystallinity: a high-resolution solid-state NMR spectroscopy approach. **Carbohydrate Polymers**, Oxford, v. 250, p. 116891-1-116891–14, 2020.

FACCHINATTO, W. M.; TORRES, B. B. M.; BALOGH, D. T. A. One-pot synthesis of poly-(3-hexylthiophene) with variable degrees of molar mass and regioregularity. **Journal of Polymer Research**, Dordrecht, v. 23 (187), p.1-8, 2016.

FAN, W.; YAN, W.; XU, Z.; NI, H. Formation mechanism of monodisperse, low molecular weight chitosan nanoparticles by ionic gelation technique. **Colloids and surfaces B: biointerfaces**, Amsterdam, v. 90, p. 21–27, 2012.

FAN, Y.; SAITO, T.; ISOGAI, A. Chitin nanocrystals prepared by TEMPO-mediated oxidation of  $\alpha$ -chitin. **Biomacromolecules**, Washington, v. 9, n. 1, p. 192–198, 2008a.

FAN, Y.; SAITO, T.; ISOGAI, A. Preparation of chitin nanofibers from squid Pen  $\beta$ -chitin by simple mechanical treatment under acid conditions. **Biomacromolecules**, Washington, v. 9, n. 7, p. 1919–1923, 2008b.

FAN, Y.; SAITO, T.; ISOGAI, A. TEMPO-mediated oxidation of  $\beta$ -chitin to prepare individual nanofibrils. **Carbohydrate Polymers**, Oxford, v. 77, n. 4, p. 832–838, 2009.

FARIA, G. C.; DUONG, D. T.; DA CUNHA, G. P.; SELTER, P.; STRASSØ, L. A.; DAVIDSON, E. C.; SEGALMAN, R. A.; HANSEN, M. R.; DE AZEVEDO, E. R.; SALLEO, A. On the growth, structure and dynamics of P3EHT crystals. **Journal of Materials Chemistry C**, Cambridge, v. 8, n. 24, p. 8155–8170, 2020.

FECHETE, R.; DEMCO, D.; BLÜMICH, B. Chain orientation and slow dynamics in elastomers by mixed magic-Hahn echo decays. **The Journal of Chemical Physics**, Melville, v. 118, p. 2411–2421, 2003.

FENG, H.; DONG, C. M. Preparation, characterization, and self-assembled properties of biodegradable chitosan-poly(L-lactide) hybrid amphiphiles. **Biomacromolecules**, Washington, v. 7, n. 11, p. 3069–3075, 2006.

FIAMINGO, A.; DELEZUK, J. A. M.; TROMBOTTO, S.; DAVID, L.; CAMPANA-FILHO, S. P. Extensively deacetylated high molecular weight chitosan from the multistep ultrasound-assisted deacetylation of beta-chitin. **Ultrasonics Sonochemistry**, Amsterdam, v. 32, p. 79–85, 2016.

FLAUZINO NETO, W. P.; SILVÉRIO, H. A.; DANTAS, N. O.; PASQUINI, D. Extraction and characterization of cellulose nanocrystals from agro-industrial residue – Soy hulls. **Industrial Crops & Products**, Amsterdam, v. 42, p. 480–488, 2013.

FOCHER, B; BELTRAME, P L; NAGGI, A; TORRI, G. Alkaline N-deacetylation of chitin enhanced by flash treatments. Reaction kinetics and structure modifications. **Carbohydrate Polymers**, Oxford, v. 12, n. 4, p. 405–418, 1990.

FOCHER, B; NAGGI, A; TORRI, G; COSANI, A; TERBOJEVICH, M. Chitosans from *Euphausia superba*. 2: characterization of solid state structure. **Carbohydrate Polymers**, Oxford, v. 18, n. 1, p. 43–49, 1992.

FORATO, L. A; BERNARDES-FILHO, R.; COLNAGO, L. A. Protein structure in KBr pellets by infrared spectroscopy. **Analytical Biochemistry**, Philadelphia, v. 259, p. 136–141, 1998.

FRANCIS SUH, J.-K; MATTHEW, H. W.T. Application of chitosan-based polysaccharide biomaterials in cartilage tissue engineering: a review. **Biomaterials**, Amsterdam, v. 21, n. 24, p. 2589–2598, 2000.

GARCIA-FUENTES, M.; ALONSO, M. J. Chitosan-based drug nanocarriers: where do we stand? **Journal of Controlled Release**, Amsterdam, v. 161, n. 2, p. 496–504, 2012.

GARCIA, R. H. S.; FILGUEIRAS, J. G.; DE AZEVEDO, E. R.; COLNAGO, L. A. Power-optimized, time-reversal pulse sequence for a robust recovery of signals from rigid segments using time domain NMR. **Solid State Nuclear Magnetic Resonance**, London, v. 104, p. 101619-1-101619-8, 2019.

GARDNER, K. H.; BLACKWELL, J. Refinement of the structure of  $\beta$ -Chitin. **Biopolymers**, Hoboken, v. 14, p. 1581–1595, 1975.

GARVEY, C. J.; PARKER, I. H.; SIMON, G. P. On the interpretation of X-ray diffraction powder patterns in terms of the nanostructure of cellulose I fibres. **Macromolecular Chemistry and Physics**, Weinheim, v. 206, n. 15, p. 1568–1575, 2005.

GAURAV, C.; NIKHIL, G.; DEEPTI, S.; KALRA, S.; GOUTAM, R.; AMIT, G. K. Albumin stabilized silver nanoparticles-clotrimazole  $\beta$ -cyclodextrin hybrid nanocomposite for enriched anti-fungal activity in normal and drug resistant *Candida* cells. **RSC Advances**, Cambridge, v. 5, n. 87, p. 71190–71202, 2015.

GIL, V. M. S.; GERALDES, C. F. G. C. **Ressonância magnética nuclear**: fundamentos, métodos e aplicações. Lisboa: Fundação Calouste Gulbenkian, 1987.

GOMES, B. F.; NUNES, L. M. S.; LOBO, C. M. S.; CARVALHO, A. S.; CABEÇA, L. F.; COLNAGO, L. A. In situ analysis of copper electrodeposition reaction using unilateral NMR sensor. **Journal of Magnetic Resonance**, Maryland Heights, v. 261, p. 83–86, 2015.

GONIL, P.; SAJOMSANG, W. Applications of magnetic resonance spectroscopy to chitin from insect cuticles. **International Journal of Biological Macromolecules**, Amsterdam, v. 51, n. 4, p. 514–522, 2012.

GONZAGA, L. A. C.; MARTINS, M. C. F.; CORREA, A. C.; FACCHINATTO, W. M.; SILVA, C. M. P.; COLNAGO, L. A.; MATTOSO, L. H. C. Production of carbon nanofibers from PAN and lignin by solution blow spinning. **Journal of Polymer Research**, Dordrecht, v. 28 (237), p. 1-12, 2021.

GOODRICH, J. D.; WINTER, W. T. Alpha-Chitin nanocrystals prepared from shrimp shells and their specific surface area measurement. **Biomacromolecules**, Washington, v. 8, n. 1, p. 252–257, 2007.

GOPALAN-NAIR, K.; DUFRESNE, A. Crab shell chitin whisker reinforced natural rubber nanocomposites. 1. Processing and swelling behavior. **Biomacromolecules**, Washington, v. 4, n. 3, p. 657–665, 2003.

GORODESKI, G. I. Estrogen increases the permeability of the cultured human cervical epithelium by modulating cell deformability. **American Journal of Physiology**, Rockville, v. 275, p. C888–C899, 1998.

GOY, R. C.; BRITTO, D.; ASSIS, O. B. G. A review of the antimicrobial activity of chitosan. **Polímeros: ciência e tecnologia**, São Carlos, v. 19, n. 3, p. 241–247, 2009.

GRAMMEN, C.; AUGUSTIJNS, P.; BROUWERS, J. In vitro profiling of the vaginal permeation potential of anti-HIV microbicides and the influence of formulation excipients. **Antiviral Research**, Amsterdam, v. 96, n. 2, p. 226–233, 2012.

GRZĄBKA-ZASADZIŃSKA, A.; AMIETSZAJEW, T.; BORYSIK, S. Thermal and mechanical properties of chitosan nanocomposites with cellulose modified in ionic liquids. **Journal of Thermal Analysis and Calorimetry**, Budapest, v. 130, n. 1, p. 143–154, 2017.

GUIBAL, E. Interactions of metal ions with chitosan-based sorbents: a review. **Separation and Purification Technology**, Oxford, v. 38, n. 1, p. 43–74, 2004.

GUPTA, K. C.; JABRAIL, F. H. Effects of degree of deacetylation and cross-linking on physical characteristics, swelling and release behavior of chitosan microspheres. **Carbohydrate Polymers**, Oxford, v. 66, n. 1, p. 43–54, 2006.

GUTHRIE, J. P. Hydrolysis of esters of oxy acids: pKa values for strong acids; Brflnsted relationship for attack of water at methyl; free energies of hydrolysis of esters of oxy acids; and a linear relationship between free energy of hydrolysis and pKa holding over a ra. **Canadian Journal of Chemistry**, Ottawa, v. 56, p. 2342–2354, 1978.

HAEBERLEN, U. **High resolution NMR in solids: selective averaging**. London: Academic Press, 1976. 187 p.

HANSEN, E. W.; KRISTIANSEN, P. E.; PEDERSEN, B. Crystallinity of polyethylene derived from solid-state proton NMR free induction decay. **Journal of Physical Chemistry B**, Washington, v. 102, n. 28, p. 5444–5450, 1998.

HARISH PRASHANTH, K. V.; KITTUR, F. S.; THARANATHAN, R. N. Solid state structure of chitosan prepared under different N-deacetylating conditions. **Carbohydrate Polymers**, Oxford, v. 50, n. 1, p. 27–33, 2002.

HARISH PRASHANTH, K. V.; THARANATHAN, R. N. Chitin/chitosan: modifications and their unlimited application potential-an overview. **Trends in Food Science and Technology**, Oxford, v. 18, n. 3, p. 117–131, 2007.

HASSAINIA, A.; SATHA, H.; BOU, S. Chitin from *Agaricus bisporus*: extraction and characterization. **International Journal of Biological Macromolecules**, Amsterdam, v. 117, p. 1334–1342, 2018.

HEUX, L.; BRUGNEROTTO, J.; DESBRIÈRES, J.; VERSALI, M. F.; RINAUDO, M. Solid state NMR for determination of degree of acetylation of chitin and chitosan. **Biomacromolecules**, Washington, v. 1, n. 4, p. 746–751, 2000.

HIRANO, S.; TSUCHIDA, H.; NAGAO, N. N-acetylation in chitosan and the rate of its enzymic hydrolysis. **Biomaterials**, Amsterdam, v. 10, n. 8, p. 574–576, 1989.

HONG, M.; YAO, X.; JAKES, K.; HUSTER, D. Investigation of molecular motions by Lee-Goldburg cross-polarization NMR spectroscopy. **Journal of Physical Chemistry B**, Washington, v. 106, n. 29, p. 7355–7364, 2002.

HONG, M. S.; CHOI, G. M.; KIM, J.; JANG, J.; CHOI, B.; KIM, J. K.; JEONG, S.; LEEM, S.; KWON, H. Y.; HWANG, H. B.; IM, H. G.; PARK, J. U.; BAE, B. S.; JIN, J. Biomimetic chitin–silk hybrids: an optically transparent structural platform for wearable devices and advanced electronics. **Advanced Functional Materials**, Weinheim, v. 28, n. 24, p. 1–11, 2018.

HOQUE, J.; ADHIKARY, U.; YADAV, V.; SAMADDAR, S.; KONAI, M. M.; PRAKASH, R. G.; PARAMANANDHAM, K.; SHOME, B. R.; SANYAL, K.; HALDAR, J. Chitosan derivatives active against multidrug-resistant bacteria and pathogenic fungi: *In vivo* evaluation as topical antimicrobials. **Molecular Pharmaceutics**, Washington, v. 13, n. 10, p. 3578–3589, 2016.

HUANG, J.; CHENG, Z. H.; XIE, H. H.; GONG, J. Y.; LOU, J.; GE, Q.; WANG, Y. J.; WU, Y. F.; LIU, S. W.; SUN, P. L.; MAO, J. W. Effect of quaternization degree on physiochemical and biological activities of chitosan from squid pens. **International Journal of Biological Macromolecules**, Amsterdam, v. 70, p. 545–550, 2014.

HUANG, M.; KHOR, E.; LIM, L. Y. Uptake and cytotoxicity of chitosan molecules and nanoparticles: effects of molecular weight and degree of deacetylation. **Pharmaceutical Research**, New York, v. 21, n. 2, p. 344–353, 2004.

HUANG, Y.; YANG, J.; CHEN, L.; ZHANG, L. Chitin nanofibrils to stabilize long-life pickering foams and their application for lightweight porous materials. **ACS Sustainable Chemistry and Engineering**, Washington, v. 6, n. 8, p. 10552–10561, 2018.

HUO, M.; ZHANG, Y.; ZHOU, J.; ZOU, A.; LI, J. Formation, microstructure, biodistribution and absence of toxicity of polymeric micelles formed by N-octyl-N,O-carboxymethyl chitosan. **Carbohydrate Polymers**, Oxford, v. 83, n. 4, p. 1959–1969, 2011.

IFUKU, S.; NOGI, M.; ABE, K.; YOSHIOKA, M.; MORIMOTO, M.; SAIMOTO, H.; YANO, H. Preparation of chitin nanofibers with a uniform width as  $\alpha$ -chitin from crab shells. **Biomacromolecules**, Washington, v. 10, n. 6, p. 1584–1588, 2009.

IFUKU, S.; NOMURA, R.; MORIMOTO, M.; SAIMOTO, H. Preparation of chitin nanofibers from mushrooms. **Materials**, Basel, v. 4, n. 8, p. 1417–1425, 2011.

IFUKU, S.; SAIMOTO, H. Chitin nanofibers: preparations, modifications, and applications. **Nanoscale**, Cambridge, v. 4, p. 3308–3318, 2012.

ING, L. Y.; ZIN, N. M.; SARWAR, A.; KATAS, H. Antifungal activity of chitosan nanoparticles and correlation with their physical properties. **International Journal of Biomaterials**, London, v. 2012, p. 1–9, 2012.

IOELOVICH, M. Crystallinity and hydrophilicity of chitin and chitosan. **Research and Reviews: journal of chemistry**, Hyderabad, v. 3, n. 3, p. 7–14, 2014. .

ISHII, D.; SAITO, T.; ISOGAI, A. Viscoelastic evaluation of average length of cellulose nanofibers prepared by tempo-mediated oxidation. **Biomacromolecules**, Whashington, v. 12, n. 3, p. 548–550, 2011.

JIANG, H.; LIANG, J.; GRANT, J. T.; SU, W.; BUNNING, T. J.; COOPER, T. M.; ADAMS, W. W. Characterization of chitosan and rare-earth-metal-ion doped chitosan films. **Macromolecular Chemistry and Physics**, Weinheim, v. 198, n. 5, p. 1561–1578, 1997.

JINTAPATTANAKIT, A.; MAO, S.; KISSEL, T.; JUNYAPRASERT, V. B. Physicochemical properties and biocompatibility of N-trimethyl chitosan: Effect of quaternization and dimethylation. **European Journal of Pharmaceutics and Biopharmaceutics**, Amsterdam, v. 70, n. 2, p. 563–571, 2008.

JOÃO, C. F. C.; ECHEVERRIA, C.; VELHINHO, A.; SILVA, J. C.; GODINHO, M. H.; BORGES, J. P. Bio-inspired production of chitosan/chitin films from liquid crystalline suspensions. **Carbohydrate Polymers**, Oxford, v. 155, p. 372–381, 2017.

JØRAHOLMEN, M. W.; BHARGAVA, A.; JULIN, K.; JOHANNESSEN, M.; ŠKALKO-BASNET, N. The antimicrobial properties of chitosan can be tailored by formulation. **Marine Drugs**, Basel, v. 18, n. 2, p. 1–15, 2020.

JØRAHOLMEN, M. W.; VANIĆ, Ž.; THO, I.; ŠKALKO-BASNET, N. Chitosan-coated liposomes for topical vaginal therapy: assuring localized drug effect. **International Journal of Pharmaceutics**, Amsterdam, v. 472, n. 1–2, p. 94–101, 2014.

JUNKASEM, J.; RUJIRAVANIT, R.; GRADY, B. P.; SUPAPHOL, P. X-ray diffraction and dynamic mechanical analyses of  $\alpha$ -chitin whisker-reinforced poly(vinyl alcohol) nanocomposite nanofibers. **Polymer International**, Oxford, v. 59, n. 1, p. 85–91, 2010.

KADOKAWA, J. I.; TAKEGAWA, A.; MINE, S.; PRASAD, K. Preparation of chitin nanowhiskers using an ionic liquid and their composite materials with poly(vinyl alcohol). **Carbohydrate Polymers**, Oxford, v. 84, n. 4, p. 1408–1412, 2011.

KASAAI, M. R. Determination of the degree of N-acetylation for chitin and chitosan by various NMR spectroscopy techniques: a review. **Carbohydrate Polymers**, Oxford, v. 79, n. 4, p. 801–810, 2010.

KAYA, M.; MUJTABA, M.; EHRLICH, H.; SALABERRIA, A. M.; BARAN, T.; AMEMIYA, C. T.; GALLI, R.; AKYUZ, L.; SARGIN, I.; LABIDI, J. On chemistry of  $\gamma$ -chitin. **Carbohydrate Polymers**, Oxford, v. 176, p. 177–186, 2017.

KHAN, A. M.; SHAH, S. S. Determination of critical micelle (cmc) of sodium dedecyl sulfate (SDs) and effect of low concentration of pyrene on its cmc using ORIGIN software. **Journal of the Chemical Society of Pakistan**, Karachi, v. 30, n. 2, p. 186–191, 2008.

KNAUL, J. Z.; KASAAI, M. R.; BUI, V. T.; CREBER, K. A. M. Characterization of deacetylated chitosan and chitosan molecular weight review. **Canadian Journal of Chemistry**, Ottawa, v. 76, n. 11, p. 1699–1706, 1998.

KOCK, F. V. C.; COLNAGO, L. A. Rapid method for monitoring chitosan coagulation using low-field NMR relaxometry. **Carbohydrate Polymers**, Oxford, v. 150, p. 1–4, 2016.

KOCK, F. V. C.; MONARETTO, T.; COLNAGO, L. A. Time-domain NMR relaxometry as an alternative method for analysis of chitosan-paramagnetic ion interactions in solution. **International Journal of Biological Macromolecules**, Amsterdam, v. 98, p. 228–232, 2017.

KONO, H. Two-dimensional magic angle spinning NMR investigation of naturally occurring chitins: precise  $^1\text{H}$  and  $^{13}\text{C}$  resonance assignment of  $\alpha$ - and  $\beta$ -chitin. **Biopolymers**, Hoboken, v. 75, n. 3, p. 255–263, 2004.

KOSE, R.; KONDO, T. Favorable 3D-network formation of chitin nanofibers dispersed in water prepared using aqueous counter collision. **Journal of Fiber Science and Technology**, Tokyo, v. 67, n. 4, p. 91–95, 2011.

KOSTOV, K. L.; BELAMIE, E.; ALONSO, B.; MINEVA, T. Surface chemical states of cellulose, chitin and chitosan studied by density functional theory and high-resolution photoelectron spectroscopy. **Bulgarian Chemical Communications**, Sofia, v. 50, p. 135–146, 2018.

KOTZÉ, A. F.; LEEUW, B. J.; LUEBEN, H. L.; BOER, A. G.; VERHOEF, J. C.; JUNGINGER, H. E. Chitosans for enhanced delivery of therapeutic peptides across intestinal epithelia: in vitro evaluation in Caco-2 cell monolayers. **International Journal of Pharmaceutics**, Amsterdam, v. 159, p. 243–253, 1997.

KOWALSKI, B. R.; SEASHOLTZ, M. B. Recent developments in multivariate calibration. **Journal of Chemometrics**, v. 5, n. 3, p. 129–145, 1991.

KRISTIANSEN, P. E.; HANSEN, E. W.; PEDERSEN, B. Phase distribution during isothermal crystallization of polyethylene probed by solid-state proton NMR free induction decay. **Journal of Physical Chemistry B**, Washington, v. 103, n. 18, p. 3552–3558, 1999.

KUBOTA, N.; EGUCHI, Y. Facile preparation of water-soluble N-acetylated chitosan and molecular weight dependence of its water-solubility. **Polymer Journal**, London, v. 29, n. 2, p. 123–127, 2005.

KUBOTA, N.; TATSUMOTO, N.; SANO, T.; TOYA, K. A simple preparation of half N-acetylated chitosan highly soluble in water and aqueous organic solvents. **Carbohydrate Research**, Oxford, v. 324, n. 4, p. 268–274, 2000.

KUMIRSKA, J.; WEINHOLD, M. X.; SAUVAGEAU, J. C. M.; THÖMING, J.; KACZYŃSKI, Z.; STEPNOWSKI, P. Determination of the pattern of acetylation of low-molecular-weight chitosan used in biomedical applications. **Journal of Pharmaceutical and Biomedical Analysis**, Amsterdam, v. 50, n. 4, p. 587–590, 2009.

KURITA, K.; ISHII, S.; TOMITA, K.; NISHIMURA, S-I; SHIMODA, K. Reactivity characteristics of squid  $\beta$ -chitin as compared with those of shrimp chitin: high potentials of squid chitin as a starting material for facile chemical modifications. **Journal of Polymer Science Part A: polymer chemistry**, Hoboken, v. 32, n. 6, p. 1027–1032, 1994.

KURITA, K.; KAMIYA, M.; NISHIMURA, S. I. Solubilization of a rigid polysaccharide: Controlled partial N-acetylation of chitosan to develop solubility. **Carbohydrate Polymers**, Oxford, v. 16, n. 1, p. 83–92, 1991.

KURITA, K.; SANNAN, T.; IWAKURA, Y. Studies on chitin, 4. Evidence for formation of block and random copolymers of N-acetyl-D-glucosamine and D-glucosamine by hetero- and homogeneous hydrolyses. **Die Makromolekulare Chemie**, Weinheim, v. 178, n. 12, p. 3197–3202, 1977.

LAMARQUE, G.; CRETENET, M.; VITON, C.; DOMARD, A. New route of deacetylation of  $\alpha$ - and  $\beta$ -chitins by means of freeze - pump out - thaw cycles. **Biomacromolecules**, Washington, v. 6, n. 3, p. 1380–1388, 2005.

LAMARQUE, G.; VITON, C.; DOMARD, A. Comparative study of the first heterogeneous deacetylation of  $\alpha$ - and  $\beta$ -chitins in a multistep process. **Biomacromolecules**, Washington, v. 5, n. 3, p. 992–1001, 2004a.

LAMARQUE, G.; VITON, C.; DOMARD, A. Comparative study of the second and third heterogeneous deacetylations of  $\alpha$ - and  $\beta$ -chitins in a multistep process. **Biomacromolecules**, Washington, v. 5, n. 5, p. 1899–1907, 2004b.

LANGOTH, N.; KAHLBACHER, H.; SCHÖFFMANN, G.; SCHMEROLD, I.; SCHUH, M.; FRANZ, S.; KURKA, P.; BERNKOP-SCHNÜRCH, A. Thiolated chitosans: design and *in vivo* evaluation of a mucoadhesive buccal peptide drug delivery system. **Pharmaceutical Research**, New York, v. 23, n. 3, p. 573–579, 2006.

LARSSON, P. T.; WICKHOLM, K.; IVERSEN, T. A CP/MAS carbon-13 NMR investigation of molecular ordering in celluloses. **Carbohydrate Research**, Oxford, v. 302, n. 1–2, p. 19–25, 1997.

- LAVALL, R. L.; ASSIS, O. B. G.; CAMPANA-FILHO, S. P. Beta-chitin from the pens of *Loligo* sp.: extraction and characterization. **Bioresource Technology**, Amsterdam, v. 98, n. 13, p. 2465–72, 2007.
- LAVERTU, M.; DARRAS, V.; BUSCHMANN, M. D. Kinetics and efficiency of chitosan reacylation. **Carbohydrate Polymers**, Oxford, v. 87, n. 2, p. 1192–1198, 2012.
- LAVERTU, M.; XIA, Z.; SERREQUI, A. N.; BERRADA, M.; RODRIGUES, A.; WANG, D.; BUSCHMANN, M. D.; GUPTA, A. A validated <sup>1</sup>H NMR method for the determination of the degree of deacetylation of chitosan. **Journal of Pharmaceutical and Biomedical Analysis**, Amsterdam, v. 32, n. 6, p. 1149–1158, 2003.
- LEE, H-C.; BRANT, D. A. Rheology of concentrated isotropic and anisotropic xanthan solutions. 1. A rodlike low molecular weight sample. **Macromolecules**, Washington, v. 35, n. 6, p. 2212–2222, 2002.
- LEVITT, M. H. **Spin dynamics: basics of nuclear magnetic resonance**. 2. ed. Chichester: John Wiley & Sons, 2008. 740 p.
- LI, H.; LIU, J.; DING, S.; ZHANG, C.; SHEN, W.; YOU, Q. Synthesis of novel pH-sensitive chitosan graft copolymers and micellar solubilization of paclitaxel. **International Journal of Biological Macromolecules**, Amsterdam, v. 44, n. 3, p. 249–256, 2009.
- LI, J.; REVOL, J. F.; MARCHESSAULT, R. H. Rheological properties of aqueous suspensions of chitin crystallites. **Journal of Colloid and Interface Science**, Philadelphia, v. 183, n. 2, p. 365–373, 1996.
- LI, W.; LIU, W.; WEN, W.; LIU, H.; LIU, M.; ZHOU, C.; LUO, B. The liquid crystalline order, rheology and their correlation in chitin whiskers suspensions. **Carbohydrate Polymers**, Oxford, v. 209, n. May, p. 92–100, 2019.
- LI, Z.; PALANIYANDI, S.; ZENG, R.; TUO, W.; ROOPENIAN, D. C.; ZHU, X. Transfer of IgG in the female genital tract by MHC class I-related neonatal Fc receptor (FcRn) confers protective immunity to vaginal infection. **Proceedings of the National Academy of Sciences of the United States of America**, Washington, v. 108, n. 11, p. 4388–4393, 2011.
- LIN, N.; HUANG, J.; DUFRESNE, A. Preparation, properties and applications of polysaccharide nanocrystals in advanced functional nanomaterials: a review. **Nanoscale**, Cambridge, v. 4, n. 11, p. 3274–3294, 2012.
- LOWE, I. J. Free induction decays of rotating solids. **Physical Review Letters**, College Park, v. 2, n. 7, p. 285–287, 1959.
- LU, Y.; SUN, Q.; SHE, X.; XIA, Y.; LIU, Y.; LI, J.; YANG, D. Fabrication and characterisation of alfa-chitin nanofibers and highly transparent chitin films by pulsed ultrasonication. **Carbohydrate Polymers**, Oxford, v. 98, n. 2, p. 1497–1504, 2013.
- MACHADO, R. M.; PALMEIRA-DE-OLIVEIRA, A.; GASPAR, C.; MARTINEZ-DE-OLIVEIRA, J.; PALMEIRA-DE-OLIVEIRA, R. Studies and methodologies on vaginal drug permeation. **Advanced Drug Delivery Reviews**, Amsterdam, v. 92, p. 14–26, 2015.

- MAO, S.; SHUAI, X.; UNGER, F.; SIMON, M.; BI, D.; KISSEL, T. The depolymerization of chitosan: effects on physicochemical and biological properties. **International Journal of Pharmaceutics**, Amsterdam, v. 281, n. 1–2, p. 45–54, 2004.
- MARTIN, L.; WILSON, C. G.; KOOSHA, F.; TETLEY, L.; GRAY, A. I.; SENEL, S.; UCHEGBU, I. F. The release of model macromolecules may be controlled by the hydrophobicity of palmitoyl glycol chitosan hydrogels. **Journal of Controlled Release**, Amsterdam, v. 80, n. 1–3, p. 87–100, 2002.
- MATSUI, S. Suppressing the zero-frequency artifact in magic-sandwich-echo proton images of solids. **Journal of Magnetic Resonance**, Maryland Heights, v. 98, n. 3, p. 618–621, 1992.
- MAUS, A.; HERTLEIN, C.; SAALWÄCHTER, K. A robust proton NMR method to investigate hard/soft ratios, crystallinity, and component mobility in polymers. **Macromolecular Chemistry and Physics**, Weinheim, v. 207, n. 13, p. 1150–1158, 2006.
- MEIBOOM, S.; GILL, D. Modified spin-echo method for measuring nuclear relaxation times. **Review of Scientific Instruments**, Weinheim, v. 29, n. 8, p. 688–691, 1958.
- MENG, J.; STURGIS, T. F.; YOUAN, B. B. C. Engineering tenofovir loaded chitosan nanoparticles to maximize microbicide mucoadhesion. **European Journal of Pharmaceutical Sciences**, Amsterdam, v. 44, n. 1–2, p. 57–67, 2011.
- METZ, G.; ZILIOX, M.; SMITH, S. O. Towards quantitative CP-MAS NMR. **Solid State Nuclear Magnetic Resonance**, London, v. 7, n. 3, p. 155–160, 1996.
- MILOT, C.; MCBRIEN, J.; ALLEN, S.; GUIBAL, E. Influence of physicochemical and structural characteristics of chitosan flakes on molybdate sorption. **Journal of Applied Polymer Science**, Hoboken, v. 68, n. 4, p. 571–580, 1998.
- MINKE, R.; BLACKWELL, J. The structure of  $\alpha$ -Chitin. **Journal of Molecular Biology**, London, v. 120, n. 2, p. 167–181, 1978.
- MIRMOHSENI, A.; SEYED DORRAJI, M. S.; FIGOLI, A.; TASSELLI, F. Chitosan hollow fibers as effective biosorbent toward dye: preparation and modeling. **Bioresource Technology**, Amsterdam, v. 121, p. 212–220, 2012.
- MORIN, A.; DUFRESNE, A. Nanocomposites of chitin whiskers from *Riftia* tubes and poly(caprolactone). **Macromolecules**, Washington, v. 35, n. 6, p. 2190–2199, 2002.
- MOTIEI, M.; KASHANIAN, S.; LUCIA, L. A.; KHAZAEI, M. Intrinsic parameters for the synthesis and tuned properties of amphiphilic chitosan drug delivery nanocarriers. **Journal of Controlled Release**, Amsterdam, v. 260, n. June, p. 213–225, 2017.
- MUNOWITZ, M. G.; GRIFFIN, R. G.; BODENHAUSEN, G.; HUANG, T. H. Two-dimensional rotational spin-echo nuclear magnetic resonance in solids: correlation of chemical shift and dipolar interactions. **Journal of the American Chemical Society**, Washington, v. 103, n. 10, p. 2529–2533, 1981.

MUSHI, N. E.; NISHINO, T.; BERGLUND, L. A.; ZHOU, Q. Strong and tough chitin film from  $\alpha$ -chitin nanofibers prepared by high pressure homogenization and chitosan addition. **ACS Sustainable Chemistry and Engineering**, Washington, v. 7, n. 1, p. 1692–1697, 2019.

MUTUNGI, C.; PASSAUER, L.; ONYANGO, C.; JAROS, D.; ROHM, H. Debranched cassava starch crystallinity determination by Raman spectroscopy: Correlation of features in Raman spectra with X-ray diffraction and  $^{13}\text{C}$  CP/MAS NMR spectroscopy. **Carbohydrate Polymers**, Oxford, v. 87, n. 1, p. 598–606, 2012.

NAGLIK, J. R.; MOYES, D. L.; WÄCHTLER, B.; HUBE, B. *Candida albicans* interactions with epithelial cells and mucosal immunity. **Microbes and Infection**, Issy-les-Moulineaux, v. 13, n. 12–13, p. 963–976, 2011.

NASKAR, S.; SHARMA, S.; KUOTSU, K. Chitosan-based nanoparticles: an overview of biomedical applications and its preparation. **Journal of Drug Delivery Science and Technology**, Amsterdam, v. 49, p. 66–81, 2019.

NAZAR, H.; FATOUROS, D. G.; VAN DER MERWE, S. M.; BOUROPOULOS, N.; AVGOUROPOULOS, G.; TSIBOUKLIS, J.; ROLDO, M. Thermosensitive hydrogels for nasal drug delivery: the formulation and characterisation of systems based on N-trimethyl chitosan chloride. **European Journal of Pharmaceutics and Biopharmaceutics**, Amsterdam, v. 77, n. 2, p. 225–232, 2011.

NIKIFORIDIS, C. V.; SCHOLTEN, E. Polymer organogelation with chitin and chitin nanocrystals. **RSC Advances**, Cambridge, v. 5, n. 47, p. 37789–37799, 2015.

NO, H. K.; MEYERS, S. P. Preparation and characterization of chitin and chitosan - a review. **Journal of Aquatic Food Product Technology**, New York, v. 4, n. 2, p. 27–52, 1995.

NOVOA-CARBALLAL, R.; FERNANDEZ-MEGIA, E.; RIGUERA, R. Dynamics of chitosan by  $^1\text{H}$  NMR relaxation. **Biomacromolecules**, Washington, v. 11, n. 8, p. 2079–2086, 2010.

OGAWA, K.; YUI, T. Crystallinity of partially N-acetylated chitosans. **Bioscience, Biotechnology, and Biochemistry**, Oxford, v. 57, n. 9, p. 1466–1469, 1993.

OGAWA, K.; YUI, T.; MIYA, M. Dependence on the preparation procedure of the polymorphism and crystallinity of chitosan membranes. **Bioscience, Biotechnology, and Biochemistry**, Oxford, v. 56, n. 6, p. 858–862, 1992.

OH, D. X.; SHIN, S.; LIM, Ch.; HWANG, D. S. Dopamine-mediated sclerotization of regenerated chitin in ionic liquid. **Materials**, Basel, v. 6, n. 9, p. 3826–3839, 2013.

OKUYAMA, K.; NOGUCHI, K.; MIYAZAWA, T.; YUI, T.; OGAWA, K. Molecular and crystal structure of hydrated chitosan. **Macromolecules**, Washington, v. 30, n. 19, p. 5849–5855, 1997.

OSORIO-MADRAZO, A.; DAVID, L.; TROMBOTTO, S.; LUCAS, J. M.; PENICHE-COVAS, C.; DOMARD, A. Kinetics study of the solid-state acid hydrolysis of chitosan: evolution of the crystallinity and macromolecular structure. **Biomacromolecules**, Washington, v. 11, n. 5, p. 1376–1386, 2010.

OTONI, C. G.; CARVALHO, A. S.; CARDOSO, M. V.C.; BERNARDINELLI, O. D.; LOREVICE, M. V.; COLNAGO, L. A.; LOH, W.; MATTOSO, L. H. C. High-pressure microfluidization as a green tool for optimizing the mechanical performance of all-cellulose composites. **ACS Sustainable Chemistry and Engineering**, Washington, v. 6, n. 10, p. 12727–12735, 2018.

OTTØY, M. H.; VÅRUM, K. M.; SMIDSRØD, O. Compositional heterogeneity of heterogeneously deacetylated chitosans. **Carbohydrate Polymers**, Oxford, v. 29, n. 1, p. 17–24, 1996.

PAILLET, M.; DUFRESNE, A. Chitin whisker reinforced thermoplastic nanocomposites. **Macromolecules**, Washington, v. 34, n. 19, p. 6527–6530, 2001.

PALMEIRA-DE-OLIVEIRA, A.; RIBEIRO, M. P.; PALMEIRA-DE-OLIVEIRA, R.; GASPAR, C.; COSTA-DE-OLIVEIRA, S.; CORREIA, I. J.; PINA VAZ, C.; MARTINEZ-DE-OLIVEIRA, J.; QUEIROZ, J. A.; RODRIGUES, A. G. Anti-Candida activity of a chitosan hydrogel: mechanism of action and cytotoxicity profile. **Gynecologic and Obstetric Investigation**, Basel, v. 70, n. 4, p. 322–327, 2010.

PALMEIRA-DE-OLIVEIRA, R.; PALMEIRA-DE-OLIVEIRA, A.; GASPAR, C.; SILVESTRE, S.; MARTINEZ-DE-OLIVEIRA, J.; MARAL, M. H.; BREITENFELD, L. Sodium tripolyphosphate: an excipient with intrinsic in vitro anti-*Candida* activity. **International Journal of Pharmaceutics**, Amsterdam, v. 421, n. 1, p. 130–134, 2011.

PALMEIRA-DE-OLIVEIRA, R.; DUARTE, P.; PALMEIRA-DE-OLIVEIRA, A.; DAS NEVES, J.; AMARAL, M. H.; BREITENFELD, L.; MARTINEZ-DE-OLIVEIRA, J. Women's experiences, preferences and perceptions regarding vaginal products: results from a cross-sectional web-based survey in Portugal. **The European Journal of Contraception and Reproductive Health Care**, Oxfordshire, v. 20, n. 4, p. 259–271, 2015.

PARK, S.; BAKER, J. O.; HIMMEL, M. E.; PARILLA, P. A.; JOHNSON, D. K. Cellulose crystallinity index: measurement techniques and their impact on interpreting cellulase performance. **Biotechnology for Biofuels**, London, v. 3, n. 1, p. 1–10, 2010.

PARK, Y.; KIM, M. H.; PARK, S. C.; CHEONG, H.; JANG, M. K.; NAH, J. W.; HAHM, K. S. Investigation of the antifungal activity and mechanism of action of LMWS-chitosan. **Journal of Microbiology and Biotechnology**, Seoul, v. 18, n. 10, p. 1729–1734, 2008.

PAVINATTO, A.; FIAMINGO, A.; BUKZEM, A. L.; SILVA, D. S.; SANTOS, D. M.; SENRA, T. A. D.; FACCHINATTO, W. M.; CAMPANA-FILHO, S. P. Chemically modified chitosan derivatives. *In*: DOTTO, G. L.; CAMPANA-FILHO, S. P.; DE ALMEIDA, L. A. (ed.). **Chitosan based materials and its applications**. Sharjah: Bentham Science Publishers, 2017. v. 3, p. 111–137.

- PENG, H. S.; LIU, X. J.; LV, G. X.; SUN, B.; KONG, Q. F.; ZHAI, D. X.; WANG, Q.; ZHAO, W.; WANG, G. Y.; WANG, D. D.; LI, H. L.; JIN, L. H.; KOSTULAS, N. Voriconazole into PLGA nanoparticles: improving agglomeration and antifungal efficacy. **International Journal of Pharmaceutics**, Amsterdam, v. 352, n. 1–2, p. 29–35, 2008.
- PENG, Z. X.; WANG, L.; DU, L.; GUO, S. R.; WANG, X. Q.; TANG, T. T. Adjustment of the antibacterial activity and biocompatibility of hydroxypropyltrimethyl ammonium chloride chitosan by varying the degree of substitution of quaternary ammonium. **Carbohydrate Polymers**, Oxford, v. 81, n. 2, p. 275–283, 2010.
- PEREIRA, F. M. V.; PFLANZER, S. B.; GOMIG, T.; GOMES, C. L.; DE FELÍCIO, P. E.; COLNAGO, L. A. Fast determination of beef quality parameters with time-domain nuclear magnetic resonance spectroscopy and chemometrics. **Talanta**, Amsterdam, v. 108, p. 88–91, 2013.
- PINES, A.; GIBBY, M. G.; WAUGH, J. S. Proton-enhanced NMR of dilute spins in solids. **The Journal of Chemical Physics**, Melville, v. 59, n. 2, p. 569, 1973.
- PINES, A.; RHIM, W. K.; WAUGH, J. S. Homogeneous and inhomogeneous nuclear spin echoes in solids. **Journal of Magnetic Resonance**, Maryland Heights, v. 6, n. 4, p. 457–465, 1972.
- PIRES, C. T. G. V. M. T.; VILELA, J. A. P.; AIROLDI, C. The effect of chitin alkaline deacetylation at different condition on particle properties. **Procedia Chemistry**, Amsterdam, v. 9, p. 220–225, 2014.
- PIRON, E.; DOMARD, A. Interaction between chitosan and uranyl ions. Part 2. Mechanism of interaction. **International Journal of Biological Macromolecules**, Amsterdam, v. 22, n. 1, p. 33–40, 1998.
- PRABAHARAN, M.; GONG, S. Novel thiolated carboxymethyl chitosan-g- $\beta$ -cyclodextrin as mucoadhesive hydrophobic drug delivery carriers. **Carbohydrate Polymers**, Oxford, v. 73, n. 1, p. 117–125, 2008.
- PRÄBST, K.; ENGELHARDT, H.; RINGGELER, S.; HÜBNER, H. Basic colorimetric proliferation assays: MTT, WST, and Resazurin. *In*: GUILBERT D.; FRIEDRICH O. (ed.). **Cell viability assays**. Methods in molecular biology. Humana Press: New York, 2017, v. 1601, p. 1-17.
- QIN, C.; XIAO, Q.; LI, H.; FANG, M.; LIU, Y.; CHEN, X.; LI, Q. Calorimetric studies of the action of chitosan-N-2-hydroxypropyl trimethyl ammonium chloride on the growth of microorganisms. **International Journal of Biological Macromolecules**, Amsterdam, v. 34, n. 1–2, p. 121–126, 2004.
- QIN, Y.; LI, P.; GUO, Z. Cationic chitosan derivatives as potential antifungals: a review of structural optimization and applications. **Carbohydrate Polymers**, Oxford, v. 236, n. February, p. 116002, 2020.

QU, G.; YAO, Z.; ZHANG, C.; WU, X.; PING, Q. PEG conjugated N-octyl-O-sulfate chitosan micelles for delivery of paclitaxel: In vitro characterization and *in vivo* evaluation. **European Journal of Pharmaceutical Sciences**, Amsterdam, v. 37, n. 2, p. 98–105, 2009.

REICHERT, D.; PASCUI, O.; DE AZEVEDO, E. R.; BONAGAMBA, T. J.; ARNOLD, K.; HUSTER, D. A solid-state NMR study of the fast and slow dynamics of collagen fibrils at varying hydration levels. **Magnetic Resonance in Chemistry**, Oxford, v. 42, n. 2, p. 276–284, 2004.

REVOL, J. F.; MARCHESSAULT, R. H. *In vitro* chiral nematic ordering of chitin crystallites. **International Journal of Biological Macromolecules**, Amsterdam, v. 15, n. 6, p. 329–335, 1993.

RHIM, W-K.; PINES, A.; WAUGH, J. S. Time-reversal experiments in dipolar-coupled spin systems. **Physical Review B**, College Park, v. 3, n. 3, p. 684–696, 1971.

RICHARDSON, S. C. W.; KOLBE, H. V. J.; DUNCAN, R. Potential of low molecular mass chitosan as a DNA delivery system: biocompatibility, body distribution and ability to complex and protect DNA. **International Journal of Pharmaceutics**, Amsterdam, v. 178, n. 2, p. 231–243, 1999.

RICHTER, S. S.; GALASK, R. P.; MESSER, S. A.; HOLLIS, R. J.; DIEKEMA, D. J.; PFALLER, M. A. Antifungal susceptibilities of *Candida* species causing vulvovaginitis and epidemiology of recurrent cases. **Journal of Clinical Microbiology**, Washington, v. 43, n. 5, p. 2155–2162, 2005.

RIEHLE, F.; HOENDERS, D.; GUO, J.; ECKERT, A.; IFUKU, S.; WALTHER, A. Sustainable chitin nanofibrils provide outstanding flame-retardant nanopapers. **Biomacromolecules**, Washington, v. 20, n. 2, p. 1098–1108, 2019.

RINAUDO, M.; MILAS, M.; LE DUNG, P. Characterization of chitosan. Influence of ionic strength and degree of acetylation on chain expansion. **International Journal of Biological Macromolecules**, Amsterdam, v. 15, n. 5, p. 281–5, 1993.

ROGOVINA, S. Z.; AKOPOVA, T. A.; VIKHOREVA, G. A. Investigation of properties of chitosan obtained by solid-phase and suspension methods. **Journal of Applied Polymer Science**, Hoboken, v. 70, n. 5, p. 927–933, 1998.

RUIHUA, H.; BINGCHAO, Y.; ZHENG, D.; WANG, B. Preparation and characterization of a quaternized chitosan. **Journal of Materials Science**, New York, v. 47, n. 2, p. 845–851, 2012.

SAADATFAR, F.; SHAYANFAR, A.; RAHIMPOUR, E.; BARZEGAR-JALALI, M.; MARTINEZ, F.; BOLOURTCHIAN, M.; JOUYBAN, A. Measurement and correlation of clotrimazole solubility in ethanol + water mixtures at  $T = (293.2 \text{ to } 313.2) \text{ K}$ . **Journal of Molecular Liquids**, Amsterdam, v. 256, p. 527–532, 2018.

SAALWÄCHTER, K. Detection of heterogeneities in dry and swollen polymer networks by proton low-field nmr spectroscopy. **Journal of the American Chemical Society**, Washington, v. 125, n. 48, p. 14684–14685, 2003.

SAALWÄCHTER, K. Proton multiple-quantum NMR for the study of chain dynamics and structural constraints in polymeric soft materials. **Progress in Nuclear Magnetic Resonance Spectroscopy**, Amsterdam, v. 51, n. 1, p. 1–35, 2007.

SAHU, A.; GOSWAMI, P.; BORA, U. Microwave mediated rapid synthesis of chitosan. **Journal of Materials Science. Materials in medicine**, New York, v. 20, n. 1, p. 171–5, 2009.

SAIDEL, M. É.; DOS SANTOS, K. C.; NAGANO, L. F. P.; MONTANARI, C. A.; LEITÃO, A. Novel anti-prostate cancer scaffold identified by the combination of in silico and cell-based assays targeting the PI3K-AKT-mTOR pathway. **Bioorganic and Medicinal Chemistry Letters**, Oxford, v. 27, n. 17, p. 4001–4006, 2017.

SAITÔ, H.; TABETA, R.; OGAWA, K.. High-resolution solid-state  $^{13}\text{C}$  NMR study of chitosan and its salts with acids: Conformational characterization of polymorphs and helical structures as viewed from the conformation-dependent  $^{13}\text{C}$  chemical shifts. **Macromolecules**, Washington, v. 20, n. 10, p. 2424–2430, 1987.

SAITO, Y.; PUTAUX, J.-I.; OKANO, T.; GAILL, F.; CHANZY, H. Structural aspects of the swelling of  $\beta$  chitin in HCl and its conversion into  $\alpha$  chitin. **Macromolecules**, Washington, v. 30, p. 3867–3873, 1997.

SAITO, Y.; OKANO, T.; GAILL, F.; CHANZY, H.; PUTAUX, J.-L. Structural data on the intra-crystalline swelling of  $\beta$ -chitin. **International Journal of Biological Macromolecules**, Amsterdam, v. 28, n. 1, p. 81–88, 2000.

SAJOMSANG, W.; RUKTANONCHAI, U. R.; GONIL, P.; NUCHUCHUA, O. Mucoadhesive property and biocompatibility of methylated N-aryl chitosan derivatives. **Carbohydrate Polymers**, Oxford, v. 78, n. 4, p. 945–952, 2009.

SANDRI, G.; ROSSI, S.; FERRARI, F.; BONFERONI, M. C.; MUZZARELLI, C.; CAMELLA, C. Assessment of chitosan derivatives as buccal and vaginal penetration enhancers. **European Journal of Pharmaceutical Sciences**, Amsterdam, v. 21, n. 2–3, p. 351–359, 2004.

SANTOS, D. M.; LEITE, I. S.; BUKZEM, A. L.; SANTOS, R. P. O.; FROLLINI, E.; INADA, N. M.; CAMPANA-FILHO, S. P. Nanostructured electrospun nonwovens of poly( $\epsilon$ -caprolactone)/quaternized chitosan for potential biomedical applications. **Carbohydrate Polymers**, Oxford, v. 186, p. 110–121, 2018.

SANTOS, D. M.; BUKZEM, A. L.; CAMPANA-FILHO, S. P. Response surface methodology applied to the study of the microwave-assisted synthesis of quaternized chitosan. **Carbohydrate Polymers**, Oxford, v. 138, p. 317–326, 2016.

SANTOS, P. M.; CORRÊA, C. C.; FORATO, L. A.; TULLIO, R. R.; CRUZ, G. M.; COLNAGO, L. A. A fast and non-destructive method to discriminate beef samples using TD-NMR. **Food Control**, Oxford, v. 38, n. 1, p. 204–208, 2014.

SANTOS, S. S.; LORENZONI, A.; FERREIRA, L. M.; MATTIAZZI, J.; ADAMS, A. I. H.; DENARDI, L. B.; ALVES, S. H.; SCHAFFAZICK, S. R.; CRUZ, L. Clotrimazole-loaded Eudragit® RS100 nanocapsules: preparation, characterization and in vitro evaluation of antifungal activity against *Candida* species. **Materials Science and Engineering C**, Amsterdam, v. 33, n. 3, p. 1389–1394, 2013.

SANTOS, S. S.; LORENZONI, A.; PEGORARO, N. S.; DENARDI, L. B.; ALVES, S. H.; SCHAFFAZICK, S. R.; CRUZ, L. Formulation and in vitro evaluation of coconut oil-core cationic nanocapsules intended for vaginal delivery of clotrimazole. **Colloids and Surfaces B: biointerfaces**, Amsterdam, v. 116, p. 270–276, 2014.

SARLES, L. R.; COTTS, R. M. Double nuclear magnetic resonance and the dipole interaction in solids. **Physical Review**, College Park, v. 111, n. 3, p. 853–859, 1958.

SAVITRI, E.; JULIASTUTI, S. R.; HANDARATRI, A.; SUMARNO; ROESYADI, A. Degradation of chitosan by sonication in very-low-concentration acetic acid. **Polymer Degradation and Stability**, London, v. 110, p. 344–352, 2014.

SAYIN, B.; SOMAVARAPU, S.; LI, X. W.; SESARDIC, D.; SENEL, S.; ALPAR, O. H. TMC – MCC (N-trimethyl chitosan – mono-N-carboxymethyl chitosan) nanocomplexes for mucosal delivery of vaccines. **European Journal of Pharmaceutical Sciences**, Amsterdam, v. 38, p. 362–369, 2009.

SCHÄLER, K.; ROOS, M.; MICKE, P.; GOLITSYN, Y.; SEIDLITZ, A.; THURN-ALBRECHT, T.; SCHNEIDER, H.; HEMPEL, G.; SAALWÄCHTER, K. Basic principles of static proton low-resolution spin diffusion NMR in nanophase-separated materials with mobility contrast. **Solid State Nuclear Magnetic Resonance**, London, v. 72, p. 50–63, 2015.

SCHENZEL, K.; FISCHER, S.; BRENDLER, E. New method for determining the degree of cellulose I crystallinity by means of FT Raman spectroscopy. **Cellulose**, Dordrecht, v. 12, n. 3, p. 223–231, 2005.

SCHIPPER, N. G. M.; VÅRUM, K. M.; ARTURSSON, P. Chitosans as absorption enhancers for poorly absorbable drugs. 1: influence of molecular weight and degree of acetylation on drug transport across human intestinal epithelial (Caco-2) cells. **Pharmaceutical Research**, New York, v. 13, n. 11, p. 1686–1692, 1996.

SCHMIDT-ROHR, K.; SPIESS, H. W. **Multidimensional solid-state NMR and polymers**. San Diego: Academic Press, 1994. 478 p.

SHAGDAROVA, B.; LUNKOV, A.; IL'INA, A.; VARLAMOV, V. Investigation of the properties of N-[(2-hydroxy-3-trimethylammonium) propyl] chloride chitosan derivatives. **International Journal of Biological Macromolecules**, Amsterdam, v. 124, p. 994–1001, 2019.

SHAMSHINA, J. L.; BERTON, P.; ROGERS, R. D. Advances in functional chitin materials: a review. **ACS Sustainable Chemistry & Engineering**, Washington, vol. 7, p. 6444–6457, 2019.

SHANMUGANATHAN, R.; EDISON, T. N. J. I.; LEWISOSCAR, F.; KUMAR, P.; SHANMUGAM, S.; PUGAZHENDHI, A. Chitosan nanopolymers: an overview of drug delivery against cancer. **International Journal of Biological Macromolecules**, Amsterdam, v. 130, p. 727–736, 2019.

SHON, K-J.; KIM, Y.; COLNAGO, L. A.; OPELLA, S. J. NMR studies of the structure and dynamics of membrane-bound bacteriophage Pfl coat protein. **Science**, Washington, v. 252, p. 1303–1305, 1991.

SHUKLA, S. K.; MISHRA, A. K.; AROTIBA, O. A.; MAMBA, B. B. Chitosan-based nanomaterials: a state-of-the-art review. **International Journal of Biological Macromolecules**, Amsterdam, v. 59, p. 46–58, 2013.

SIERRA-MARTÍN, B.; ROMERO-CANO, M. S.; COSGROVE, T.; VINCENT, B.; FERNÁNDEZ-BARBERO, A. Solvent relaxation of swelling PNIPAM microgels by NMR. **Colloids and Surfaces A: physicochemical and engineering aspects**, Amsterdam, v. 270–271, n. 1–3, p. 296–300, 2005.

SIEW, A.; LE, H.; THIOVOLET, M.; GELLERT, P.; SCHATZLEIN, A.; UCHEGBU, I. Enhanced oral absorption of hydrophobic and hydrophilic drugs using quaternary ammonium palmitoyl glycol chitosan nanoparticles. **Molecular Pharmaceutics**, Washington, v. 9, n. 1, p. 14–28, 2012.

SIKORSKI, P.; HORI, R.; WADA, M. Revisit of  $\alpha$ -chitin crystal structure using high resolution X-ray diffraction data. **Biomacromolecules**, Washington, v. 10, n. 5, p. 1100–1105, 2009.

SILVA, C. A.; NOBRE, T. M.; PAVINATTO, F. J.; OLIVEIRA, O. N. Interaction of chitosan and mucin in a biomembrane model environment. **Journal of Colloid and Interface Science**, Philadelphia, v. 376, n. 1, p. 289–295, 2012.

SILVA, D. S.; ALMEIDA, A.; PREZOTTI, F.; CURY, B.; CAMPANA-FILHO, S. P.; SARMENTO, B. Synthesis and characterization of 3,6-O,O'-dimyristoyl chitosan micelles for oral delivery of paclitaxel. **Colloids and Surfaces B: biointerfaces**, Amsterdam, v. 152, p. 220–228, 2017.

SILVA, D. S.; ALMEIDA, A.; PREZOTTI, F. G.; FACCHINATTO, W. M.; COLNAGO, L. A.; CAMPANA-FILHO, S. P.; SARMENTO, B. Self-aggregates of 3,6-O,O'-dimyristoylchitosan derivative are effective in enhancing the solubility and intestinal permeability of camptothecin. **Carbohydrate Polymers**, Oxford, v. 177, p. 178–186, 2017.

SILVA, D. S.; SANTOS, D. M.; ALMEIDA, A.; MARCHIORI, L.; CAMPANA-FILHO, S. P.; RIBEIRO, S. J. L.; SARMENTO, B. N-(2-hydroxy)-propyl-3-trimethylammonium, O-myristoyl chitosan enhances the solubility and intestinal permeability of anticancer curcumin. **Pharmaceutics**, Basel, v. 10, n. 4, p. 1–18, 2018.

SILVA, D. S.; FACCHINATTO, W. M.; SANTOS, D. M.; BONI, F. I.; VALDES, T. A.; LEITÃO, A.; GREMIÃO, M. P. D.; COLNAGO, L. A.; CAMPANA-FILHO, S. P.; RIBEIRO, S. N-(2-hydroxy)-propyl-3-trimethylammonium, O-palmitoyl chitosan: Synthesis, physicochemical and biological properties. **International Journal of Biological Macromolecules**, Amsterdam, 2021.

SIMMONS, T. J.; MORTIMER, J. C.; BERNARDINELLI, O. D.; PÖPPLER, A. C.; BROWN, S. P.; DE AZEVEDO, E. R.; DUPREE, R.; DUPREE, P. Folding of xylan onto cellulose fibrils in plant cell walls revealed by solid-state NMR. **Nature Communications**, London, v. 7, p. 1–9, 2016.

SINHA, N.; GRANT, C. V.; WU, C. H.; DE ANGELIS, A. A.; HOWELL, S. C.; OPELLA, S. J. SPINAL modulated decoupling in high field double- and triple-resonance solid-state NMR experiments on stationary samples. **Journal of Magnetic Resonance**, Maryland Heights, v. 177, n. 2, p. 197–202, 2005.

SNYMAN, D.; HAMMAN, J. H.; KOTZE, A. F. Evaluation of the mucoadhesive properties of N-trimethyl chitosan chloride. **Drug Development and Industrial Pharmacy**, Philadelphia, v. 29, n. 1, p. 61–69, 2003.

SOBEL, J. D. Vulvovaginal candidosis. **The Lancet**, London, v. 369, n. 9577, p. 1961–1971, 2007.

SOGIAS, I. A.; KHUTORYANSKIY, V. V.; WILLIAMS, A. C. Exploring the factors affecting the solubility of chitosan in water. **Macromolecular Chemistry and Physics**, Weinheim, v. 211, n. 4, p. 426–433, 2010.

SOGIAS, I. A.; WILLIAMS, A. C.; KHUTORYANSKIY, V. V. Why is chitosan mucoadhesive? **Biomacromolecules**, Washington, v. 9, n. 7, p. 1837–1842, 2008.

SOLICH, P.; HÁJKOVÁ, R.; POSPÍLOVÁ, M.; DÍCHA, J. Determination of methylparaben, propylparaben, clotrimazole and its degradation products in topical cream by RP-HPLC. **Chromatographia**, Heidelberg, v. 56, p. 181–184, 2002.

SONIA, T. A.; SHARMA, C. P. *In vitro* evaluation of N-(2-hydroxy) propyl-3-trimethyl ammonium chitosan for oral insulin delivery. **Carbohydrate Polymers**, Oxford, v. 84, n. 1, p. 103–109, 2011.

SORIANO-RUIZ, J. L.; CALPENA-CAPMANY, A. C.; CAÑADAS-ENRICH, C.; FEBRER, N. B.; SUÑER-CARBÓ, J.; SOUTO, E. B.; CLARES-NAVEROS, B. Biopharmaceutical profile of a clotrimazole nanoemulsion: evaluation on skin and mucosae as anticandidal agent. **International Journal of Pharmaceutics**, Amsterdam, v. 554, n. October, p. 105–115, 2019.

SORLIER, P.; DENUZIÈRE, A.; VITON, C.; DOMARD, A. Relation between the degree of acetylation and the electrostatic properties of chitin and chitosan. **Biomacromolecules**, Washington, v. 2, n. 3, p. 765–772, 2001.

SOSNIK, A.; DAS NEVES, J.; SARMENTO, B. Mucoadhesive polymers in the design of nano-drug delivery systems for administration by non-parenteral routes: a review. **Progress in Polymer Science**, London, v. 39, n. 12, p. 2030–2075, 2014.

ŠTĚPÁNEK, M.; PODHÁJECKÁ, K.; TESAŘOVÁ, E.; PROCHÁZKA, K.; TUZAR, Z.; BROWN, W. Hybrid polymeric micelles with hydrophobic cores and mixed polyelectrolyte/nonelectrolyte shells in aqueous media. 1. Preparation and basic characterization. **Langmuir**, Washington, v. 17, n. 14, p. 4240–4244, 2001.

STRUSZCZYK, H. Microcrystalline chitosan. I. Preparation and properties of microcrystalline chitosan. **Journal of Applied Polymer Science**, Hoboken, v. 33, n. 1, p. 177–189, 1987.

TABRIZ, A.; ALVI, M. A. U. R.; NIAZI, M. B. K.; BATOOL, M.; BHATTI, M. F.; KHAN, A. L.; KHAN, A. U.; JAMIL, T.; AHMAD, N. M. Quaternized trimethyl functionalized chitosan based antifungal membranes for drinking water treatment. **Carbohydrate Polymers**, Oxford, v. 207, 2018, p. 17–25, 2019.

TAKEGOSHI, K.; MCDOWELL, C. A. A “magic echo” pulse sequence for the high-resolution NMR spectra of abundant spins in solids. **Chemical Physics Letters**, Amsterdam, v. 116, n. 2–3, p. 100–104, 1985.

TAKETA, T. B.; SANTOS, D. M.; FIAMINGO, A.; VAZ, J. M.; BEPPU, M. M.; CAMPANA-FILHO, S. P.; COHEN, R. E.; RUBNER, M. F. Investigation of the internal chemical composition of chitosan-based LbL films by depth-profiling X-ray photoelectron spectroscopy (XPS) analysis. **Langmuir**, Washington, v. 34, n. 4, p. 1429–1440, 2018.

TANNER, S. F.; CHANZY, H.; VINCENDON, M.; ROUX, J. C.; GAILL, F. High-resolution solid-state carbon-13 nuclear magnetic resonance study of chitin. **Macromolecules**, Washington, v. 23, n. 15, p. 3576–3583, 1990.

TATSUMI, D.; ISHIOKA, S.; MATSUMOTO, T. Effect of fiber concentration and axial ratio on the rheological properties of cellulose fiber suspensions. **Journal of Society of Rheology**, Japan, v. 30, n. 1, p. 27–32, 2002.

TAYEL, A. A.; MOUSSA, S.; EL-TRAS, W. F.; KNITTEL, D.; OPWIS, K.; SCHOLLMAYER, E. Anticandidal action of fungal chitosan against *Candida albicans*. **International Journal of Biological Macromolecules**, Amsterdam, v. 47, n. 4, p. 454–457, 2010.

THAKHIEW, W.; DEVAHASTIN, S.; SOPONRONNARIT, S. Physical and mechanical properties of chitosan films as affected by drying methods and addition of antimicrobial agent. **Journal of Food Engineering**, London, v. 119, n. 1, p. 140–149, 2013.

TODT, H.; GUTHAUSEN, G.; BURK, W.; SCHMALBEIN, D.; KAMLOWSKI, A. Water/moisture and fat analysis by time-domain NMR. **Food Chemistry**, Amsterdam, v. 96, n. 3, p. 436–440, 2006.

TONELLI, A. E.; SCHILLING, F. C. Carbon-13 NMR chemical shifts and the microstructure of polymers. **Accounts of Chemical Research**, Washington, v. 14, n. 8, p. 233–238, 1981.

VACHOUD, L.; ZYDOWICZ, N.; DOMARD, A. Formation and characterisation of a physical chitin gel. **Carbohydrate Research**, Oxford, v. 302, n. 3–4, p. 169–177, 1997.

VAN ROSSUM, B. J.; FÖRSTER, H.; DE GROOT, H. J. M. High-field and high-speed CP-MAS <sup>13</sup>C NMR heteronuclear dipolar-correlation spectroscopy of solids with frequency-switched Lee-Goldburg homonuclear decoupling. **Journal of Magnetic Resonance**, Maryland Heights, v. 124, n. 2, p. 516–519, 1997.

VAN VLECK, J. H. The dipolar broadening of magnetic resonance lines in crystals. **Physical Review**, College Park, v. 74, n. 9, p. 1168–1183, 1948.

VANIĆ, Ž.; ŠKALKO-BASNET, N. Nanopharmaceuticals for improved topical vaginal therapy: can they deliver? **European Journal of Pharmaceutical Sciences**, Amsterdam, v. 50, n. 1, p. 29–41, 2013.

VÅRUM, K. M.; ANTHONSEN, M. W.; GRASDALEN, H.; SMIDSRØD, O. Determination of the degree of N-acetylation and the distribution of N-acetyl groups in partially N-deacetylated chitins (chitosans) by high-field N.M.R. spectroscopy. **Carbohydrate Research**, Oxford, v. 211, n. 1, p. 17–23, 1991.

VERLEE, A.; MINCKE, S.; STEVENS, C. V. Recent developments in antibacterial and antifungal chitosan and its derivatives. **Carbohydrate Polymers**, Oxford, v. 164, p. 268–283, 2017.

VIËTOR, R. J.; NEWMAN, R. H.; HA, M. A.; APPERLEY, D. C.; JARVIS, M. C. Conformational features of crystal-surface cellulose from higher plants. **Plant Journal**, Chichester, v. 30, n. 6, p. 721–731, 2002.

VILLAS-BOAS, F.; FACCHINATTO, W. M.; COLNAGO, L. A.; VOLANTI, D. P.; FRANCO, C. M. L. Effect of amylolysis on the formation, the molecular, crystalline and thermal characteristics and the digestibility of retrograded starches. **International Journal of Biological Macromolecules**, Amsterdam, v. 163, p. 1333–1343, 2020.

VINOGRADOV, E.; MADHU, P. K.; VEGA, S. High-resolution proton solid-state NMR spectroscopy by phase-modulated Lee–Goldburg experiment. **Chemical Physics Letters**, Amsterdam, v. 314, n. 5–6, p. 443–450, 1999.

VINSOVÁ, J.; VAVRIKOVÁ, E. Chitosan derivatives with antimicrobial, antitumour and antioxidant activities - a review. **Current Pharmaceutical Design**, Sharjah, v. 17, n. 32, p. 3596–607, 2011.

WÄCHTLER, B.; WILSON, D.; HUBE, B. *Candida albicans* adhesion to and invasion and damage of vaginal epithelial cells: stage-specific inhibition by clotrimazole and bifonazole. **Antimicrobial Agents and Chemotherapy**, Washington, v. 55, n. 9, p. 4436–4439, 2011.

WANG, J.; WANG, Z.; LI, J. WANG, B.; LIU, J.; CHEN, P.; MIAO, M.; GU, Q. Chitin nanocrystals grafted with poly(3-hydroxybutyrate-co-3-hydroxyvalerate) and their effects on thermal behavior of PHBV. **Carbohydrate Polymers**, Oxford, v. 87, n. 1, p. 784–789, 2012.

WANG, S. L.; CHIO, S. H. Deproteinization of shrimp and crab shell with the protease of *Pseudomonas aeruginosa* K-187. **Enzyme and Microbial Technology**, Philadelphia, v. 22, n. 7, p. 629–633, 1998.

WANG, T.; LIU, T.; WANG, Z.; TIAN, X.; YANG, Y.; GUO, M.; CHU, J.; ZHUANG, Y. A rapid and accurate quantification method for real-time dynamic analysis of cellular lipids during microalgal fermentation processes in *Chlorella protothecoides* with low field nuclear magnetic resonance. **Journal of Microbiological Methods**, Amsterdam, v. 124, p. 13–20, 2016.

WANG, T.; HONG, M. Solid-state NMR investigations of cellulose structure and interactions with matrix polysaccharides in plant primary cell walls. **Journal of Experimental Botany**, Oxford, v. 67, n. 2, p. 503–514, 2016.

WAYS, T. M. M.; LAU, W. M.; KHUTORYANSKIY, V. V. Chitosan and its derivatives for application in mucoadhesive drug delivery systems. **Polymers**, Basel, v. 10, n. 3, p. 1–37, 2018.

WEBSTER, A.; OSIFO, P. O.; NEOMAGUS, H. W. J. P.; GRANT, D. M. A comparison of glycans and polyglycans using solid-state NMR and X-ray powder diffraction. **Solid State Nuclear Magnetic Resonance**, London, v. 30, n. 3–4, p. 150–161, 2006.

WEINHOLD, M. X.; SAUVAGEAU, J. C. M.; KUMIRSKA, J.; THÖMING, J. Studies on acetylation patterns of different chitosan preparations. **Carbohydrate Polymers**, Oxford, v. 78, n. 4, p. 678–684, 2009.

WEITEKAMP, D. P.; GARBOW, J. R.; PINES, A. Determination of dipole coupling constants using heteronuclear multiple quantum NMR. **The Journal of Chemical Physics**, Melville, v. 77, n. 6, p. 2870–2883, 1982.

WHALEY, S. G.; BERKOW, E. L.; RYBAK, J. M.; NISHIMOTO, A. T.; BARKER, K. S.; ROGERS, P. D. Azole antifungal resistance in *Candida albicans* and emerging non-albicans *Candida* species. **Frontiers in Microbiology**, Lausanne, v. 7, p. 1–12, 2017. h173.

WORAPHATPHADUNG, T.; SAJOMSANG, W.; GONIL, P.; TREETONG, A.; AKKARAMONGKOLPORN, P.; NGAWHIRUNPAT, T.; OPANASOPIT, P. PH-Responsive polymeric micelles based on amphiphilic chitosan derivatives: Effect of hydrophobic cores on oral meloxicam delivery. **International Journal of Pharmaceutics**, Amsterdam, v. 497, n. 1–2, p. 150–160, 2016.

WU, J.; ZHANG, K.; GIROUARD, N.; MEREDITH, J. C. Facile route to produce chitin nanofibers as precursors for flexible and transparent gas barrier materials. **Biomacromolecules**, Washington, v. 15, n. 12, p. 4614–4620, 2014.

XIAO, B.; WAN, Y.; WANG, X.; ZHA, Q.; LIU, H.; QIU, Z.; ZHANG, S. Synthesis and characterization of N-(2-hydroxy)propyl-3-trimethyl ammonium chitosan chloride for potential application in gene delivery. **Colloids and Surfaces B: biointerfaces**, Amsterdam, v. 91, n. 1, p. 168–174, 2012.

XING, R.; LIU, S.; GUO, Z.; YU, H.; WANG, P.; LI, C.; LI, Z.; LI, P. Relevance of molecular weight of chitosan and its derivatives and their antioxidant activities *in vitro*. **Bioorganic & Medicinal Chemistry**, Oxford, v. 13, n. 5, p. 1573–1577, 2005.

XU, R.. Methods to resolve mobility from electrophoretic laser light scattering measurement. **Langmuir**, Washington, v. 9, n. 11, p. 2955–2962, 1993.

YUAN, Y.; CHESNUTT, B. M.; HAGGARD, W. O.; BUMGARDNER, J. D. Deacetylation of chitosan: material characterization and *in vitro* evaluation via albumin adsorption and pre-osteoblastic cell cultures. **Materials**, Basel, v. 4, n. 8, p. 1399–1416, 2011.

ZENG, J. B.; HE, Y. S.; LI, S. L.; WANG, Y. Z. Chitin whiskers: an overview. **Biomacromolecules**, Washington, v. 13, n. 1, p. 1–11, 2012.

ZENG, M.; GAO, H.; WU, Y.; FAN, L.; LI, A. Preparation and characterization of nanocomposite films from chitin whisker and waterborne poly(ester-urethane) with or without ultra-sonification treatment. **Journal of Macromolecular Science, Part A: pure and applied chemistry**, New York, v. 47, n. 8, p. 867–876, 2010.

ZHANG, R.; MIYOSHI, T.; SUN, P. **NMR methods for characterization of synthetic and natural polymers**. [S. l.]: The Royal Society of Chemistry, 2019. 565 p.

ZHANG, W.; HU, M.; SHI, Y.; GONG, T.; DEZZUTTI, C. S.; MONCLA, B.; SARAFIANOS, S. G.; PARNIAK, M. A.; ROHAN, L. C. Vaginal microbicide film combinations of two reverse transcriptase inhibitors, EFdA and CSIC, for the prevention of HIV-1 sexual transmission. **Pharmaceutical Research**, New York, v. 32, n. 9, p. 2960–2972, 2015.

ZHANG, Y.; XUE, C.; XUE, Y.; GAO, R.; ZHANG, X. Determination of the degree of deacetylation of chitin and chitosan by X-ray powder diffraction. **Carbohydrate Research**, Oxford, v. 340, n. 11, p. 1914–1917, 2005.

ZHOU, Y.; SHI, H.; ZHAO, Y.; MEN, Y.; JIANG, S.; ROTTSTEGGE, J.; WANG, D. Confined crystallization and phase transition in semi-rigid chitosan containing long chain alkyl groups. **CrystEngComm**, Cambridge, v. 13, n. 2, p. 561–567, 2011.

## APPENDIX A

Figure 56 - XRD resulted profile of  $\alpha$ Ch (a);  $\beta$ Ch (b); Ch60 (c); Ch45 (d); Ch35 (e); Ch25 (f); Ch15 (g) and Ch5 (h) samples after the subtraction of amorphous contribution. The  $L_{020}$  and  $L_{110}$  values were obtained from  $FWHM$  by peak deconvolution.

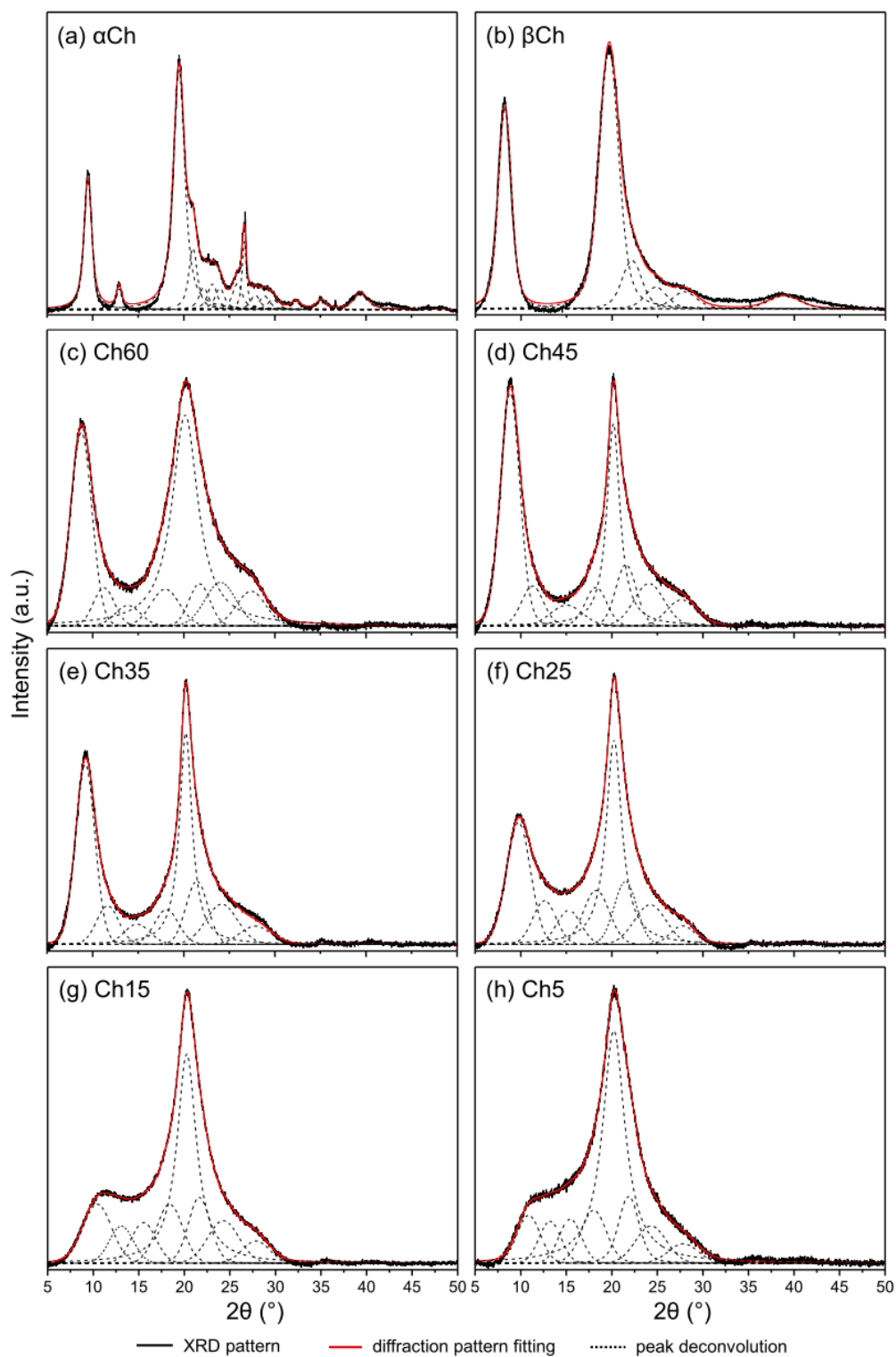
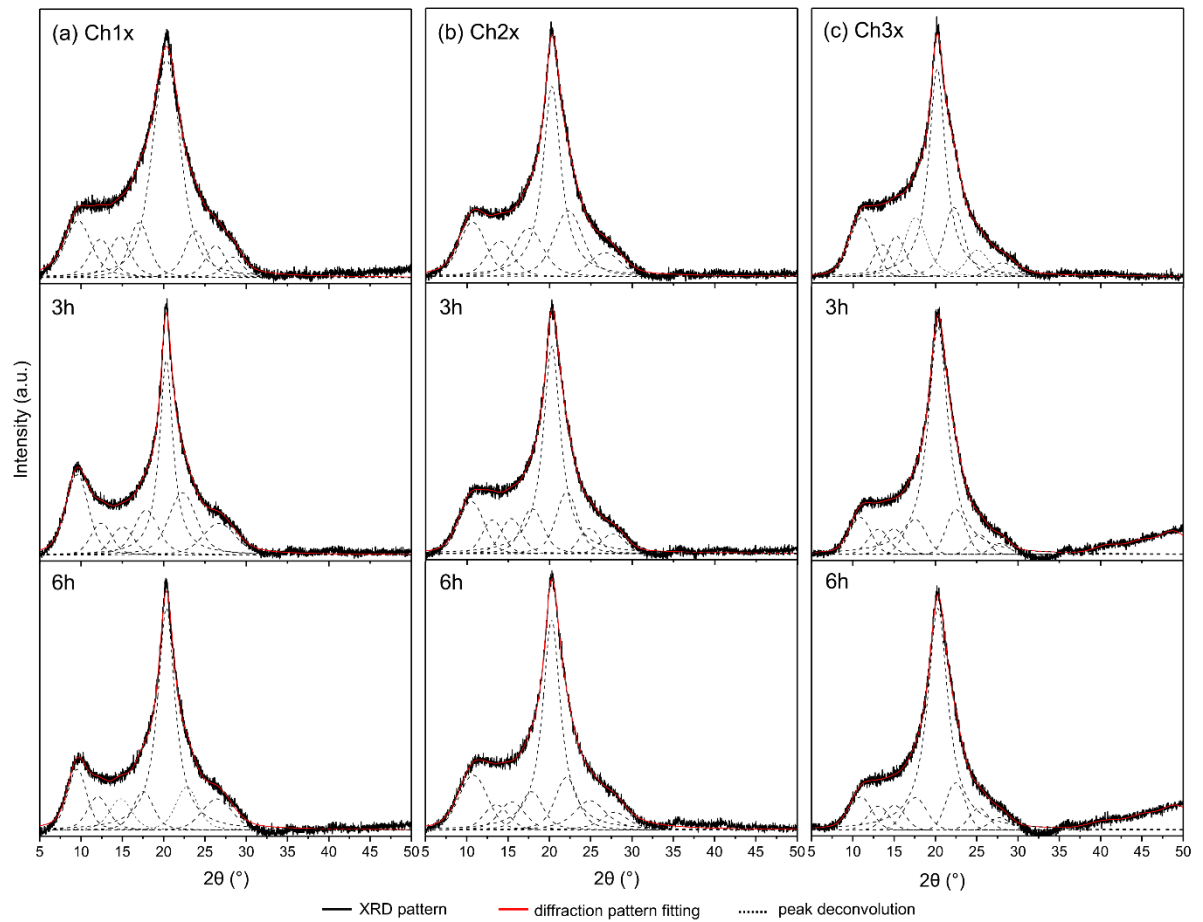


Figure 57 - XRD resulted profile of USAD Ch1x (a); Ch2x (b); Ch3x (c) with respect to the resulted profile of depolymerized (3h and 6h) samples, after the subtraction of amorphous contribution. The  $L_{020}$  and  $L_{110}$  values were obtained from  $FWHM$  by peak deconvolution.



## APPENDIX B

Figure 58 - XRD resulted profile of BCHL and CWHL (a); BCHI and CWHI (b); BCHS and CWHS (c) samples after the subtraction of amorphous contribution. The  $L_{020}$  and  $L_{110}$  values were obtained from  $FWHM$  by peak deconvolution.

